December 2013

Deformation and Fluid Interactions in the Mineral Fork Diamictites, Antelope Island, Utah

Kimberly Rose Johnson
University of Wisconsin-Milwaukee

DEFORMATION AND FLUID INTERACTIONS IN THE MINERAL FORK DIAMICTITES, ANTELOPE ISLAND, UTAH

by

Kimberly R. Johnson

A Thesis Submitted in

Partial Fulfillment of the

Requirements for the Degree of

Master of Science

in Geosciences

at

The University of Wisconsin-Milwaukee

December 2013

ABSTRACT

DEFORMATION AND FLUID INTERACTIONS IN THE MINERAL FORK DIAMICTITES, ANTELOPE ISLAND, UTAH

by

Kimberly R. Johnson

The University of Wisconsin-Milwaukee, 2013
Under the Supervision of Professor Dyanna Czeck

Diamictite from the Mineral Fork Formation on Antelope Island, Utah was deformed to various degrees on the footwall of the Willard Thrust Fault during the Sevier Orogeny. The diamictite contains clasts of differing strength resulting in quartzite clasts deformed the least, pink granitic clasts deformed to a greater degree, and softer green gneissic clasts deformed the most. The pink granitic and green gneissic clasts have similar compositions, but deform differently. This preliminary study explores the factors contributing to the different strain responses in the two clast types and the relations between fluids and deformation using three methods: synchrotron Fourier Transform Infrared spectroscopy (FTIR), X-Ray Fluorescence (XRF), and petrographic analyses of microstructures through point counting. An innovative use of a synchrotron infrared beamline is used to measure water content in quartz grains and create grain maps. Analyses of water peak heights and peak areas show that water is present in quartz in quartzite, granitic, and gneissic clasts, with no significant difference in the amount of water between the types. Water is present at all strain magnitudes and

often contained in fluid inclusions and microfractures suggesting fluid interaction during deformation. X-Ray Fluorescence (XRF) allows for the chemical analysis (major, minor, and trace elements) of the two clast types. Concentrations of Al_2O_3 and TiO_2, which are relatively immobile, remained approximately the same from low to high strain and are similar to concentrations in the Farmington Canyon Complex, the protolith. This suggests that no volume loss occurred in the clasts with deformation. The concentrations of relatively mobile SiO_2 also correlated with the parent rock. A decrease in sodium and increase in magnesium indicate fluid interaction with the clasts resulting in feldspar alteration to phengitic muscovite. Petrographic analyses of these samples reveal microstructures suggesting brittle deformation, dislocation creep (ductile deformation), and recovery processes evidenced by recrystallization and grain boundary migration. Fluid movement was likely aided by both microfractures and movement of dislocations. This exploratory study reveals evidence of fluid-rock interaction in both clast types, through both brittle and ductile deformation mechanisms.

TABLE OF CONTENTS

APPENDICES

LIST OF FIGURES

LIST OF TABLES

ACKNOWLEDGMENTS

I would like to thank:

Dr. Dyanna Czeck, my advising professor, for her input, flexibility, and assistance with the preparation of this thesis. I am extremely grateful to her for guidance and continuous help over the course of a few years.

Dr. Lindsay McHenry and Dr. Barry Cameron for their assistance in the XRF lab and FTIR lab respectively, their willingness to be on my thesis committee, and their assistance with revisions of this thesis.

Dr. W. Adolph Yonkee at Weber State University for his guidance and instruction in the field and in the lab.

Tristan Kloss and Micah Holzbauer for their assistance in collecting and mailing samples from the field.

This project was partially funded by NSF Grant EAR-0838240

Chapter 1: Introduction

1.1 Purpose

Despite the clear importance of fluids in deformation (e.g., Griggs, 1967; Tullis and Yund, 1989), varying effects of fluids are difficult to quantify in most naturally deformed rocks. This difficulty stems from the transient nature of fluid in rocks, the lack of strain markers in most naturally deformed rocks, and a lack of detailed fluid analyses. In this and related projects, both fluid-rock interaction and strain accumulation are quantified in a naturally deformed diamictite, providing information on relationships between deformation mechanisms, fluid pathways, hydrolytic weakening, and reaction softening. Here, in order to study the complex relationships between fluid and deformation in the diamictite, geochemical measurements are used to track compositional changes, microstructural analysis is used to study deformation mechanisms, and Fourier Transform Infrared (FTIR) spectroscopy and synchrotron FTIR are used to analyze location of water within quartz grains.

Few deformed rocks have quantifiable strain markers. In this project, we use deformed diamictites of the Mineral Fork Formation because the clasts can be used as strain markers that recorded deformation along the Willard Thrust Fault, part of the system of thrust faults active during the Sevier orogeny in north-central Utah. There are many advantages to using diamictites for this study. Not only does the Mineral Fork formation contain outcrops ranging from low to high strain, but the clasts within the diamictites act as strain markers so that strain may be quantified. This is not possible in

larger bodies of the clast material (gneiss and granite) that are typically devoid of strain markers. Another important advantage the Mineral Fork Formation offers is the varied composition of the clasts in a single outcrop (i.e. quartzite, granites and granitoid gneiss, paragneiss). Multiple lithologies allow for the study of how various clasts respond to the same stress rather than being restricted to one rock type. Additionally, detailed strain analyses can be performed on the diamictites using various clasts that exhibit different amount of strain within the diamictite. The drawback of using diamictite clasts is that the inherent heterogeneities will cause localized stress, strain, and strain rate concentrations. In order to minimize the effect of these heterogeneities, clasts were selected where no apparent localization of strain appeared in outcrop scale, and measured samples were selected from the center of the clasts, away from edge effects.

Within the diamictites, the deformation/ fluid interactions are complex. Fluid quantities and chemistries were unlikely to be homogeneous or static throughout the rock. The matrix and each clast type would have responded differently to the presence of fluid. In addition, each mineral grain within the rock would respond differently to the presence of fluid depending on size, composition, microstructures, and other parameters. Since previous studies linking quantitative strains with quantitative fluid measurements are rare, this research uses a novel approach. For this first step in studying deformation and fluid interactions in these rocks, I focus primarily on the deformation and fluid interaction of quartz within the granitic, paragneissic, and quartzite clasts. Quartz is the best mineral for this initial study because it is one of the

best-studied minerals for experimental deformation (e.g. Kronenberg, 1990; Hirth and Tullis, 1992; Chernak et al., 2009), and its flow laws are most often used as a proxy for flow in the continental crust (e.g., Brace & Kohlstedt, 1980; Poirier, 1985; Kirby and Kronenberg, 1987; Tsenn and Carter, 1987).

There are three main types of O-H species in quartz: molecular water (fluid inclusions), H's or OH's related to impurities, and OH point defects (Cordier and Doukhan, 1989). The most common form of water in quartz occurs as fluid inclusions (Kronenberg and Wolf, 1990). In order to measure the quantities of water and related species within the quartz grains, Fourier Transform Infrared (FTIR) spectroscopy and synchrotron FTIR are employed with quartz grains in the granitic and paragneissic clasts. Detailed microstructural observations on a petrographic microscope are used to constrain the location of water within the grains (fluid inclusions, point defects, etc.).

In addition to this detailed focus on quartz, the bulk fluid in the rocks is examined in a variety of ways. Since fluids are often involved in deformation under a variety of metamorphic conditions and are mobile in much of the crust (e.g. Etheridge et al., 1984, Anderson et al., 1991, Schedl et al., 1992), it would seem likely that some material may be introduced or removed during deformation (Srivastava et al., 1995). In particular, relatively mobile elements such as silica may be preferentially removed from deformation zones, resulting in relative enrichment of immobile elements such as aluminum. This may result in bulk volume loss within more highly deformed zones. Therefore, X-Ray Fluorescence (XRF) is utilized to determine relative concentrations of

major and minor elements in low versus high strain rock samples to make some inferences about the fluid composition and determine whether preferential volume loss occurred during deformation.

1.2 Fluids in Faults

The deformation of rocks is significantly affected by fluids (e.g., Griggs, 1967; Tullis and Yund, 1989; Carter et al., 1990; Kronenberg et al., 1990; Paterson, 1990; Wawrzyniec et al., 1999). Therefore, it is important to study the effect of fluids on deformation. Fluids can alter rock strength (Paterson and Luan, 1990) and affect metamorphic reactions (Anderson et. al., 1991), deformation mechanisms (Chernak et al., 2009), and strain accumulation (Kronenberg et al., 1990). The role fluids play in controlling deformation style is not always straightforward because fluids affect many different processes and favor both ductile flow and brittle failure, depending partly on fluid composition, pressure, and pathways (Wawrzyniec et al., 1999). For example, hydrolytic weakening and grain-boundary migration may enhance ductility (Griggs, 1967), and brittle failure can occur if fluid pressure instantaneously exceeds rock strength (Fischer and Paterson, 1989). The lithology, fluid composition and amount, deformation conditions, and the inherent heterogeneities in a rock can all influence the type of deformation that occurs.

Many lab experiments have focused on the effects of fluids on mineral and rock

deformation since the important findings of Griggs and Blacic (1964 and 1965). Experimental studies have shown that the interconnectivity of pore spaces in metamorphic rocks controls fluid behavior (Watson and Brenan, 1987; Laporte and Watson, 1991; Holness and Graham, 1995). Fluids can display nonwetting behavior where they are immobile in rocks during static conditions, but can change to wetting behavior due to deformation (Tullis et al., 1996). Fluid composition can also affect wetting behavior, which changes the amount or style of deformation (Wawrzyniec et al., 1999). Through the progression of fault-related deformation, fluid chemistry can change as well, affecting grain-scale deformation mechanisms in rocks (O'Kane et al., 2007).

In particular, fluid-enhanced deformation in quartz is of particular interest because quartz is a major component of crustal rocks and has a wide variety of deformation behaviors at typical crustal conditions. For example, in ductile deformation, fluid inclusions may intersect mobile dislocations, which may be crucial to hydrolytic weakening of quartz as it creates reservoirs of water in contact with advancing dislocations (Paterson, 1990). In fact, the spacing of fluid inclusions in quartz may be more influential to the weakening of the rock than the bulk water content (Kronenberg et al., 1990). Microcracking is another mechanism that can provide a means for molecular water to travel through quartz, aiding in its hydrolytic weakening (Kronenberg et al., 1986).

Fluid composition may also affect deformation, as even small variations in fluid composition can affect wetting behavior and deformation style (e.g. Wawrzyniec et al.,

1999; Chernak et al., 2009). A study by Wawrzyniec et al., 1999 focused on differing compositions in fluid inclusions, where the entrapment conditions for the inclusions are likely >500°C and >5kbar. Wetting characteristics of carbonic fluids are different than those of aqueous fluids, thus producing dissimilar deformation in postmylonitic structures (Wawrzyniec et al., 1999). Carbonic fluids cannot flow as they are trapped in isolated pore spaces, causing locally increased fluid pressure and brittle failure via closely spaced brittle faults (Wawrzyniec et al., 1999). In contrast, aqueous solutions allow ductile deformation to continue into lower temperatures and pressures (Wawrzyniec et al., 1999). Another example of fluid composition affecting deformation style is seen in a study by Selverstone et al., 2003 involving Black Hills and Heavitree quartzite. The Black Hills quartzite developed bands likely as a result of the presence of immiscible brines and CO_2 during deformation (Selverstone et al., 2003). In contrast, the Heavitree quartzite displays localized brittle failure, possibly due to the introduction of salt that caused fluid separation at experimental conditions (Selverstone et al., 2003). Overall, metamorphic fluid composition can lead to significant changes in rock rheology.

While fluid composition affects deformation, the deformation environment can also change quartz's reaction to stress as it may cause chemical reactions. For example, within carbonic fluids under oxidizing conditions, CO_2 reduces water fugacity resulting in quartz strengthening (Chernak et al., 2009). Moderately reducing conditions create reactions that weaken quartz, and extremely reducing conditions increase quartz strength as CO_2 is reduced to methane (Chernak et al., 2009). Therefore, the oxygen fugacity of the deformation environment coupled with the presence of CO_2 can cause

either strengthening or weakening of quartz to occur (Chernak et al., 2009).

As more research is done, an increasing number of factors associated with fluids and deformation are uncovered. Fluid composition, pathways, and temperature, pressure, and environmental conditions all contribute to the final effect that fluids have on deformation. For example, faults may act as either fluid barriers or conduits based on fault mechanics, microstructures, fluid chemistry, and deformation conditions. Localization of deformation can also occur as a result of fluid composition and deformation environment. Fluids can alter the strength profile of the crust, potentially creating much weaker crust at higher levels than would normally occur. Consequently, the presence of fluids can allow metamorphic facies and ductile deformation mechanisms to occur in environments of lower temperatures and pressures than expected.

1.3 Microstructural Analysis and Deformation Mechanisms

Microstructural analysis is an important aspect to structural geology and can help elucidate fluid-rock interactions during deformation. Scale of observation is critical because what appears to be ductile flow at larger scales can actually be small scale transient brittle fracturing (Vernon, 2004). Microstructural studies provide information about how a rock has responded to stress at the microscopic scale. The three main groups of deformation styles are brittle deformation, diffusion processes, and

dislocation creep.

Brittle deformation is the most common deformation style in the upper crust. It tends to occur in a frictional flow regime, located above the frictional viscous transition at roughly 10-15km depth (Stewart et al., 2000). Low temperatures (0 to 300±50°C) (Sibson, 1982), and high strain rates (Passchier and Trouw, 2005) tend to favor brittle deformation styles. Brittle deformation includes fracturing and frictional processes that can lead to cataclastic flow (Vernon, 2004). This process involves brittle fracturing that causes a loss of cohesion, leading to frictional sliding along fracture surfaces in the rock. A reduction in grain size occurs due to fracturing and shearing off of asperities during frictional sliding, which may result in granular flow. Ductile grain-boundary sliding (granular flow) involves relative grain movement without a loss of cohesion, normally in the absence of fluids and with little to no confining pressure (Vernon, 2004). Cataclastic flow is a type of brittle deformation that is a combination of frictional processes and microfracturing. It can appear to be ductile deformation at a macroscopic or even microscopic scale, but can be seen as brittle deformation at the small scale, often with aid of a transmission electron microscope (TEM) (Vernon, 2004). Voids created during cataclastic flow may be filled with quartz, carbonate, or other material precipitated from solution, which can inhibit the rate of cataclastic flow (Passchier and Trouw, 2005).

Diffusion in rocks can occur within the grain lattice, along grain boundaries, along the interface between pore fluid and the mineral grains, or freely through fluid-filled pore spaces. Although these diffusion paths cannot be distinguished by studying microstructures, we do know that components are more likely to diffuse through the

lattice of smaller grains, and diffuse along grain boundaries of larger grains. One of the most common types of diffusion is diffusive mass transfer ("DMT"), also called "solution transfer" or "pressure solution," where diffusion is enhanced by free flowing fluids, causing changes in grain shape and removal and re-deposition of material from high to low stress sites (Vernon, 2004). Common microstructures resulting from DMT include selvage seams and stylolites. Selvages are composed of insoluble materials that accumulate along grain boundaries as soluble materials are removed. Stylolites are jagged, indented grain boundaries formed as species rapidly diffuse out of the rock. They commonly occur in limestones and marbles because calcite is extremely soluble when hydrated.

Crystal plastic flow, or dislocation creep, is a deformation process that is prevalent in ductile deformation and occurs without loss of cohesion on the grain scale (Vernon, 2004). This process causes one part of the crystal to undergo shear with respect to adjacent parts, causing a change in the shape of the grain (Vernon, 2004). This movement occurs due to dislocations, linear defects, moving through the crystal lattice. Dislocations are linear defects formed when one row of atoms break away from the rest of the crystal lattice. Stress causes dislocations to form, and will cause dislocations to continue to move as additional stress is applied. Their movement allows solid crystalline materials to change shape without breaking. This solid state flow is common in the mid-lower crust and the upper mantle, with microstructures occurring in rocks deformed at greenschist facies and higher. Dislocation creep causes distortion in the crystal lattice forming common microstructures such as undulose extinction, kink

bands, deformation lamellae, subgrains, and deformation twins (Vernon, 2004). Movement of dislocations also aids in water movement through the crystal.

1.4 Context of study

This study is a precursor to other studies completed by our research group (Czeck, et al., 2009; Nachbor, A.C., 2011; Barszewski, C.E., 2012; Yonkee et al., 2013). The research presented here represents the early stages of this group project. It is an exploratory study to determine if the findings merit continued study of the deformation and fluid characteristics of Antelope Island diamictites and other rocks related to the Willard Thrust system and to devise the best investigation techniques. Additionally, this study innovatively utilizes FTIR spectroscopy and synchrotron FTIR to determine water content of structurally deformed diamictites to seek evidence for patterns of fluid-rock interaction.

Advantages to using the synchrotron for this study include the small aperture size. All of the spectra collected and analyzed in this study were taken with a 20μm aperture or less. The Synchrotron also contains software called Atlμs in addition to Omnic, which allows the user to set up a map where spectra will be taken at multiple locations and run automatically by the machine. These advantages that the synchrotron provides create unique opportunities for studying water in quartz grains.

Chapter 2: Geologic Background

2.1 Regional Geology

The study area is located on Antelope Island in northern Utah (Fig. 1), which is the largest island in the Great Salt Lake. It is located within the Willard Thrust sheet (Fig. 2), which was active during the Sevier Orogeny, approximately 150-50 million years ago (Willis et al., 2000). Proterozoic diamictites on Antelope Island (Fig. 3) are located within the footwall of the Willard Thrust (Fig. 4A), and are the focus of this study. The Willard Thrust sheet is well exposed in this area due to younger uplift and erosion (Yonkee, 2005).

The Willard Thrust sheet is part of the Idaho-Utah-Wyoming thrust belt, which is characterized by folds and thrusts that caused shortening and eastward movement of strata during the Sevier Orogeny (Yonkee, 2005). The belt is divided into two thrust systems: a western and an eastern thrust system. The western thrust system includes the Willard, Paris, and Meade thrusts. The Willard is the furthest west of the major thrusts of the Sevier orogenic belt (Fig. 2), and also indicates the location where Proterozoic and Archean rocks were involved with thrusting (Evans and Neves, 1992). Parts of the Willard thrust sheet were subsequently uplifted and tilted during the formation of the eastern thrust system and the Wasatch anticlinorium (Yonkee, 2005).

The Sevier thrust system was created by the subduction of the Farallon plate beneath continental crust proximal to modern day central California (Willis, 1999). This contraction began in the latest Jurassic or earliest Cretaceous, and produced shortening

of about 5% to 30% in most areas used for this study (Yonkee, 1992; Willis, 1999). The Willard Thrust sheet is made up of a 10-15 km thick section of rocks that have been shifted about 50 km eastward by the thrust system (Yonkee, 2005). Upper levels of the Willard thrust sheet exhibit relatively little metamorphism, while lower levels underwent greenschist-facies metamorphism (Yonkee, 2005). Fluid inclusion data show peak temperatures around 300-400°C near the base of the thrust sheet at 10-15 km below the surface (Yonkee, 2005). Locally, both Precambrian crystalline basement and sedimentary cover rocks were deformed by the Sevier orogeny, exhibiting different reactions to the stress.

In the Willard Thrust Fault region, the crystalline basement rocks, named the "Farmington Canyon Complex" by Eardley and Hatch (1940) demonstrate extremely heterogeneous deformation with ductile deformation zones ranging from 50m to only centimeters wide, which crosscut previous gneissic layering (Yonkee, 1992). At shallow levels, basement rock is internally deformed by fractures and minor faults, contrasted by greenschist-facies alteration with penetrative cleavage and vein arrays at deeper levels (Yonkee, 1992).

Sedimentary cover rocks consist of a thin layer of late Proterozoic diamictite overlain by dolomite and slate, named the Mineral Fork and Kelley Canyon Formations respectively. A Cambrian quartzite known as Tintic Quartzite lies above these rock layers. The sedimentary cover rocks display more homogeneous deformation than the basement, with widespread cleavage, minor folds, and vein arrays accommodating internal deformation (Yonkee, 1992). Cleavage displayed in the Mineral Fork diamictites

is consistent with cleavage in the basement rocks, and is defined by flattened clasts of basement rock (Yonkee, 1992).

2.2 Study Area

The Farmington Canyon complex consists of many rock types that underwent a series of intrusions and deformation. It includes some of the oldest basement rocks in Utah, consisting mainly of Archean gneiss (Fig. 3 for distribution on Antelope Island). These Precambrian rocks exhibit high-grade metamorphism displaying foliation, tight isoclinal folds, and mineral lineations that were formed during Early Proterozoic deformation approximately 1.7 billion years ago (Willis et al., 2000). Yonkee et al. (2000a) have split the Precambrian Farmington Canyon Complex into ten different rock types which consist of 1) layered gneiss, 2) biotite schist, 3) quartz-rich gneiss, 4) metamorphosed ultra-mafic rock, 5) hornblende-plagioclase gneiss, 6) banded gneiss, 7) granitic gneiss, 8) granite and pegmatite, 9) chloritic gneiss, and 10) phyllonite and mylonite (see Yonkee, et al., 2000a for comprehensive descriptions and locations of these basement rock types). The history of these rocks began in the Archean when they were deposited as a supracrustal sequence. Metamorphism and deformation of this sequence occurred during the Late Archean. In the Early Proterozoic, granite intruded these rocks, followed by the main phase of deformation (Yonkee et al., 2000a). Next, late stage granites intruded, and in the Middle to Late Proterozoic, the rocks were

uplifted and eroded, creating the current nonconformity. Sedimentary cover rocks were deposited on this uneven erosional surface from the Late Proterozoic into the Mesozoic. Lastly, Mesozoic thrusting associated with the Sevier orogeny caused deformation and alteration, forming chloritic gneiss, phyllonite, and mylonite (Yonkee et al., 2000a).

Sampling locations lie in the Elephant Head section of Antelope Island (Fig. 3), which is located in the footwall of the Willard Thrust sheet (Fig. 4). In this area, Mineral Fork diamictites that were metamorphosed to greenschist facies and ductilely deformed were collected for use in this study. The Mineral Fork Formation is a matrix-supported diamictite (Fig. 5, Fig. 6) that was deposited in the late Proterozoic, approximately 770-720 million years ago (Willis et al., 2000). It lies nonconformably above the Farmington Canyon Complex of gneisses, separated by almost one billion years of missing geologic record (Willis et al., 2000). Due to the uneven erosional surface on which the Mineral Fork was deposited, this formation greatly varies in thickness, from 0 to 60 meters.

The Mineral Fork Formation is composed of a dark colored matrix-supported diamictite that has clasts of varying lithologies. For this study, clasts are grouped into three main types, including a pink granite, green gneiss, and quartzite (Fig. 6). Other clast types occur on Antelope Island, including schist and amphibolites (mafic volcanics), but they are far less abundant, and therefore are not included in this study. All of the clast types in the Mineral Fork diamictite are believed to have been derived from the Farmington Canyon Complex (Willis et al., 2000).

Within the Mineral Fork Formation, one can observe a wide range of strain magnitudes (Fig. 5). A penetrative cleavage, formed by micas in the rock matrix, is

generally well developed and oriented approximately at a strike of 191° with a dip of 32° west (as an average of 11 outcrops from summer 2008 field work). Average mineral lineations, formed by the micaceous matrix and small quartz and feldspar clasts, are oriented on average at a trend of 288° or 115° with a plunge between 34° and 24°. The black to dark green colored matrix is micaceous and contains inconsistent amounts of sand-sized quartz and feldspar (Yonkee et al., 2000b). In higher strained outcrops, the matrix is more greenish in color due to chloritization (Fig. 5, Fig. 6). This alteration at high strain indicates the likely presence of fluid during deformation.

Clast size is highly variable, and ranges from small clasts one centimeter or less in diameter, up to boulders two meters in diameter (Yonkee et al., 2000b). The clasts collected for this research are generally between 6 to 12 centimeters in diameter. Roughly 20 to 60 percent of the Mineral Fork diamictites are composed of clasts within the matrix material, which range from angular to rounded (Yonkee et al., 2000b). Many of the clasts were deformed, stretched, and flattened during the Sevier orogenic event in the Mesozoic. In low strain outcrops, the clast to matrix ratio appears to be greater than in high strain outcrops. This is probably due to the fact that small clasts which are easily identified in low strain outcrops are indistinguishable in high strain outcrops.

In addition to the Mineral Fork Formation, the sedimentary cover on Antelope Island also consists of the overlying Kelley Canyon Formation and the Tintic Quartzite. Doelling and others (1990) divided the Kelley Canyon Formation into two members: a lower dolomite and an upper slate member (Yonkee et al., 2000b). It varies in thickness

from 20 to 80 meters. Contact with the lower diamictite is sharp, and most of the unit is weakly deformed by fractures, thin veins, and open folds (Yonkee et al., 2000b). The lower dolomite member has calcareous slate interbedded in the fine-grained crystalline dolomite near the top of the unit (Yonkee et al., 2000b). The dolomite member conformably grades into the upper slate member, and locally is incorporated into it at the contact (Yonkee et al., 2000b). The slate member has well developed cleavage from widespread deformation, which makes the thickness difficult to determine, likely ranging from 15 to 75 meters (Yonkee et al., 2000b). The Tintic Quartzite overlies, probably unconformably, the Kelley Canyon Formation. It weathers to form sharp cliffs on Antelope Island that appear tan in color. Variable deformation and irregular exposures hinder the determination of thickness, but the unit is likely more than 250 meters thick on Antelope Island. (Yonkee et al., 2000b).

This study originated because of inherent differences qualitatively observed between the granitic and gneissic clast types. They appear to have the same general shapes and sizes at low strain. In high strain samples, the gneissic clasts qualitatively appear to have undergone more ductile deformation than the granitic clasts, evidenced by their more elongated appearance. Highly strained clasts are strongly deformed into flattened and stretched bodies that often have indistinct boundaries (Fig. 5, Fig. 6B). Quartzite clasts exhibit the least amount of flattening and deformation of the three clast types. Quantitative strain analysis that has since been conducted by research

collaborator, Dr. Adolph Yonkee from Weber State University has yielded results consistent with our observations (Yonkee et al., 2013).

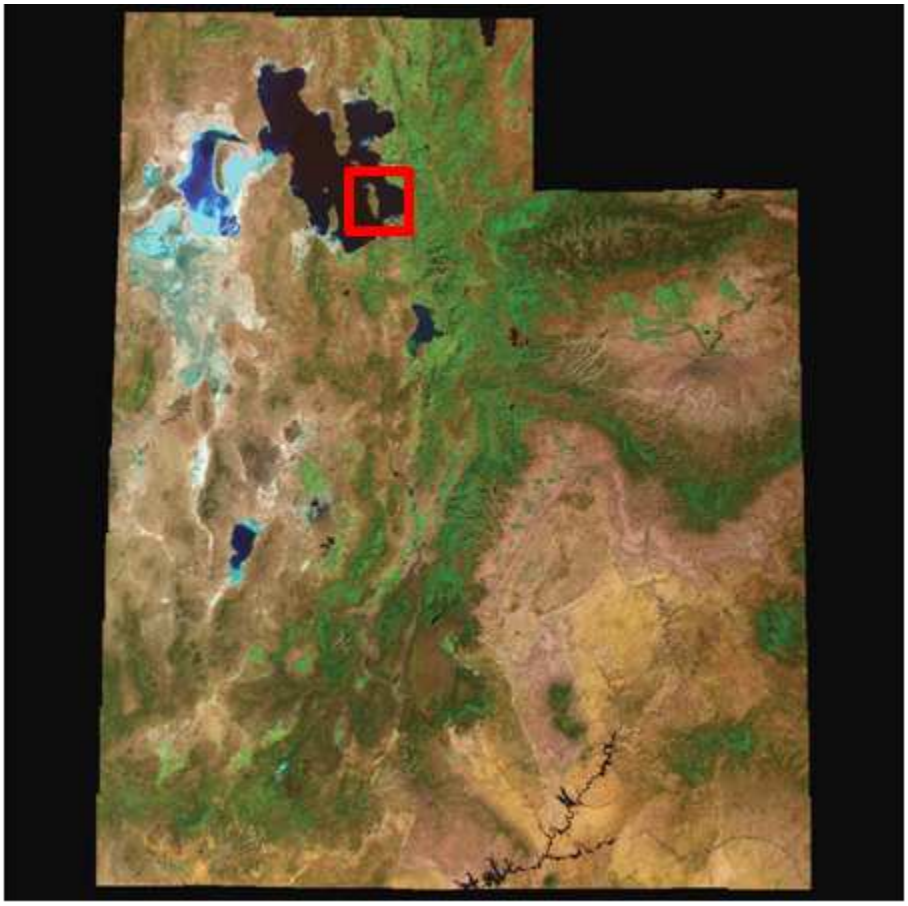

Figure 1. Satellite image of Utah, with Antelope Island outlined with a red box in the central northern section in the Great Salt Lake. Modified from http://www.nr.usu.edu/Geography-Department/utgeog/images/utah.gif

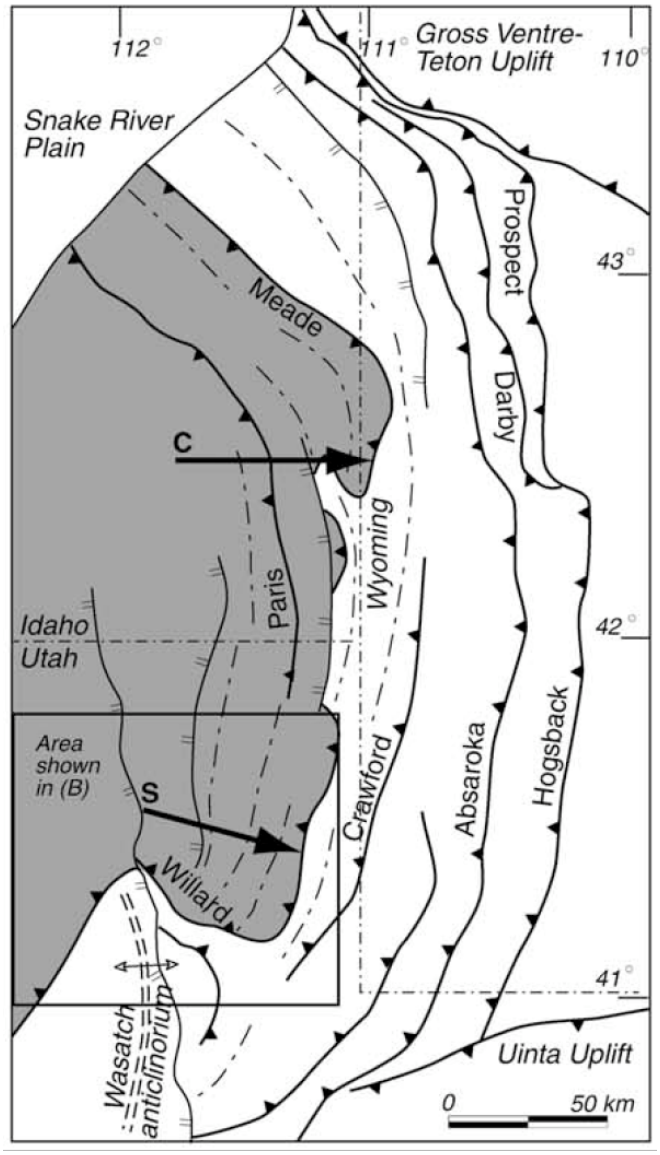

Figure 2. Regional view of the Idaho-Utah-Wyoming thrust belt. Major faults and uplifts are labeled, and fold trends are indicated by dashed lines. The central (C) and southern (S) parts of the map have large arrows showing the general estimates of displacement direction and magnitude for those areas (Royse, 1993; Yonkee, 1997). The square surrounding the southern (S) part of the map is shown in detail in Figure 4 A. Modified from Yonkee, 2005.

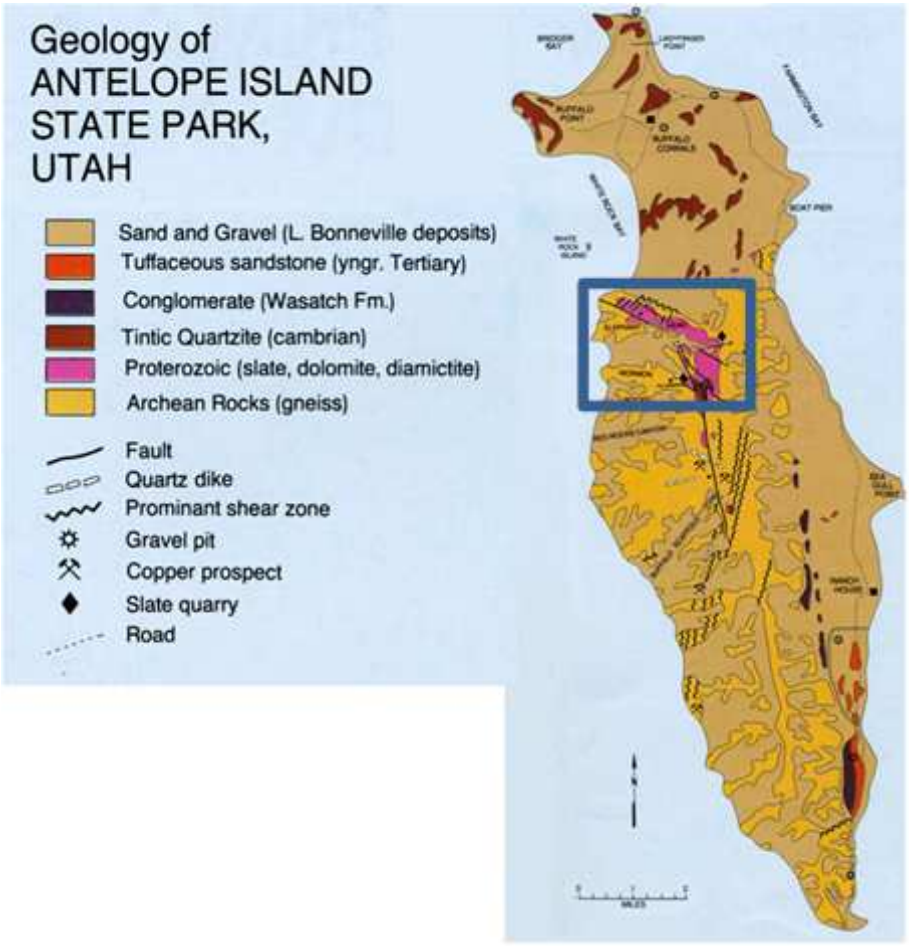

Figure 3. Geologic Map of Antelope Island. Elephant Head is outlined by the blue box, which contains Proterozoic rocks, including the Mineral Fork diamictites used in this study. Modified from "Geology & Antelope Island State Park, Utah" by State of Utah Department of Natural Resources, Utah Geological and Mineral Survey.

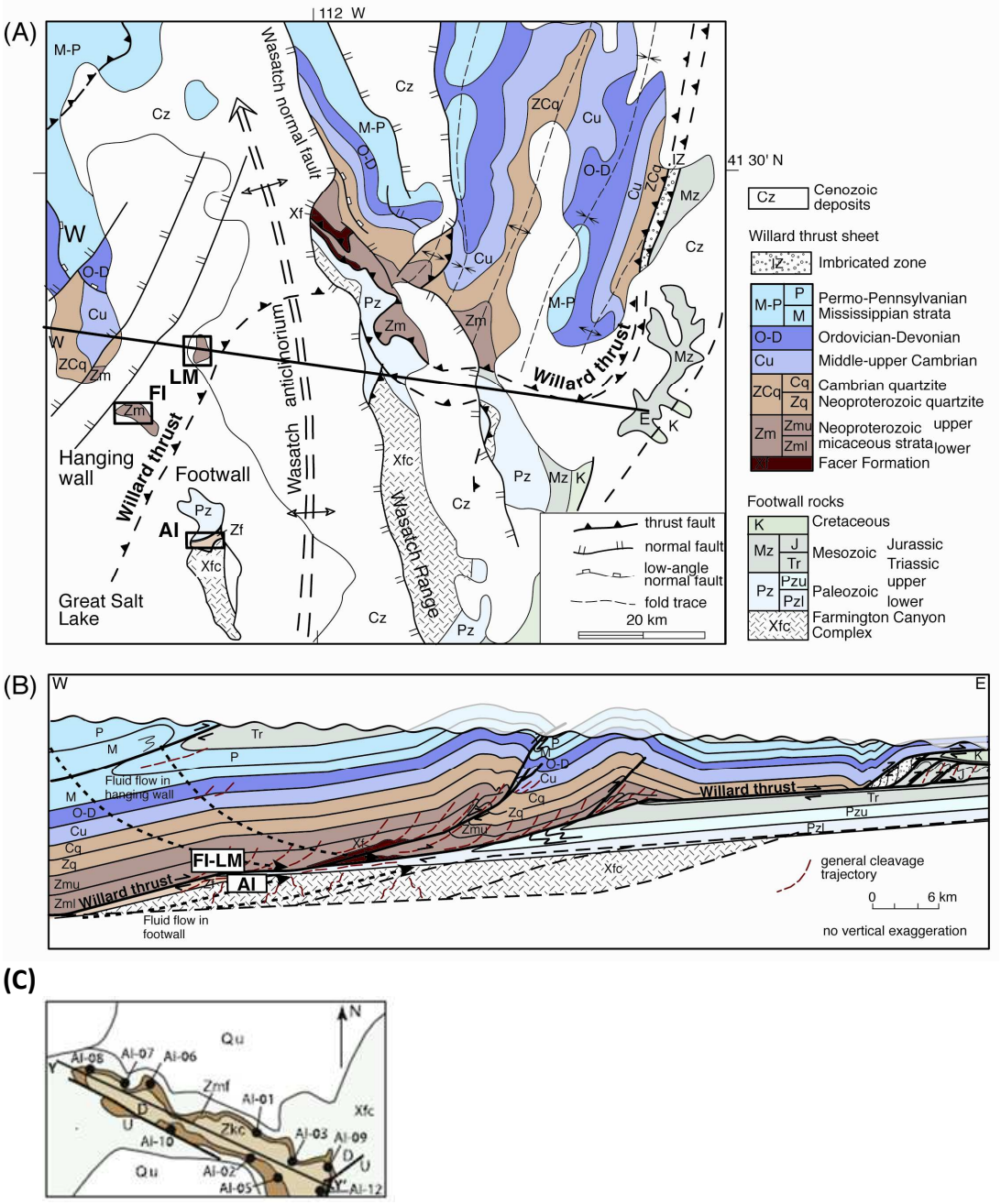

Figure 4. A. Geologic map of northern Utah displaying the Willard thrust system and related structures. The black box labeled AI - Antelope Island, indicates the study area for this project. Little Mountain (LM) and Fremont Island (FI) are locations where the diamictite is exposed on the hanging wall, studied by other members of the research group. B. Cross section of the Willard Thrust system, including the location of Antelope Island (AI) in the footwall relative to locations in the hanging wall; LM and FI. C. Sample locations on Antelope Island from the Mineral Fork Formation across the Proterozoic rock outcrop (Fig. 3). Modified from Yonkee et al. (2013).

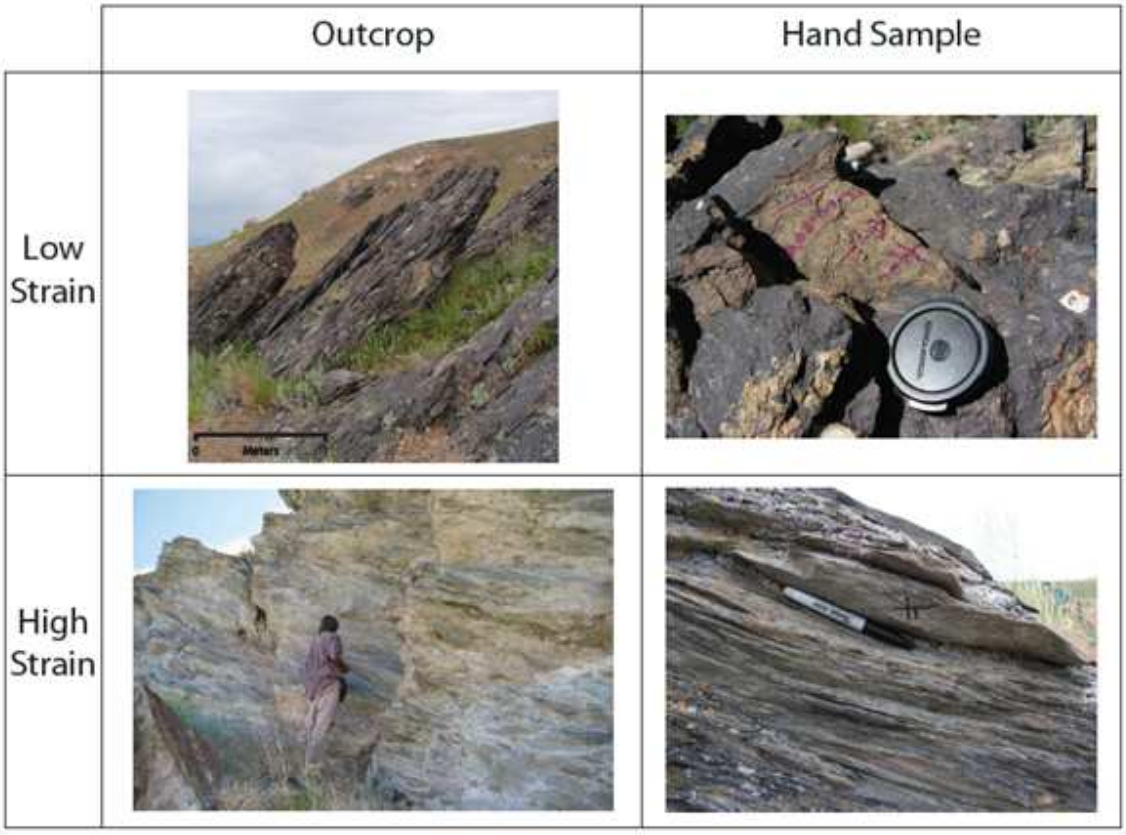

Figure 5. The Mineral Fork Formation diamictites are shown in both outcrop and hand sample scale. Clear differences in foliation development can be seen between high and low strain rocks. Variations in the matrix material are also apparent. Low strain rocks have a darker matrix, while high strain rocks have a greenish matrix, indicative of chloritization and alteration.

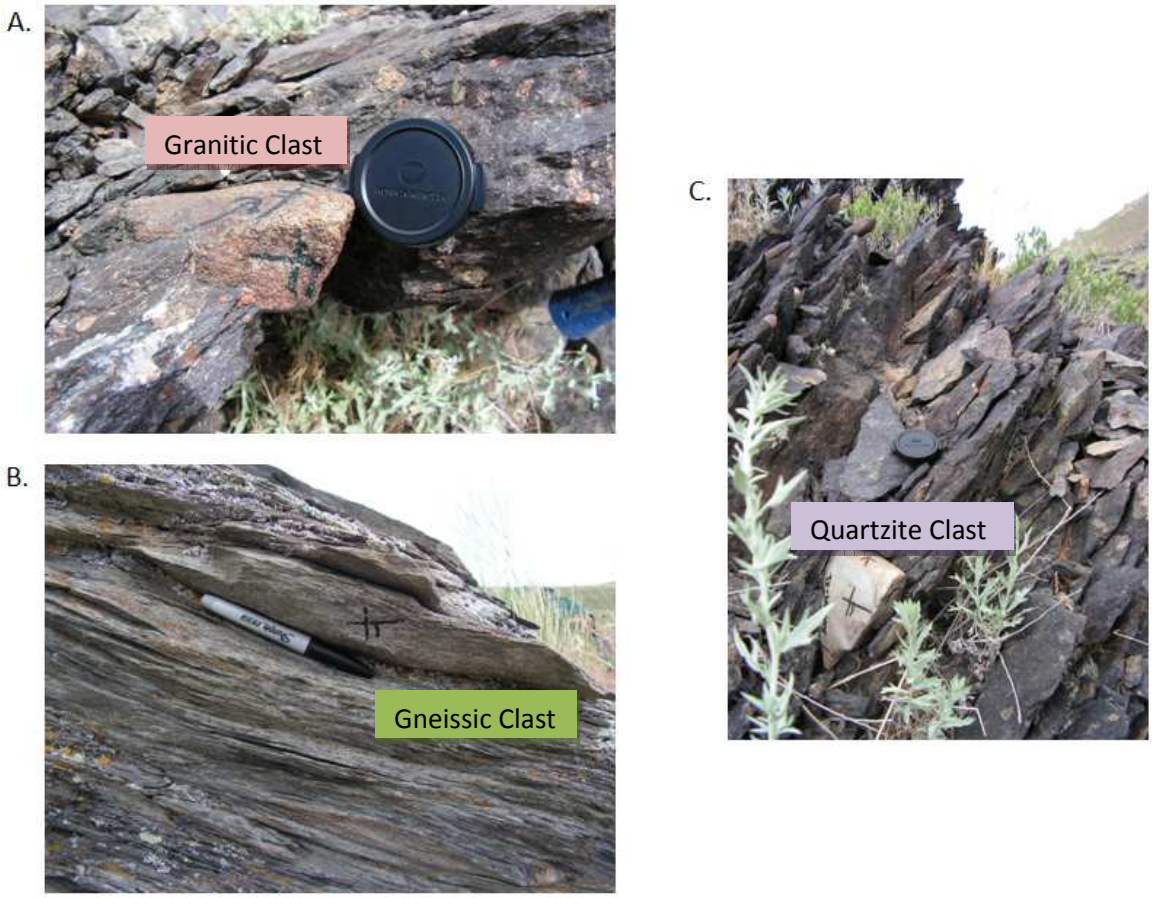

Figure 6. A. Moderate strain outcrop of the Mineral Fork diamictite on Antelope Island containing a pink granitic clast. B. A high strain outcrop containing a green gneissic clast. C. Another moderate strain outcrop with a quartzite clast. Foliations are visible in both moderate and high strain outcrops.

Chapter 3: Methods

3.1 Field Methods

Samples were collected for this study and the tandem strain analysis from Antelope Island, Utah over a period of two weeks during the summer of 2008. Dr. Dyanna Czeck and research partner Dr. Adolph Yonkee aided in the selection of outcrops based on apparent strain levels to achieve sampling across the strain gradient. Selected outcrops also contained three perpendicular faces suitable for strain analyses, which has since been performed by Dr. Yonkee. These data were utilized to expand on previous strain estimates (Yonkee, 2005) in subsequent studies (e.g. Czeck, 2009; Yonkee et al., 2013). Eleven different outcrops were sampled across the strain gradient (twelve were originally identified, but Location 04 has since been omitted from this study because there was not sufficient outcrop for strain analysis; Fig. 7).

Clasts from each outcrop were chosen based on their size and clast type. At least two of each clast type (pink granitic, green gneissic, and quartzite) were selected from each outcrop, and they were collected while preserving their orientation. Clasts had a minimum size requirement as each clast had to be large enough to obtain a billet for thin sections, a sample for FTIR analysis, and a sample for XRF analysis. Overall, approximately 70 samples were collected and shipped back to Milwaukee from Antelope Island. In this study, we explore twenty nine samples ranging from relatively low to high strain using FTIR analyses at the synchrotron, XRF analyses, and point counting to determine petrographic and microstructural analyses.

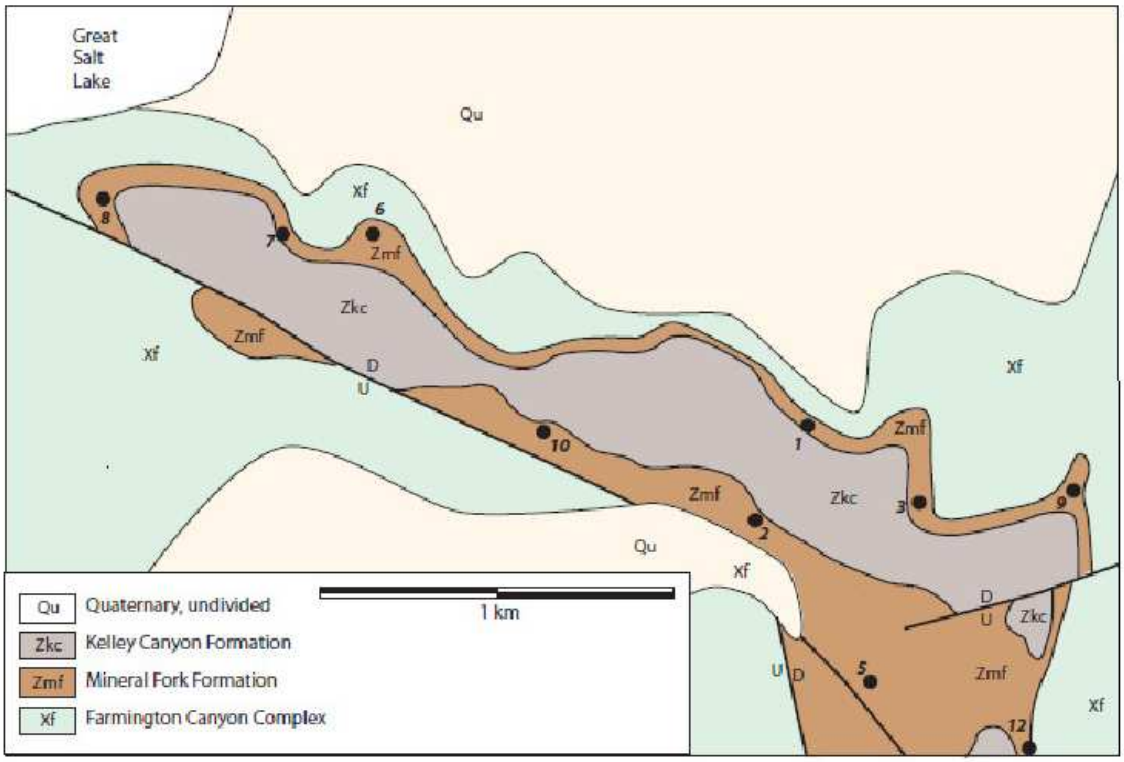

Figure 7. Geologic map of sample locations for the Mineral Fork Formation (Zmf) which outcrops on Elephant Head in Antelope Island, Utah. Location of map indicated in Fig. 4. (courtesy of Adolph Yonkee)

3.2 FTIR/Synchrotron

Fourier Transform Infrared (FTIR) Spectroscopy is a method that uses an infrared beam and a Continuμm microscope to determine the composition of a sample. This instrument can be run in either reflectance or transmission mode. For this study, transmission mode is utilized, which means that the infrared beam travels through the sample. The portion of the beam that has traveled through the sample is received by the detector beneath the stage. The amount of beam that travels through the sample is called the signal. When using this instrument, there needs to be an adequate amount of signal in order to acquire accurate data. Therefore, the sample must be thin enough to allow the infrared beam to travel through it in order to collect data. Spectra are produced once the infrared beam has been transmitted through the sample, which show the amount of absorbance that occurred at various wavenumbers.

Water peaks generally occur within the hydroxyl region, which spans from 4000-2500cm^{-1} wavenumber (Kekulawala, et al., 1978). It is generally accepted that at least three types of absorbing OH species exist in quartz: molecular water, H's or OH's related to impurities, and OH point defects (Cordier and Doukhan, 1989). Molecular water takes the form of small inclusions trapped during the growth of the mineral crystal. H's or OH's related to impurities often occur with Al^{3+} or Na^{+} (Cordier and Doukhan, 1989). OH point defects occur in an otherwise pure material. Molecular water tends to create

the signature broad water peak ranging from 4000-2500cm^{-1}, while OH stretches create peaks at 3350cm^{-1} and 3650cm^{-1}.

For this project, the water content of quartz crystals was analyzed at UW-Milwaukee using a Continuμm microscope made by Thermo Spectra-Tech and a Nicolet Nexus 470 FT-IR, as well as the UW-System Synchrotron Radiation Center (SRC) in Stoughton, WI.

3.2.1 Sample preparation

Preparation of samples for oriented thin sections and samples for FTIR spectroscopy includes cutting rocks along the XZ plane of finite strain (parallel to lineation and perpendicular to foliation). In order to avoid edge effects as much as possible, all thin sections and FTIR samples are taken from the middle of clasts. Similarly, the center of quartz grains is the focus for the FTIR analyses when finding representative water concentrations to minimize edge effects on the grain-scale and to avoid interference from neighboring grains. The typical grain size of the quartz grains is 50-200 microns.

In order to measure water content in quartz using FTIR spectroscopy, double-sided polished wafers were created. During the production of wafers, it was thought that thin sections could be used to collect data at the synchrotron instead of double sided wafers. FTIR analysis on thin sections, rather than wafers, was desirable because

any analyzed water contents could be compared to microstructures observed under a petrographic microscope. Therefore, a total of fourteen wafers were created and run with another seventeen thin sections analyzed. To make a wafer, a small sample is placed into an orthodontic resin. Once the resin is set, crystal bond is heated in order to adhere the sample to a slide. One side of the sample is then polished flat using micron grit alumina sheets. The samples need an extremely smooth polish, so it is necessary to gradually decrease the size of the grit from 60μm down to 9μm alumina grit paper. After one side is ground and polished, the sample is flipped and again, crystal bond is heated to adhere it on the opposite side. The entire sample is ground down until it is approximately 20 micrometers thick. When this thickness is achieved, the sample is soaked in acetone to dissolve away the orthodontic resin and crystal bond so that only the sample chip remains. The resulting sample is ready for analysis and placed onto a salt disc to be run in the FTIR spectrometer.

Oriented thin sections were created from the oriented clasts collected on Antelope Island. Billets were cut and sent to Spectrum Petrographics Inc. in Vancouver, Washington to be made into standard polished thin sections without cover slips. Twenty-nine samples from locations 05 (moderate strain), 06 (high strain), and 09 (low strain) (Fig. 7) were utilized for point counting and microstructural analyses, and also for FTIR spectroscopy. Thin sections are between 30-40 microns thick, and the company uses an acrylic adhesive as the epoxy that holds the sample to the glass slide.

3.2.2 Standard FTIR

The Nicolet Nexus 470 FT-IR at UW-Milwaukee was used purely for the preliminary samples reported in the proposal stage of this project because multiple water peaks emerged through this method. The presence of multiple peaks presents a problem in calculating water concentrations because one definitive peak is used in the calculation. The Bouguer-Lambert-Beer law (Beer's Law) is used to calculate water concentrations, taking into account the power of radiation from the front and rear of the sample, the wavenumber, and the thickness of the sample. Beer's Law follows:

$$T = \frac{I}{I_o} = \exp[-\alpha(v)b]$$

To find water content using this equation, average peak heights were estimated and the sample thickness differences were assumed negligible for these samples, which are assumptions that could lead to substantial inaccuracies in results. With the identification of these issues, the synchrotron FTIR was fully adopted for further analyses in order to collect more accurate, more precise, and spatially constrained data, as described below.

3.2.3. Synchrotron FTIR

The Synchrotron Radiation Center (SRC) in Stoughton, WI was used to produce grain maps consisting of spectra taken at multiple points on a sample. Data for this study was collected using IR Beam line 031 on the Aladdin storage ring. The area maps

generated at the SRC help to identify and quantify absorbances and main water locations (Fig. 12).

The synchrotron is important to this project because it not only allows data to be obtained using FTIR microspectroscopy, but allows data to be collected spatially at a finer scale rather than only at a single point. This spatial collection of data produces area maps that show the amount of signal received at each point. Analysis of the individual spectra on each area map is made possible by Thermo Fisher Scientific Omnic 7 software. These maps can be manipulated to create new maps that show areas of high versus low water content across a single grain. This is accomplished using the program Omnic and an add-on called Atlμs.

Using Atlμs, one may select a specific spectrum to examine. When it is pasted into a new window in Omnic, either the peak height or peak area tool can be utilized to measure the height of the water peak. First, a baseline is established across the bottom of the spectrum. Next, either a peak height is reported at a specific wavenumber, or an area is designated between two wavenumbers, and the tool reports the peak area. The peak height and area quantify the amount of absorbance, i.e. the amount of water in each sample. With these data, the area under the water peak can create a map highlighting areas within the mineral that have the greatest amount of water. Thus, it is possible to explore the spatial distribution of water throughout the quartz grains, fractures, and grain boundaries with the synchrotron and associated software. It is, however, important to note that the actual water concentrations for each sample are not calculated in this study. Computing water concentrations would require a thickness

measurement of the samples, which is not physically possible with thin sections. Therefore, in this study, the thin sections are all assumed to be approximately the same thickness, so the water concentrations from one sample to the next should be comparable. In other words, higher absorbances correlate to higher water concentrations. Future work could attempt to calculate sample thickness of thin sections using interference fringes in reflectance mode.

In order to obtain accurate spectra from the Synchrotron, a background reading is first taken, and is subtracted from subsequent spectral readings. A background reading accounts for anything in the environment or on the sample that may be absorbed in addition to the sample itself. Background readings for double-sided wafers are taken through the salt disc on which the wafer sits. For thin sections, background readings were taken toward the edge of the slide, through the glass as well as the adhesive material in order to exclude any effects the glass or epoxy might have. This background reading is then used in conjunction with each of the readings taken across the grain map. As the background is subtracted from the individual spectra, a final accurate spectrum is produced at each point for the grain maps.

Grain maps produced in this study use an aperture that is 20 μm or less, and their area ranges anywhere from 200-6,000μm^2. Spectra are recorded at specific points across the grain maps. To obtain the final colored grain map ranging from red to blue, the Omnic software interpolates data in between the points containing actual spectra.

In order to ensure that the materials used to create the thin sections would not interfere with the water peaks, I selected a location on thin section A08-05-Y1 to

examine (Fig. 8). Upon inspection of the spectrum created in the adhesive (Fig. 9), it does not appear that the adhesive has any significant effect on the absorbance in spectra in the area of interest (between 3000 and 4000cm^{-1}). To be sure this is not an anomaly, spectra from additional points across the map were added to the same plot (Fig. 10). The multiple spectra have the same trend, where there is no notable effect between 3000 and 4000cm^{-1}, but a negative absorbance peak of approximately -0.21 cm^{-1} exists at approximately 2960 cm^{-1}, which is likely the result of CH stretching frequencies.

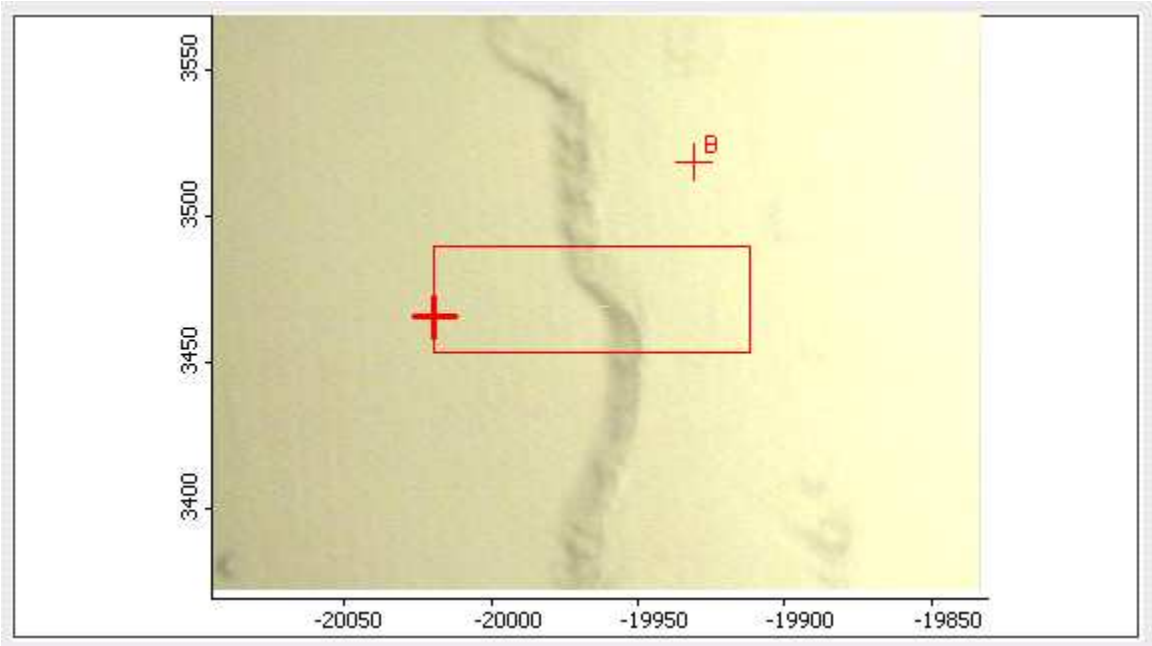

Figure 8. Location selected on thin section A08-05-Y1 to investigate the possible effects of the epoxy used in thin section creation on the sample spectra. This spot is located away from the rock itself toward the edge of the thin section where there is only epoxy and glass.

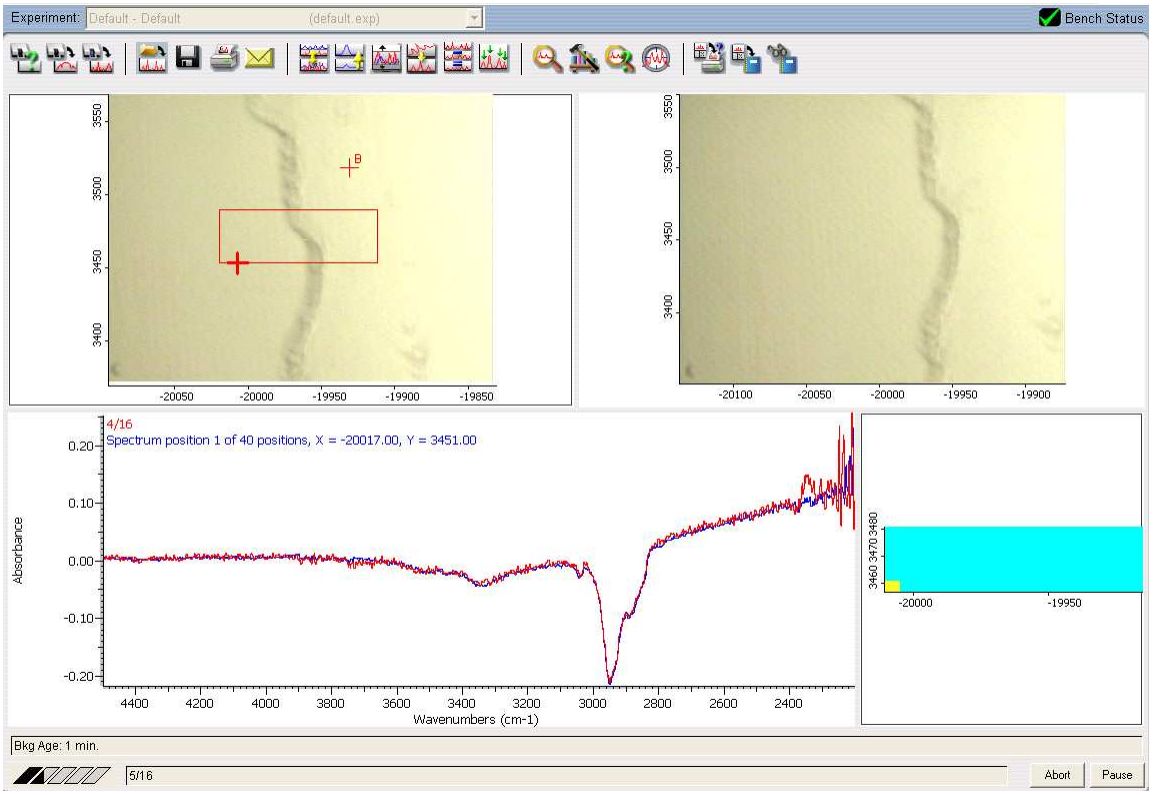

Figure 9. The area map and its associated spectrum studied to determine if the adhesive would affect spectra taken for the rock samples (from Omnic). This map spans across the adhesive and its outer boundary (top left). The resulting spectra are shown at the bottom. Note the lack of peaks in the area between 3000 and 4000cm^{-1} wavenumber. A negative peak with an absorbance of about -0.21cm^{-1} does exist at approximately 2960 cm^{-1}.

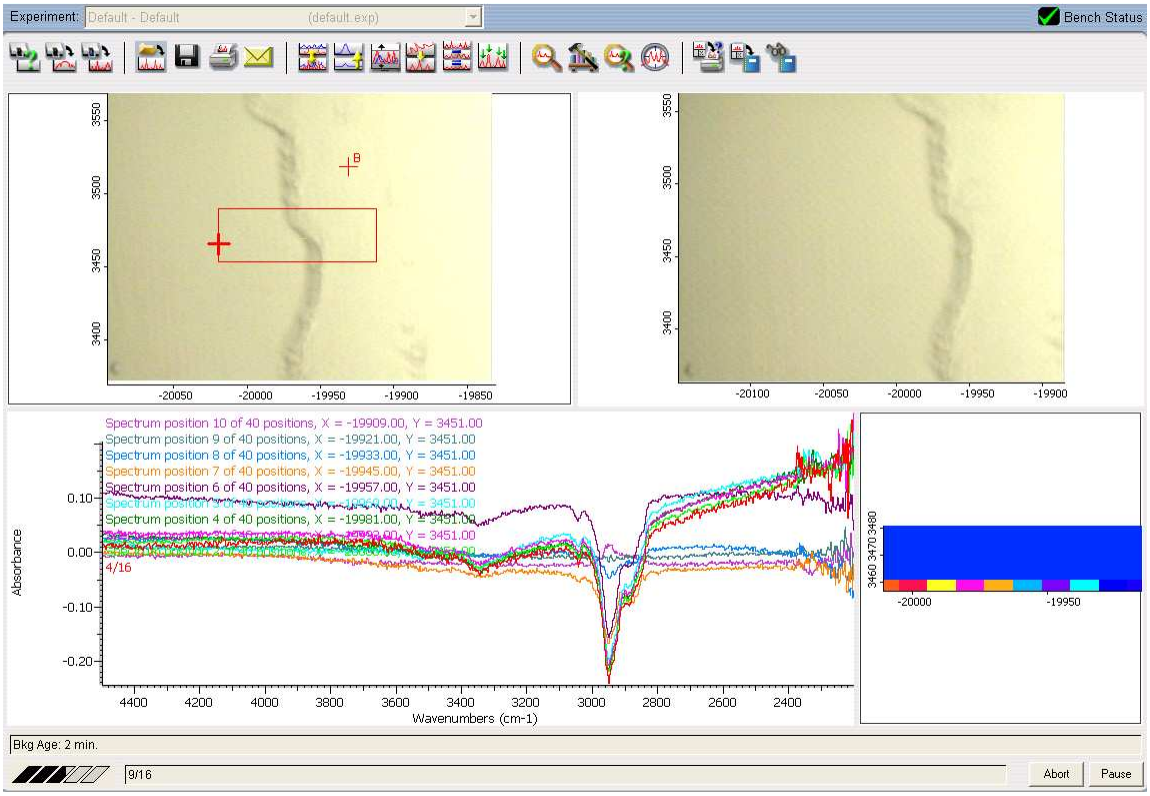

Figure 10. Multiple spectra plotted across the same area map from Fig. 9. The trend in the adhesive used on the slide is similar across the entire area map, with no significant effect between 3000 and 4000cm^{-1} wavenumber, and a negative peak at approximately 2960 cm^{-1} wavenumber.

3.3 X-Ray Fluorescence

X-Ray Fluorescence (XRF) is a method used to determine the chemical composition of samples. Rocks need to be ground down into a fine powder and fused into beads to be used in the XRF. This instrument determines relative concentrations of major and minor elements in low versus high strain rock samples, which may potentially be used to determine whether fluids altered the rocks and volume loss occurred during deformation.

3.3.1 Sample preparation

To prepare for X-Ray Fluorescence (XRF) measurements, clasts are first separated from the matrix material using the rock saw. Using samples from the center of clasts helps to limit the effects of weathering in our results. This limited amount of sample does, however, prevent analyses from being representative of the bulk for elements that are found only within trace minerals. Next, the samples are pulverized in a jaw crusher and ground down further with a tungsten carbide shatterbox. Once the samples are finely powdered, they are placed into an oven and heated to 105°C overnight to remove any possible water. The next day, they are transferred to a desiccator where they cool to prevent water from re-entering the samples.

Once cooled, samples must be prepared as fused beads for XRF. First, approximately one gram of ammonium nitrate is added to the weighing dish. Next, precisely 10.0000 grams of Claisse LiT:LiM (50:50) flux with 1% LiBr as a non-wetting

agent is added to the weighing dish. This measurement must be accurate to within 0.0003 grams. Finally, exactly 1.000 gram of sample is added to the weighing dish and the contents are thoroughly mixed. A Claisse M4 Fluxer produces the fused beads following a 21-minute routine that includes an oxidation step. The maximum temperature that the fluxer reaches in this routine is approximately 1050°C. For samples with low totals, loss on ignition (LOI) is determined by re-drying the samples, pre-heating crucibles, and then heating the samples in a furnace at 1050°C to replicate the temperature reached by the Fluxer. Samples are weighed before and after they are heated.

3.3.2 XRF analysis

A Bruker S4 Pioneer WD-XRF at University of Wisconsin-Milwaukee Department of Geosciences was used to measure the samples, providing concentration data for major, minor, and trace elements. Sample concentrations were derived using a calibration curve based on eleven USGS rock standards using Bruker's FQuant software. For more detailed information regarding the calibrations and other lab procedures, see McHenry (2009).

Eighteen clast samples were analyzed from Antelope Island. Three locations consisting of high (A08-06), medium (A08-05), and low (A08-09) strain rocks were utilized (Fig. 7), including six clasts from each location; two green paragneissic, two pink granitic, and two quartzite clasts from each outcrop.

All major elements in the rocks were analyzed and tracked in the different clast types across the strain gradient. Of particular interest for this study are elements that may indicate changes in volume. For example, Si may be soluble in many aqueous solutions, thus becoming mobile. Therefore, a loss of Si with increasing strain is used as an indicator of overall volume loss with deformation. In tandem with Si depletion, we may expect to see a gain in heavier elements like Al, Mg, and Ti if Si becomes mobile during deformation (e.g. Newman and Mitra, 1993).

The data from XRF analyses will also be used to find other potential trends in element gain or loss between clast types and strain rates. For example, some changes in major elements with strain may be indicative of certain metamorphic reactions that were enhanced by fluid or strain softening (e.g. Newman and Mitra, 1993; Yonkee et al., 2003). Trace element concentrations may also be useful because they may offer clues as to the chemistry of any interacting fluids.

3.4 Petrographic Analysis

The software Petrog was used for point counting on thin sections to study the mineralogy and microstructures in the Mineral Fork Formation. The thin sections were oriented so that their surface is along the XZ plane. This plane is parallel to lineation and perpendicular to foliation. Examining the samples at this orientation allows us to

study microstructures that formed on the plane with greatest strain contrast (maximum elongation direction = X and maximum shortening direction = Z).

The software program Petrog was designed for the petroleum industry to point count thin sections from deep sea cores. Since the rocks in this study are significantly different in both mineralogy and microstructure, data were recorded manually on original spreadsheets. The spreadsheets include one hundred points examined on each slide along with their coordinates, mineral type, grain size (maximum and minimum diameters), and microstructure types.

An area was selected to examine on each thin section, and then the computer program Petrog assigned coordinates to each of the 100 points in that area. Point counting was performed on twenty-eight thin sections: five granitic, four paragneissic, and three quartzite clasts were analyzed from high strain site 06. For the moderate strain site 05, we analyzed two of each rock type. Low strain site 09 analysis included four granitic, two gneissic, and four quartzite clasts.

The long and short axes of the grains were measured and recorded. Many of the grains had approximately the same long and short axes. The long axis only was reported for comparison in this study.

Once the spreadsheets were completed, microstructures are grouped into categories relating to deformation processes including brittle, crystal plastic (dislocation creep), and diffusive mass transfer (DMT). Combining these data allows us to relate the

mineral percentages, microstructures, and deformation mechanisms to not only the three different rock types, but also to the various levels of strain across Antelope Island.

3.4.1 Microstructural study

The microstructures recorded in the spreadsheets during point counting include: undulose extinction, intragranular fractures, deformation lamellae, recrystallization, zoning, inclusions, subgrains, and grain boundary migration. Other noteworthy microstructures at each point were also recorded in a separate column.

The deformation mechanism that each microstructure is most likely associated with can help classify these microstructures. Microfractures are associated with brittle deformation (Fig. 11A). Fluid inclusions can form as primary or secondary water, and either can affect deformation (Fig. 11B). Crystal plastic deformation or dislocation creep forms warping of the crystal lattice that results in undulose extinction, deformation lamellae (Fig. 11F), and subgrains. Undulose extinction appears as a wavy extinction, and is caused by crystal lattice dislocation migration due to stress (Fig. 11C). Subgrains form when small misorientations separate two parts of a grain with different crystal orientations (Fig. 11D). Recovery mechanisms associated with dislocation creep include grain boundary migration resulting in bulged grain boundaries (Fig. 11G) and dynamic recrystallization resulting in strain free grains (Fig. 11E).

A. Microfractures

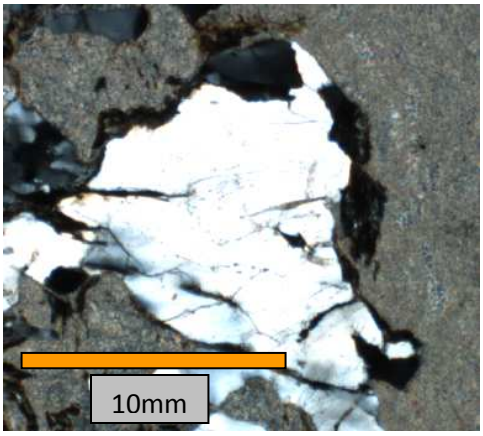

B. Fluid Inclusions

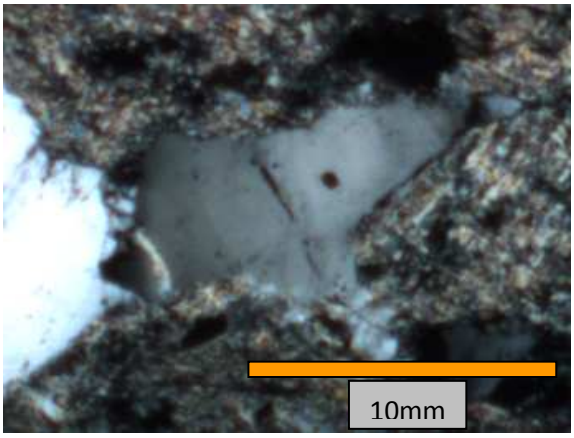

C. Undulose Extinction

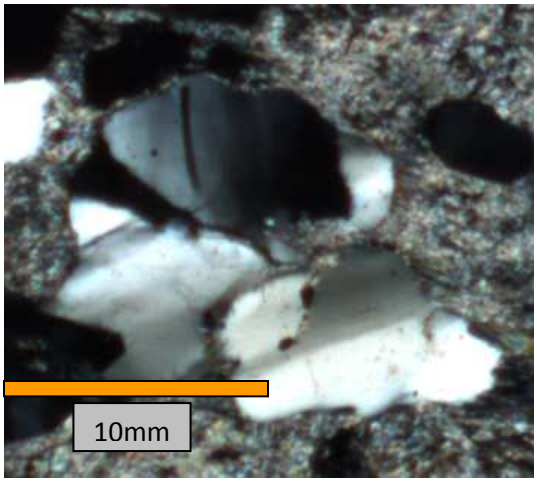

D. Subgrains

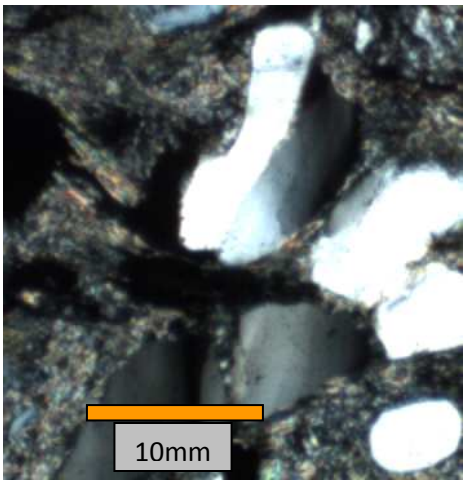

Figure 11. Photomicrographs of microstructures in quartz grains showing A. microfractures, B. fluid inclusions, C. undulose extinction, D. subgrains, E. recrystallization, F. deformation lamellae, and G. grain bulging, indicative of grain boundary migration.

E. Recrystallization

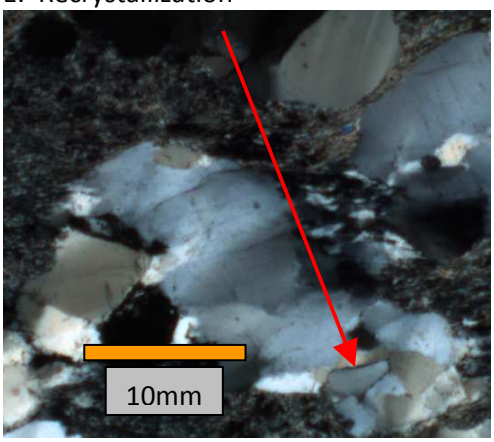

F. Deformation Lamellae

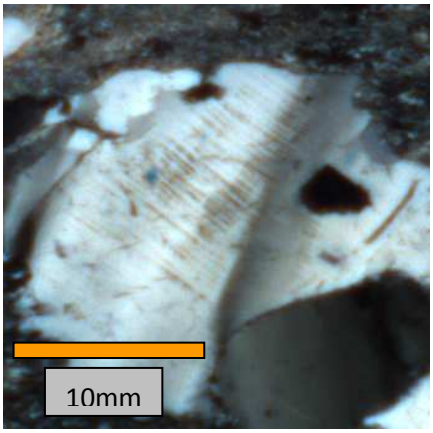

G. Bulged Grain Boundary

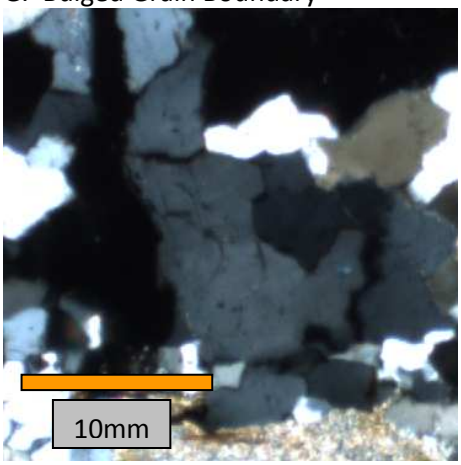

Chapter 4: Results

4.1 FTIR/Synchrotron

Fourier Transform Infrared Spectroscopy is utilized in this study as an innovative technique for studying minerals in deformed rocks. As this study is a precursor to other investigations performed by our research group (Czeck et al., 2011; Yonkee et al., 2013), exploratory FTIR data were collected on quartz grains in a broad manner. Quartz grains were selected for FTIR spectroscopy because quartz is the most common mineral in the crust, fluid inclusions in quartz are extensively studied, and quartz is frequently tested in laboratory experiments. Quartz grains, boundaries, fractures, and inclusions were all investigated with the goal of determining the location of potential water within the grains. Locating water in quartz grains may allow us to correlate the presence of water in specific locations with its affect on rock deformation.

4.1.1 Abundance of Water in Quartz Grains

The absorbances for the low, moderate, and high strain samples can be compared using data from this study (Fig. 12). The majority of the low strain samples (A08-09; Fig. 12, right chart), regardless of lithology, show a relatively small amount of water with absorbances mostly below 0.2. However, paragneiss clast A08-09-Z4 is an exception with the majority of the quartz grain mapped in this sample having water peak absorbances around 0.5. This water was located throughout the quartz grain itself, which demonstrates that even within one deformation regime, water amounts and

locations within quartz grains can be quite variable.

Moderate strain samples (A08-05; Fig. 12, center chart) generally have higher water content, with the majority of the samples having water peak absorbances between 0.2 and 0.3, regardless of clast type. Interestingly, the high strain samples (A08-06; Fig. 12, left chart) contain less water peak absorbances than the moderately strained samples. The majority of high strain samples have water peak heights less than 0.2. Therefore, an apparent gain of water from low to moderate strain occurs, followed by a loss of water from moderate to high strain rocks. This generalized trend is independent of clast type.

4.1.2 Grain Maps

Use of the Synchrotron for this study offers many advantages, including the ability to focus on an area of interest within a quartz grain and study where water occurs using grain maps. Additionally, we can overlay those grain maps on the optical image of the quartz grain. The outcome is a 2-D photo mosaic of the quartz grain overlain by a colored map with red as high concentrations, then yellow, green, and blue as lower concentrations ("hot" colors as high and "cold" colors as low; Fig. 13 and 14). Our hope was to spatially constrain the location of water within grains to determine if it was uniformly distributed or localized along grain boundaries, inclusions, fractures, or other features.

Creating one of these grain maps (Fig. 13B) is a multi-step process that involves several decisions that can affect the outcome of the map. An area of interest is chosen

in quartz and the map is outlined (Fig. 13A) so that the synchrotron can take a reading (spectrum) at each point in the map (Fig. 13C). The peak area tool in Omnic allows the user to create a baseline, choose a range of wavenumbers, and find the area under the curve in the spectrum for water (Fig. 14B). From here, a map can be created that shows the largest area under that curve in red, and the smallest areas in blue (Fig. 14C). This colored map is used in conjunction with the photomicrograph mosaic of the quartz grain to generate the completed grain map (Fig. 13B). Additional grain maps produced at the synchrotron are included in Appendix A.

During analysis of spectra and grain maps, we made some unexpected observations. Figure 12 shows the average absorbance of water where it occurs most frequently across each map from the analyzed samples (maps provided in Appendix A). The majority of the grain maps show a red color (Fig. 13B) at fractures, fluid inclusions, or grain boundaries (Fig. 12). Establishing a baseline and the peak area using the peak area tool and applying those constraints across the grain map should have created a color coordinated map with red for the highest areas under the water peak and blue for the lowest water peak areas. However, upon closer examination, it was discovered that quite often the red areas on the grain maps do not necessarily display the largest water peaks in the spectrum. Often, the inclusions, grain boundaries, or fractures simply produce the most noise. To determine where the most water occurs, a baseline must be established to find a corrected peak height or area. This corrected peak height or area would show the relative high and low concentrations of water across the quartz grain. It appears that the baseline determined using the peak area tool (Fig. 14B) did

not correctly apply that baseline to all of the other spectra on the map. Therefore, the colors shown on the grain maps are not representative of water concentration. Instead they show where the spectra have the most noise. The sharp peaks resulting from noise can cause a higher overall area for a water peak. However, this only occurs because those peaks can spike up to 5 absorbances or higher, which is a much larger absorbance than any of the regular water peaks observed in these samples. That additional absorbance often creates red areas on a map, which would only indicate thick sections of the sample, or places that do not allow the beam to cleanly pass through. Therefore, the colored grain maps may not show accurate portrayals of high versus low water concentration. It is unknown why the peak area tool did not properly apply the same constraints on all the spectra to produce a colored map showing the correct highest versus lowest water concentrations, or if the tool did properly constrain the water peak area but the noise caused the maps to be unreliable.

This phenomenon also occurs with colored maps created without using the peak area tool. When the map is first created, there is a vertical line in the center of the spectrum at approximately 2,950cm^{-1} wavenumber (Fig. 14A). This line can be toggled back and forth to any wavenumber, and the colored map will change accordingly. However, the colored map shows which areas have the highest overall absorbance. This does not account for noise or absorbances that need a baseline established to find the true peak height (water concentration). Therefore, these maps often do not necessarily show where the water content is the highest, but where there is the most interference or noise. These areas tend to be in fractures, along grain boundaries, and in inclusions.

With these unfortunate developments, finding any possible water trends grew increasingly difficult as the maps proved to be ineffective at accurately showing water locations. Therefore, individual water peaks were examined to find any difference in water concentration between the quartz grain, inclusions, or other features. In some granitic and paragneiss clasts in the low strain rocks (A08-09), fluid inclusions and fractures in quartz held a much larger amount of water than the quartz grain itself (Fig. 12). For example, two granitic samples, A08-09-Y4 and A08-09-Y5_Map2, had water peak heights of 0.2 and 0.25 respectively in fractures, but water peaks of only 0.1 and 0.15 respectively in the rest of the quartz grain (Fig. 12). Some samples of granitic (A08-09-Y2) and paragneiss (A08-09-Z3 and A08-09-Z4) contain a fairly large amount of water in fluid inclusions (absorbances of 0.4, 0.6, and 0.5 respectively) while the surrounding quartz grain in those samples contains little to no water (Fig. 12). In Figure 12, when more than one absorbance is noted, the bolded absorbance number correlates to the bolded location reported beneath it.

To further quantify water peak height data, the lowest and highest water absorbances were recorded along with the location of the highest water location in each sample across the strain gradient (Fig. 15 & 16). While many clasts contained their highest water peaks along fractures or in fluid inclusions, all samples showed water distributed throughout the quartz grain itself. This holds true regardless of strain gradient and clast type. Fluid inclusions in the clasts generally corresponded with the highest water peak in all clast types and at all strain magnitudes. However, both quartzite and paragneissic clasts did not have their highest water concentrations at fluid

inclusions at high strain magnitudes (site 06), while granitic clasts continued to have their highest concentrations at fluid inclusions. This trend may explain the overall increase in high water content for granitic clasts with increasing strain. Quartzite clasts demonstrate similar amounts of lowest and highest concentrations of water across the strain gradient, while paragneissic clasts tend to decrease in their highest water concentrations from low to high strain.

4.1.3 Water Peaks

While exploring the location of water in quartz using grain maps, we discovered three sharp peaks that occur periodically within our expected broad water peak in many samples' spectra. These additional peaks occur in some samples but not others, and sometimes in pairs. Therefore, in addition to studying the location of water in the quartz grains, this study also investigates the occurrence of these additional peaks. Figure 17 quantifies these data.

The most common additional peak is found at 3,350cm^{-1} and occurs across the strain gradient in low, moderate, and high strain rocks (Fig. 17). This peak also appears in all three clast types (quartzite (X's), pink granitic (Y's), and green paragneiss (Z's)). Two peaks occurring at 2,950cm^{-1} and 3,550cm^{-1} tend to appear together and are only found in three pink clasts (Y's) from high strain samples. Another pair of peaks occurs at 3,350cm^{-1} and 3,650cm^{-1} and are found in a larger variety of samples. These peaks are found most often in quartzite samples (X's), but also occur in two pink clasts, and appear across the strain gradient in low, moderate, and high strain samples. The

3,650cm^{-1} peak also occurs by itself in all clast types and all strain types. One sample (A08-06-Y1) contained the largest amount of water seen in this study, with a large water peak at 3,400cm^{-1} (Fig. 17). The absorbance of water throughout the quartz grain in this sample was 0.97 (Fig. 12) with the overall water peak appearing different than that in all of the other samples. A08-06-Y1 had a larger, broader water peak than the other samples analyzed in this study.

The peaks at 3,350cm^{-1} and 3,650cm^{-1} represent different species of OH bonds. Many of the spectra across the quartz grain itself tend to have one or both of these peaks in addition to the broad water peak from 4000-2500cm^{-1} wavenumber (Kekulawala, et al., 1978). Interestingly, the water in fluid inclusions and sometimes microfractures often do not contain these OH peaks. Instead, they tend to have broad water peaks lacking any sharp, smaller peaks. This may indicate a change in fluid composition between the quartz grain and the inclusion, and potentially a different time of fluid emplacement between the two.

A.

Low Strain (09)

Quartzite		
Sample	Absorbance	Where H20 occurs
X1	0.18	Inclusion
X2	0.1	Very lil H_2O in general
X2_Map2	0.2	In Qtz. Grain
X3	0.15-0.2	More in line of Incl.'s
X4	0.1	Lg. Fluid Inclusion

Orthogneiss		
Sample	Absorbance	Where H20 occurs
Y1	N/A	No good H_20 curves
Y1_Map2	0.175	Lg. Black spot (Incl.?)
Y2	0.15-**0.4**	**High (0.4) in Incl.**
Y4	0.1-**0.2**	**Fract.'s**
Y5	N/A	H_20 curves not good
Y5_Map2	0.15-**0.25**	**Fract.'s**

Paragneiss		
Sample	Absorbance	Where H20 occurs
Z3	0-**0.6**	**Inclusion**, No H20 in Qtz.
Z3_Map2	0.25	In Qtz. Grain
Z4	0-**0.5**	**Inclusion**, No H20 in Qtz.
Z4_Map2	0.5	In Qtz. Grain

KEY	
Bold =	Bolded absorbance correlates to the bolded location ("where water occurs")
	Non-bolded absorbance = average absorbance for the overall Qtz. Map
Average absorbance less than 0.2cm^{-1}	
Average absorbance of 0.2-0.3cm^{-1}	
Average absorbance above 0.3cm^{-1}	

Figure 12. These charts display the average absorbance in quartz for each sample (color coordinated; see key) and the area in the quartz grain map that showed the highest water content. All sample names begin with 'A08' and are separated into low (A.), moderate (B.), and high strain (C.). For example, the first sample in the chart to the left would be a quartzite sample named 'A08-06-X1'. The sample names are colored based on clast type: pink granitic clasts are red, green gneissic clasts are green. Abbreviations used in the charts are defined as follows: Lg. = large, Qtz. = quartz, Fract. = fracture, Bound.'s = boundaries.

B.

Moderate Strain (05)

Quartzite		
Sample	Absorbance	Where H20 occurs
X1	0.2	Inclusion & in Qtz.
X1_Map2	0.2	Fract. & in Qtz.
X2	0.175	Equal through-out
X2_Map2	0.2	Fract. & Qtz.

Orthogneiss		
Sample	Absorbance	Where H20 occurs
Y1	0.25	Equal through-out
Y2	0.275	Equal through-out
Y2_Map2	0.4	Lg. Fluid Inclusion

Paragneiss		
Sample	Absorbance	Where H20 occurs
Z1	0.1	Fracture
Z2	0.2	Bound's of an Incl.

C.

High Strain (06)

Quartzite		
Sample	Absorbance	Where H20 occurs
X1	0.15	Inclusion & Fract's
X1_Map2	0.25	Inclusion & Fract's
X2	0.07	Fract's
X2_Map2	0.2	Seems random
X3	0.155	Inclusion & Fract.
X4	0.25	Grain Bound.

Orthogneiss		
Sample	Absorbance	Where H20 occurs
Y1	0.97	In Qtz. Grain
Y2	>0.005	Little to no H_20
Y2_Map2	0.15	Inclusion& Qtz
Y3	0.12	None in the Qtz.
Y3_Map2	0.1	Inclusion
Y4	0.18 - 3,400 0.02 avg.	Inclusion No H20 in Qtz.
Y4_Map2	0.2	Inclusion
Y5	0.06 or less	None in Qtz.

Paragneiss		
Sample	Absorbance	Where H20 occurs
Z1	0.2	Fract's
Z2	0.2	None in Qtz
Z3	0.15	Inclusion
Z3_Map2	0.1	Inclusion
Z4	0.12	Inclusion & Qtz. Grain
Z4_Map2	0.3	Inclusion & Qtz. Grain

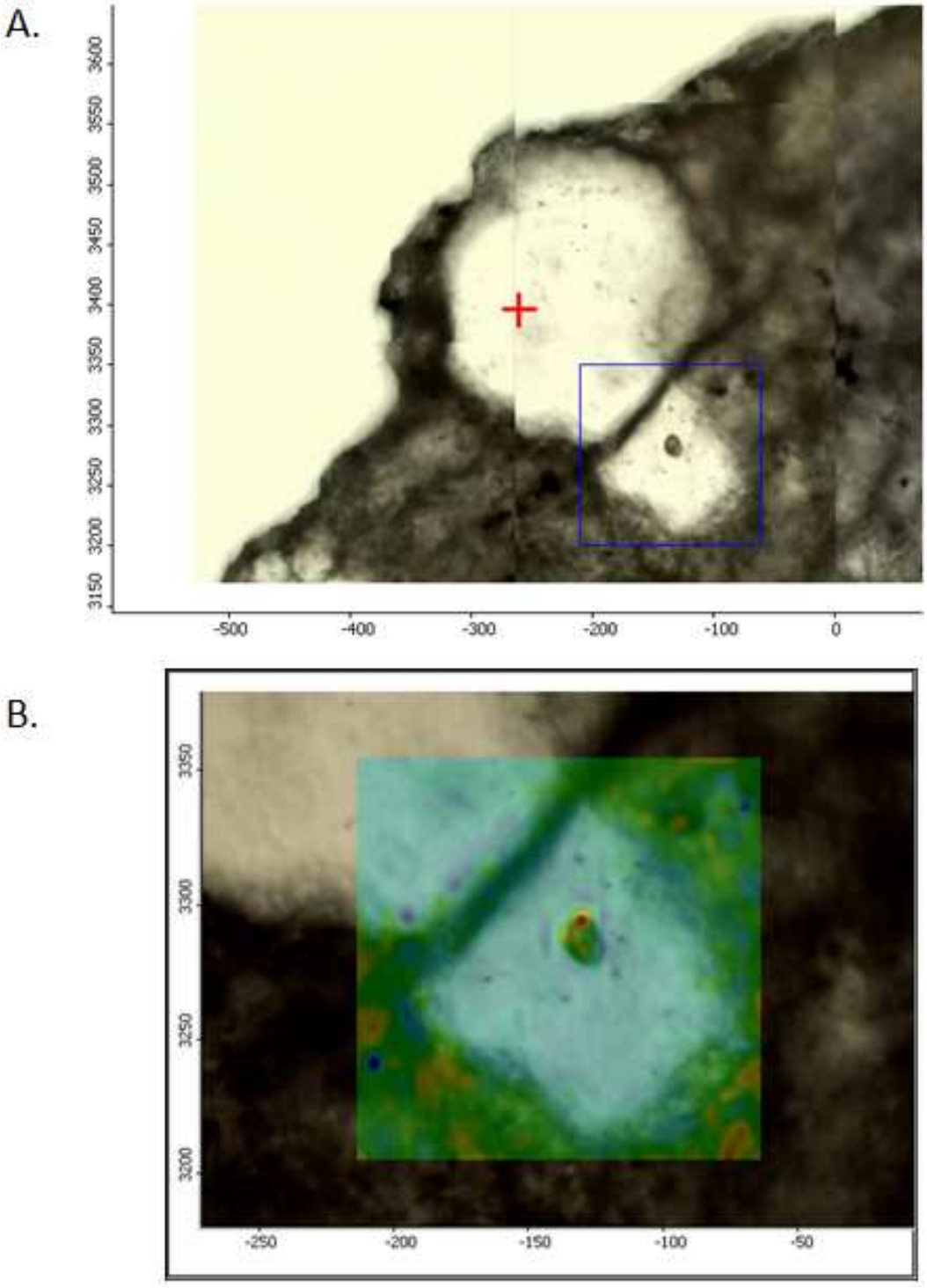

Figure 13. A. Photo mosaic of the selected quartz grain in sample A08-09-Z4, showing the location of the area map to be plotted in the blue rectangle. B. End result showing the water concentrations in color overlying the image of the quartz grain.

A.

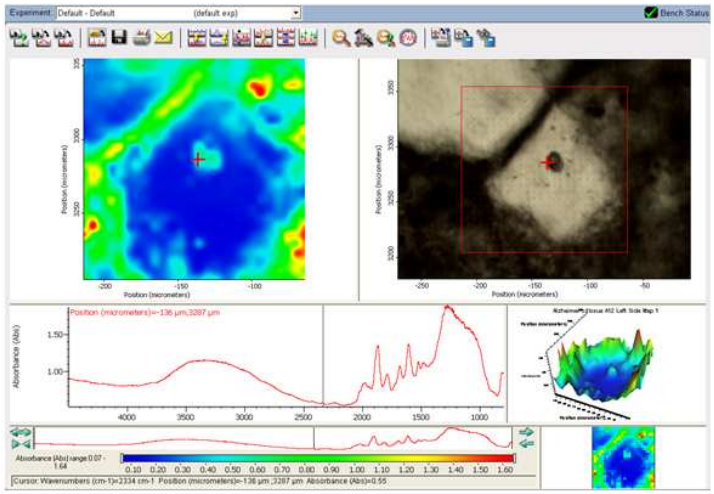

B.

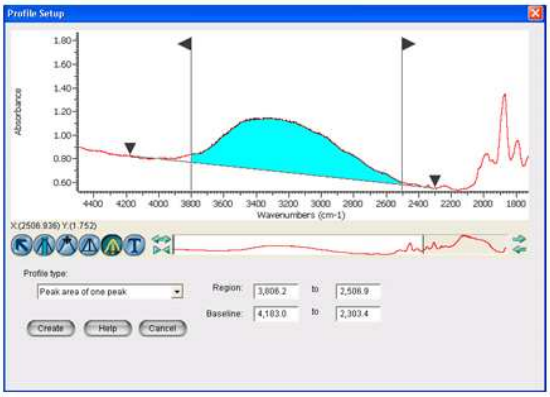

C.

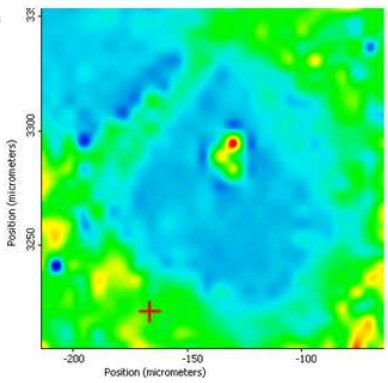

Figure 14. A. Initial screen when data collection is complete on the area map. Note the vertical line at roughly 2,950cm^{-1} wavenumber that may be shifted to change the colored map. B. Water peak area is found using the peak area tool, creating the following color map in (C.) showing the location of the largest water peaks using the area under the curve. All images are from Omnic.

Low Strain (09)

Quartzite			
Sample	Low Absorb.	High Absorb.	Location of High
X1	0.19	0.532	Inclusion
X2	0.133	0.141	Qtz grain
X2_Map2	0.19	0.192	Qtz grain
X3	0.13	0.222	Inclusion
X4	0.106	0.126	Inclusion
AVG.	**0.15**	**0.24**	

Orthogneiss			
Sample	Low Absorb.	High Absorb.	Location of High
Y1	0	0.09	Boundary
Y1_Map2	0.134	0.414	Inclusion
Y2	0.151	0.469	Inclusion
Y4	0.086	0.177	Microfract.
Y5	0	0.25	Boundary
Y5_Map2	0.161	0.247	Microfract.
AVG.	**0.09**	**0.27**	

Paragneiss			
Sample	Low Absorb.	High Absorb.	Location of High
Z3	0	0.593	Inclusion
Z3_Map2	0.228	0.276	Microfract.
Z4	0	0.413	Inclusion
Z4_Map2	0.412	0.438	Qtz grain
AVG.	**0.16**	**0.43**	

Moderate Strain (05)

Quartzite			
Sample	Low Absorb.	High Absorb.	Location of High
X1	0.153	0.208	Inclusion
X1_Map2	0.149	0.166	Microfract.
X2	0.155	0.362	Inclusion
X2_Map2	0.157	0.177	Qtz grain
AVG.	**0.15**	**0.23**	

Orthogneiss			
Sample	Low Absorb.	High Absorb.	Location of High
Y1	0.201	0.26	Inclusion
Y2	0.218	0.461	Inclusion
Y2_Map2	0.309	0.346	Microfract.
AVG.	**0.24**	**0.36**	

Paragneiss			
Sample	Low Absorb.	High Absorb.	Location of High
Z1	0.113	0.187	Microfract.
Z2	0.185	0.324	Inclusion
AVG.	**0.15**	**0.26**	

High Strain (06)

Quartzite			
Sample	Low Absorb.	High Absorb.	Location of High
X1	0.128	0.139	Qtz grain
X1_Map2	0.235	0.275	Qtz grain
X2	0	0.128	Microfract.
X2_Map2	0.189	0.206	Qtz grain
X3	0.147	0.15	Qtz grain
X4	0.198	0.22	Qtz grain
AVG.	**0.15**	**0.19**	

Orthogneiss			
Sample	Low Absorb.	High Absorb.	Location of High
Y1	0.993	1.026	Qtz grain
Y2	0	0.133	Qtz grain
Y2_Map2	0.131	0.24	Microfract.
Y3	0.093	0.277	Inclusion
Y3_Map2	0.137	0.326	Inclusion
Y4	0	0.38	Inclusion
Y4_Map2	0.228	0.846	Inclusion
Y5	0	0.155	Qtz grain
AVG.	**0.20**	**0.42**	

Paragneiss			
Sample	Low Absorb.	High Absorb.	Location of High
Z1	0.196	0.244	Microfract.
Z2	0.17	0.183	Qtz grain
Z3	0	0	--
Z3_Map2	0.099	0.103	Qtz grain
Z4	0.112	0.386	Inclusion
Z4_Map2	0.264	0.344	Qtz grain
AVG.	**0.14**	**0.21**	

Figure 15. The lowest and highest absorbances observed in all clast types from the three sample locations are shown above. Average low and high absorbances have been calculated for each clast type at each strain magnitude and are shown in the last row of each chart.

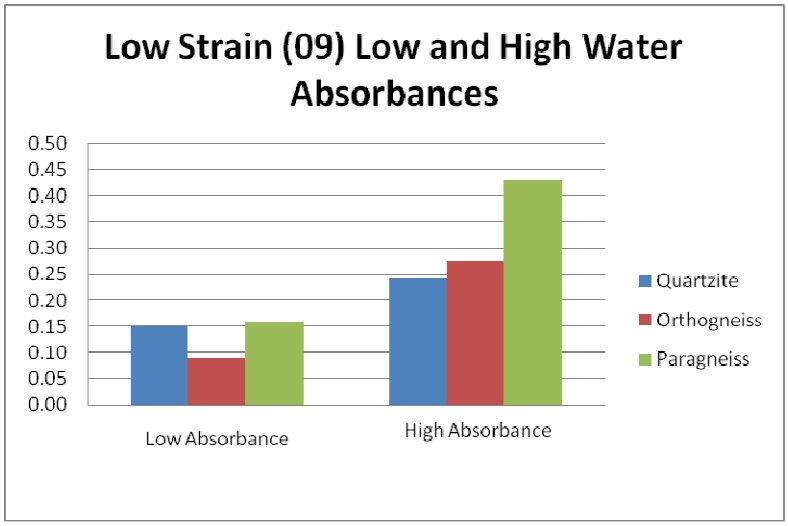

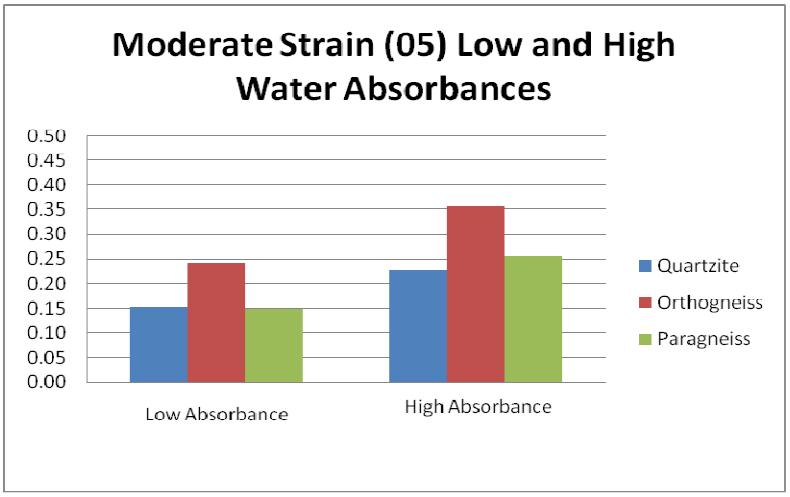

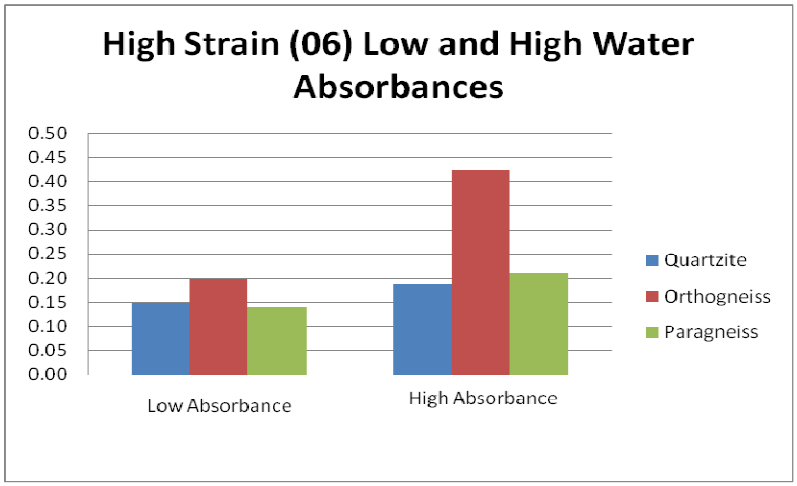

Figure 16. The average low versus high water absorbances in quartz grains are shown for low, moderate, and high strain rocks. Each clast type is represented by a different color as shown in the key.

A.

Low Strain (09)

Quartzite	
Sample	Main H_20 Peaks
X1	3,350cm^{-1}
X2	3,650cm^{-1}
X2_Map2	3,350cm^{-1} & 3,650cm^{-1}
X3	3,350cm^{-1}
X4	3,350cm^{-1} & 3,650cm^{-1}

Orthogneiss	
Sample	Main H_20 Peaks
Y1	N/A
Y1_Map2	3,350cm^{-1}
Y2	3,350cm^{-1} & 3,650cm^{-1}
Y4	3,350cm^{-1}
Y5	3,650cm^{-1}
Y5_Map2	3,350cm^{-1}

Paragneiss	
Sample	Main H_20 Peaks
Z3	3,650cm^{-1}
Z3_Map2	3,350cm^{-1}
Z4	N/A (sine wave)
Z4_Map2	3,350cm^{-1}

KEY
Peak height = 3,350cm^{-1}
Peak height = 3,650cm^{-1}
Peak height = 3,350cm^{-1} and 3,650cm^{-1}
Peak height = 2,950cm^{-1} and 3,625cm^{-1}
Peak height = 3,400cm^{-1}

Figure 17. Charts A, B, and C include additional peaks that are prominent in the traditional broad O-H peak between 3200-3600 wavenumber. Sample names are colored based on clast type (i.e. red for pink granitic clasts, green for paragneissic clasts). The key defines colors based on the peak height they represent.

B.

Moderate Strain (05)

Quartzite	
Sample	Main H_20 Peaks
X1	3,350cm^{-1} & 3,650cm^{-1}
X1_Map2	3,350cm^{-1} & 3,650cm^{-1}
X2	3,350cm^{-1} & 3,650cm^{-1}
X2_Map2	3,350cm^{-1}

Orthogneiss	
Sample	Main H_20 Peaks
Y1	3,350cm^{-1}
Y2	3,350cm^{-1}
Y2_Map2	3,350cm^{-1}

Paragneiss	
Sample	Main H_20 Peaks
Z1	3,350cm^{-1}
Z2	3,350cm^{-1}

C.

High Strain (06)

Quartzite	
Sample	Main H_20 Peaks
X1	3,350cm^{-1} & 3,650cm^{-1}
X1_Map2	3,350cm^{-1}
X2	3,650cm^{-1}
X2_Map2	3,350cm^{-1}
X3	3,350cm^{-1}
X4	3,350cm^{-1}

Orthogneiss	
Sample	Main H_20 Peaks
Y1	3,400cm^{-1}
Y2	2,950cm^{-1} & 3,550cm^{-1}
Y2_Map2	3,350cm^{-1}
Y3	2,950cm^{-1} & 3,625cm^{-1}
Y3_Map2	3,350cm^{-1}
Y4	3,400cm^{-1} & 3,625cm^{-1}
Y4_Map2	3,350cm^{-1}
Y5	2,950cm^{-1} & 3,625cm^{-1}

Paragneiss	
Sample	Main H_20 Peaks
Z1	3,350cm^{-1}
Z2	3,350cm^{-1}
Z3	3,650cm^{-1}
Z3_Map2	3,350cm^{-1}
Z4	3,350cm^{-1}
Z4_Map2	3,350cm^{-1}

4.2 XRF Results

X-Ray Fluorescence (XRF) analyses were conducted on eighteen samples collected from Antelope Island. Six of these samples were high strain (A08-06), six were moderate strain (A08-05), and six were low strain samples (A08-09). The data collected and analyzed for this thesis are compiled into a series of tables (Appendix B). Geochemistry data from this study are compared to the geochemical results from the basement and its shear zones (Yonkee et al., 2003) and a more extensive dataset for the diamictite matrix and clasts that includes the results from this thesis (Yonkee et al., 2013).

There are intrinsic limitations for this study on Antelope Island diamictites regarding XRF analysis. Since this study focuses on the clasts within a diamictite, the mass of the samples is far less than the minimum necessary for representative compositional analysis. Therefore, elements that are not in the major minerals of these clasts are likely not representative in the data. For example, elements that tend to be concentrated in accessory phases such as P in apatite and Zr in zircon will likely present problematic percentages.

Minor contamination from the steel jaw crusher, the lab environment, and the tungsten carbide shatterbox is possible but should not be sufficient to affect the major and minor element concentrations.

Because of their low concentrations, most trace elements analyzed had unacceptably large analytical errors (>10%) and/or were not distinguishable from background when considering their lower limits of detection (<2 LLD). Of the trace elements, only Y, Zr, and Ba consistently met the percent error and LLD requirements and are thus included in this study. Major and minor elements Na, P, and Mn had high percent errors in some cases as well. It is generally accepted that in order to confidently report results, they must be at least two times the LLD. The LLD represents the smallest amount of an element that the XRF instrument can accurately detect. Data are also considered invalid if the percent error is greater than 10%. Percent error deals with the counting statistics and error inherent in the instrument. The percent error reported does not account for repeatability or error introduced during sample preparations. When readings do not meet the minimum criteria to report accurate results, data for that element has been replaced with 'ND' in the tables included in the appendices of this study.

Elements making up the majority of both pink granitic and green gneissic samples include silica, aluminum, iron, and potassium (Table 1). These two clast types have extremely similar compositions. Quartzite samples contain mainly SiO_2, as expected.

Data shown in Table 1 are compared with the geochemical findings of Yonkee et al., 2003 to determine if the Farmington Canyon Complex (FCC) is the likely protolith for these clasts. Major components silica, aluminum, and iron reported by Yonkee et al.,

2013 fall within the range for pink granitic clasts in this study. Green gneissic clasts in this study have similar silica and iron, but higher aluminum. Overall, as clasts changed from low to high strain, there were not statistically significant differences in their composition. Calcium is the only element that showed an increase in concentration with strain for both pink granitic and green gneissic clasts.

Sample	Granitic Clasts (Y)	Gneissic Clasts (Z)	Quartzite Clasts (X)
SiO2 (%)	69.04 - 73.14	67.53 - 74.89	98.53 - 99.90
Al2O3 (%)	11.90 - 12.69	12.06 - 12.54	0.71 - 0.90
Fe2O3 (%)	6.35 - 6.92	4.10 - 9.47	0.27 - 0.70
K2O (%)	4.24 - 4.76	4.75 - 5.06	0.17 - 0.21
MgO (%)	1.20 - 1.46	1.14 - 1.56	0.11 - 0.12
Na2O (%)	0.31 - 0.95	ND - ND	ND - ND
CaO (%)	0.15 - 0.60	0.11 - 0.73	ND - ND
TiO2 (%)	0.17 - 0.56	0.41 - 0.59	ND - ND
P2O5 (%)	0.06 - 0.23	0.13 - 0.18	ND - ND
Mn (%)	-5.53 - 9.87	-1.63 - 8.97	ND - ND

Table 1. General clast compositions, including pink granite (Y), green paragneiss (Z), and quartzite (X) clasts. The range reported is the average composition +/- one standard deviation.

4.3 Petrographic Analysis Results

Three sites from Antelope Island were chosen for detailed petrographic analyses, including site 06 (A08-06, high strain), site 05 (A08-05, moderate strain), and site 09 (A08-09, low strain). Five granitic clasts, four micaceous gneissic clasts, and three quartzite clasts were analyzed from site 06. Two of each clast type were analyzed from site 05. Four granitic and quartzite clasts, and two gneissic clasts were analyzed from site 09.

Thin section observations revealed that gneissic clasts are mainly composed of quartz grains and micaceous matrix, including only about 5-10% feldspar and opaque minerals. Granitic clasts are also primarily composed of quartz grains and micaceous matrix, and additionally contain minor amounts of plagioclase, biotite, and opaque minerals. Feldspars are often sericitized across the strain gradient. For both gneissic and granitic clasts, typical constituents are 50-60% fine-grained matrix material , 35-45% quartz grains or grain aggregates, and 1-10% opaque minerals. Quartzite clasts contained quartz grains with far less matrix than the granitic and gneissic clasts. The micaceous matrix is composed of biotite, muscovite, sericitized feldspars, and an increasing amount of chlorite from low to high strain. Foliation also becomes increasingly visible on thin sections in matrix and in clasts from low to high strain.

Grain sizes were measured and recorded for each sample. It would be beneficial to differentiate grain sizes based on mineralogy. Often, one mineral type has larger grains than another. For example, quartz grains in high strain samples can be much larger than feldspar and mica grains, while there are some large plagioclase grains in low

strain samples.

Quartzite clasts contain quartz grains that are generally between 100-400 μm in diameter. Pink granite and green paragneiss clasts have a similar range in grain sizes, with most grains ranging from 100-600μm. Larger grains do occur, with the largest quartz grain in this study measuring 2,400μm, but these larger grains occur much less frequently. Both gneissic and granitic samples have very similar ranges of grain sizes from low to high strain (Fig. 18B). Quartzite samples contain a cluster of grain sizes, mostly 500μm and smaller regardless of strain (Fig. 18C). Gneissic and granitic clasts display a broader range of grain sizes than quartzite clasts, which may result from the monomineralic nature of quartzite or the protolith grain size.

Since quartz and micaceous matrix were the most common materials in these rock samples, detailed microstructural analyses are focused mainly on quartz grains. Alkali feldspars and plagioclase feldspars were counted during analyses, but were too scarce to provide an accurate measure of microstructural assemblages.

As a precursor to future work (i.e. Czeck et al., 2011; Yonkee et al., 2013), this study focuses on finding possible patterns between microstructures and clast type or strain magnitude. These microstructural observations are compared to the FTIR and Synchrotron studies in an attempt to determine possible effects of fluid on deformation and possible source and sink sites for dissolved material. Additionally, the point counting data are used to determine if there is a link between strain magnitudes and deformation mechanisms. The microstructures are classified based on the deformation mechanism likely responsible for their formation. In this analysis, microfractures are

considered to be formed by brittle deformation. Undulose extinction, deformation lamellae, recrystallization, and subgrains form during crystal plastic deformation (dislocation creep) (Fig. 19). Bulged grain boundaries were observed, indicating grain boundary migration as the deformation mechanism. There were no abundant microstructures recorded that formed as a result of DMT.

Average percentages of microstructures in quartz grains have been calculated and graphed for each clast type (Fig. 19 A, B, and C, Table 2). The average microstructures are compared from each location to determine variations that occur across the strain gradient.

Quartzites display relatively few microfractures compared to other clast types across the strain gradient (6-17%). Granitic clasts show a general decrease in microfractures from low to high strain. The drop from 68% microfractures to only about 33% may indicate an initial brittle reaction to stress at low strain for granitic clasts, and these fractures were subsequently annealed at higher strains. Gneissic clasts contain similar abundances of microfractures from low to high strain.

Quartzite clasts contain quartz that displays undulose extinction 99.7% of the time, while 80-86% of quartz grains in granitic and gneissic clasts have undulose extinction. In both granitic and gneissic clasts, grain boundary migration increased significantly at site 06 in high strain (11-14%). In fact, the average microstructures occurring in granitic and gneissic clasts are strikingly similar across the strain gradient (Table 2).

Quartzite displays few deformation lamellae across the strain gradient (6-7% of

analyzed grains) while both granitic and gneissic clasts have fewer with increasing strain (35-7% for granitic, 25-10% for gneissic). Quartzite also contains a small amount of quartz grains with subgrains (7-8%), except at a moderate strain (site 05) with 24% of quartz grains containing subgrains. Both granitic and gneissic clasts display similar amounts of subgrains across strain (35-38% of analyzed quartz grains) except at low strain. 54% of quartz grains in gneissic clasts contain subgrains at low strain, with fewer at moderate and high strain.

From low to high strain, the number of recrystallized grains increased in all clast types. Quartz grains in quartzite consistently display more recrystallization than quartz grains in the other clast types. Low strain quartz exhibits 16-18% more recrystallization than in granitic and gneissic clasts respectively. Moderate strain quartz grains from quartzite clasts have 57-58% more recrystallization than that in granitic and gneissic clasts, and high strain quartz has 39-44% more recrystallization. The drop in percentages for high strain samples is a result of a dramatic increase in the amount of recrystallization in quartz in both granitic and gneissic clasts, where recrystallization was almost nonexistent at low and moderate strains for these samples.

A. Low Strain Gneissic Sample High Strain Gneissic Sample

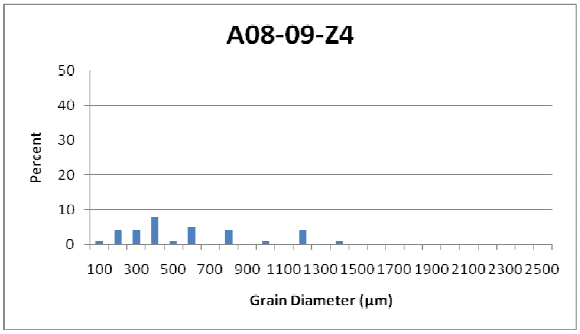

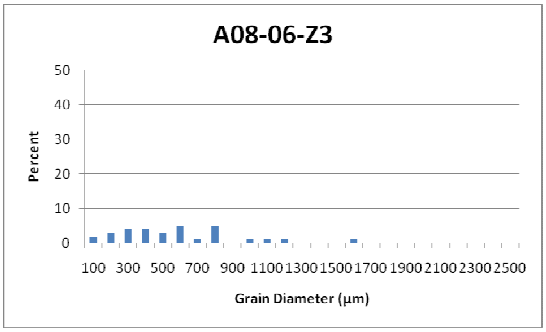

B. Low Strain Gneissic Sample High Strain Gneissic Sample

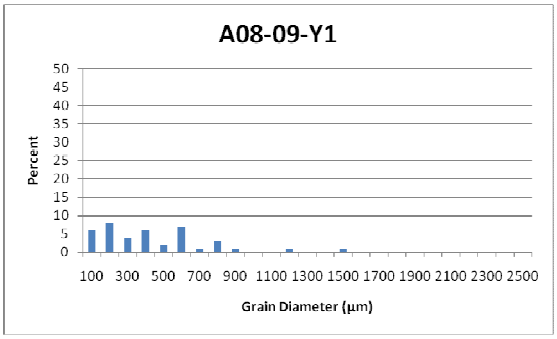

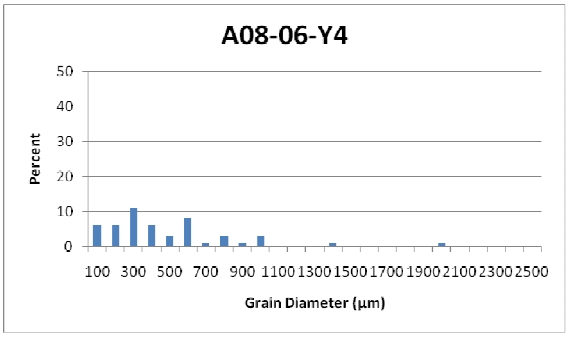

C. Low Strain Gneissic Sample High Strain Gneissic Sample

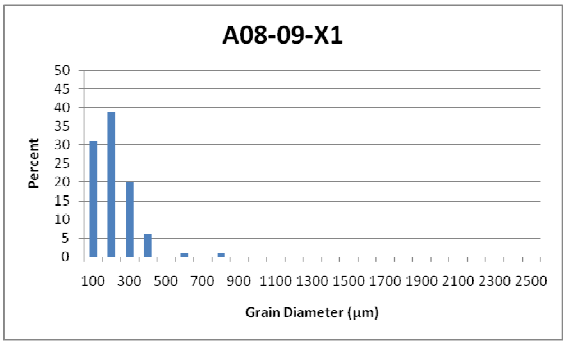

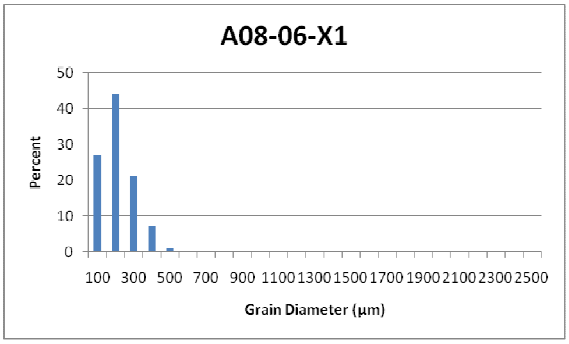

Figure 18. Low strain (site 09) and high strain (site 06) comparisons of A. two gneissic samples (Z) , B. two granitic clasts (Y), and C. quartzite samples. In granitic samples (B), grain sizes are similar between the low and high strain samples. In quartzite samples (C), both examples of low and high strain exhibit smaller grain sizes than either the gneissic or granitic clasts. The quartzite also displays a much smaller range of grain sizes than any other clast type. Grain size is strain independent.

A.

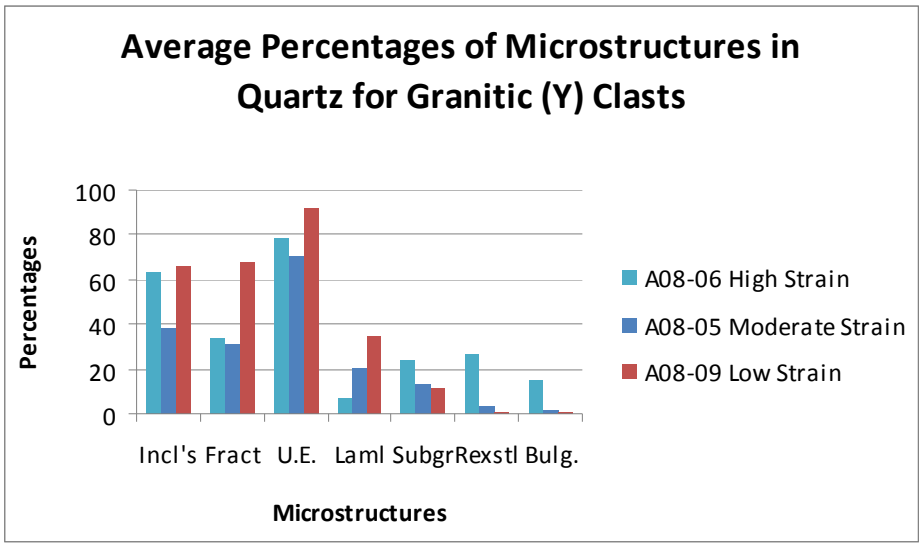

KEY

Code	Description
Incl's	Fluid Inclusions
Fract	Microfractures
U.E.	Undulose Extinction
Laml	Deformation Lamellae
Subgr	Subgrains
Rexstl	Recrystallization
Bulg.	Bulged Grain Boundary

Figure 19. Graphs A, B, and C show averge quantitative microstructural data for individual clast types. Each graph represents a different clast type, and each graph includes data from each of the three sample sites. This allows for comparison of microstructural data across a strain gradient. The microstructures are represented in the graphs are shown in the key above.

B.

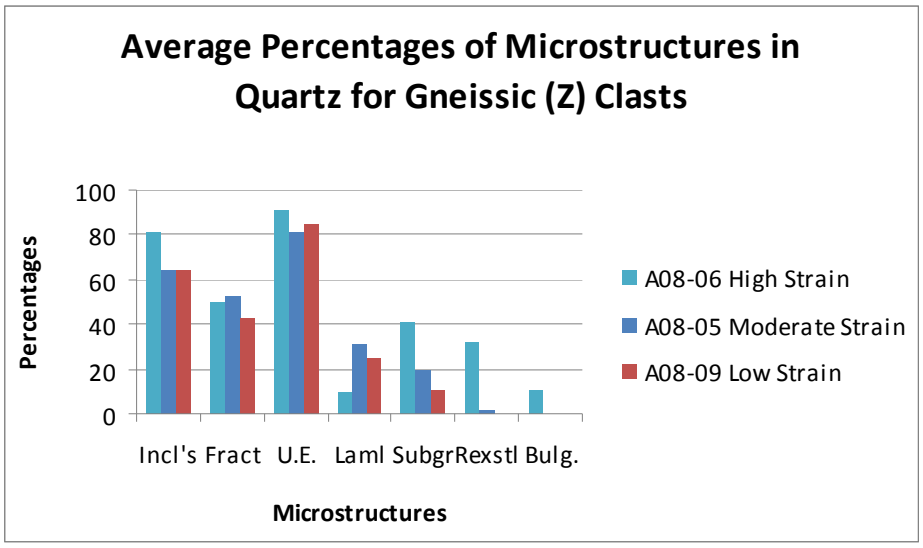
Average Percentages of Microstructures in Quartz for Gneissic (Z) Clasts
Percentages
100
80
60
40
20
0
Incl's
Fract
U.E.
Laml
Subgr
Rexstl
Bulg.
Microstructures
A08-06 High Strain
A08-05 Moderate Strain
A08-09 Low Strain

C.

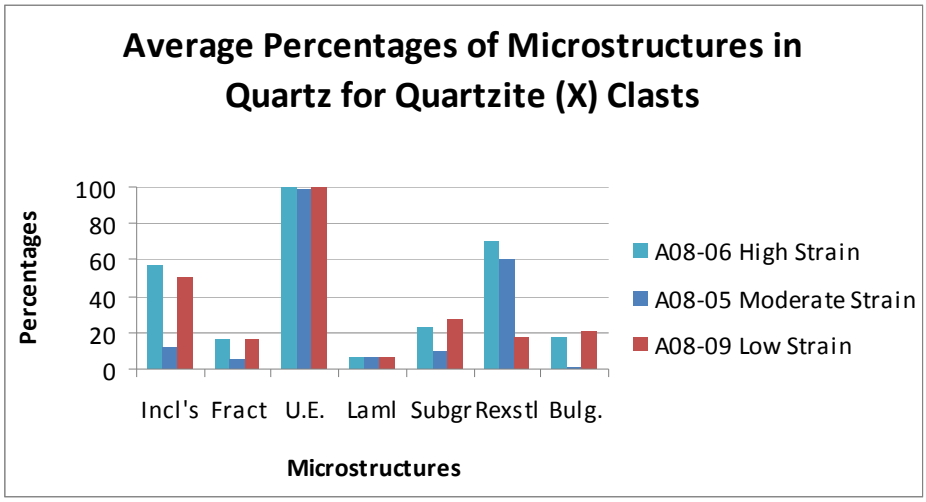
Average Percentages of Microstructures in Quartz for Quartzite (X) Clasts
Percentages
100
80
60
40
20
0
Incl's
Fract
U.E.
Laml
Subgr
Rexstl
Bulg.
Microstructures
A08-06 High Strain
A08-05 Moderate Strain
A08-09 Low Strain

		Incl's	*Fract*	*U.E.*	*Laml*	*Subgr*	*Rexstl*	*Bulg.*
A08-09 (Low Strain)	**Avg. Gneissic**	64	43	85	25	54	0	0
	Avg. Quartzite	51	17	100	6	7	18	21
	Avg. Granitic	66	68	92	35	35	1	1
A08-05 (Mod Strain)	**Avg. Gneissic**	65	53	81	31	38	2	0
	Avg. Quartzite	13	6	99	7	24	60	2
	Avg. Granitic	39	31	70	21	37	3	2
A08-06 (High Strain)	**Avg. Gneissic**	81	50	91	10	35	32	11
	Avg. Quartzite	58	16	100	7	8	71	18
	Avg. Granitic	64	34	78	7	38	27	15

Table 2. Average percentage of microstructures calculated for each clast type at each location. These percentages are shown in graph form in Fig. 15 A, B, and C for a visual comparison of data.

Chapter 5: Discussion

5.1 FTIR/Synchrotron

The FTIR results recorded using area grain maps proved to be unreliable in this study. The prospect of using the Synchrotron to create grain maps and overlie them with an optical image of the quartz is exciting. Unfortunately, the "concentrations" shown on these maps do not show areas of high vs. low water concentration, but rather the amount of noise in the measurement. Noise can create sharp, thin absorbance peaks, which do not indicate water abundances. A peak height tool can be used to determine the relative amount of water from one point to the next (determined by the varying height of the peak), but with grain size maps consisting of 50-500 points, using that tool alone would be inefficient. This tool can be used to create a baseline and then set boundaries for the area of a water peak. A useful map could be created if this baseline and corresponding area could be applied to each spectrum across the grain maps. Future researchers could work to combine these methods to resolve these problems.

Another possible limitation of the current data is that thin sections were used on the Synchrotron. The glass used to mount the thin sections may not be completely water or OH free, although spot tests of the glass did not identify any peaks within the water range. In addition, the adhesive used to create the thin sections may contain OH groups and other materials that could interfere with the water peak. However, spectra for all materials used to create the thin sections (including the adhesive) do not appear

to interfere with a water peak. Additionally, background readings taken toward the edge of the thin sections with only the glass and adhesive did not produce peaks between 3000 and 4000cm^{-1} wavenumber (Fig. 9 and 10). However, subsequent researchers in our group found problems with FTIR thin section analysis that suggested that the adhesive may not be homogenous and might in fact have constituents that interfere with water peaks (Nachbor, 2011). Therefore, it is unknown exactly what effect the adhesive might have on the readings, which is particularly problematic because the adhesive does not cover the slide homogeneously. A thorough investigation as to whether Synchrotron data from thin sections can be safely used or the development of a different sample preparation technique that doesn't require glass and/or adhesive could help address this concern.

Samples in this study were oriented based on deformation lineations and foliations. Thin sections were cut along the XZ plane of the clasts. Research has shown that during quartz crystal growth, water may tend to concentrate on specific crystal faces depending on the rate of crystal growth, fluid variability, and orientation of the crystal lattice (Ihinger and Zink, 2000). Thus study did not examine multiple orientations of the quartz crystal itself because we focused on the relationship between water and microstructures such as fractures. However, it is possible that the amount of water contained in the quartz grains could vary when examined along various crystal orientations.

As a result of the issues discovered with the grain maps intended for use in this study, the remainder of this discussion will be restricted to interpreting water peak

heights and their locations (Fig. 12 and 15). These analyses were completed under the assumption that the glass and adhesive do not interfere with water peaks. Average water peak heights were determined from measuring between ten and fifteen throughout grains, with any anomalies recorded as well (Fig. 12). In addition to the peak height, the locations of typical water peaks with respect to fractures, grain boundaries, fluid inclusions, and any grain features were recorded. During the analyses, three distinctive, sharp water peaks stood out. The wavenumbers of these peaks are recorded in Figure 19. The average absorbance of water within quartz grains is shown in Figure 12. Some grains are outliers, with two granitic clasts (A08-06-Y1 and A08-05-Y2) and one gneissic clast (A08-09-Z4) containing more than twice the amount of water of the other samples.

Sharp peaks between 3000 and 4000cm^{-1} wavenumber include 3350cm^{-1}, 3650cm^{-1}, 3350 and 3650cm^{-1} (together), 2950 and 3625 cm^{-1} (together), and 3400cm^{-1}, which only occurs in the sample with the highest water content (A08-06-Y1). The peak at 3650cm^{-1} likely represents an OH stretching group. Another hydrogen bonded OH group likely occurs at 3350cm^{-1} where hydrogen is bonded to oxygen in the quartz structure (Kronenberg et al., 1990). C-H stretching is likely the result of the peak found at 2950 cm^{-1}. The additional peak occurring at 3400cm^{-1} is enigmatic as sharp peaks from quartz and water are not commonly reported at this wavenumber. Liquid water in quartz is conventionally characterized by a broad absorption peak ranging from 4,000-2500cm^{-1}. All of these peaks complicate the calculation of water in these samples, as they occur within the broad water peak. The peaks at 3400cm^{-1} and 2950 cm^{-1} only

occur in high strain samples in pink granitic clasts. These peaks including the C-H bond may be a result of a chemical reaction that occurred with deformation exclusively in the granitic clasts.

Generally, maximum absorbances at wavenumbers associated with water occurred in fluid inclusions and fractures in quartz grains, particularly at low strains. This observation suggests that the water within the quartz grains is not from primary crystallization, but instead from infiltration during deformation. However, most quartz grains at all strain magnitudes did show absorbances indicating that water was also located within the grains themselves, away from any obvious fractures or fluid inclusions. These observations suggest that some primary water was still present as defects within the quartz crystal structure, water moved along dislocation paths within the grain, or water that was once in fractures was incorporated into the crystal during fracture annealing. In particular, the highest absorbances in quartzite and paragneiss clasts at high strain were not associated with any fractures or obvious fluid inclusions.

5.2 XRF Analysis

Geochemical data analyses support our grouping of granitic and gneissic clasts in the field, but the groups do show some overlap. The data for both clast types cluster together (Fig. 20 and 21), and they are not distinguishable within one standard deviation of their mean compositions for any particular element (Table 1, Appendix B). Table 1

reveals that gneissic clasts possess a larger range of average compositions within one standard deviation than granitic clasts, which suggests that gneissic clasts contain a larger variety of lithologies than granitic clasts. We have observed this variation between clasts in the field, as gneissic clasts range from paragneisses to highly deformed, chloritized, mica-rich, verging on phyllonitic clasts. Granitic clasts display far less lithologic diversity.

Trace element data are limited in this study because many trace elements were below the lower limit of detection for our XRF calibration, or the measurements had high analytical errors. On plots displaying Zr and Ba vs. Al_2O_3 (Fig. 21), granitic and gneissic clasts plot similarly and do not reveal any trends associated with the strain gradient. The remaining trace elements detected also show no significant differences between clasts and strains.

Different clast types from the same outcrops sometimes show some compositional differences beyond one standard deviation. Interestingly, all of the concentrations of major and minor elements at low strain (site 09) are within one standard deviation between the granitic and gneissic clasts (Fig. 22A). This suggests that prior to an increase in deformation, these two clast types likely began with similar compositions. The composition of clasts from moderate and high strain rocks (site 05 and 06) show the following relationships at some outcrops (Fig. 22B and C): granitic clasts have higher concentrations of iron, phosphorus, and aluminum (all at moderate strain site 05) and sodium (high strain site 06) than gneissic clasts, gneissic clasts have higher concentrations of silica and potassium (moderate strain site 05), and titanium

and phosphorous (high strain site 06) than granitic clasts.

Note that granitic clasts at moderate strain have a higher concentration of phosphorous, but gneissic clasts have a higher concentration at a high strain. Gneissic clasts maintained a fairly consistent concentration of phosphorous, with 0.17-0.19% at moderate strain and 0.15-0.17% at high strain. The granitic clasts showed a decrease in phosphorous, beginning with 0.19-0.27% at moderate strain, dropping to 0.05-0.07% at high strain. Due to the likelihood that phosphorous is largely contained within the accessory mineral apatite, the small sample size used for XRF may result in a distorted view of the phosphorous contained within a sample. For example, if the XRF sample happened to contain a cluster of apatite grains, the phosphorous concentrations would be much higher than if the XRF sample was taken from a neighboring part of the clast without apatite. Therefore, the variations in phosphorous may not be representative of significant differences between the clasts or changes with strain.

Future work could help to distinguish between clast types using additional chemical analyses (see Yonkee et al., 2013 for analyses conducted after this study).

One question that must be addressed is whether or not the clasts in our study are derived from the Farmington Canyon Complex basement rock. Figure 20 shows major elements sodium, magnesium, titanium, and potassium plotted against aluminum, with dashed circles representing chemical compositions of the Farmington Canyon Complex reported by Yonkee et al., 2003. Most of the major element concentrations are very similar to the basement and clasts, suggesting that we have accurately identified the protolith of the clasts.

A few of the elemental concentrations do vary between the clast and the basement, and those deviations can be used to understand some of the characteristics of deformation and fluid flow. Figure 20A and 20B show a decrease in sodium and increase in magnesium from protolith to Antelope Island clasts, indicating likely fluid interaction and resultant feldspar alteration into phengitic muscovite.

Sometimes, the interaction of fluids with deforming rocks can result in volume loss, and identifying this volume change can be critical to accurately assess strain in rocks. For example, apparent flattening strains can be the result of plane strain with volume loss (Ramsay, 1967). If there had been significant volume loss in the rocks, the concentration of mobile elements would decrease during deformation and conversely, the concentration of immobile elements would increase during deformation. Examining mobile elements like silica and immobile elements like titanium (Fig. 20C and D) shows minimal change in chemical composition from the protolith (FCC) to diamictite clasts, indicating no volume loss with deformation despite the presence of fluids.

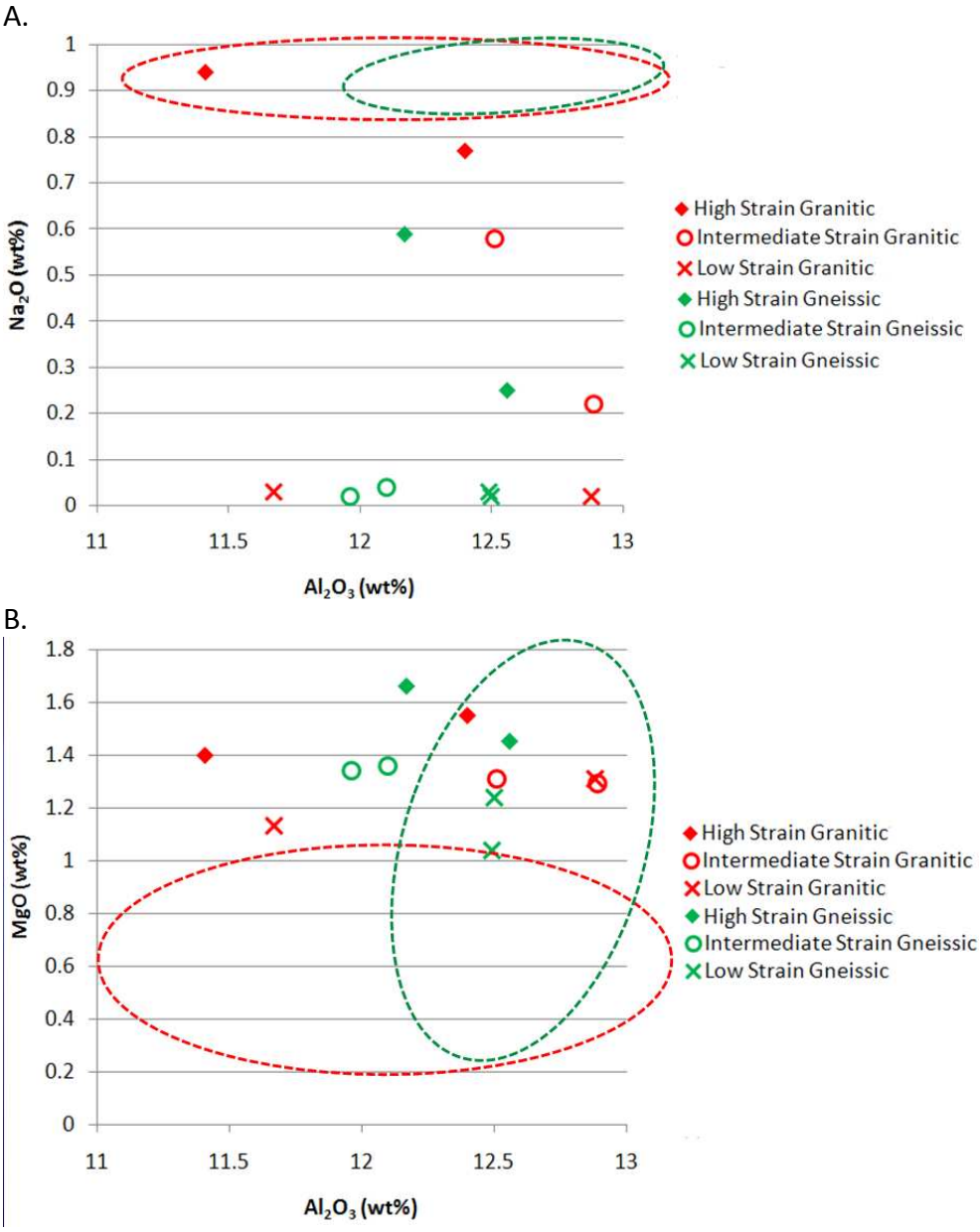

Figure 20. Major elements Na_2O (A.), MgO (B.), TiO_2 (C.), Si_2O (D.), K_2O (E.) and CaO (F.) vs. Al_2O_3 are plotted for Antelope Island samples. Low, intermediate, and high strain samples of pink granitic and green gneissic clasts are plotted and labeled in the key. The dashed circles represent the chemical compositions of the likely protolith, the Farmington Canyon Complex (FCC) crystalline basement. Red circles represent FCC granite and green represent FCC gneiss.

C.

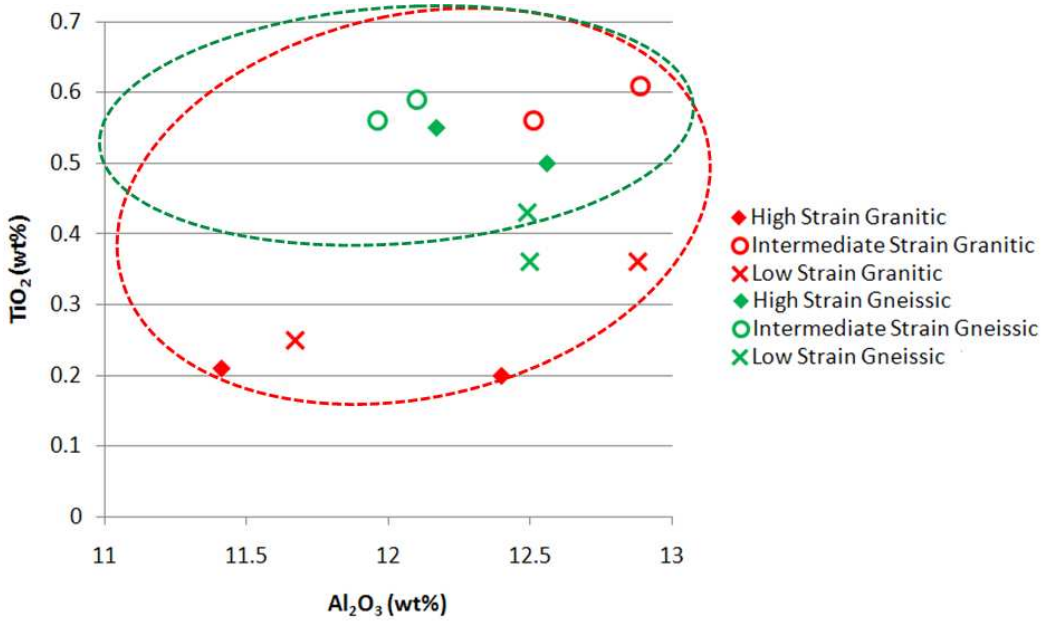
0.7
0.6
0.5
0.4
0.3
0.2
0.1
0
11
11.5
12
12.5
13
TiO2 (wt%)
Al2O3 (wt%)
High Strain Granitic
Intermediate Strain Granitic
Low Strain Granitic
High Strain Gneissic
Intermediate Strain Gneissic
Low Strain Gneissic

D.

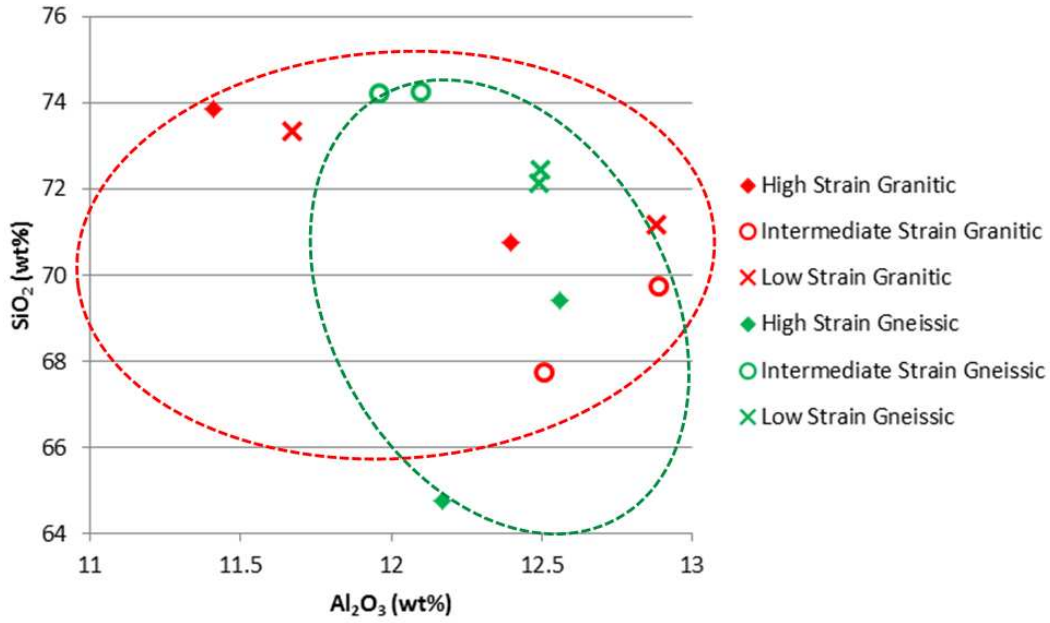
76
74
72
70
68
66
64
11
11.5
12
12.5
13
SiO2 (wt%)
Al2O3 (wt%)
High Strain Granitic
Intermediate Strain Granitic
Low Strain Granitic
High Strain Gneissic
Intermediate Strain Gneissic
Low Strain Gneissic

E.

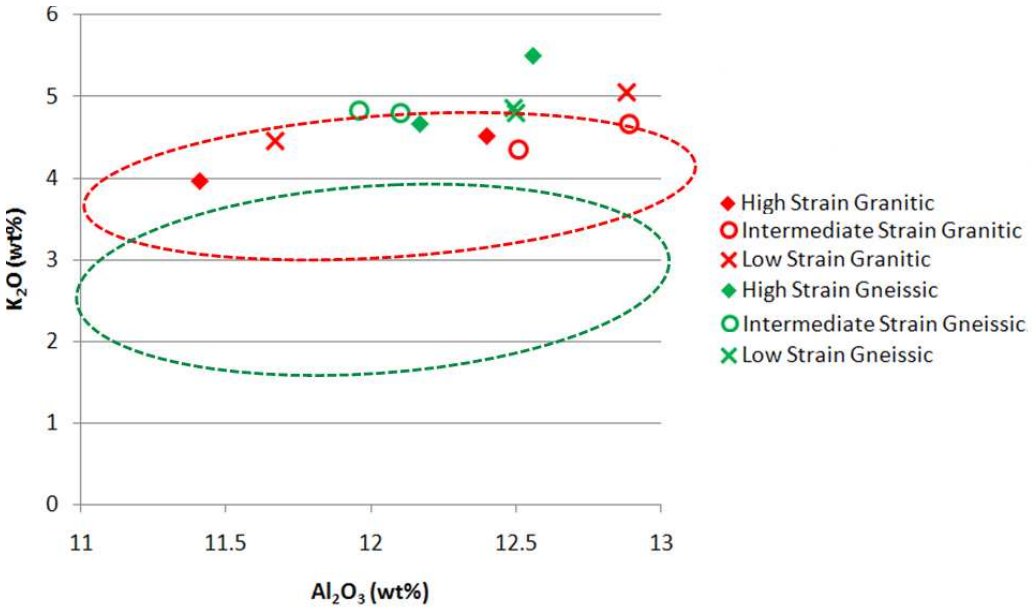
6
5
4
3
2
1
0
11
11.5
12
12.5
13
K_2O (wt%)
Al_2O_3 (wt%)
High Strain Granitic
Intermediate Strain Granitic
Low Strain Granitic
High Strain Gneissic
Intermediate Strain Gneissic
Low Strain Gneissic

F.

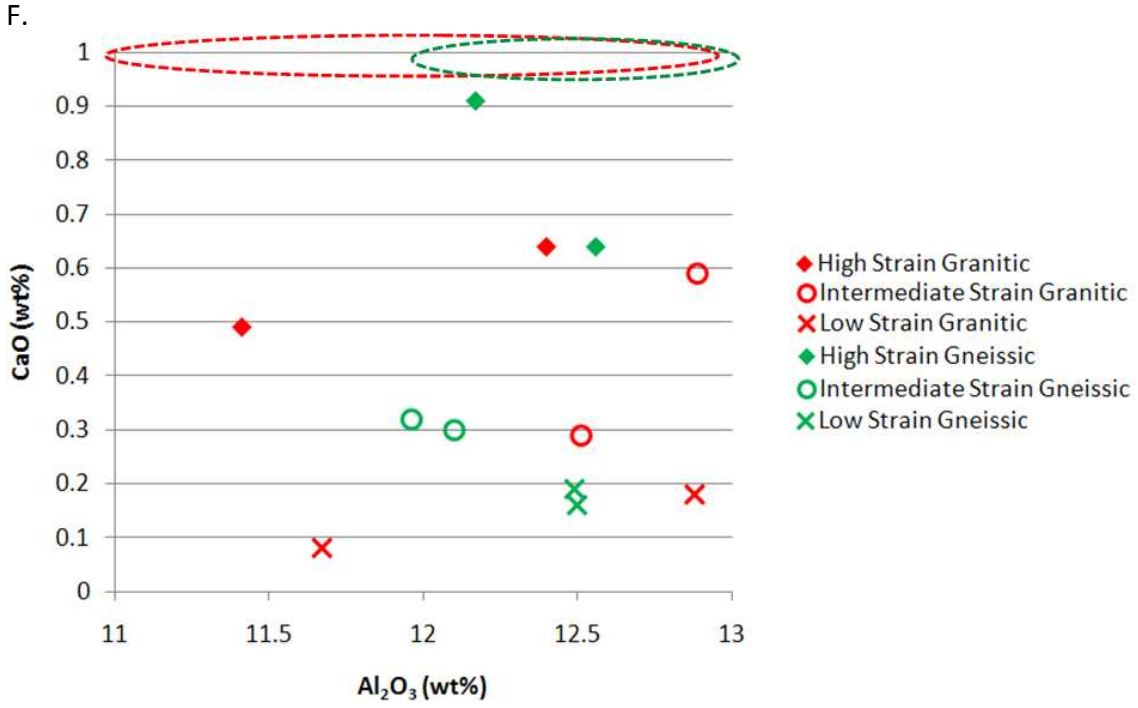
1
0.9
0.8
0.7
0.6
0.5
0.4
0.3
0.2
0.1
0
11
11.5
12
12.5
13
CaO (wt%)
Al_2O_3 (wt%)
High Strain Granitic
Intermediate Strain Granitic
Low Strain Granitic
High Strain Gneissic
Intermediate Strain Gneissic
Low Strain Gneissic

A.

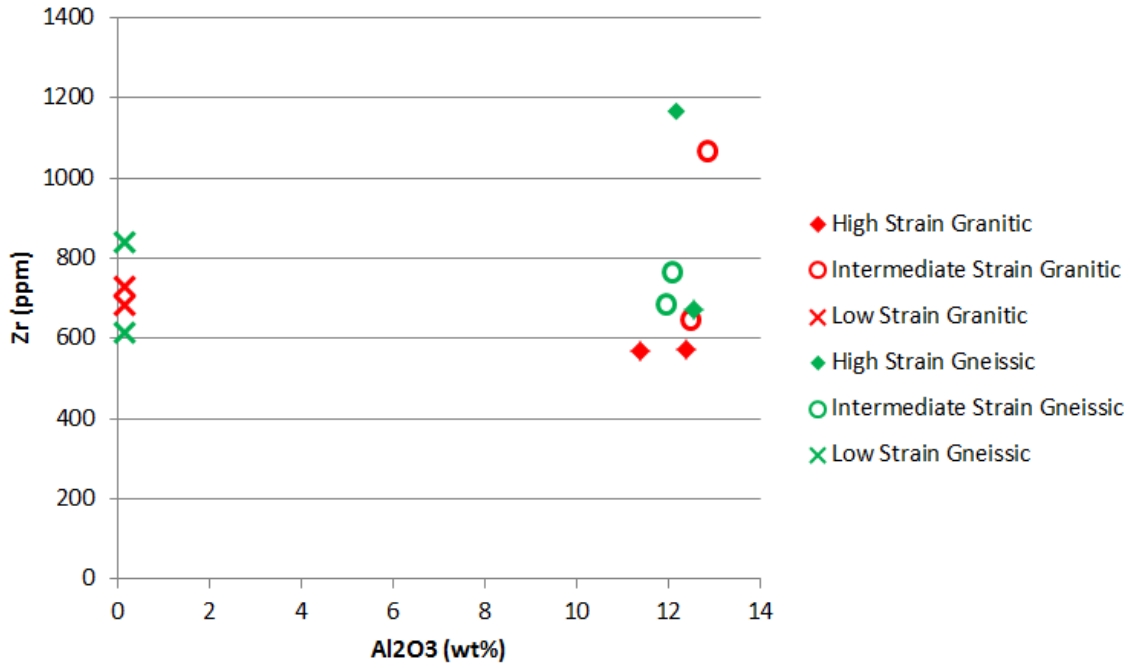

B.

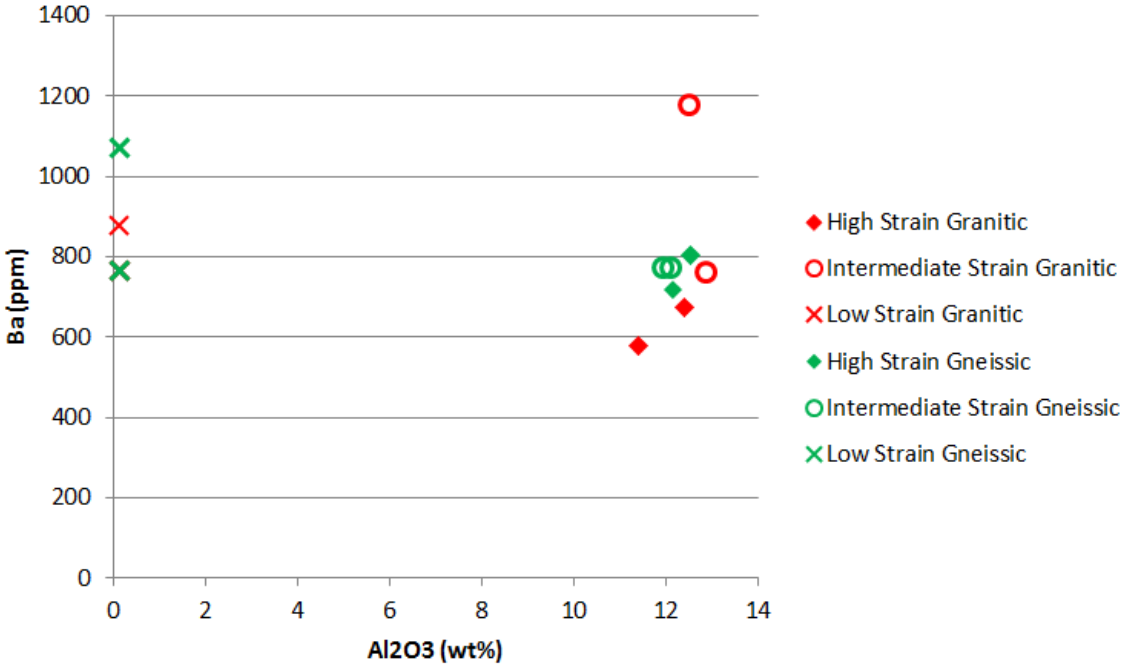

Figure 21. Trace element plots of Zr and Ba vs. Al_2O_3. Gneissic clasts generally contain a higher amount of Zr, and Ba amounts are similar between the two clast types.

A.

Low Strain

Sample	Na2O (%)	MgO (%)	Al2O3 (%)	SiO2 (%)	P2O5 (%)	K2O (%)	CaO (%)	TiO2 (%)	Fe2O3 (%)	Mn (%)	Sum (%)
Quartzite	ND	0.00	0.01	0.99	ND	0.00	ND	ND	0.01	ND	101.08
STD	ND	0.00	0.00	0.01	ND	0.00	ND	ND	ND	ND	
Granitic	ND	0.01	0.12	0.72	0.00	0.05	0.00	0.00	0.07	0.00	98.24
STD	ND	0.00	0.01	0.02	ND	0.00	0.00	0.00	0.00	ND	
Gneissic	ND	0.01	0.12	0.72	0.00	0.05	0.00	0.00	0.07	0.00	98.29
STD	ND	0.00	0.00	0.00	0.00	0.00	0.00	0.00	0.00	ND	

B.

Moderate Strain

Sample	Na2O (%)	MgO (%)	Al2O3 (%)	SiO2 (%)	P2O5 (%)	K2O (%)	CaO (%)	TiO2 (%)	Fe2O3 (%)	Mn (%)	Sum (%)
Quartzite	ND	0.11	0.76	99.78	ND	0.17	ND	ND	0.25	ND	101.16
STD	ND	ND	0.08	0.58	ND	0.03	ND	ND	ND	ND	
Granitic	0.40	1.30	12.70	68.73	0.23	4.51	0.44	0.59	6.55	0.04	95.69
STD	0.25	0.01	0.27	1.41	0.04	0.22	0.21	0.04	1.36	0.01	
Gneissic	ND	1.35	12.03	74.22	0.18	4.81	0.31	0.58	4.20	0.07	97.96
STD	ND	0.01	0.10	0.04	0.01	0.02	0.01	0.02	0.17	0.02	

C.

High Strain

Sample	Na2O (%)	MgO (%)	Al2O3 (%)	SiO2 (%)	P2O5 (%)	K2O (%)	CaO (%)	TiO2 (%)	Fe2O3 (%)	Mn (%)	Sum (%)
Quartzite	ND	0.12	0.75	98.46	ND	0.18	0.09	ND	0.68	ND	100.34
STD	ND	0.01	0.13	0.37	ND	0.04	ND	ND	0.66	ND	
Granitic	0.86	1.48	11.91	72.29	0.06	4.24	0.57	0.21	6.41	0.03	98.19
STD	0.12	0.11	0.70	2.19	0.01	0.39	0.11	0.01	0.52	0.00	
Gneissic	0.42	1.56	12.37	67.11	0.16	5.08	0.78	0.53	9.56	0.05	97.80
STD	0.24	0.15	0.28	3.30	0.01	0.59	0.19	0.04	3.21	0.02	

Figure 22. A. Average major and minor element concentrations at low strain, site A08-09. Standard deviations are calculated for the mean concentration of each clast type. B. and C. Average major and minor element concentrations at moderate strain (site A08-05) and at high strain (A08-06) respectively. Standard deviations for the mean concentrations are also present. Elements that are more abundant in one clast type over the other are highlighted in pink if they are more abundant in granitic clasts or green if they are more abundant in gneissic clasts.

5.3 Petrographic Analysis

5.3.1 Grain size vs. Strain Gradient

Average grain size values for gneissic and granitic clasts fall within a similar range (100-600μm) for all Antelope Island sites, which is comparable to the average grain size in the Farmington Canyon Complex furthering the case that the clasts are derived from the FCC.

Quartzite clasts have a significantly smaller mean grain size than either granitic or gneissic clasts. Less size variation is also apparent in quartzites, likely because quartzite clasts have a uniform quartz mineralogy. Low strain quartzite samples from site A08-09 exhibit slightly smaller grain sizes relative to higher strain samples from site 06 overall. Examining grains ranging from 100-400μm reveals that 91% of all quartz grains in the low strain samples fall within this range, compared to only 84% of quartz grains at high strain. Therefore, grain size increases slightly from low to high strain in quartzites.

Counting one hundred points on clasts from the Mineral Fork diamictites and recording mineral type, grain size, and observed microstructures allows for patterns to be observed. One would expect to find quartz, feldspar, and biotite mineral grains when examining granitic and gneissic clasts. However, the clasts primarily consist of quartz. The next most common substance is a micaceous matrix. Quartz minerals and matrix material occur in similar quantities in both granitic and gneissic clasts across the strain gradient. This suggests that feldspars on Antelope Island, at all strains, were

largely altered. With increasing feldspar alteration or sericitization, we see an increased amount of fine-grained micaceous matrix. The majority of feldspar grains remaining in the samples showed partial alteration to muscovite, indicating sericitization. The alteration of feldspars is also evidenced by the geochemical analyses in this study. Antelope Island granitic and gneissic clasts show an increase in magnesium and decrease in sodium relative to the basement protolith, indicating feldspar alteration to phengitic muscovite.

5.3.2 Microstructures

The microstructures examined in this study can be classified based on the deformation mechanism with which they are most likely associated. Microfractures are considered to be formed by brittle deformation. This study includes both microfractures within a single grain (intragranular) as well as microfractures extending across multiple grains (intergranular) in both the point counting and FTIR/Synchrotron data collection.

Observed microstructures including undulose extinction, deformation lamellae, zoning, and subgrains are all considered to form by crystal plastic deformation (dislocation creep). Bulged grain boundaries are evidence for grain boundary migration, part of the recovery processes associated with dislocation creep. Likewise, recrystallization occurs as a recovery mechanism associated with dislocation creep.

All clast types at all strains showed evidence for brittle deformation mechanisms and crystal plasticity and the two processes seemed to have been concurrent. There

were no abundant microstructures recorded that were associated with DMT.

Fluid inclusions were also recorded during point counting analyses to help identify patterns between fluid movement and deformation. Primary fluid inclusions may be trapped in crystals as they grow (Vernon, 2004). Primary water should be found within the quartz crystal itself and not associated with fractures or trains of fluid inclusions. The FTIR results did not show any differences between the locations of water in gneissic and granitic clasts, which suggests that primary water in quartz does not explain the difference in strain between the two clast types.

This study focuses on secondary fluids in the Antelope Island clasts to determine if water emplaced during deformation caused their contrasting reactions to strain. Secondary fluid inclusions are formed after crystal growth, and may demonstrate fluid-rock interaction during deformation. Fluid travel may be assisted through brittle (i.e. microfractures) or ductile (i.e. dislocations) deformation. Granitic clasts contained a large amount of microfractures (68%) at a low strain (Fig. 15) which may have acted as conduits for fluids. Increased fluids could potentially cause localized increases in fluid pressure, producing brittle deformation with an increase in strain.

5.3.3 Quartz microstructures

Microfractures are found in quartz grains in all types of clasts across strain magnitudes, evidencing brittle deformation mechanisms. Curiously, the abundance of microfractures is variable between clast types. Brittle fracturing was abundant in granitic and gneissic clasts and was most abundant in granitic clasts at high strain.

Granitic clasts appear to have the fewest microfractures in moderate strain, and more in low and high strains. The point counting data show that gneissic clasts generally increase in microfractures from low to moderate strain, and slightly decrease from moderate to high. This could either suggest that microfractures healed with increasing strain, or may simply result from variability between samples. Quartzite follow the opposite pattern compared to the gneissic clasts, with microfractures decreasing from low to moderate strain, and increasing from moderate to high strain. Again, sample variability may account for these inconsistencies. Alternatively, the different strengths of the clasts may control the distribution of fractures. The stronger clasts (quartzites and granites) are more likely to deform brittley while the weaker clasts (gneisses) are more likely to deform ductilely. It is not clear why there were fewer fractures recorded in quartzite clasts because these clasts are typically stronger (and show less deformation) than gneissic clasts so one might assume they would tend to deform brittlely more than ductilely. Increasing the sample size may reveal trends in microfractures as opposed to variability between samples.

Crystal plastic deformation mechanisms are found in quartz grains in all clast types across the entire strain gradient. Therefore it was likely that the majority of clast deformation was accommodated by the motion of dislocations through quartz crystals. The abundance of grains with undulose extinction remains relatively stable across the strain gradient. An average of 89% of the quartz grains demonstrate movement of dislocations of their crystal lattice. The abundance of subgrains in quartz grains generally increases from low to moderate strain, and then decreases from moderate to

high strain. This decrease in abundance of subgrains at high strain may occur as a result of dynamic recrystallization causing recovery in clasts at site 06. Deformation lamellae generally decrease in abundance with increasing strain. Dislocations and fluid inclusions typically define deformation lamellae, so it is unclear as to why they would decrease with increasing strain.

Evidence for recovery mechanisms (bulged grain boundaries and recrystallized grains) related to dislocation creep were most prevalent in quartzite clasts and most prevalent at high strains in all clasts. Recrystallization of quartz grains increases from low to high strain in all clast types. The majority of microstructures associated with crystal plastic deformation tend to increase in abundance from low to moderate strain, but then decrease in abundance from moderate to high strain in quartz grains. This phenomenon may result from recovery processes occurring between moderate and high strains. The increase in recrystallization seen from low to high strain is another indication that dynamic recovery occurs with increased strain at location A08-06. The large degree of recovery in quartzite clasts may explain the lack of fractures observed, as the fracture features may have been obliterated with recrystallization.

Chapter 6: Conclusions

This preliminary study sought to assess the usefulness of three methods for identifying fluid-rock interactions in diamictites along the Willard Thrust Fault. The study was the first amongst several in our research group and acted as a proof-of-concept for subsequent work. FTIR and the synchrotron were utilized to find the relative amount of water in quartz grains based on water peak heights and peak areas. The use of the FTIR synchrotron was new to structural geology research and has the potential to allow researchers to assess the detailed quantities of water within deformed grains and the spatial relationships between that water and microstructures. XRF data provided geochemical information that helps determine changes that may have taken place during deformation. Petrographic analyses provide a comparison of grain sizes and microstructures between clasts types along a strain gradient to find trends and possible fluid pathways. Several conclusions can be made based on data presented in this preliminary study:

6.1. Methodology

- FTIR synchrotron data translated into grain maps are too variable to be useful. The colors that should show high water absorbance (red) do not correlate to the water peak height or area.

- Thin sections were utilized in this study for both the petrographic analyses and the synchrotron. One concern with the synchrotron is whether the use of thin sections might have any negative effect on

acquiring accurate water absorbances due to potential water contained within the glass or adhesive and variations in thickness of both.

6.2 Antelope Island diamictites and their deformation

- Similarities in compositions determined from XRF data suggest that the Antelope Island diamictites are likely derived from the local crystalline basement rock, the Farmington Canyon Complex (FCC data from Yonkee, 2003).

- Granitic and gneissic clasts have very similar compositions.

- Microstructures across the strain gradient show evidence that both brittle and dislocation creep deformation mechanisms with various recovery processes were active during the deformation of the diamictites at all levels of strain in all clast types.

- Microstructural data reveal an abundance of microfractures in pink granitic clasts at low strain, which corresponds to observations of their brittle deformation in the field. Fewer microfractures were observed in granitic clasts at moderate and high strains suggesting many fractures annealed with increasing deformation. Evidence for dislocation creep was abundant at all strain magnitudes, but evidence for recovery processes, particularly recrystallization and grain boundary migration, was particularly prevalent at high strains.

- An abundance of microfractures were observed in gneissic clasts at all strain magnitudes suggesting that fractures formed early in the deformation history and remained or new fractures formed as old ones annealed. Similar to granitic clasts, evidence for dislocation creep was abundant at all strain magnitudes, but evidence for recovery processes, particularly recrystallization and grain boundary migration, was particularly prevalent at high strains.

- In contrast, few fractures formed in quartzite clasts whereas evidence for dislocation creep was prevalent at all strains. Recrystallization was the dominant recovery mechanism and was particularly active at moderate to high strains.

6.3 Fluids in deformation

- Deformation in the Mineral Fork diamictite was accompanied by fluid flow. Multiple lines of evidence for this fluid influx are found at a variety of scales.

- Chloritization of the rocks at high strains suggests fluid enhanced metamorphism. This chloritization suggests that fluids altered rocks more with increasing strain, although detailed geochemical analysis could not support this conclusion due to large compositional variability within clast types.

- Compared to the crystalline basement, the low and intermediate strain clasts have decreased Na and clasts at all strains have increased Mg. These geochemical changes occurred during fluid-enhanced metamorphic reactions as feldspars reacted to form mica. Yonkee et al. (2003) noted similar geochemical trends in basement shear zones.

- The rocks experienced little to no volume loss as evidenced by no significant decrease in the concentrations of highly mobile elements like Si between the basement protolith and deformed clasts. This conclusion is further supported by lack of enrichment of immobile elements such as Ti and Al.

- The presence of water (observed as water peak height) within quartz grains increases from low to moderate strain rocks, regardless of clast type. This may represent an increase in fluid presence with deformation.

- Measuring individual peak heights shows water along fractures and grain boundaries as well as in the middle of intact quartz grains. Microfractures likely propagate during deformation, increasing water infiltration along fractures. Dislocation creep may have accompanied fracturing to facilitate fluid flow through the individual quartz grains. Another potential cause of water peaks within the quartz grains is a combination of fracturing and annealing in the grains.

The work in this thesis demonstrated that the Mineral Form diamictites were suitable for a detailed study of fluid and deformation interactions and that the general techniques could be used with some slight changes in design. The work here became the basis for further work by our research group (Nachbor, 2011; Barszewski, 2012; Yonkee et al., 2013) and more future work, especially in the utilization of synchrotron FTIR to study water within deformed minerals, is warranted.

Chapter 7. References

Anderson, T., Austrheim, H., and Burke, E.A.J., 1991. Fluid-induced retrogression of granulites in The Bergen Arcs nappe complex, Caledonides of W. Norway: Fluid inclusion evidence from amphibolites-facies shear zones. Lithos 27, p. 29-42.

Barszewski, C.E., 2012. Microstructural and cathodoluminescence (SEM-CL) analyses of clasts in a tectonically deformed diamictite. M. S. Thesis, University of Wisconsin-Milwaukee.

Brace, W. F. and Kohlstedt, D. L., 1980. Limits on lithospheric stress imposed by laboratory experiments. Journal of Geophysical Research 85 (B11), 6248-6252.

Carter, N.L., Kronenberg, A.K., Ross, J.V. and Wiltschko, D.V., 1990. Control of fluids on deformation of rocks. In: R.J. Knipe and E.H. Rutter (Editors), Deformation Mechanisms, Rheology and Tectonics. Geol. Soc. London, Spec. Publ. 54, 1-13.

Chernak, L. J., G. Hirth, J. Selverstone, and J. Tullis (2009). Effect of aqueous and carbonic fluids on the dislocation creep strength of quartz, Journal of Geophysical Research 114.

Cordier, P., Doukhan, J.C., 1989. Water solubility in quartz and its influence on ductility. European Journal of Mineralogy, vol. 1, no. 2, p. 221-237.

Czeck, D.M., Yonkee, W.A., Johnson, K.R., 2009. Linking fluid-rock interaction and strain accumulation in a naturally deformed diamictite: Geological Society of America Abstracts with Programs, vol. 41, no. 7, p. 415.

Czeck, D.M., Yonkee, W.A., Nachbor, A.C., Johnson, K.R., Barszewski, C.E., Pantone, S., 2011. Fluid-rock interaction in deformed diamictites, Willard thrust fault, Sevier orogenic belt, Utah (USA): Macroscopic strain and alteration patterns. Penrose Conference, Catalonia, Spain. June-July 2011.

Doelling, H.H., Willis, G.C., Jensen, M.E., Hecker, Suzanne, Case, W.F., and Hand, J.S., 1990. Geologic map of Antelope Island, Davis County, Utah: Utah Geological and Mineral Survey Map 127, p. 27, scale 1:24,000.

Eardley, A.J., and Hatch, R.A., 1940. Pre-Cambrian crystalline rocks of north-central Utah. Journal of Geology, vol. 48, p. 58-72.

Etheridge, M.A., Wall, V.J., Cox, S.F., and Vernon, R.H., 1984. High fluid pressures during regional metamorphism and deformation: implications for mass transport and deformation mechanisms. Journal of Geophysical Research 89, p. 4344-4358.

Evans, J.P., and Neves, D.S., 1992. Footwall deformation along Willard thrust, Sevier orogenic belt: Implications for mechanisms, timing, and kinematics. Geological Society of America Bulletin 104, p. 516-527.

Fischer, G.J., and Paterson, M.S., 1989. Dilitancy during rock deformation at high temperatures and pressures. Journal of Geophysical Research, vol. 94, p. 17, 607-17, 617.

Gleason, G. C. and DeSisto, S., 2008. A natural example of crystal-plastic deformation enhancing the incorporation of water into quartz. Tectonophysics 446, p. 16–30.

Griffiths, P.R., and de Haseth, J.A., 2007. Fourier Transform Infrared Spectrometry, 2nd Ed.: John Wiley & Sons, Inc., Hoboken, New Jersey, p. 529.

Griggs, D.T, 1967. Hydrolytic weakening of quartz and other silicates: Royal Astronomical Society Geophysical Journal 14, p. 19–31.

Griggs, D.T., and Blacic, J.D., 1964. The strength of quartz in the ductile regime. vol. 45, p. 102-103.

Griggs, D.T., and Blacic, J.D., 1965. Quartz: Anomalous weakness of synthetic crystals. Science vol. 147, p. 292-295.

Hirth, G., and Tullis, J., 1992. Dislocation creep regimes in quartz aggregates. Journal of Structural Geology, vol. 14, no. 2, p. 145-159.

Holness, M., and Graham, C., 1995. P-T-X effects on equilibrium carbonate-H2O-CO2-NaCl dihedral angles: Constraints on carbonate permeability and the role of deformation during fluid infiltration. Contributions to Mineralogy and Petrology, vol. 119, p. 301-313.

Ihinger, P.D., and Zink, S.I., 2000. Determination of relative growth rates of natural quartz crystals. Nature vol. 404, p. 865-869.

Kekulawala, K.R.S.S., Paterson, M.S., and Boland, J.N., 1978. Hydrolytic weakening in quartz. Tectonophysics vol. 46, p. 1-6.

Kirby, S.H. and Kronenberg, A.K., 1987. Rheology of the lithosphere: Selected topics. Rev. Geophys. 25, p. 1219-1244.

Kronenberg, A.K., Kirby, S.H., Aines, R.D., Rossman, G.R., 1986. Solubility and diffusional uptake of Hydrogen in quartz at high water pressures: Implications for hydrolytic weakening. Journal of Geophysical Research, vol. 91, no. B12, p. 12723-12744.

Kronenberg, A.K., Segall, P. and Wolf, G.H, 1990. Hydrolytic weakening and penetrative deformation within a natural shear zone. In: A.G. Duba, W.B. Durham, J.W. Handin and H.F. Wang (Editors), The Brittle-Ductile Transition in Rocks). Am. Geophys. Union, Geophys. Monogr. 56, p. 21-36.

Kronenberg, A.K., Wolf, G.H., 1990. Fourier transform infrared spectroscopy determinations of intragranular water content in quartz-bearing rocks: implications for hydrolytic weakening in the laboratory and within the earth. Tectonophysics 172, p. 255-271.

Laporte, D., and Watson, E.B., 1991. Direct observation of near-equilibrium pore geometry in synthetic quartzites at 600-800°C and 2-10.5 kbar. Journal of Geology 99, p. 873-878.

McHenry, L.J., 2009. Element mobility during zeolitic and argillic alteration of volcanic ash in a closed-basin lacustrine environment: Case study Olduvai Gorge, Tanzania. Chemical Geology 265, p. 540-552.

Nachbor, A.C., 2011. Fluid effects on deformation in the mineral fork diamictites, Antelope Island, Utah. M. S. Thesis, University of Wisconsin-Milwaukee.

Nakashima S., Matayoshi, H., Yuko T., Michibayashi, K., Masuda, T., Kuroki, N., Yamagishi, H., Ito, Y., and Nakamura, A., 1995. Infrared microspectroscopy analysis of water distribution in deformed and metamorphosed rocks. Tectonophysics 245, p. 263-276.

Newman, J., and Mitra, G., 1993. Lateral variations in fault zone thickness as influenced by fluid-rock interactions, Linville Falls fault, North Carolina. Journal of Structural Geology 15, p. 849-863.

O'Kane, A., Onasch, C.M., Farver, J.R., 2007. The role of fluids in low temperature, fault-related deformation of quartz arenite. Journal of Structural Geology 29, p. 819-836.

Passchier, C.W., and Trouw, R.A., 2005. Microtectonics, 2nd Ed.: Berlin, Springer, p. 366

Paterson, M.S., 1990. The interaction of water with quartz and its influence in dislocation flow. In: S. Karato and M. Toriumi (Editors), Rheology of Solids and of the Earth. Oxford Univ. Press, Oxford, p. 107-142.

Paterson, M.S., and Luan, F.C., 1990. Quartzite rheology under geological conditions. In: Knipe, R.J., and Rutter, E.H. (Editors), Deformation mechanisms, rheology and tectonics. Geological Society Special Publication no. 54, p. 299-307.

Poirier, J.P., 1985. Creep of Crystals: High-Temperature Deformation Processes in Metals, Ceramics, and Minerals, Cambridge Univ. Press, New York, p. 260

Ramsay. J. G., 1967. Folding and fracturing of rocks: New York, McGraw Hill, p. 568.

Royse, Jr., F. 1993. An overview of the geologic structure of the thrust belt in Wyoming, northern Utah, and eastern Idaho, in: Snoke, A.W., Steidtmann, J.R., Roberts, S.M. (Eds.), Geology of Wyoming Geological Survey of Wyoming Memoir 5, p. 272-311.

Schedl, A., McCabe, C., Montanez, I.P., Fullager, P.D., and Valley, J.W., 1992. Alleghanian regional diagenesis – a response to the migration of modified metamorphic fluids derived from beneath Blue Ridge – Piedmont thrust sheet. Journal of Structural Geology 100, p. 339-352.

Sibson, R.H., 1982. Fault zone models, heat flow, and the depth distribution of earthquakes in the continental crust of the United States. Bulletin of the Seismological Society of America, vol. 72, no. 1, p. 151-163.

Srivastava, H.B., Hudleston, P., and Earley, D. III., 1995. Strain and possible volume loss in a high-grade ductile shear zone. Journal of Structural Geology, vol. 17, no. 9, p. 1217-1231.

Stewart, M., Holdsworth, R.E., Strachan, R.A., 2000. Deformation processes and weakening mechanisms within the frictional-viscous transition zone of the major crustal-scale faults: insights from the Great Glen fault zone, Scotland. Journal of Structural Geology 22, p. 543-560.

Tsenn, M.C. and Carter, N.L., 1987. Upper limits of power law creep of rocks. Tectonophysics 136, p. 1-26.

Tullis, J. and Yund, R. A., 1989. Hydrolitic weakening of quartz aggregates: the effects of water and pressure on recovery. Geophysical Research Letters 16, p. 1343-1346.

Tullis, J., Yund, R., and Farver, J., 1996. Deformation-enhanced fluid distribution in feldspar aggregates and implications for ductile shear zones: Geology, vol. 24, p. 63-66.

Vernon, R.H., 2004. A practical guide to rock microstructure. Cambridge University Press, Cambridge, UK, p. 594.

Watson, E.B., and Brenan, J., 1987. Fluids in the Lithosphere; 1. Experimentally determined wetting characteristics of CO_2-H_2O fluids and their implications for fluid transport, host-rock physical characteristics, and fluid inclusion formation: Earth and Planetary Science Letters, vol. 85, p. 497-515.

Wawrzyniec, T., Selverstone, J., and Axen, G. J., 1999. Correlations between fluid composition and deep-seated structural style in the footwall of the Simplon low-angle normal fault, Switzerland. Geology 27, p. 715–718.

Willis, G.C., 1999. The Utah Thrust System – An Overview. Utah Geological Association Publication 27, p. 1-10.

Willis, G.C., Yonkee, W.A., Doelling, H.H., and Jensen, M.E., 2000. Geology of Antelope Island State Park, Utah. Utah Geological Association Publication 28, p. 337-363.

Yonkee, W.A., 1992. Basement-cover relations, Sevier orogenic belt, northern Utah. Geological Society of America Bulletin, vol. 104, p. 280-302.

Yonkee, W.A., 1997. Kinematics and mechanics of the Willard thrust sheet, central part of the Sevier orogenic wedge, north-central Utah in Link, P. K. and Kowallis, B. J. , eds., Proterozoic to Recent stratigraphy, tectonics, and volcanology, Utah, Nevada, southern Idaho and central Mexico,. Geological Society of America Field Guide/ Brigham Young University Geology Studies 42 (Part 1), 341-354.

Yonkee, W.A., Czeck, D.M., Nachbor, A.C., Barszewski, C., Pantone, S., Balgord, E.A., Johnson, K.R., 2013. Strain accumulation and fluid-rock interaction in a naturally deformed diamictite, Willard thrust system, Utah (USA): Implications for crustal rheology and strain softening. Journal of Structural Geology 50, p. 91-118.

Yonkee, W.A., Willis, G.C., and Doelling, H.H., 2000a. Petrology and Geologic History of the Precambrian Farmington Canyon complex, Antelope Island, Utah *in* King, J.K. and Willis, G.C., eds., The Geology of Antelope Island, Davis County, Utah, Utah Geological Survey *Miscellaneous Publication 00-1*, p. 5-36.

Yonkee, W.A., Willis, G.C., and Doelling, H.H., 2000b. Proterozoic and Cambrian sedimentary and low-grade metasedimentary rocks on Antelope Island *in* King, J.K. and Willis, G.C., eds., The Geology of Antelope Island, Davis County, Utah, Utah Geological Survey *Miscellaneous Publication 00-1*, p. 37-48.

Appendix A: Additional FTIR Area Quartz Grain Maps

A.1 Low Strain

Low Strain Quartzite: A08-09-X1

Most water peaks in this sample looked similar to the one below.

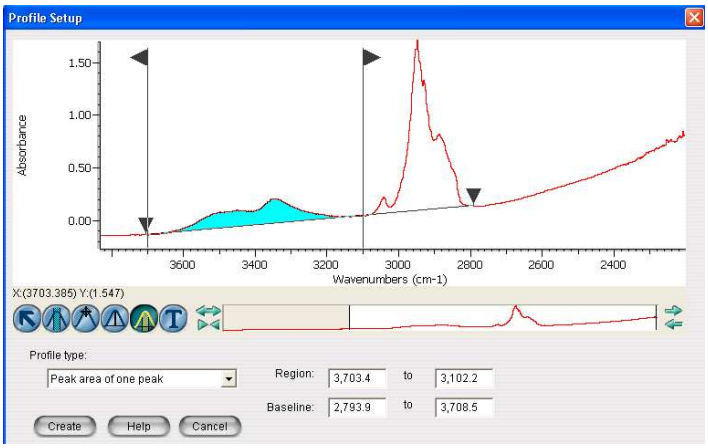

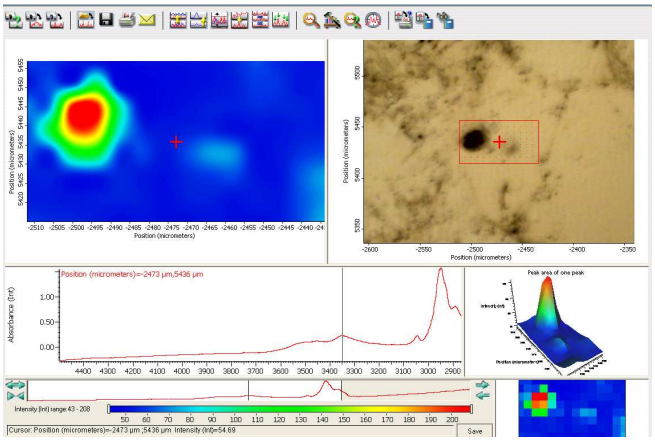

The water peak in the middle of the black spot (inclusion or bubble) looked different than those seen everywhere else on the slide. See below.

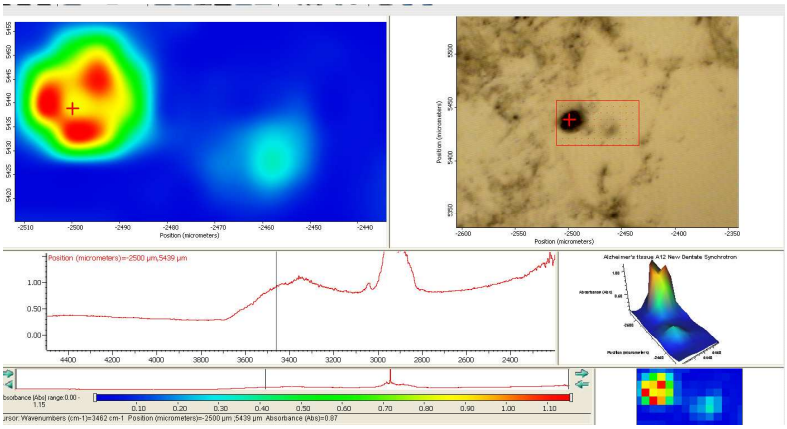

Low Strain Quartzite: A08-09-X2

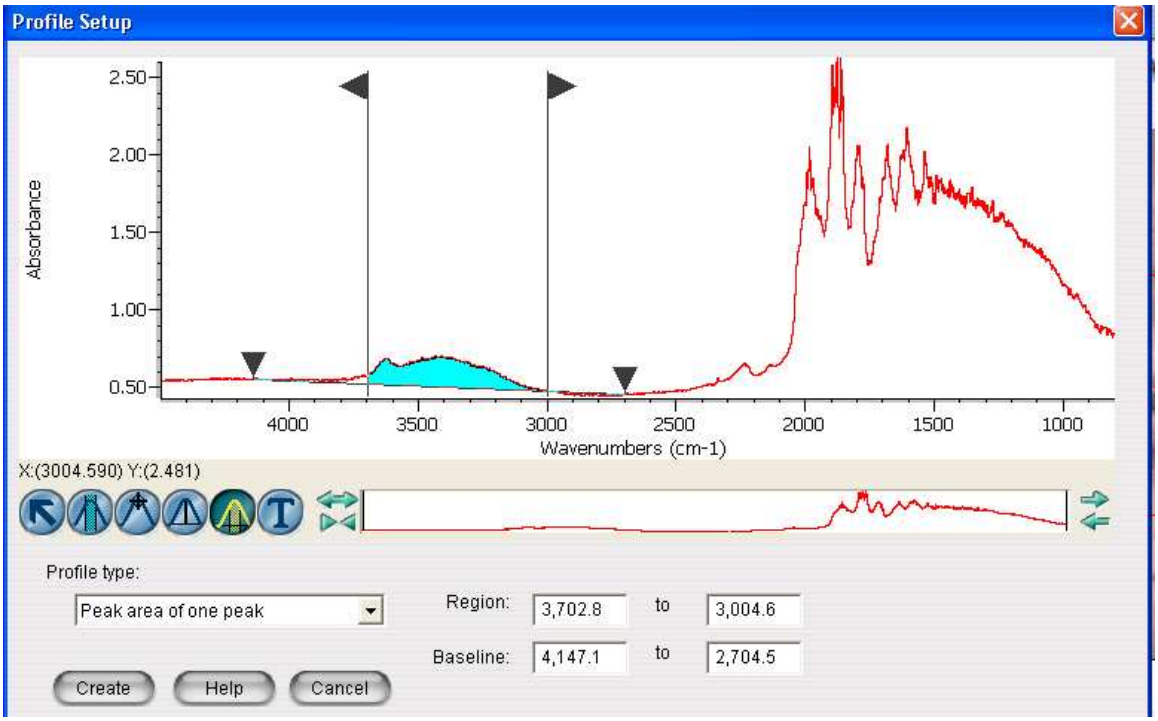

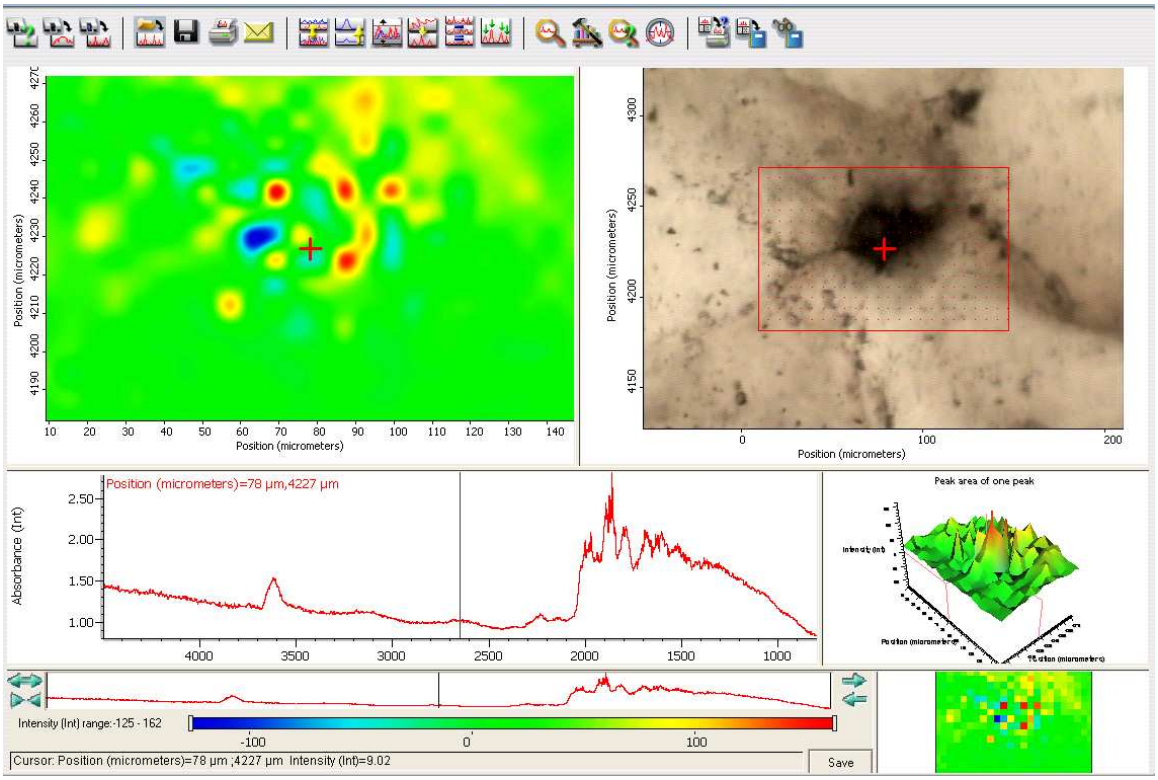

Low Strain Quartzite: A08-09-X2_Map2

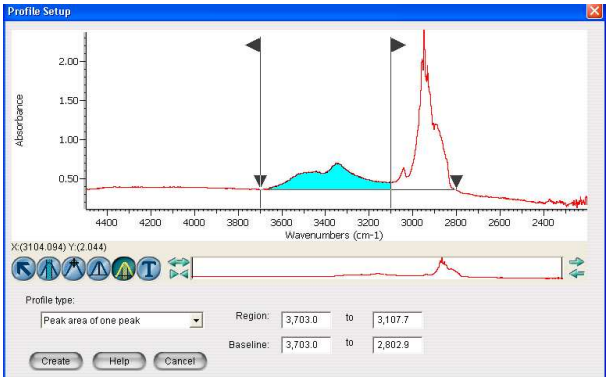

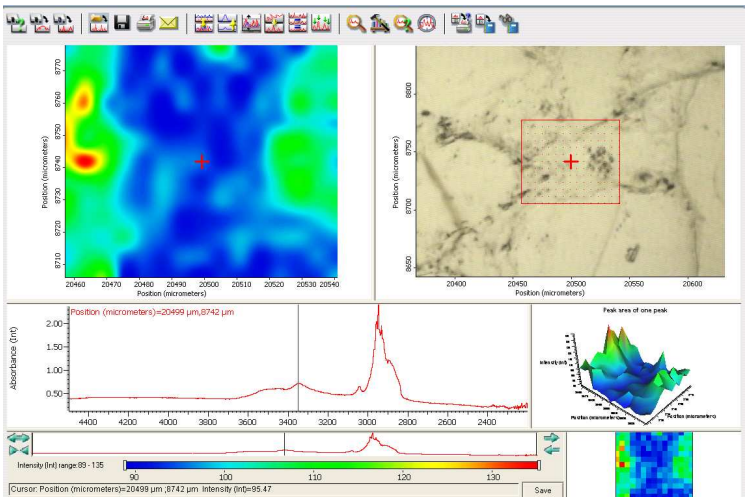

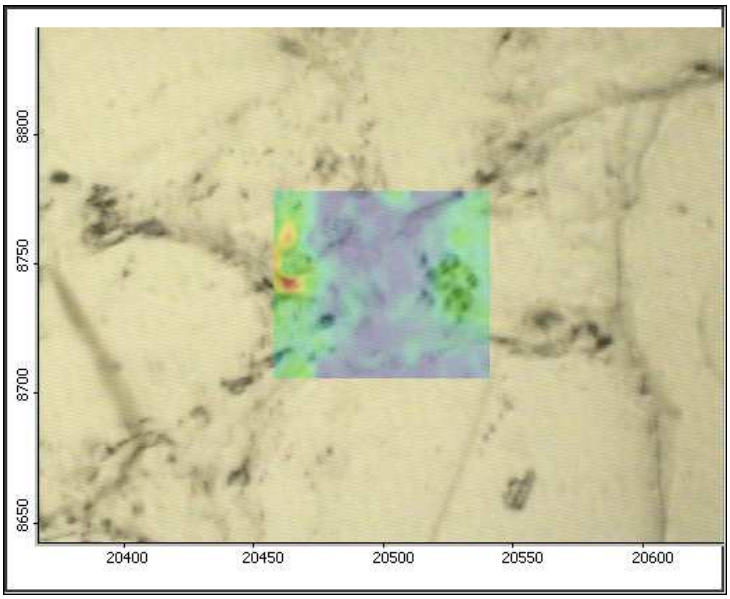

Low Strain Quartzite: A08-09-X3

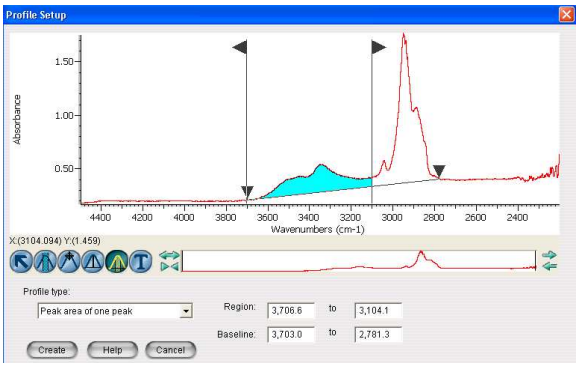

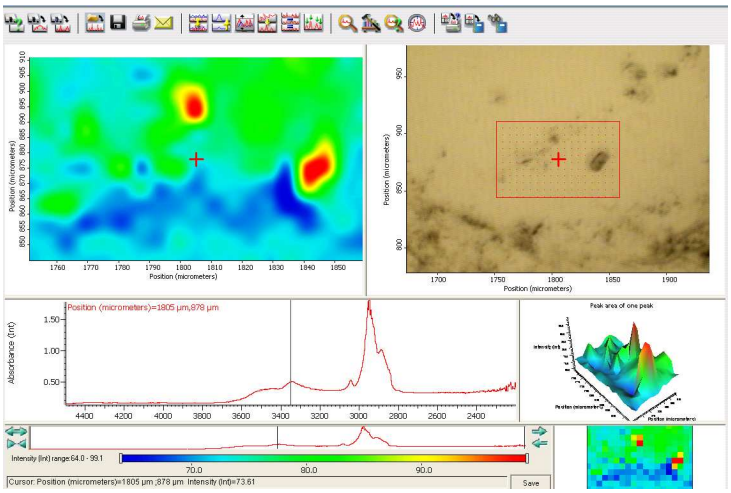

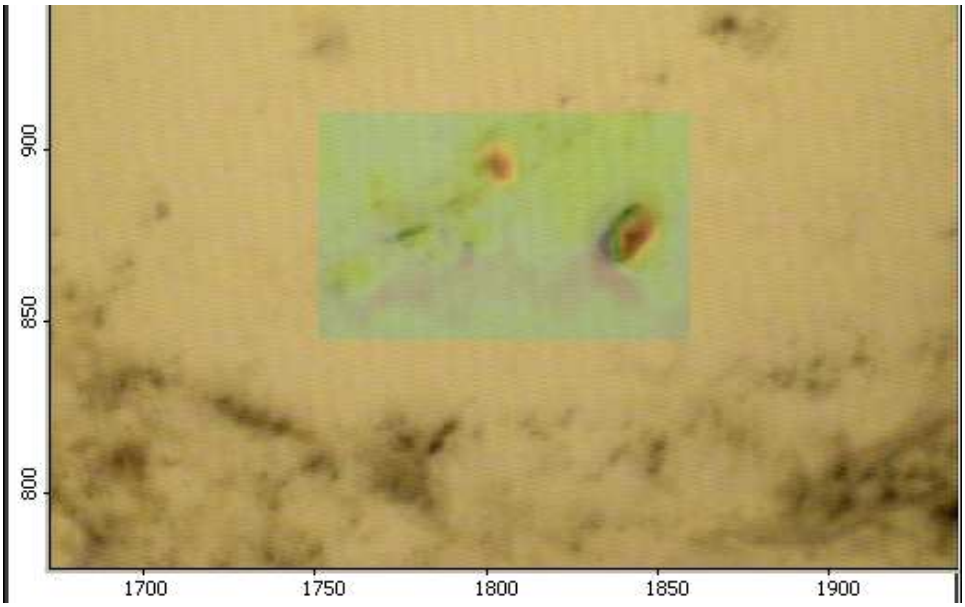

Low Strain Quartzite: A08-09-X4

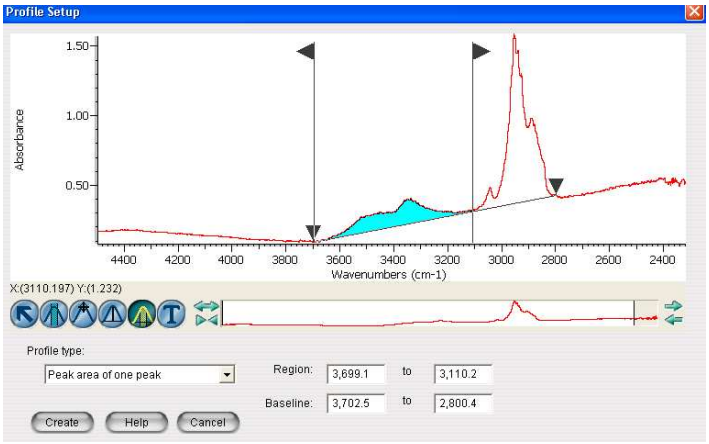

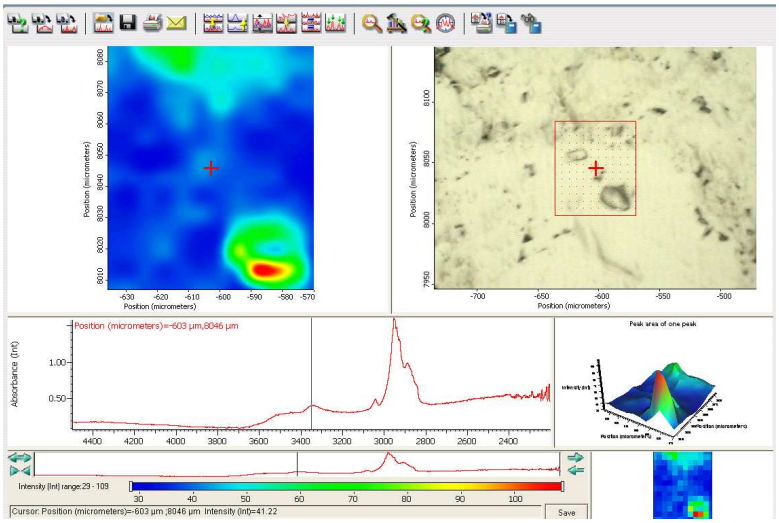

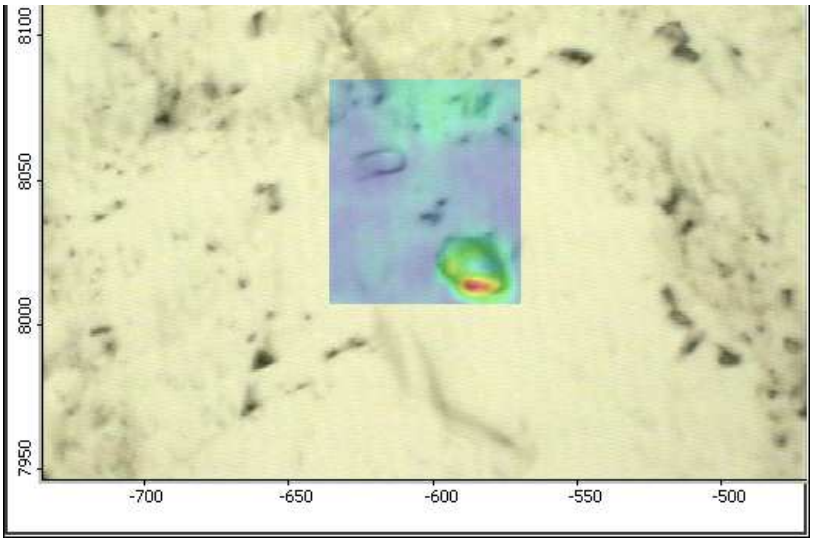

Low Strain Granitic Clast: A08-09-Y1

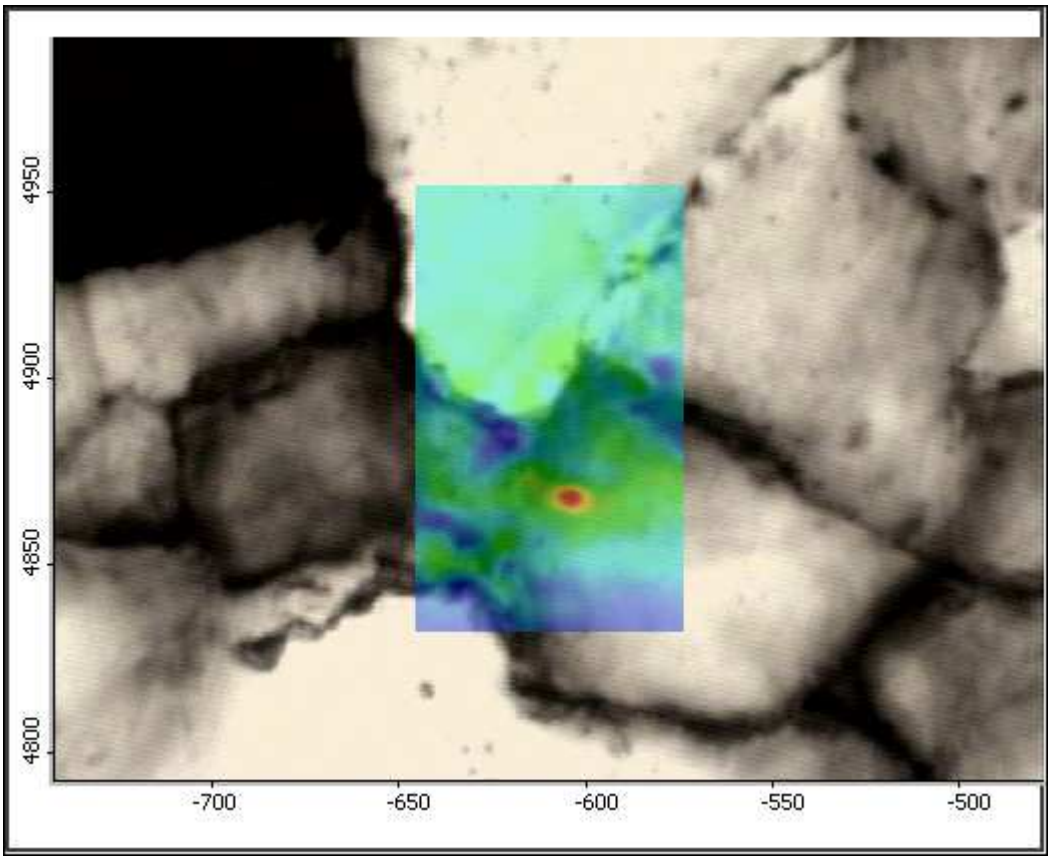

Low Strain Granitic Clast: A08-09-Y1_Map2

Water peak in the black area is shown below. Water peaks throughout the rest of the map had a similar shape to those shown for most other samples (containing the peak at 3,350cm^{-1}).

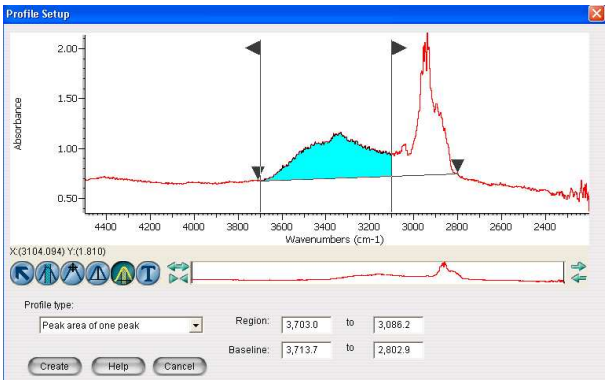

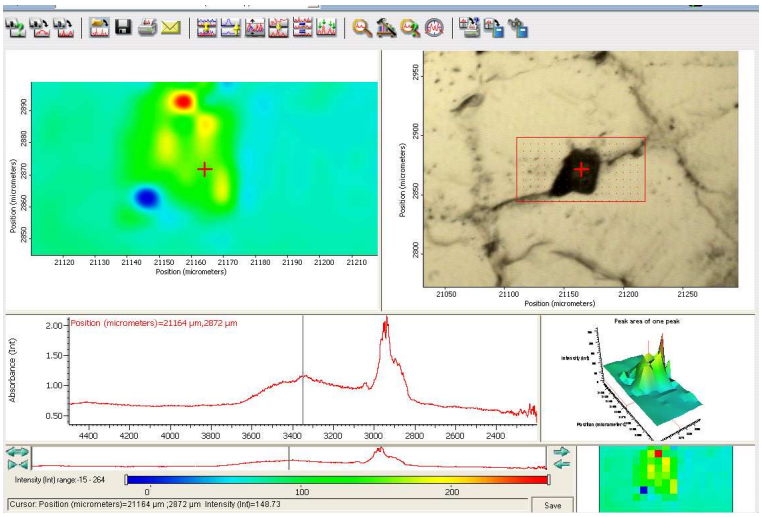

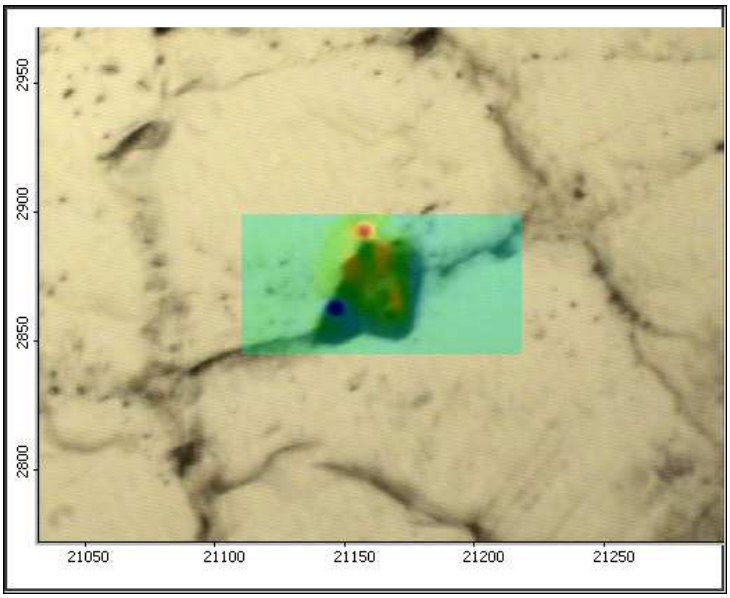

Low Strain Granitic Clast: A08-09-Y2

Water peak in the inclusion is shown below. Water peaks throughout the rest of the map (with the exception of another fluid inclusion) had a similar shape to those shown for most other samples (containing the peak at 3,350cm^{-1}).

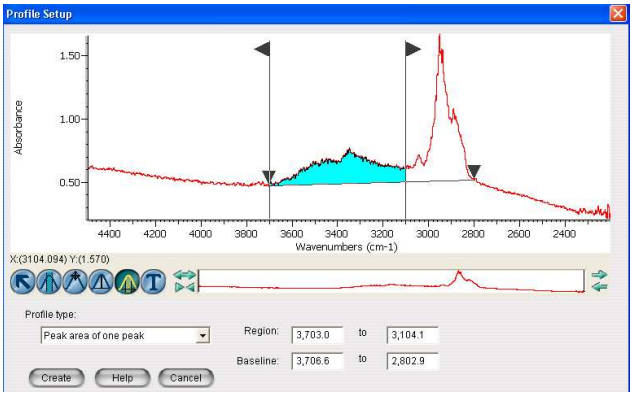

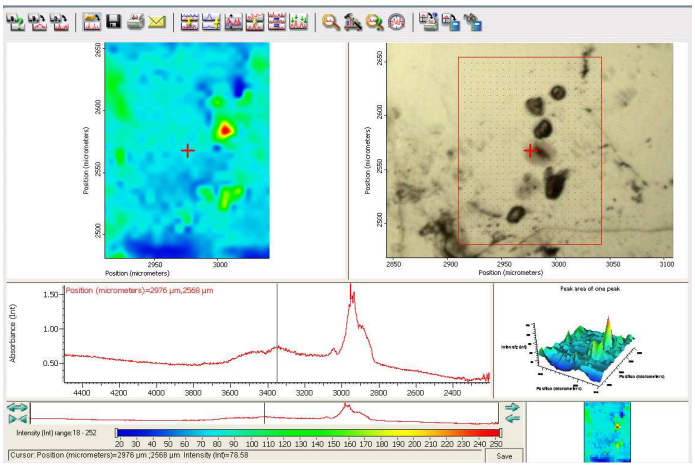

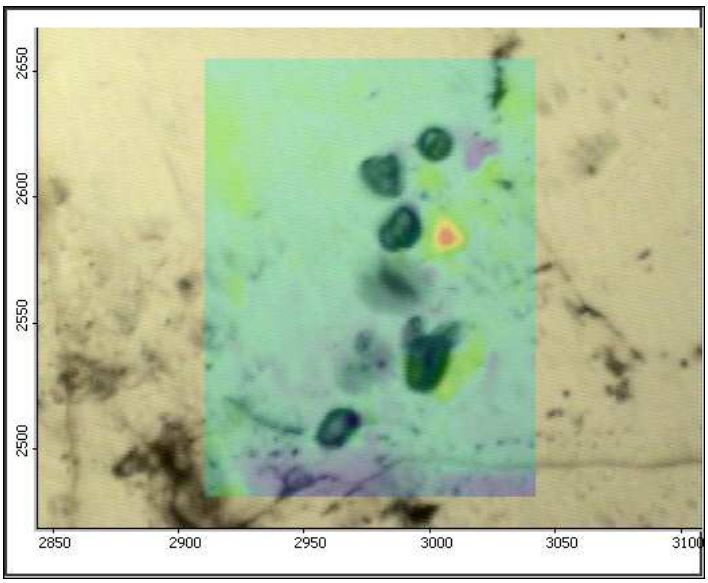

Low Strain Granitic Clast: A08-09-Y4

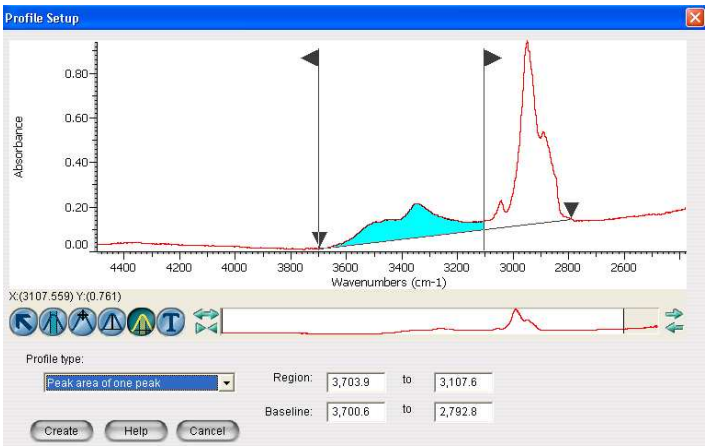

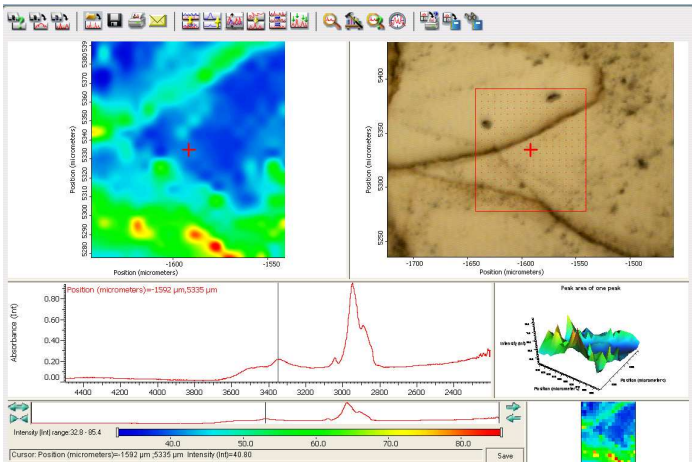

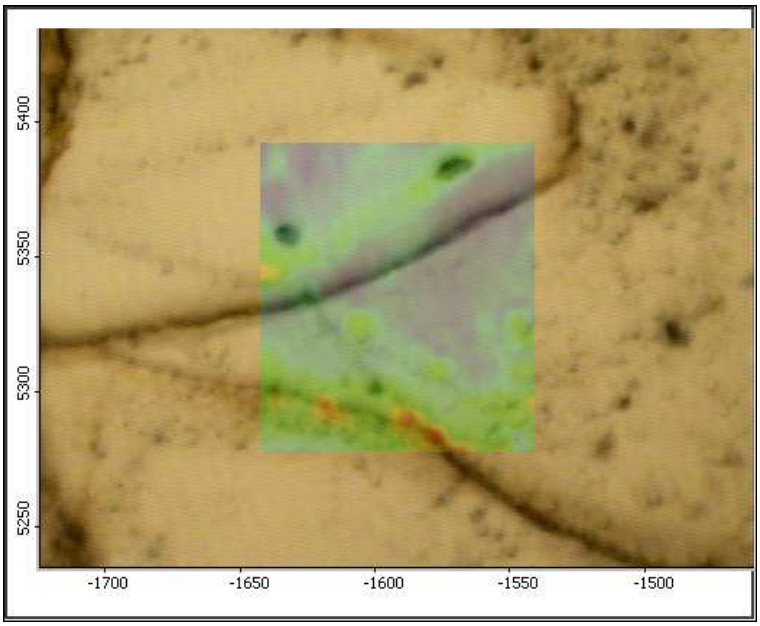

Low Strain Granitic Clast: A08-09-Y5

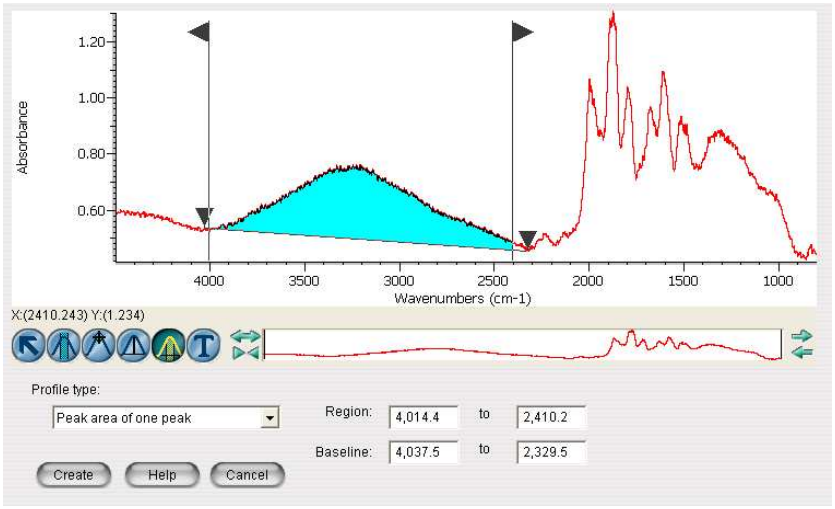

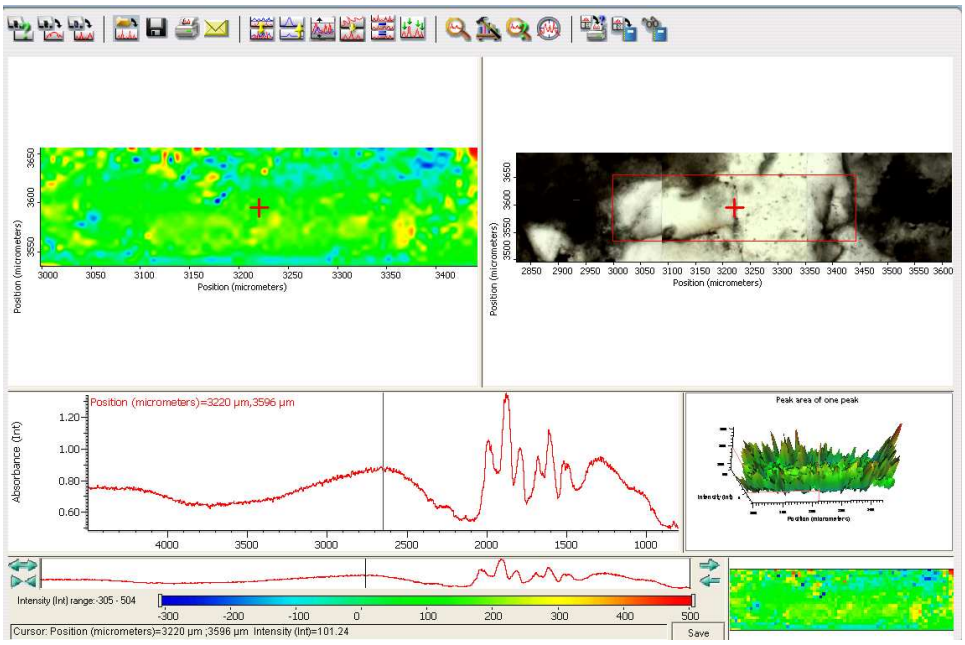

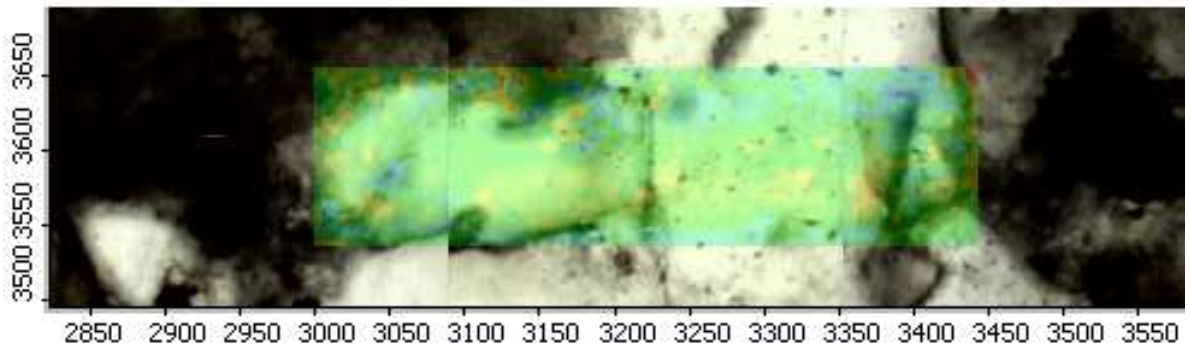

Low Strain Granitic Clast: A08-09-Y5_Map2

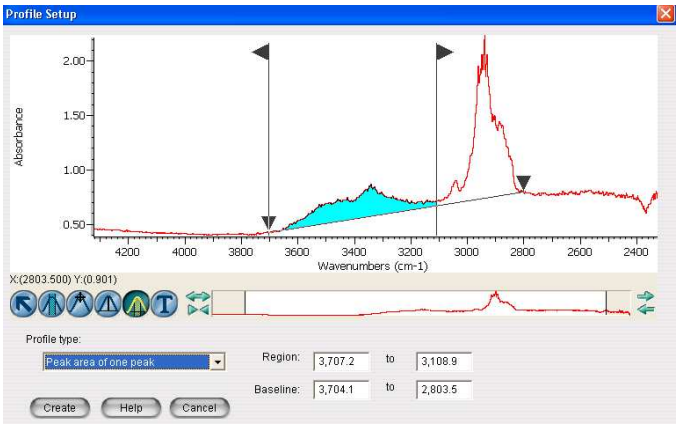

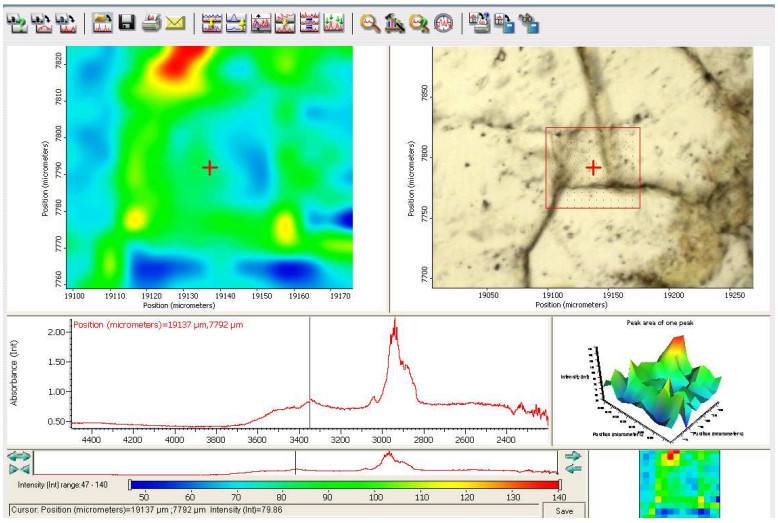

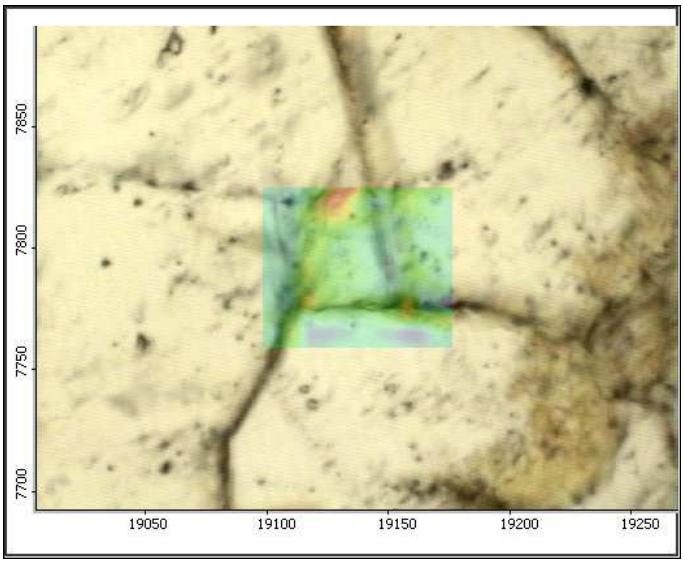

Low Strain Gneissic Clast: A08-09-Z3

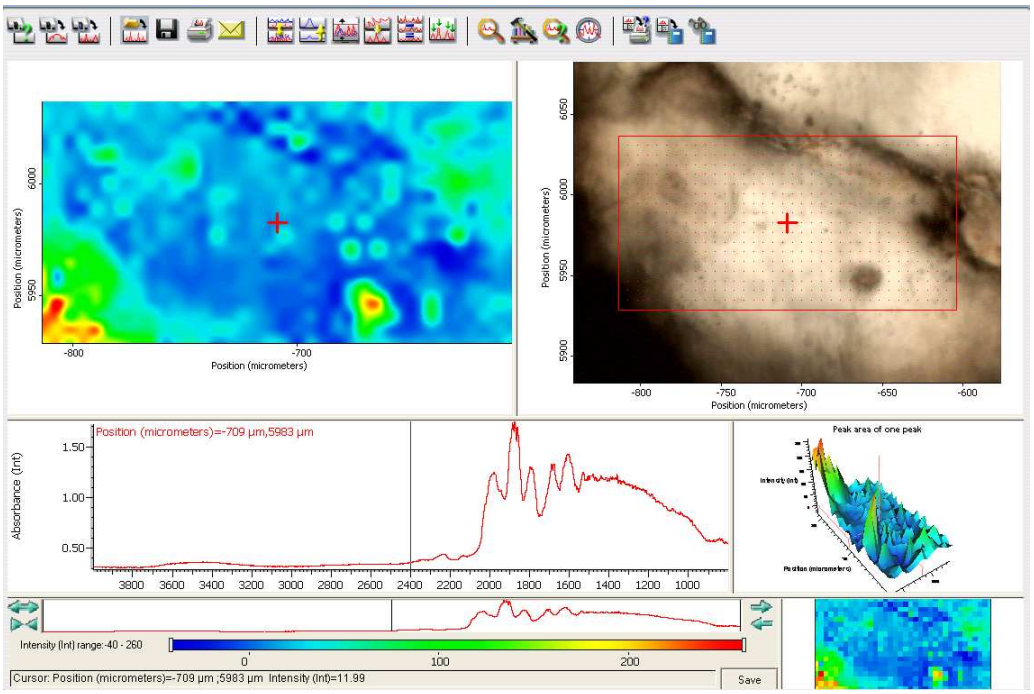

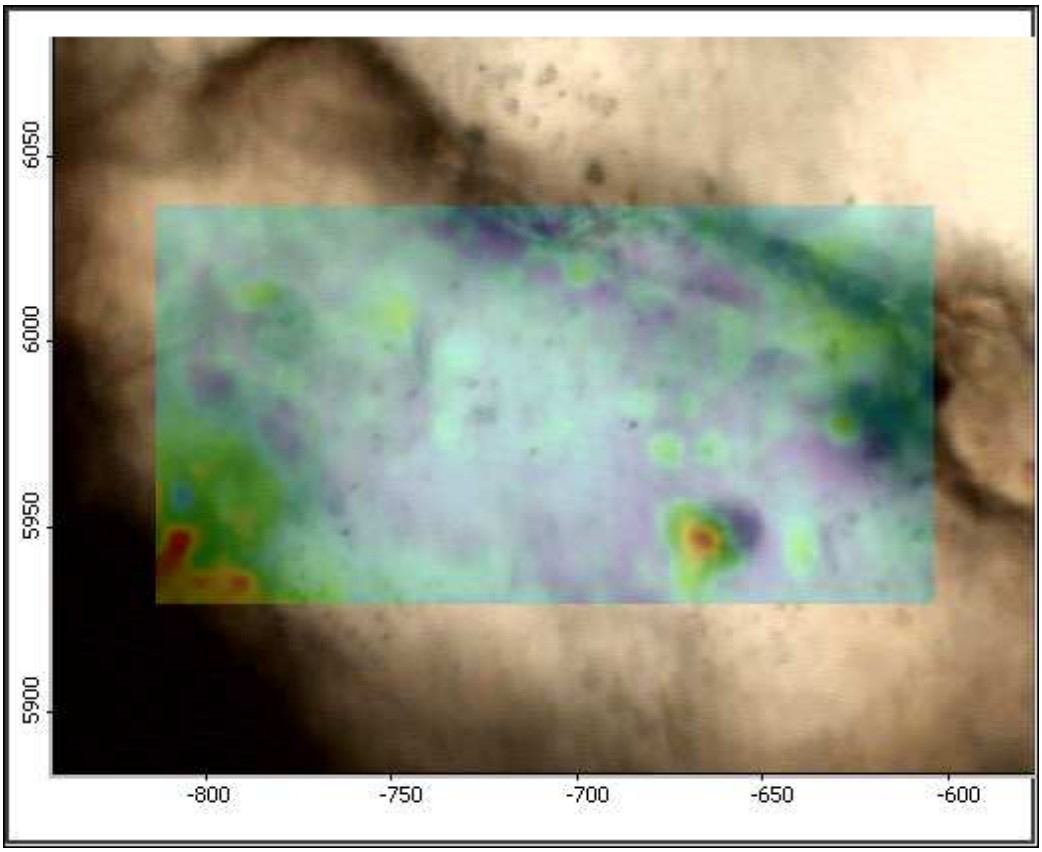

Low Strain Gneissic Clast: A08-09-Z3_Map2

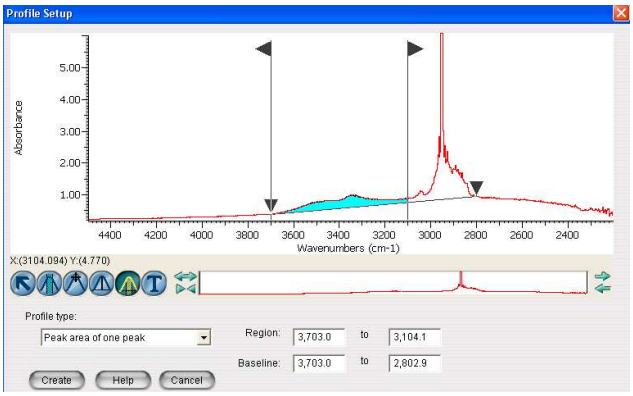

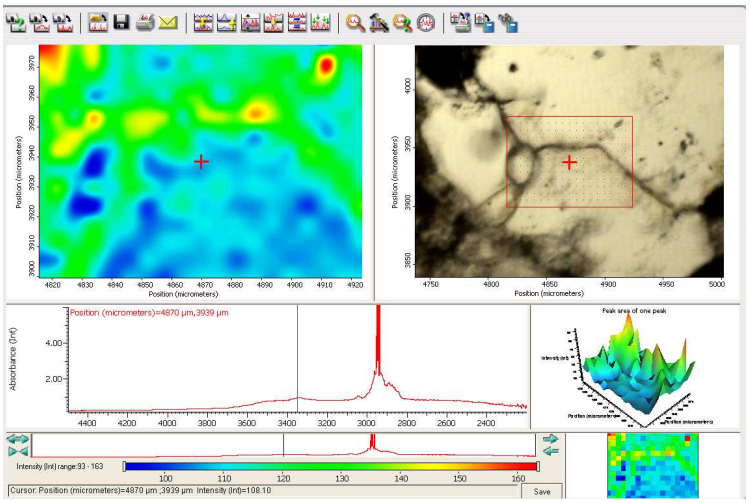

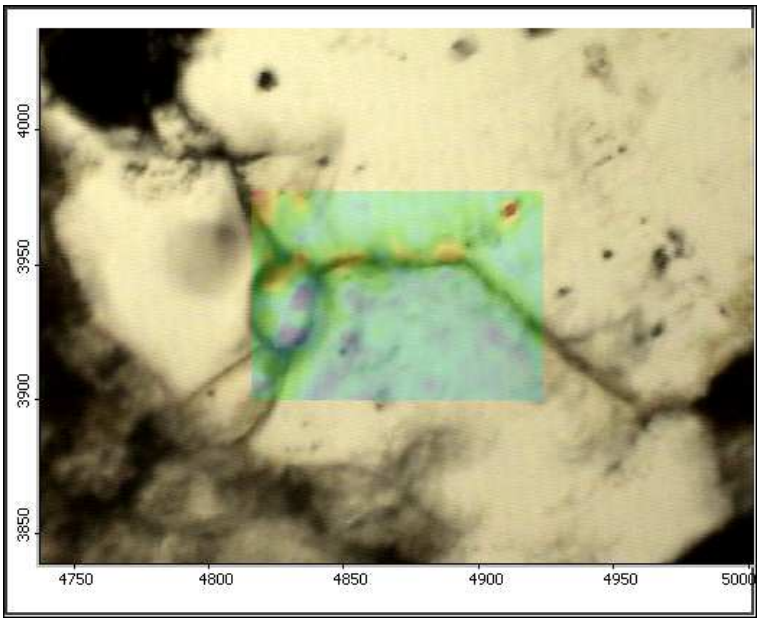

Low Strain Gneissic Clast: A08-09-Z4

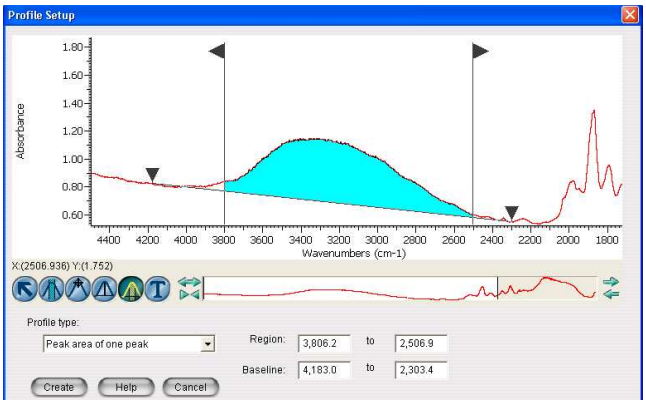

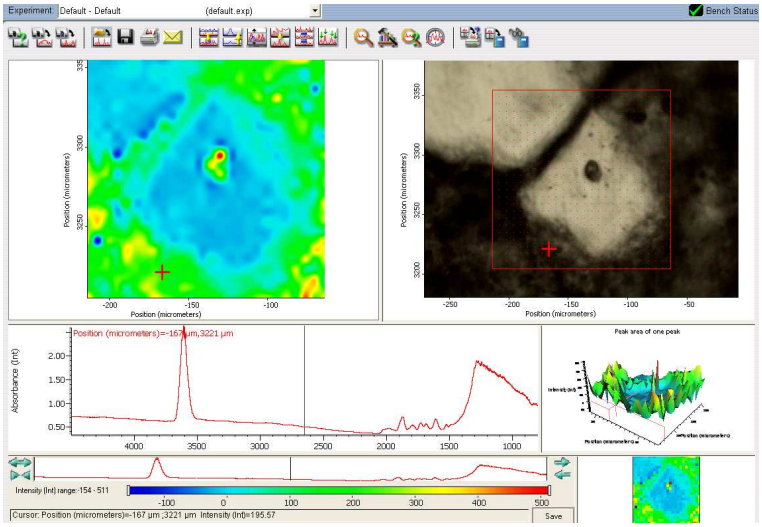

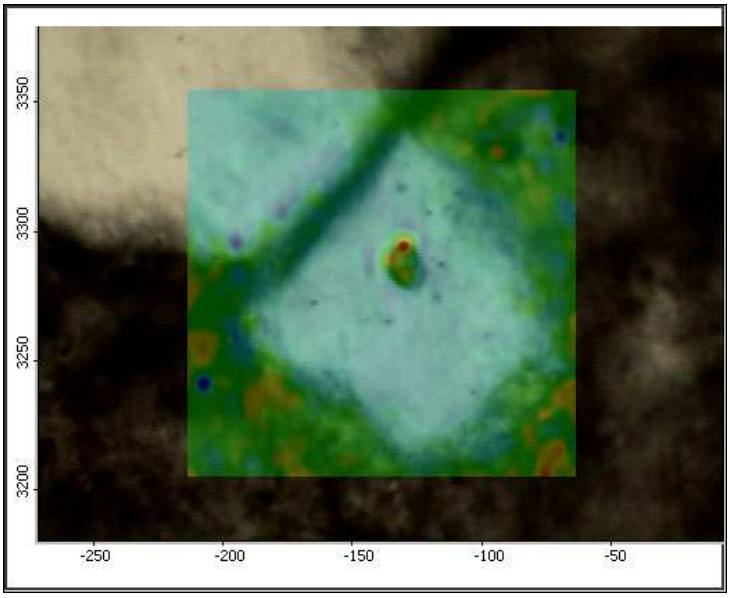

Low Strain Gneissic Clast: A08-09-Z4_Map2

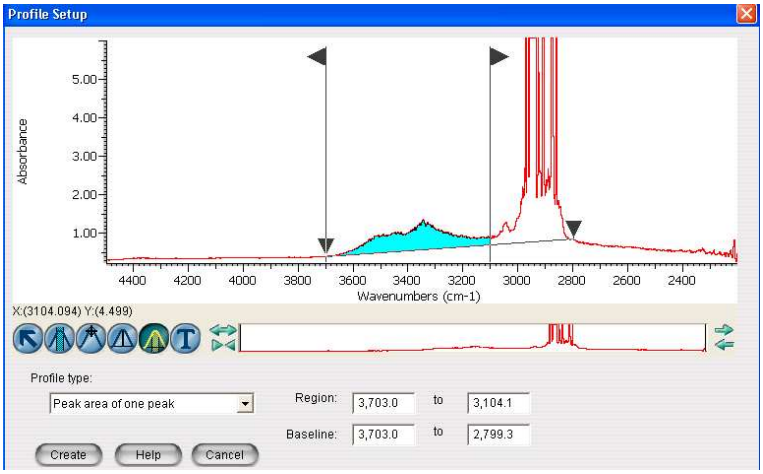

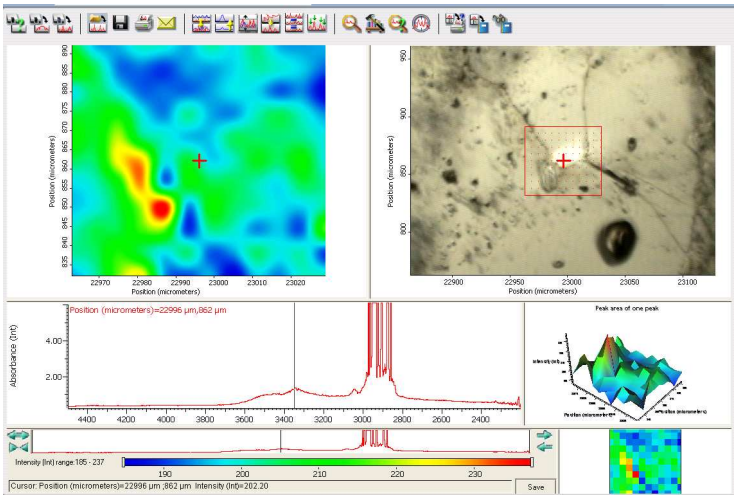

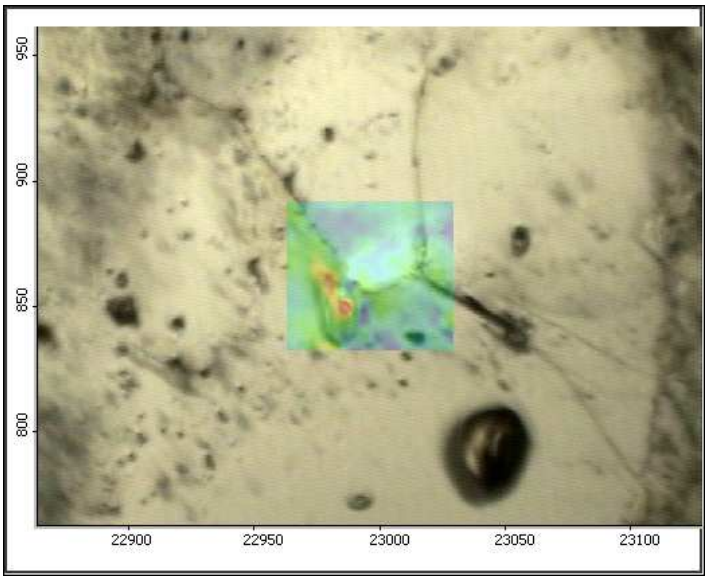

A.2 Moderate Strain

Moderate Strain Quartzite: A08-05-X1

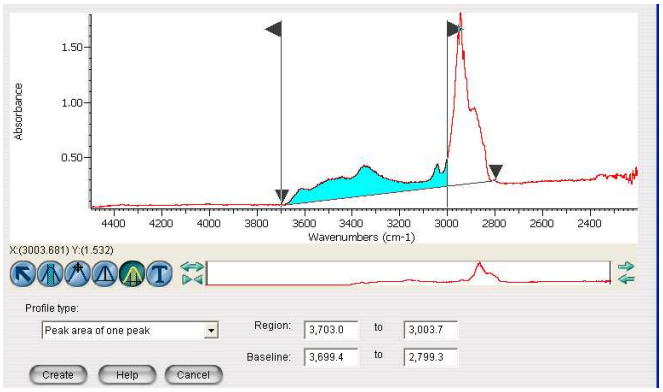

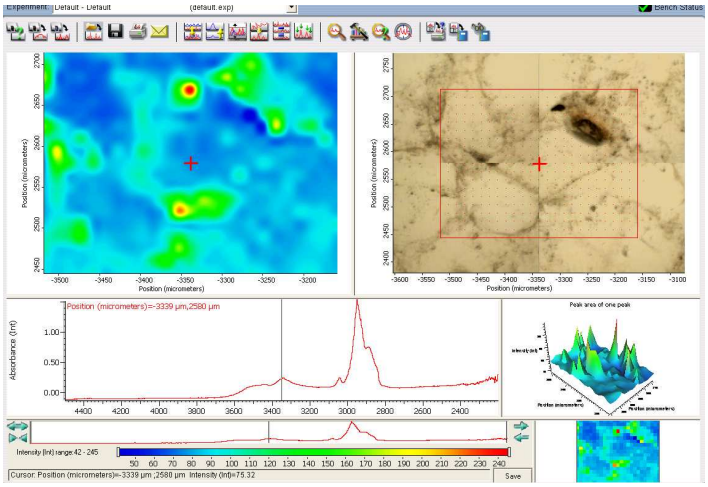

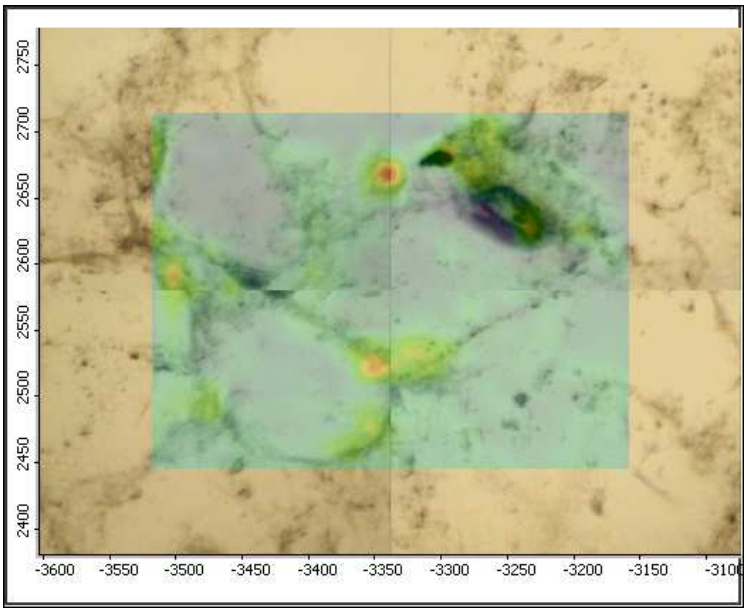

Moderate Strain Quartzite: A08-05-X1_Map2

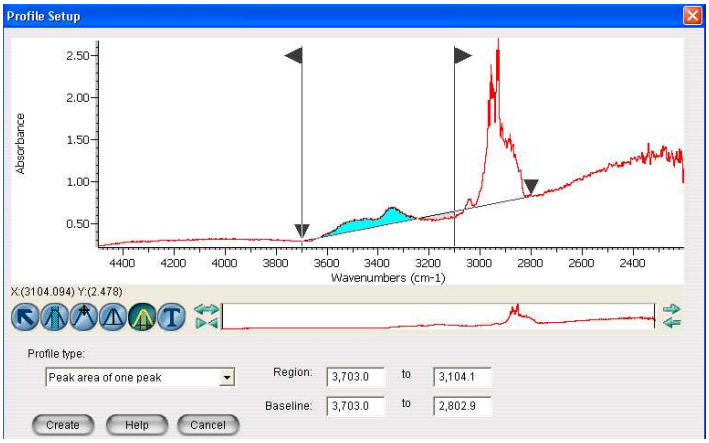

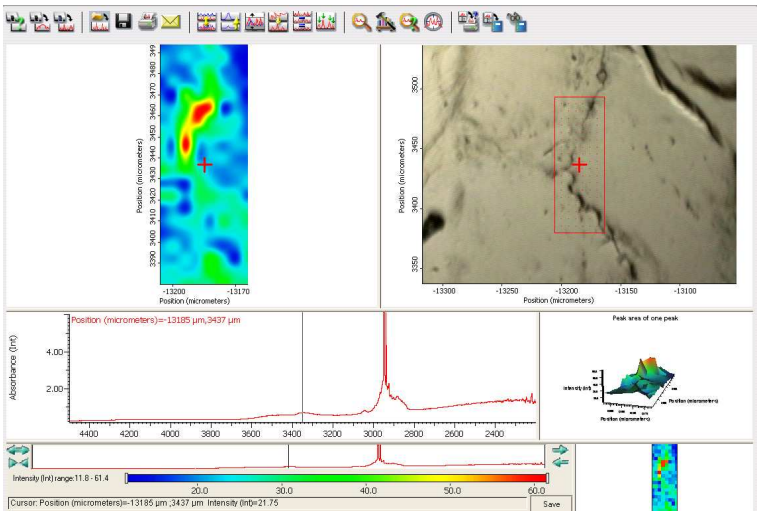

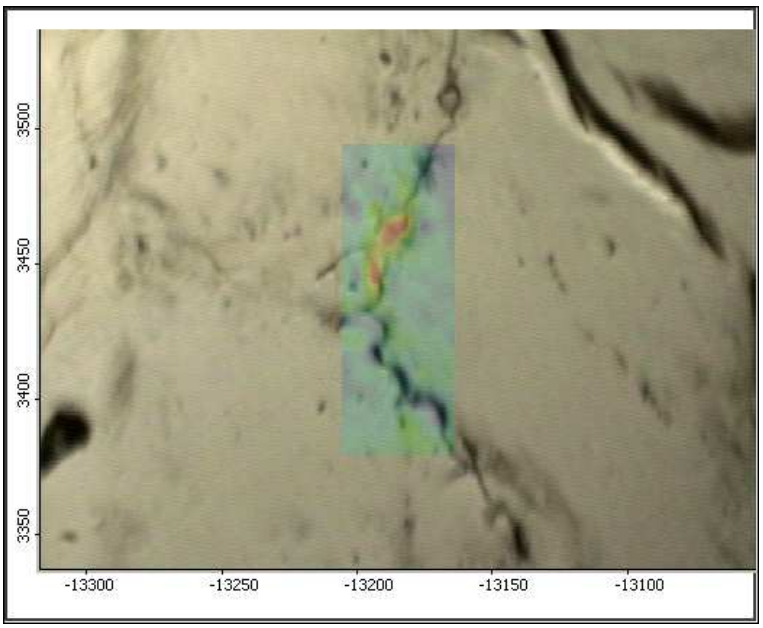

Moderate Strain Quartzite: A08-05-X2

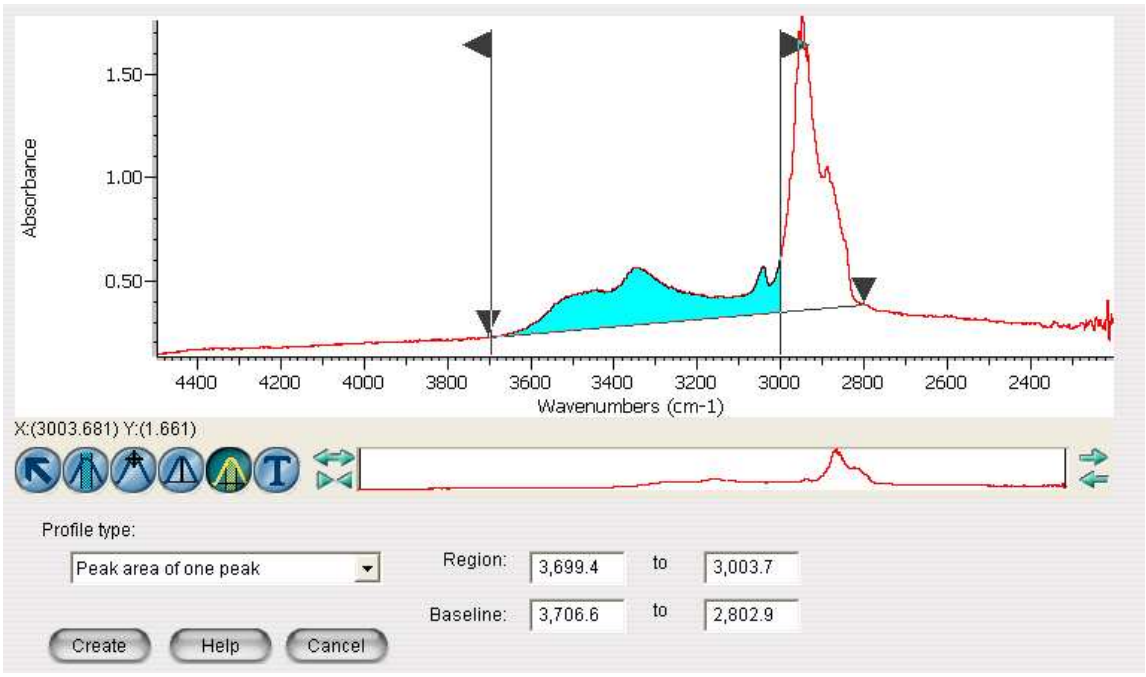

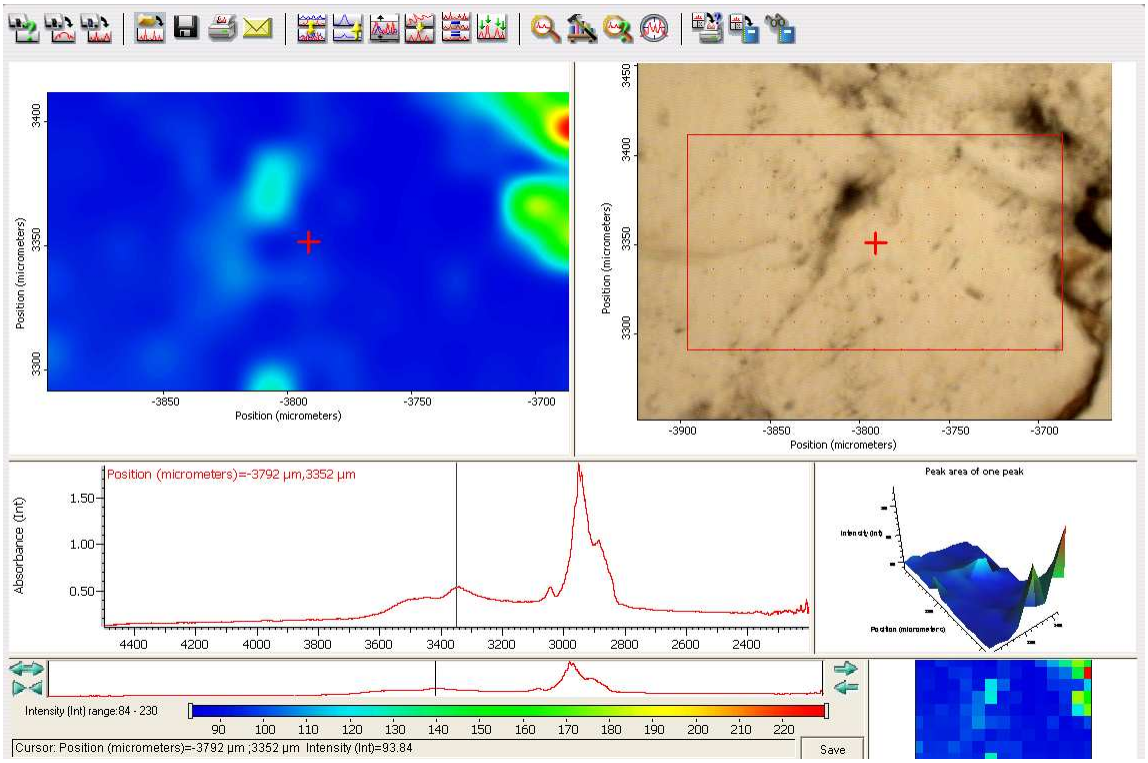

Moderate Strain Quartzite: A08-05-X2_Map2

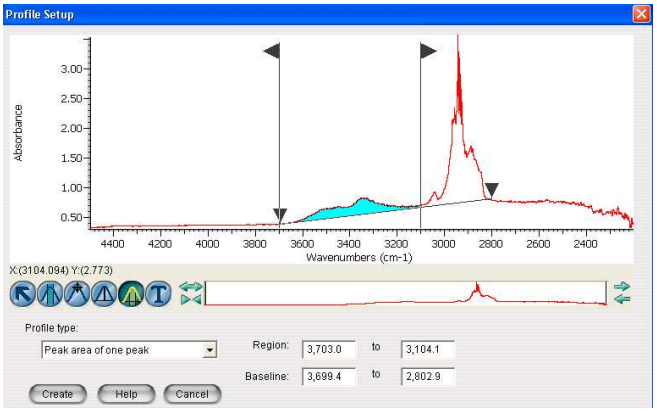

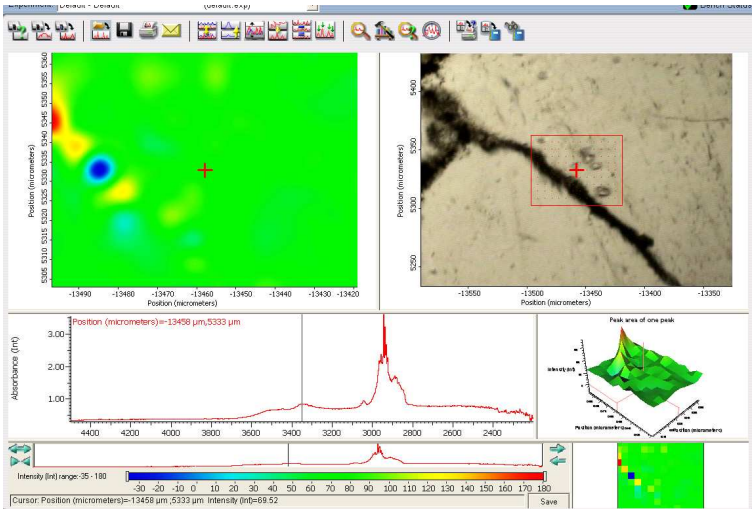

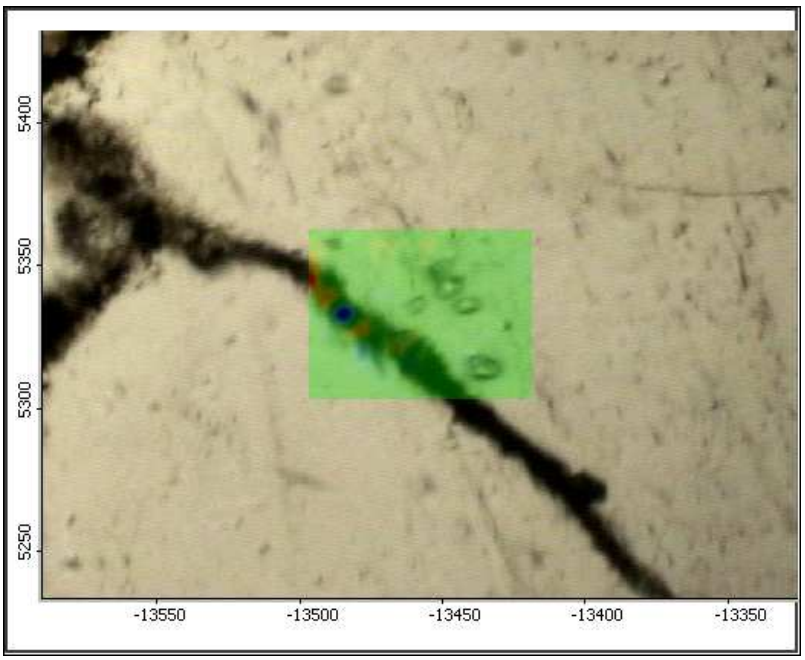

Moderate Strain Granitic Clast: A08-05-Y1

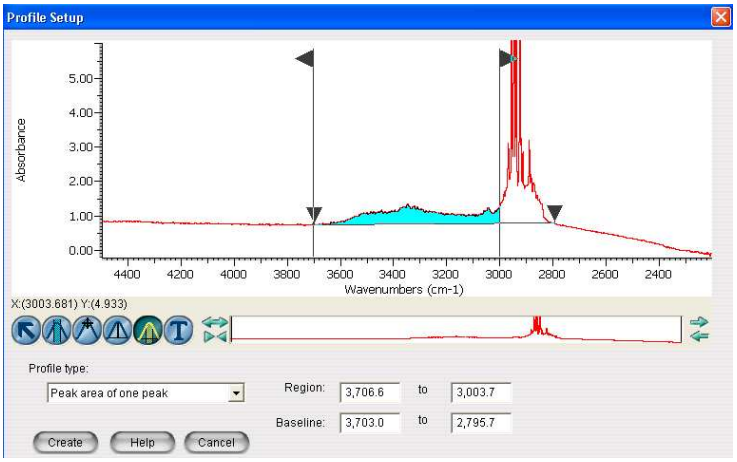

Examples of how noise got much worse as signal decreased through the mapping which took 2 hours. The bottom of the map is created first, top is last.

Bottom:

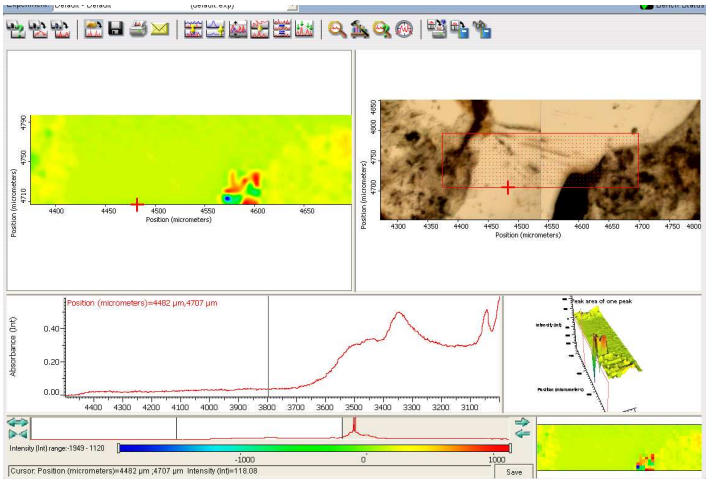

Top:

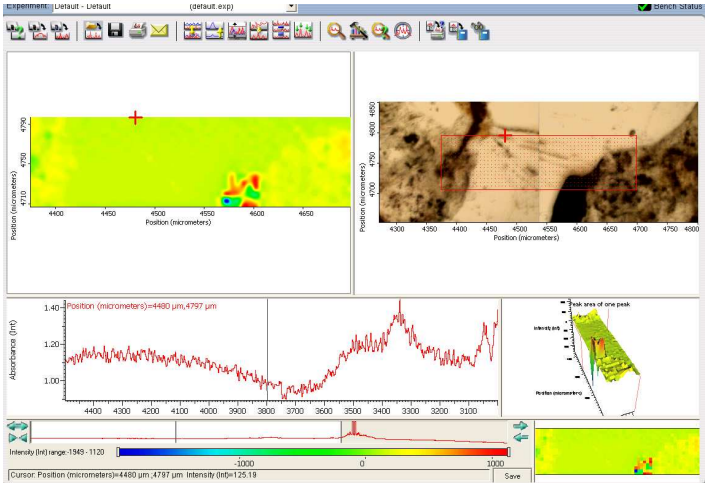

Moderate Strain Granitic Clast: A08-05-Y2

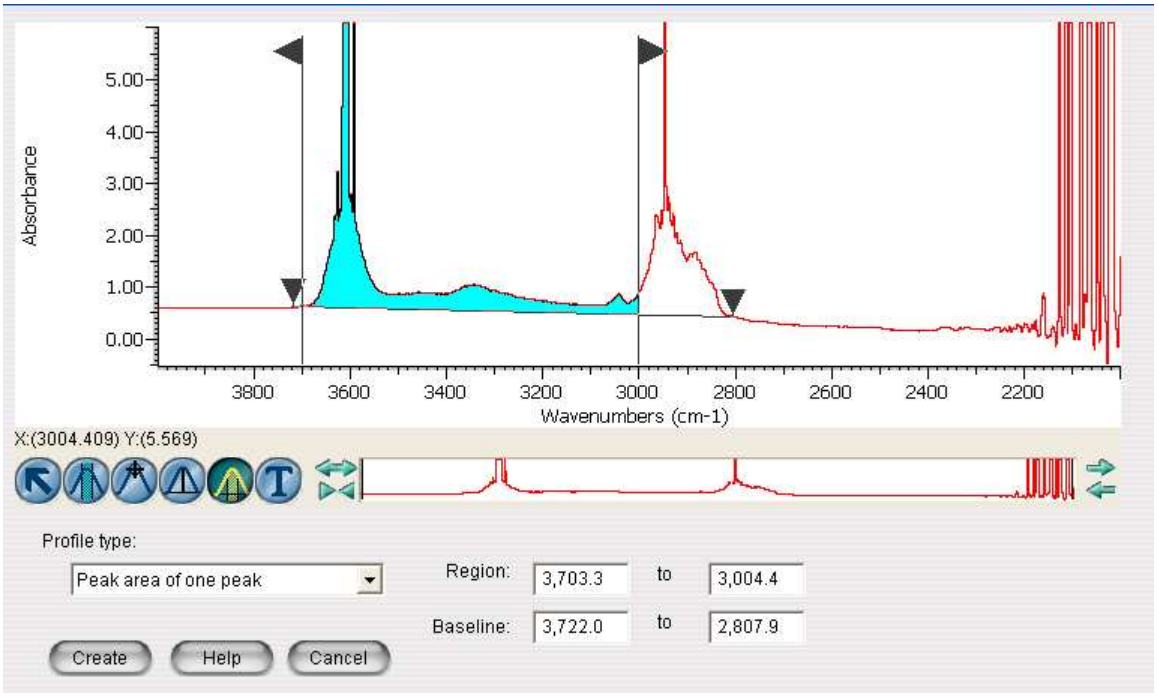

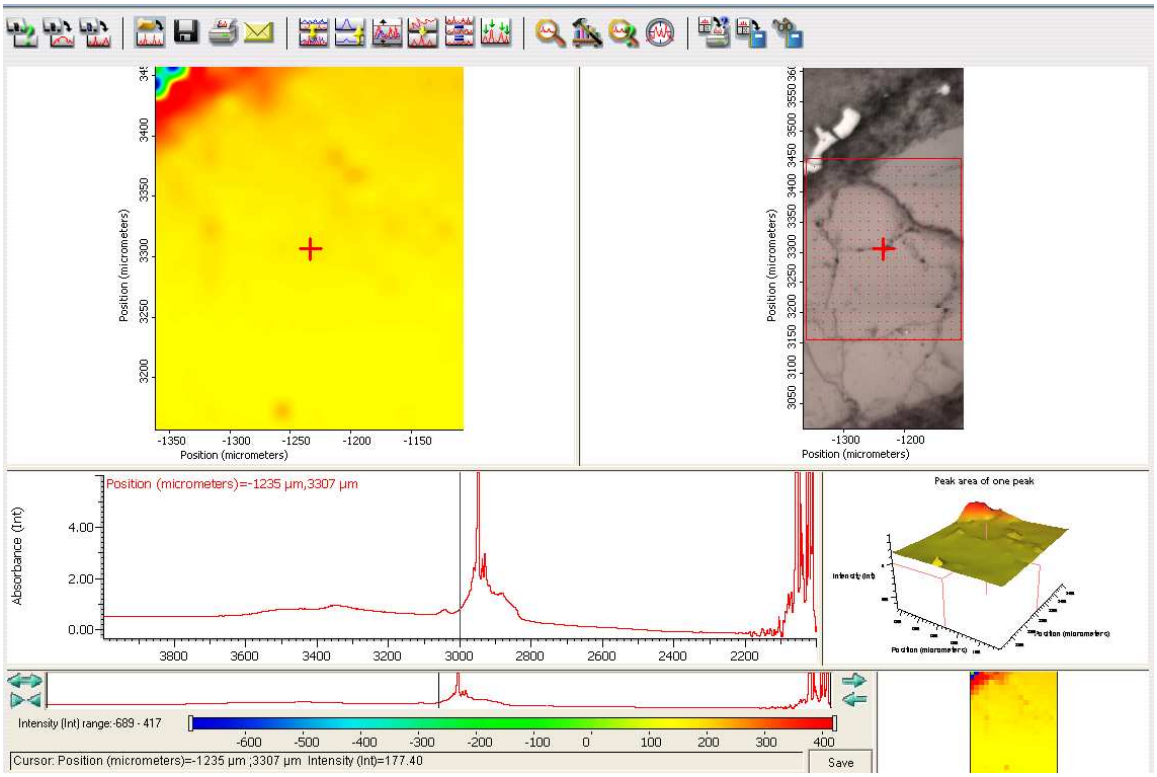

Moderate Strain Granitic Clast: A08-05-Y2_Map2

Spectra are noisy because the signal was decreasing as these maps were taken around 4:30am (a long time after the initial synchrotron injection for the day).

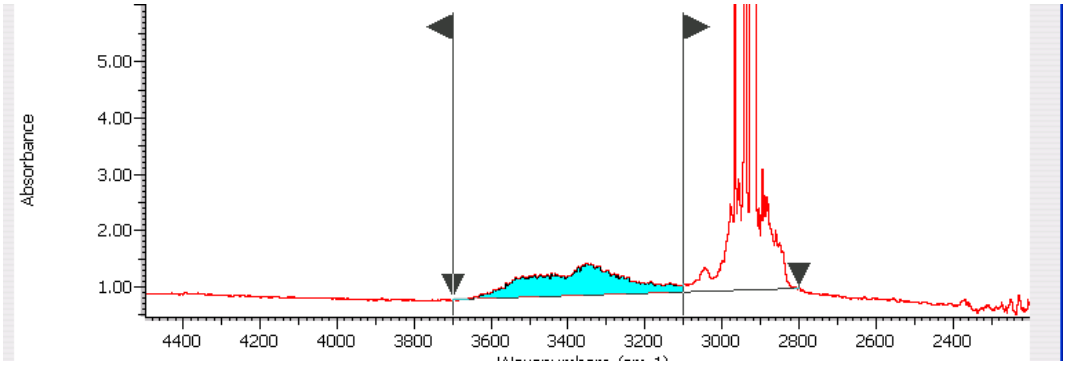

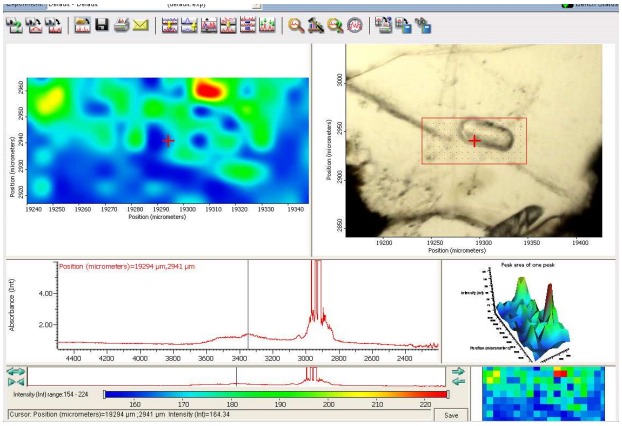

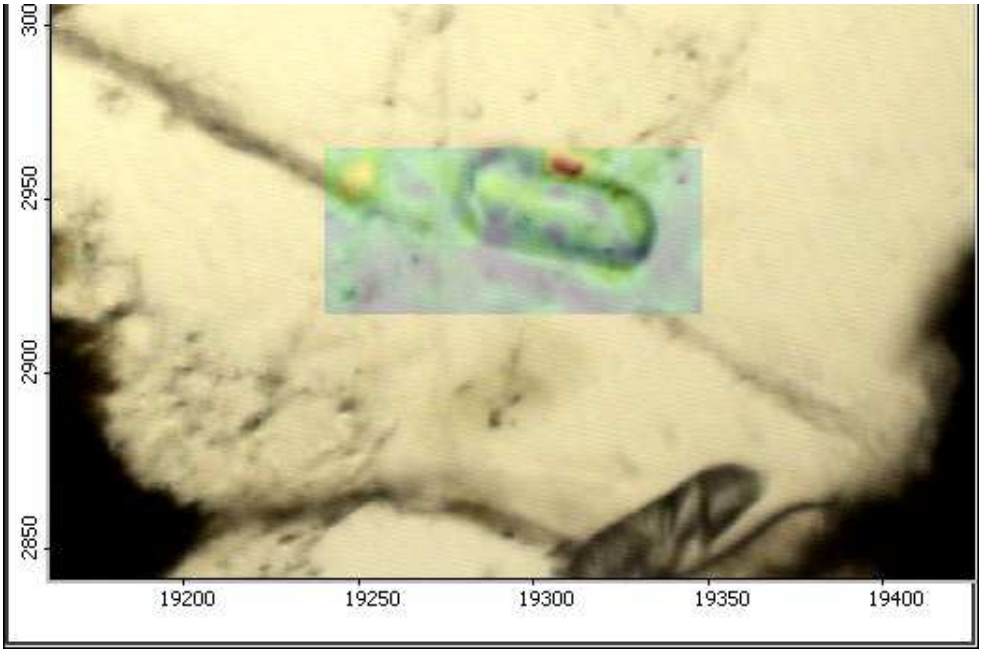

Moderate Strain Gneissic Clast: A08-05-Z1

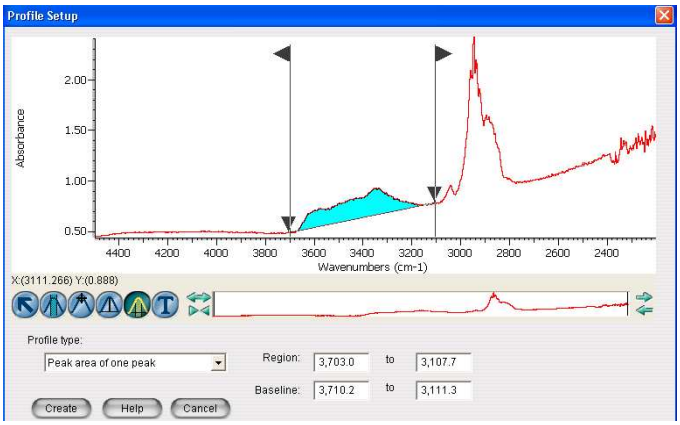

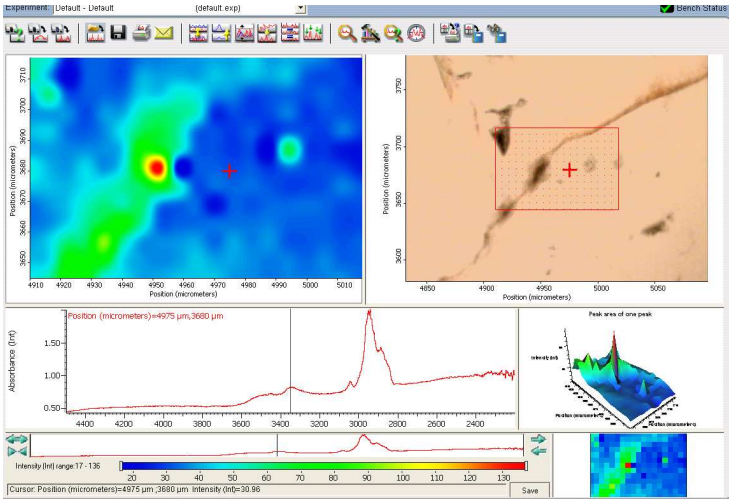

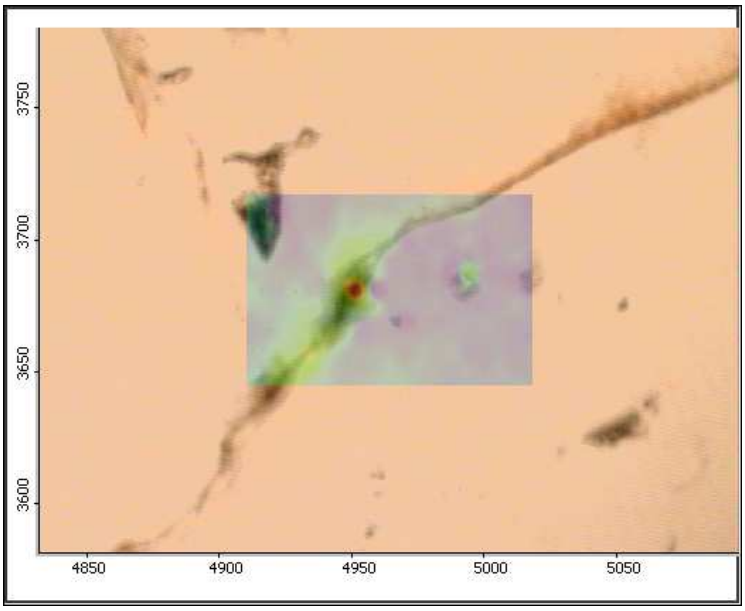

(1) Moderate Strain Gneissic Clast: A08-05-Z2

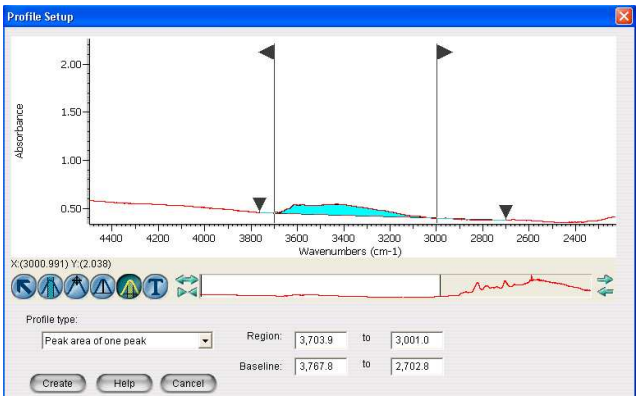

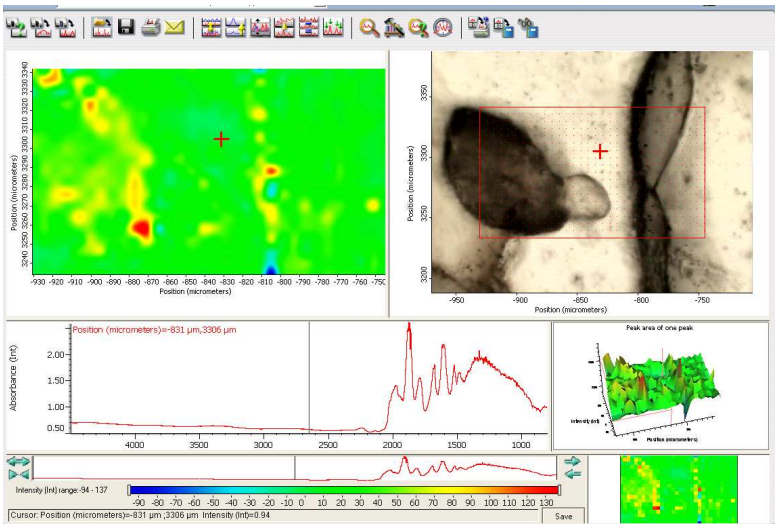

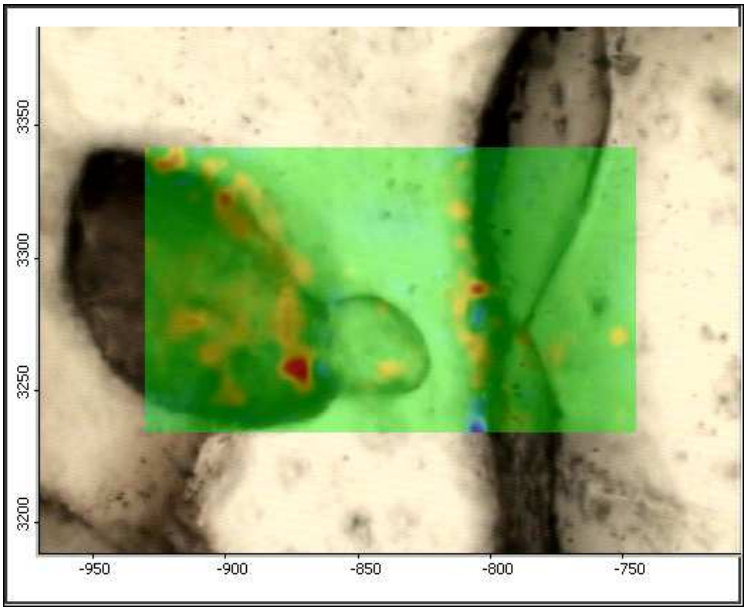

(2) Moderate Strain Gneissic Clast: A08-05-Z2

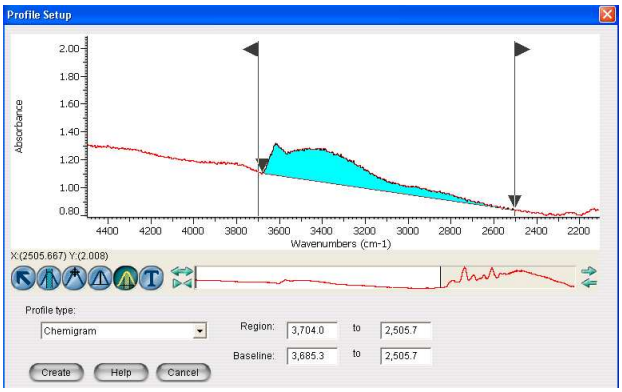

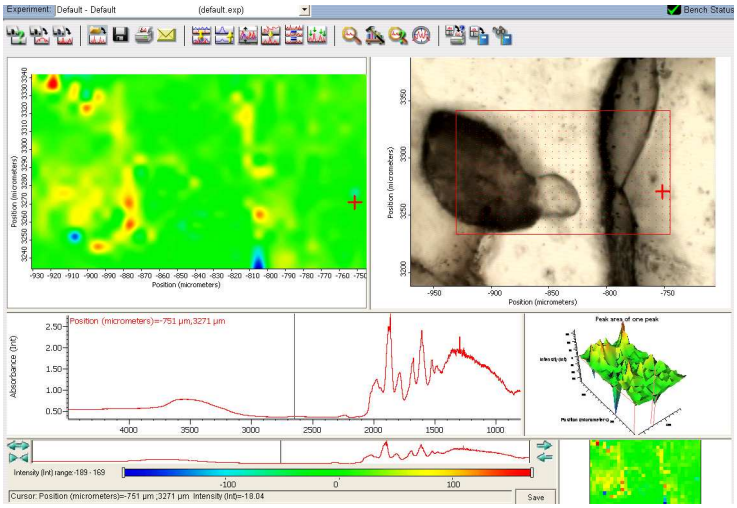

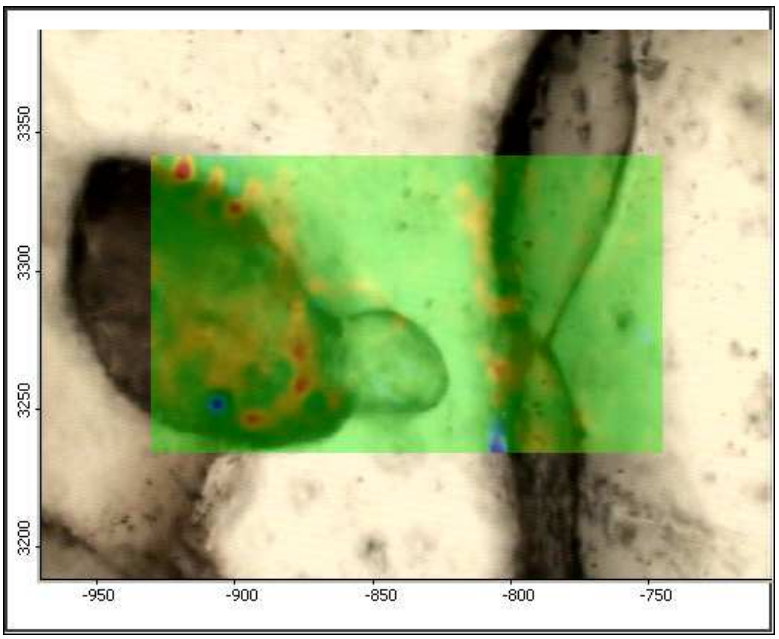

(3) Moderate Strain Gneissic Clast: A08-05-Z2

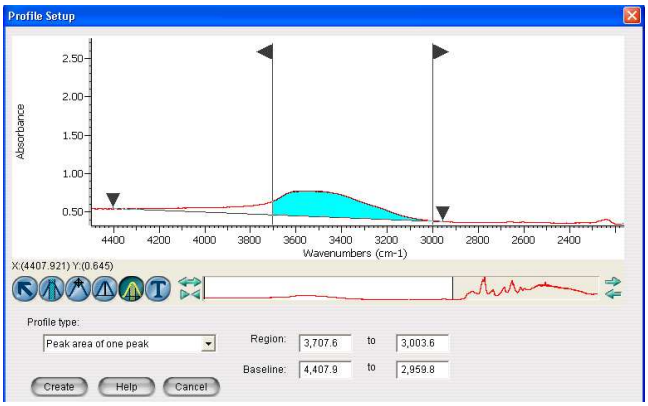

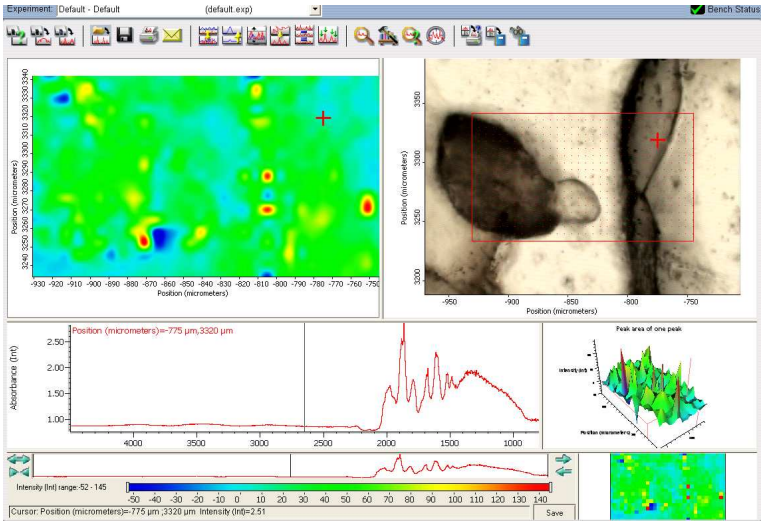

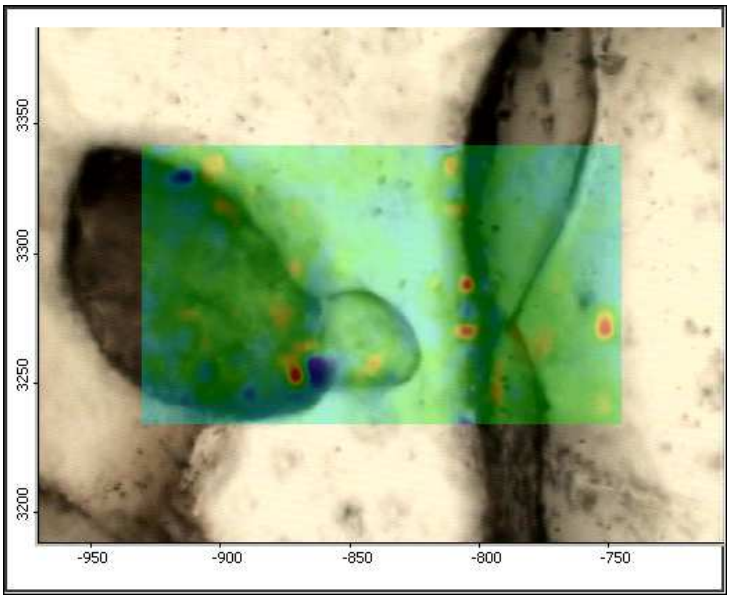

Moderate Strain Gneissic Clast: A08-05-Z2_Map2

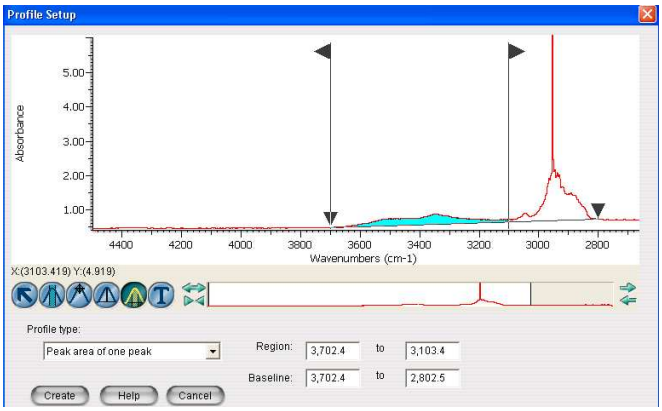

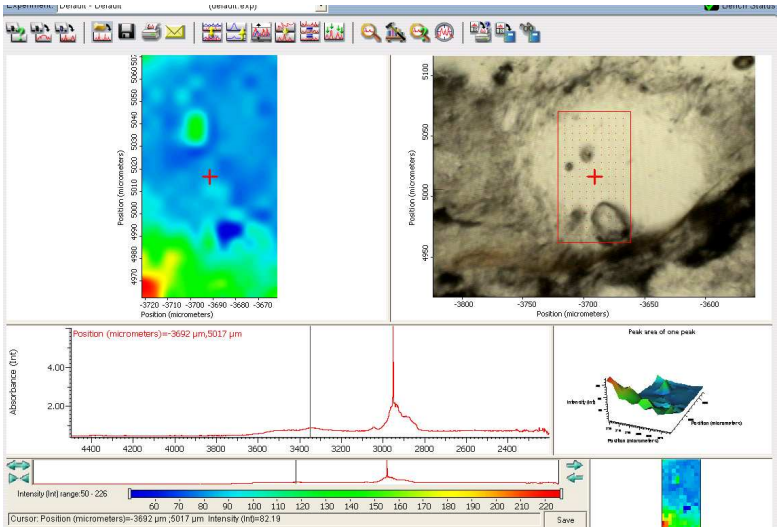

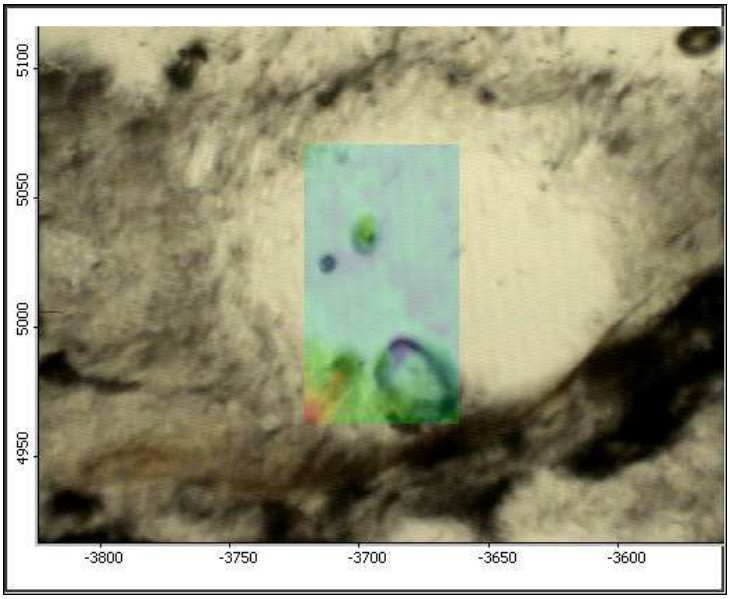

A.3 High Strain

High Strain Quartzite: A08-06-X1

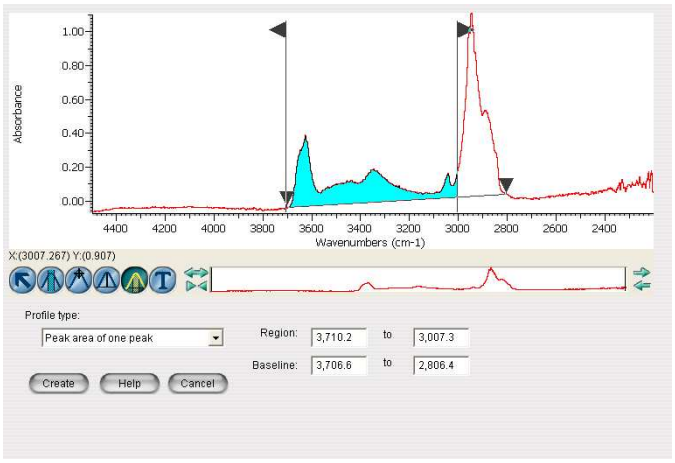

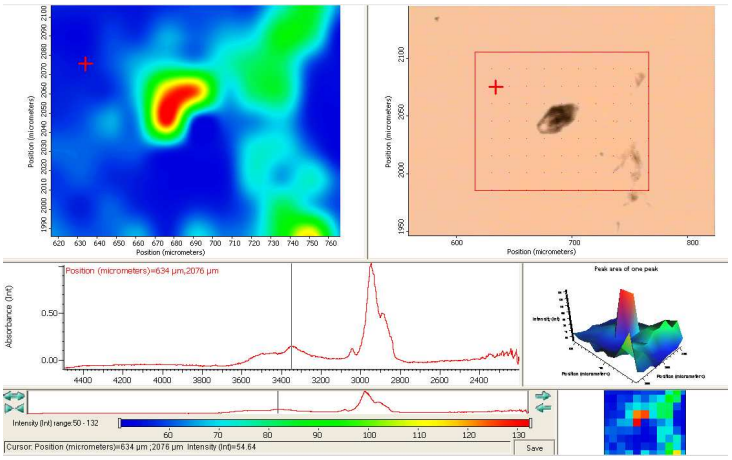

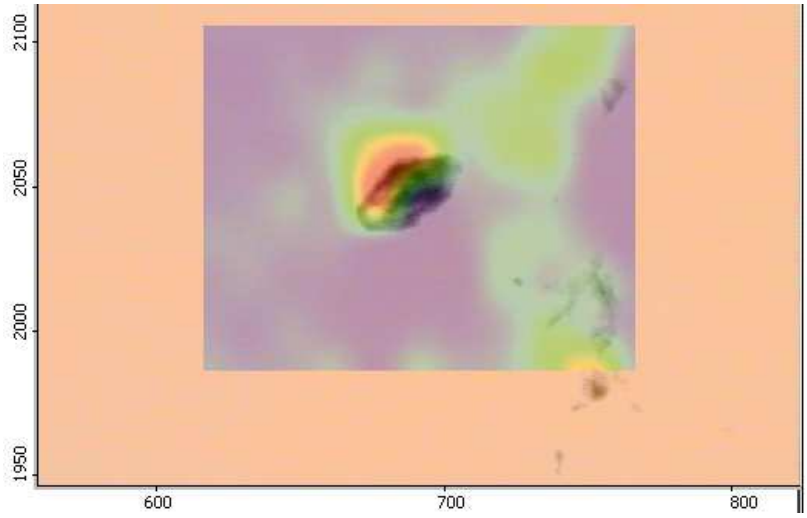

High Strain Quartzite: A08-06-X1_Map2

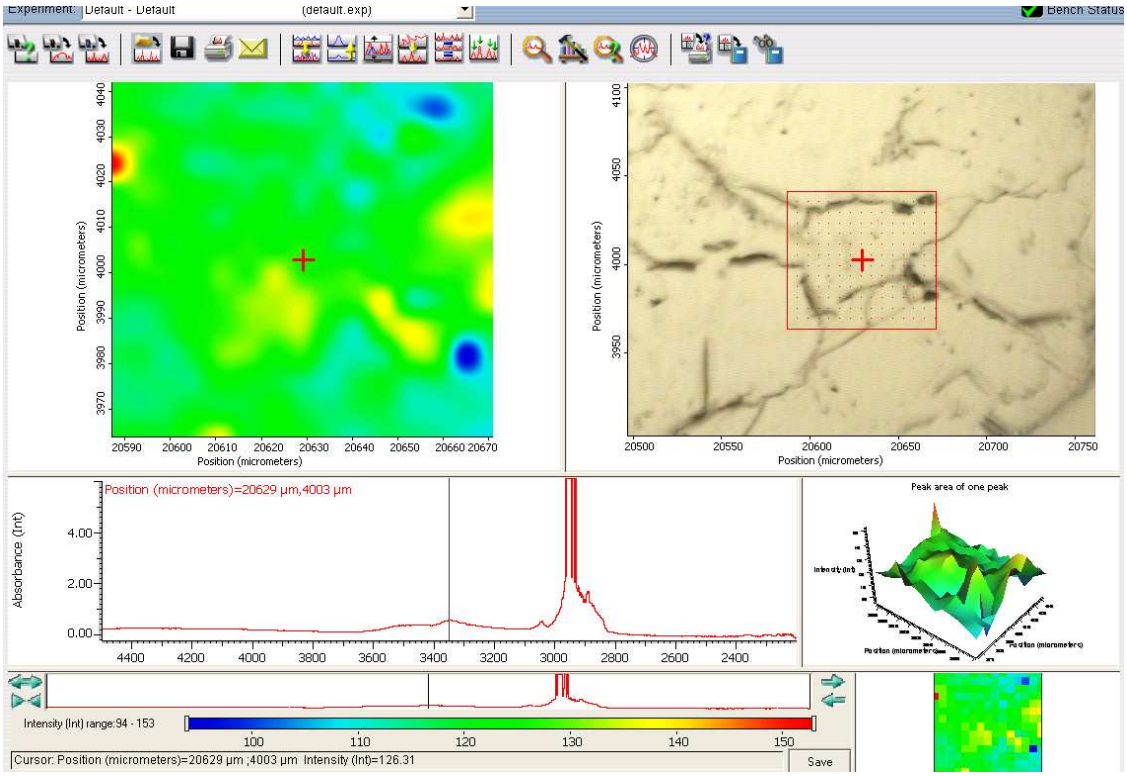

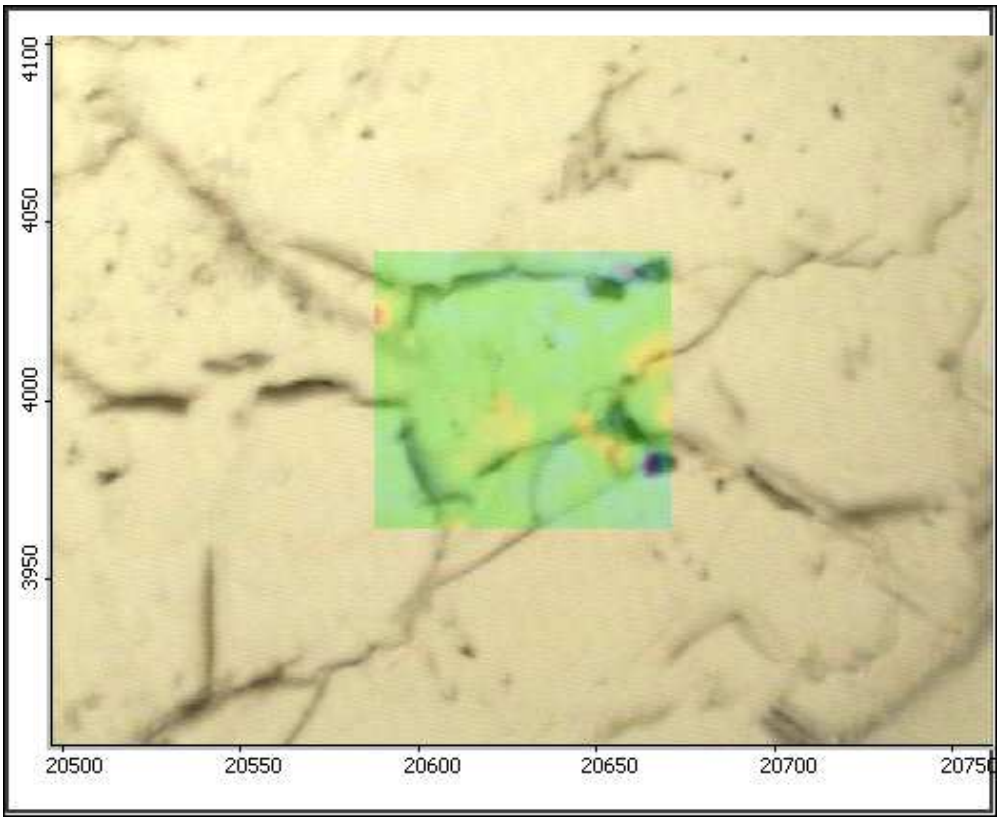

High Strain Quartzite: A08-06-X2

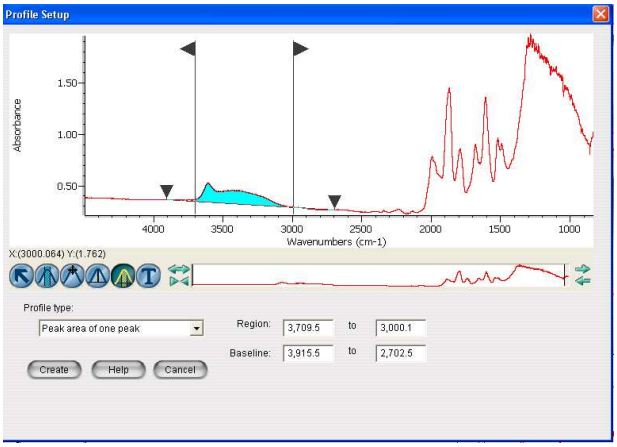

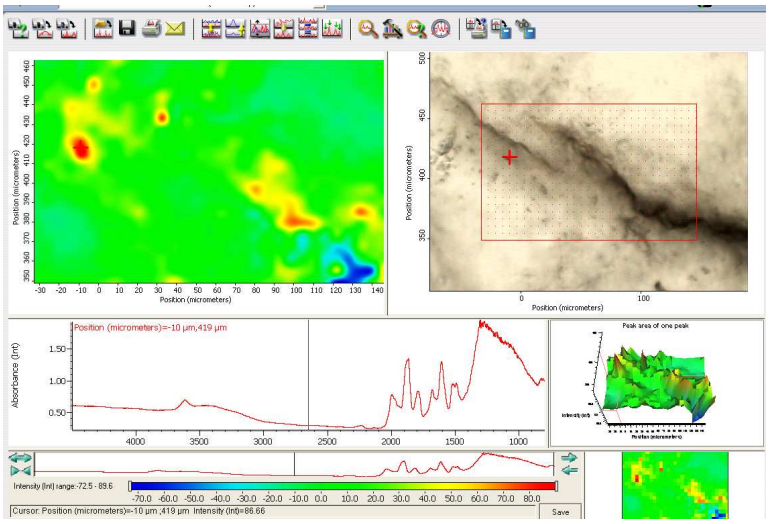

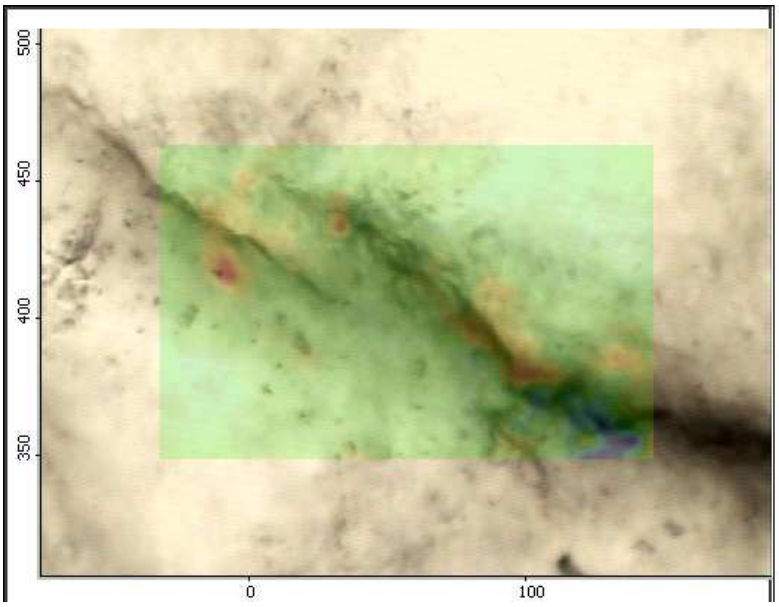

High Strain Quartzite: A08-06-X2_Map2

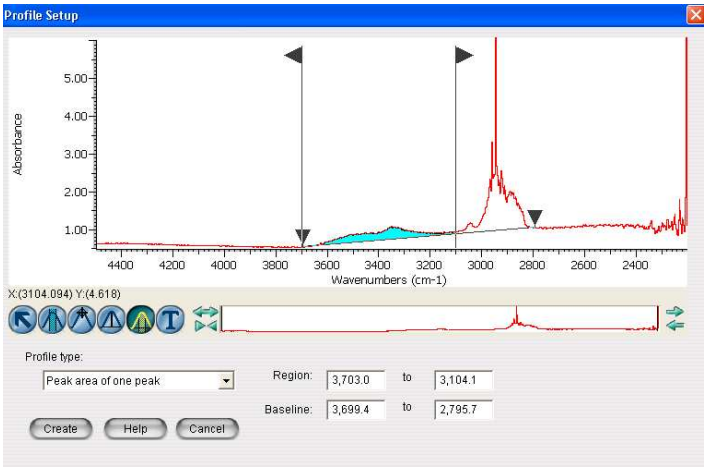

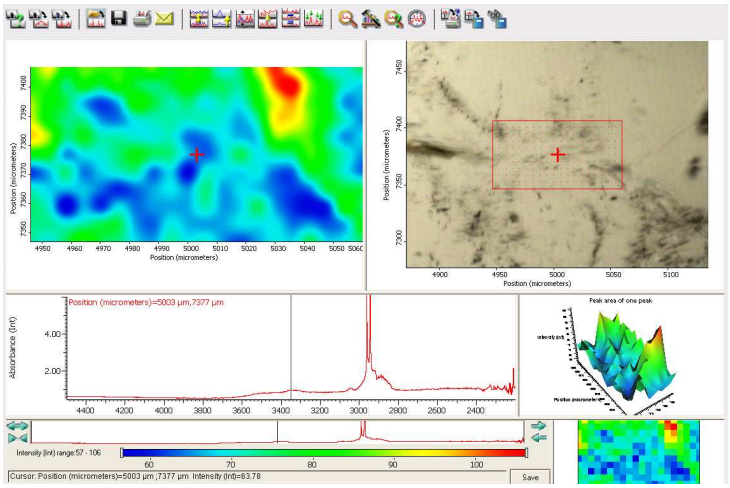

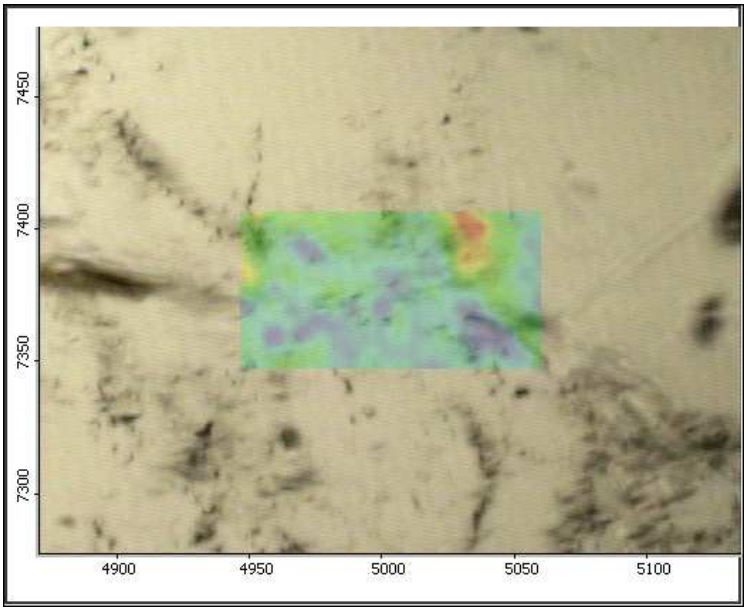

High Strain Quartzite: A08-06-X3

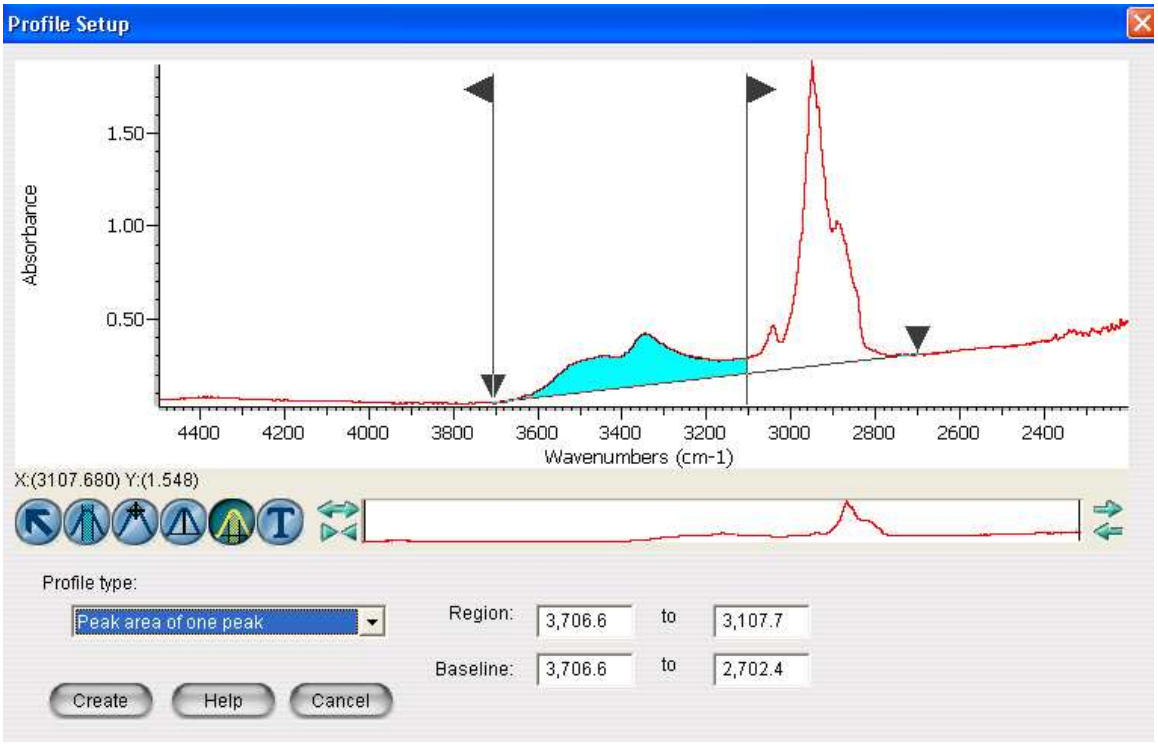

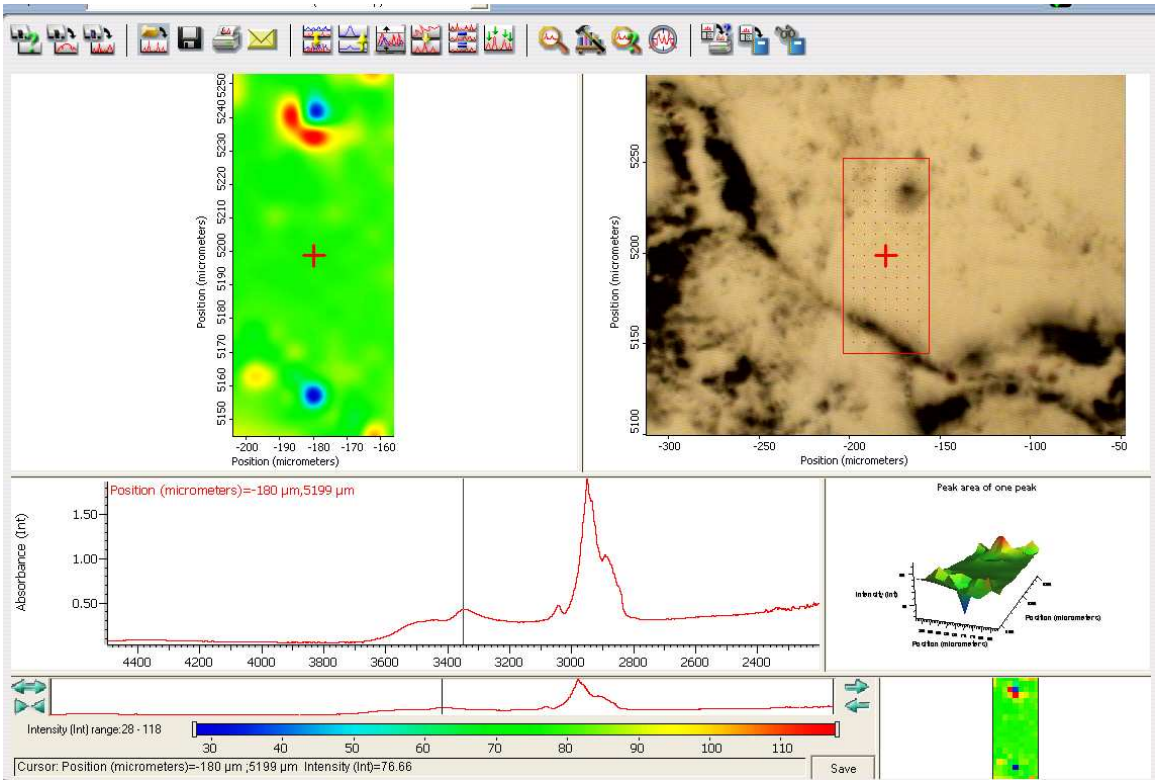

High Strain Quartzite: A08-06-X4

I used 3700-2700cm^{-1} for the baseline, and 3700-3100cm^{-1} for the area under the peak in order to keep out the small peak that is next to the Hydrocarbons (between 2800-3000cm^{-1}).

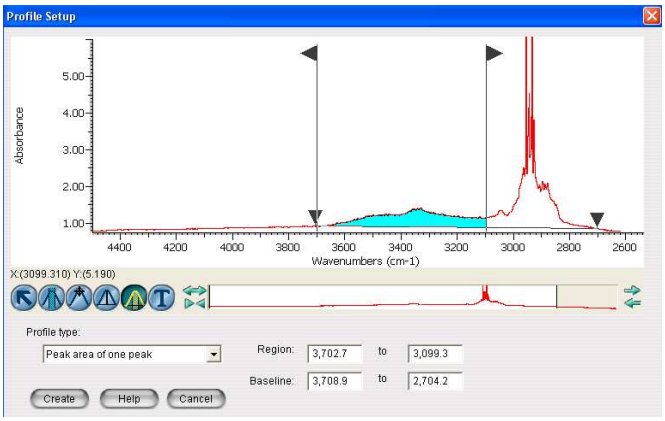

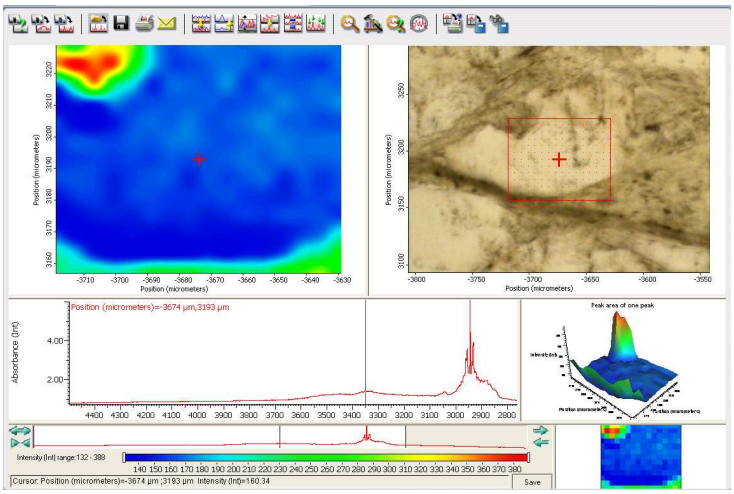

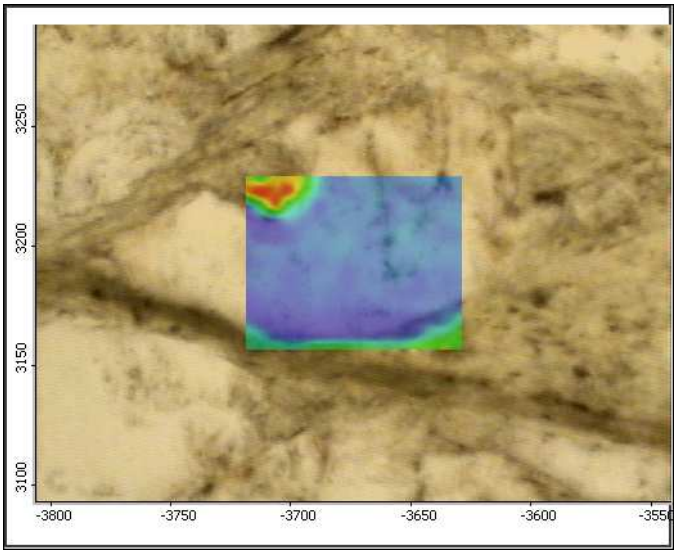

High Strain Granitic Clast: A08-06-Y1

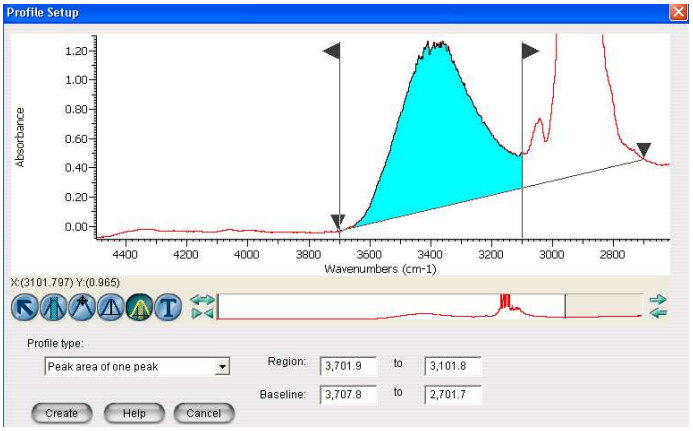

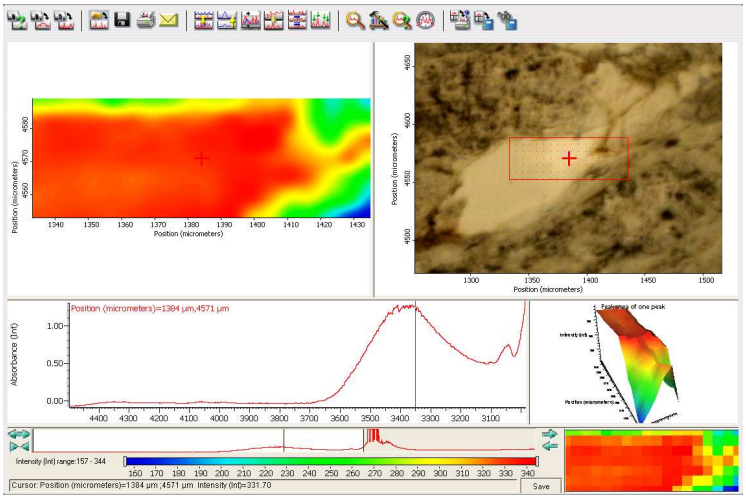

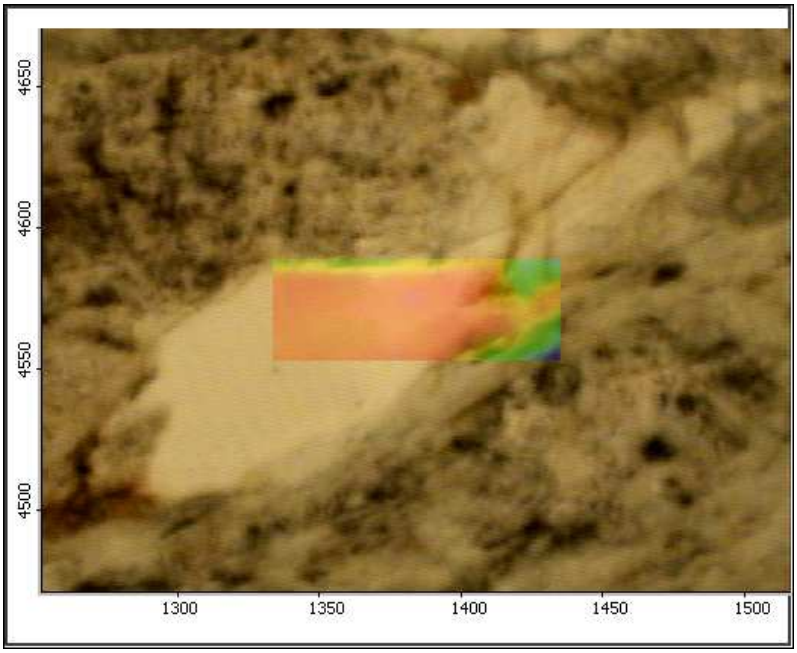

High Strain Granitic Clast: A08-06-Y2

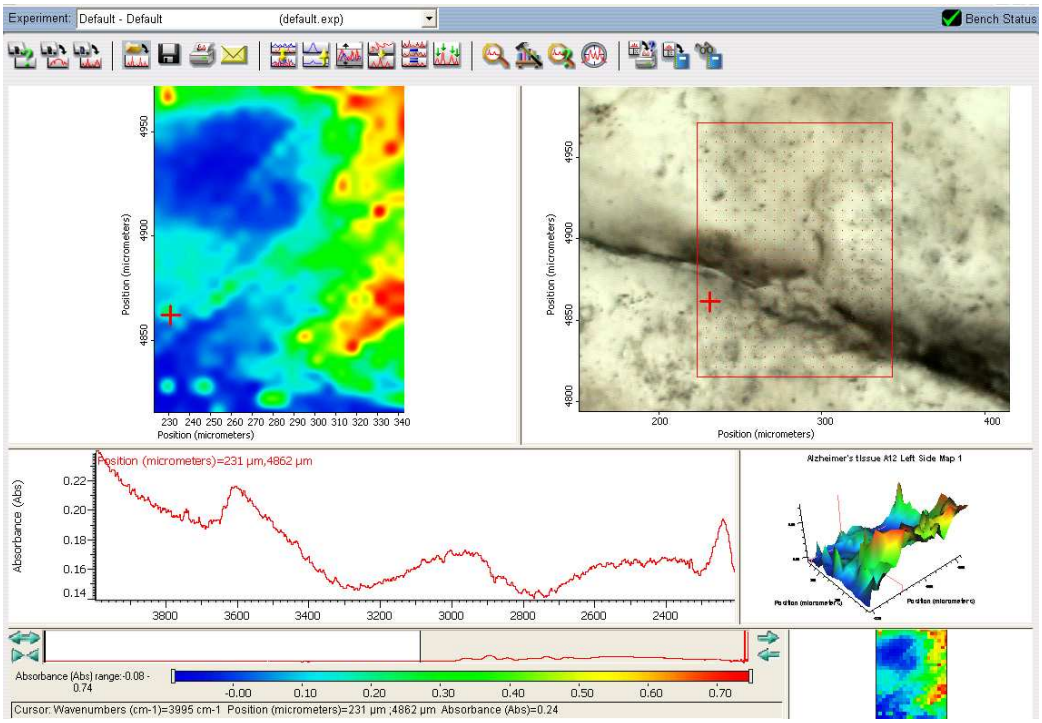

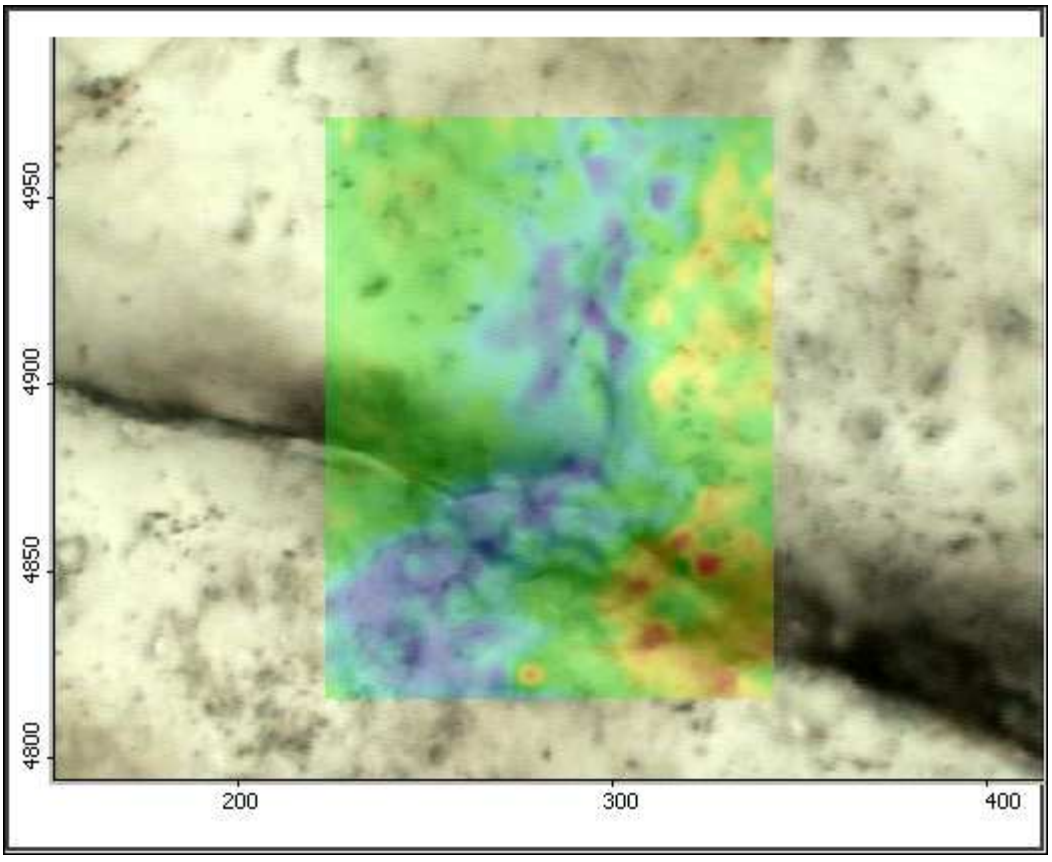

High Strain Granitic Clast: A08-06-Y2_Map2

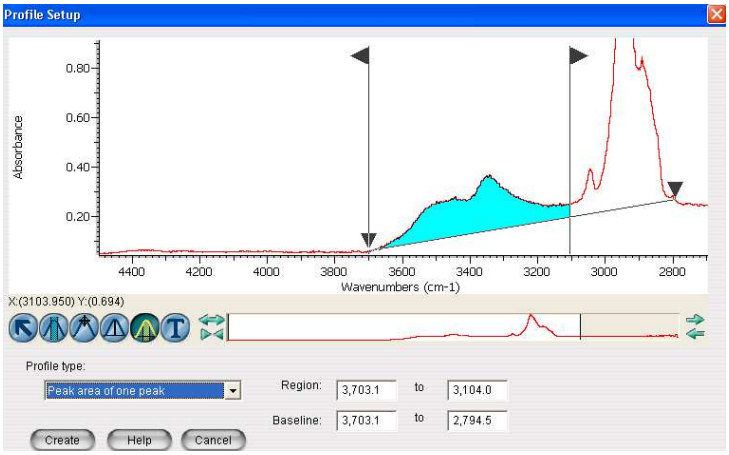

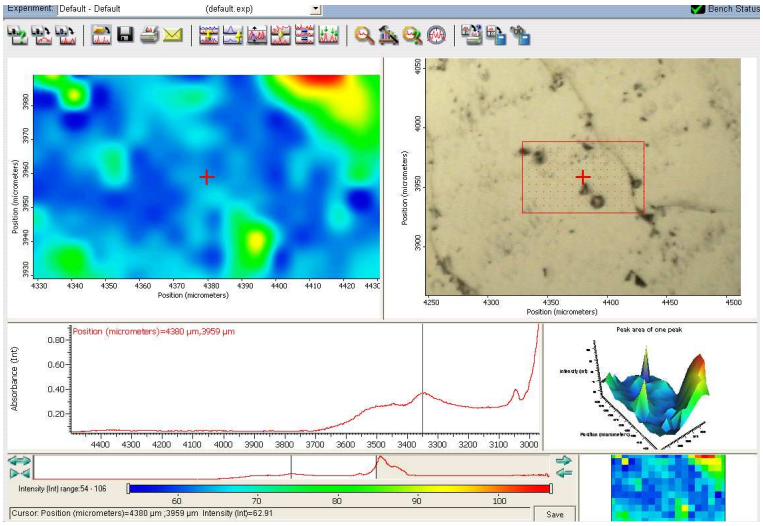

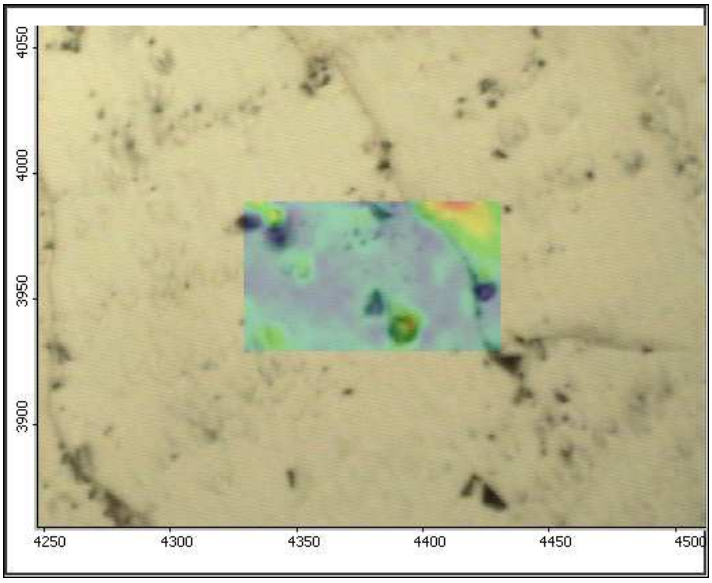

High Strain Granitic Clast: A08-06-Y3

This is water in a fluid inclusion. Other areas on the map had little to no water peak.

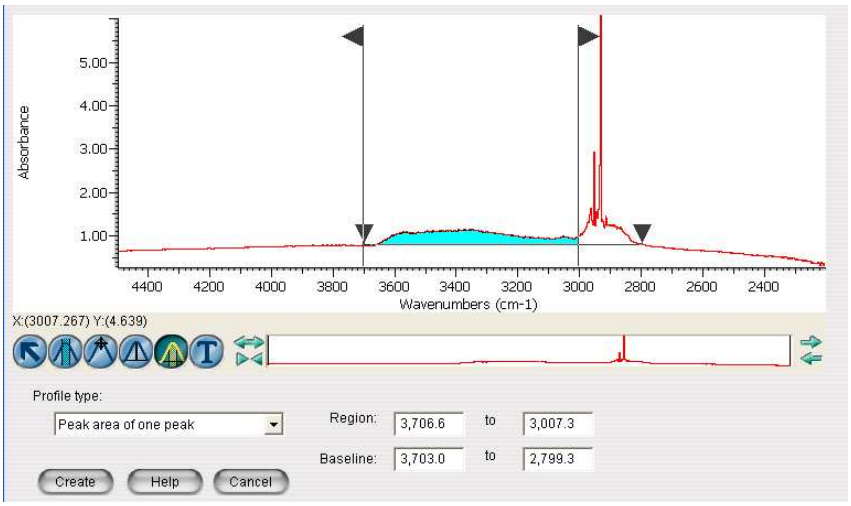

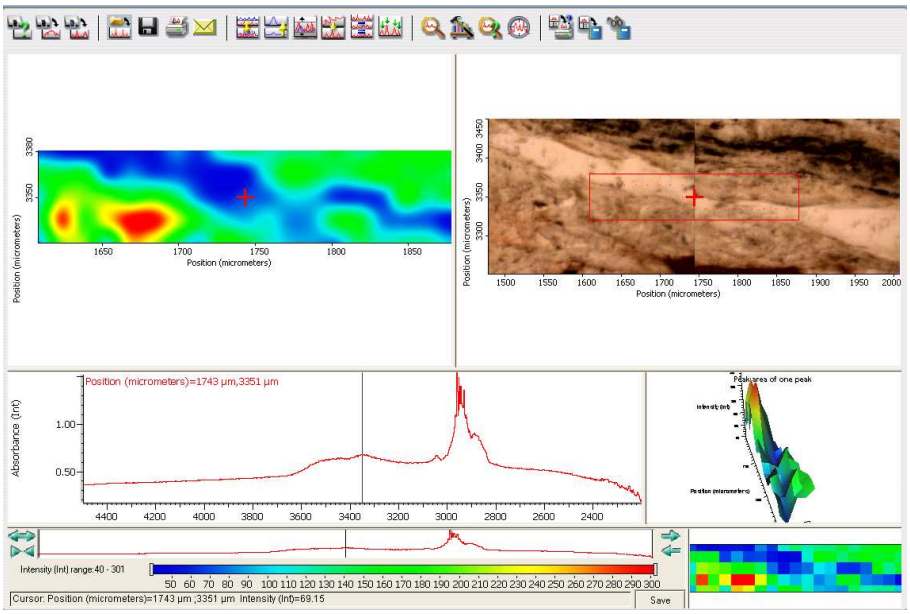

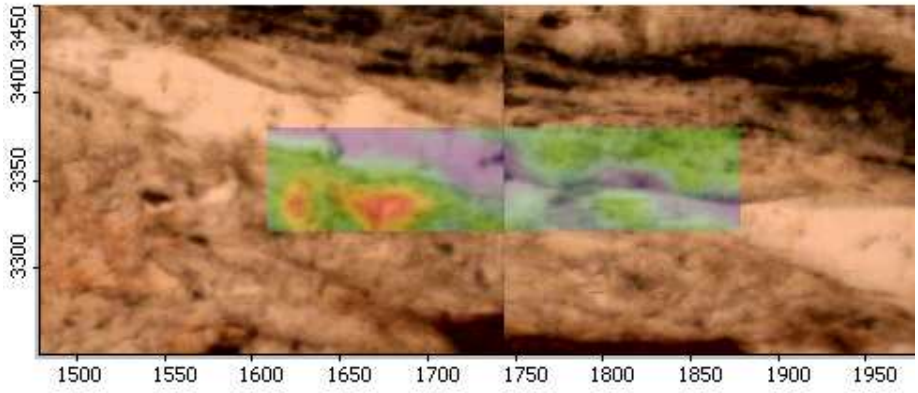

High Strain Granitic Clast: A08-06-Y3_Map2

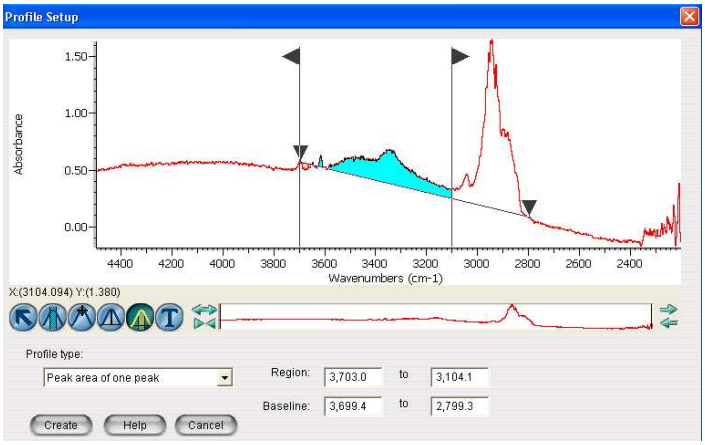

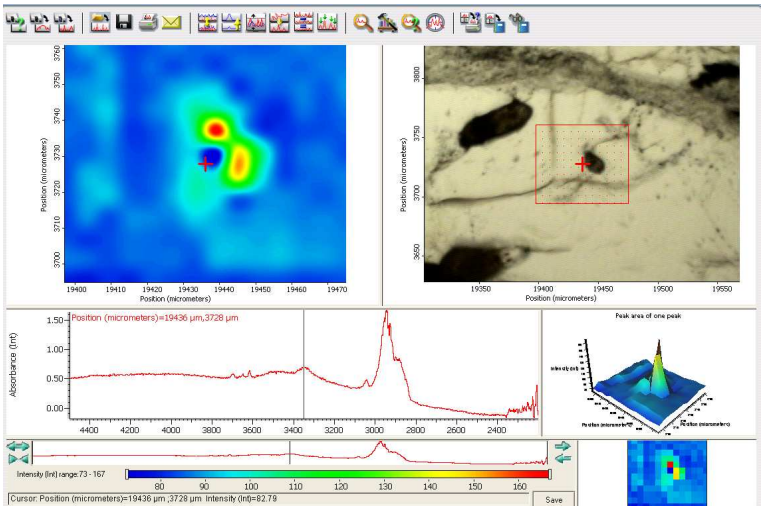

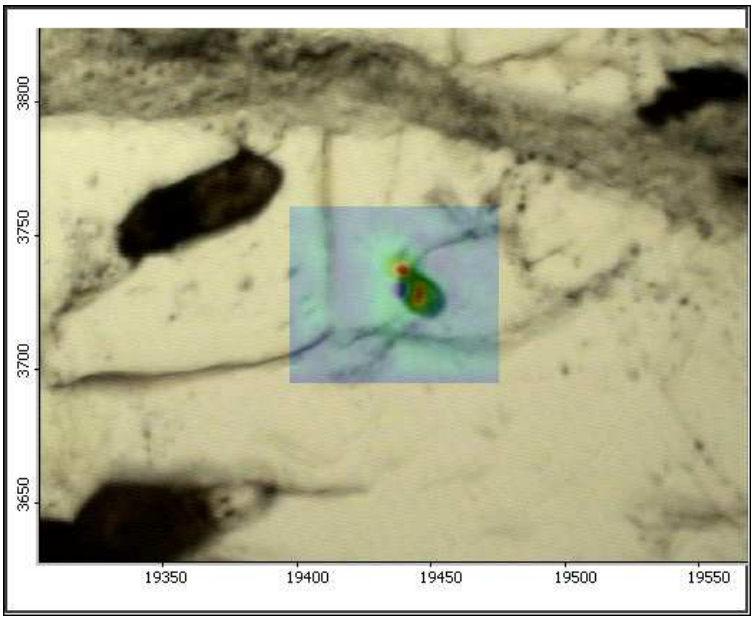

High Strain Granitic Clast: A08-06-Y4

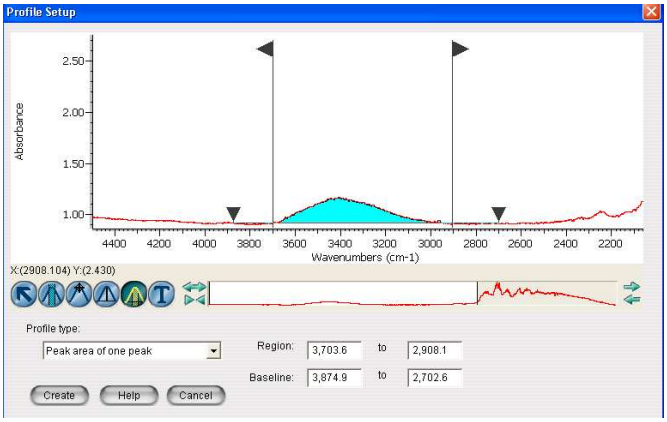

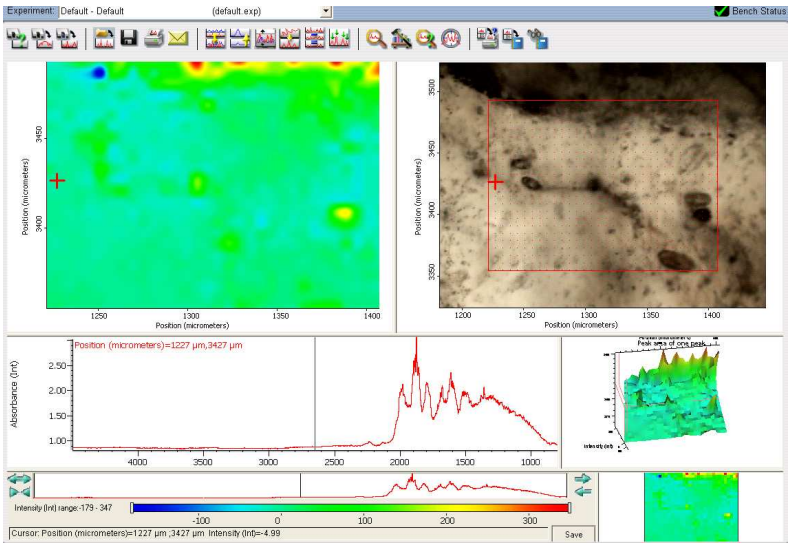

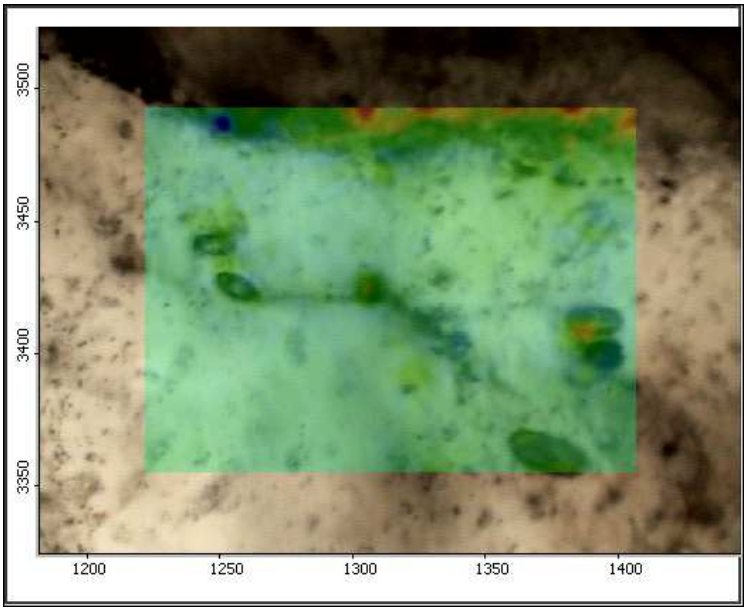

High Strain Granitic Clast: A08-06-Y4_Map2

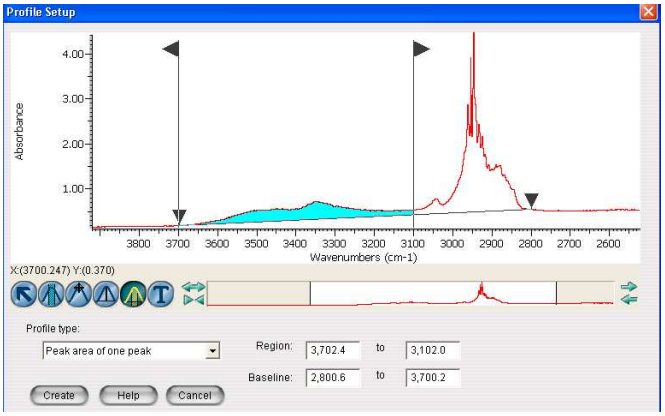

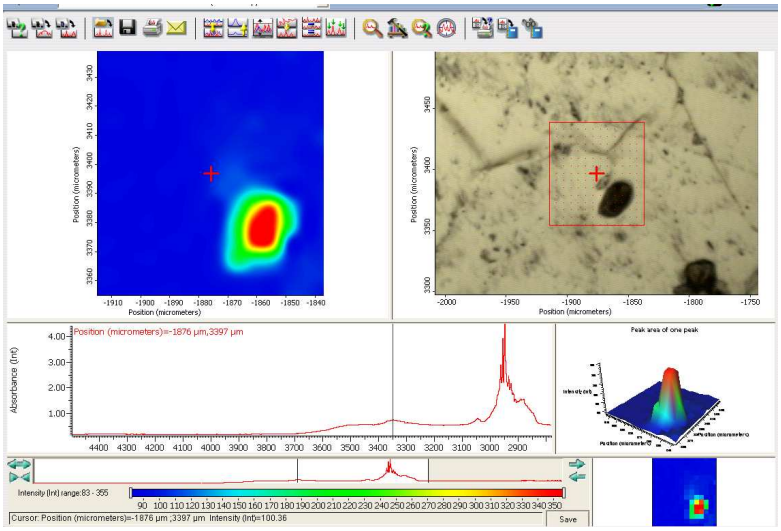

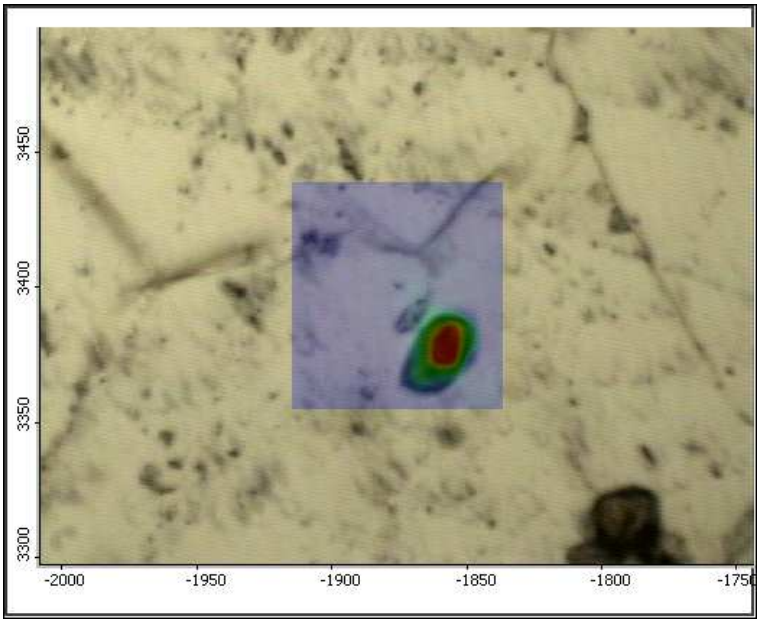

High Strain Granitic Clast: A08-06-Y5 (Overnight Map)

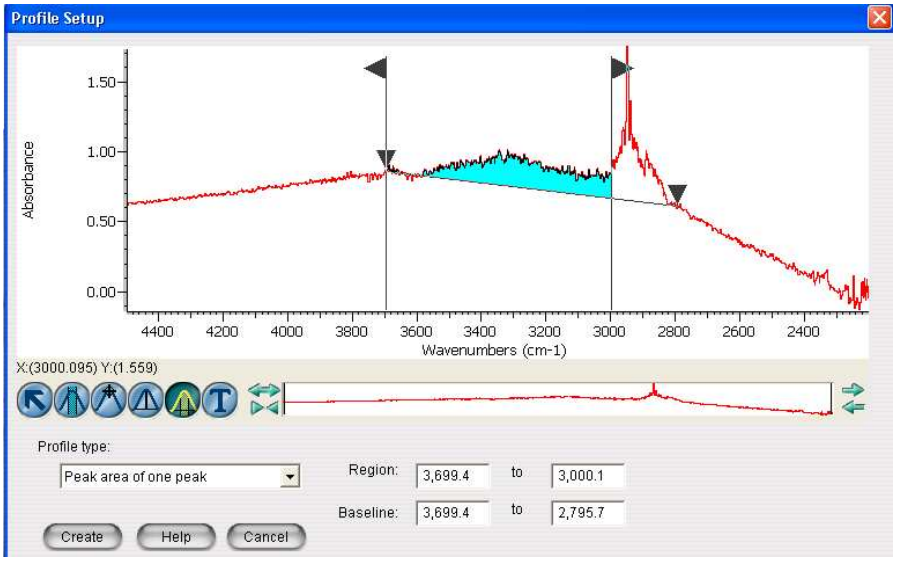

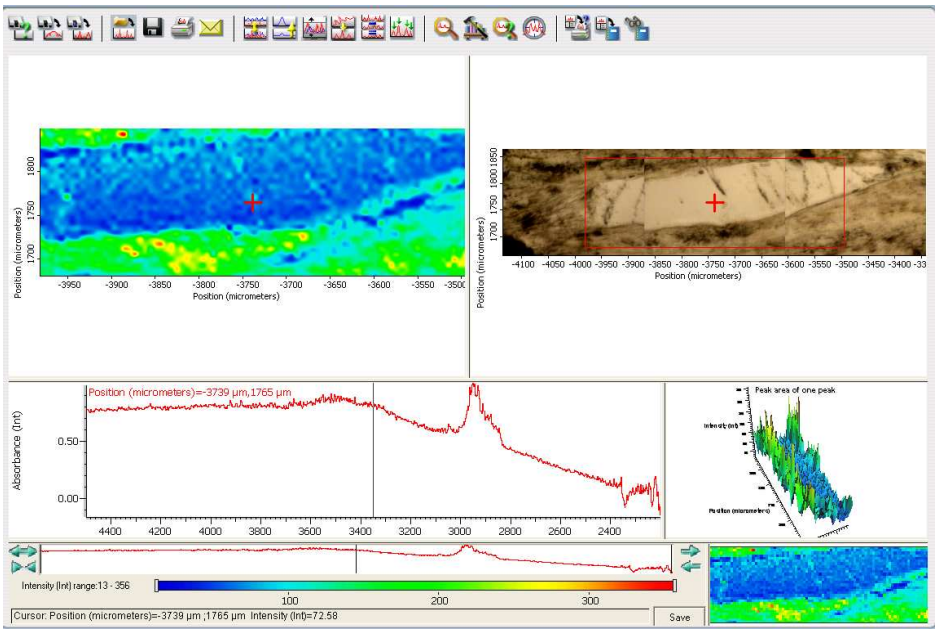

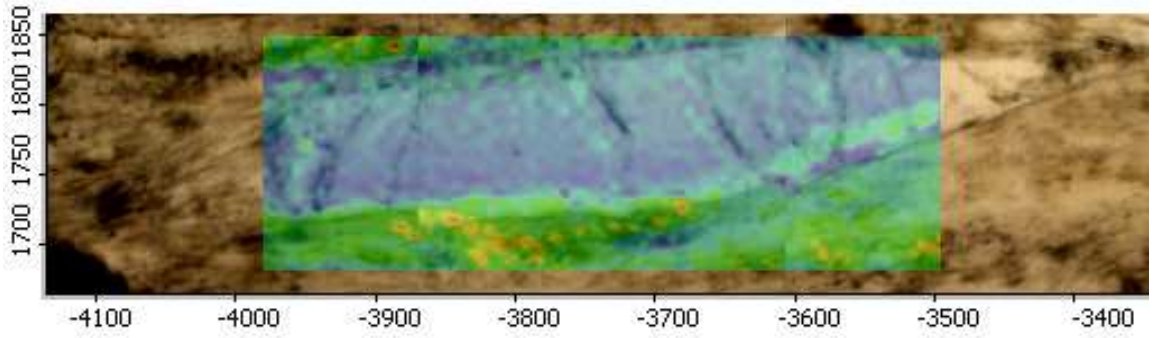

High Strain Gneissic Clast: A08-06-Z1

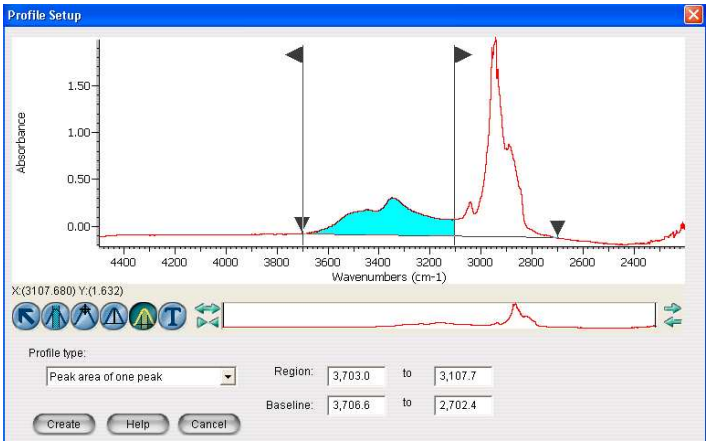

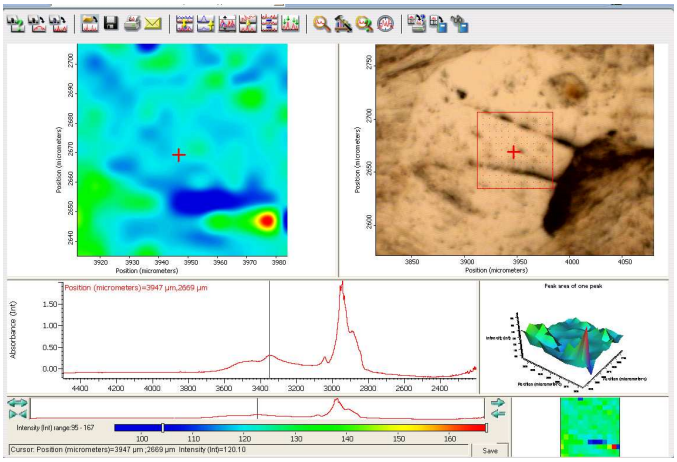

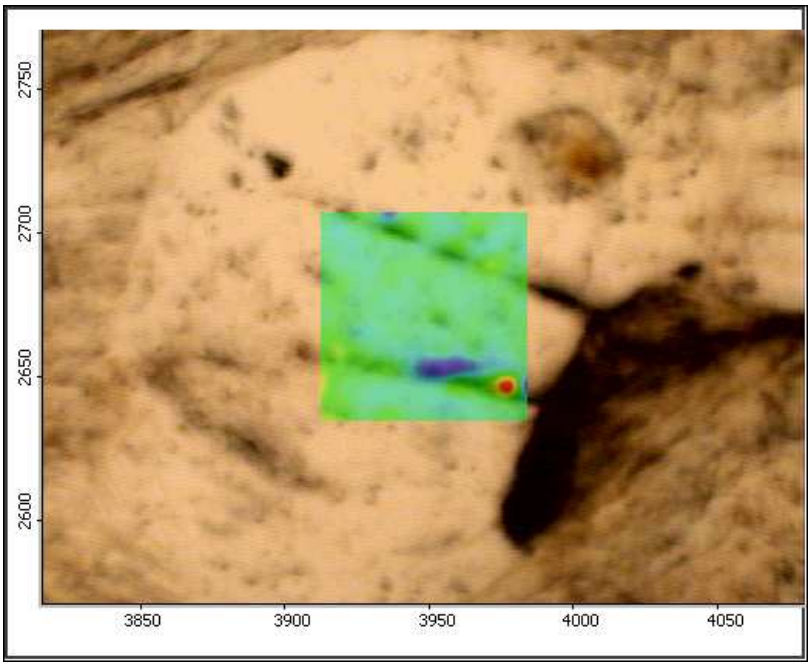

High Strain Gneissic Clast: A08-06-Z2

The area under the water curve was shortened the area to 3100 to keep out hydrocarbon peaks.

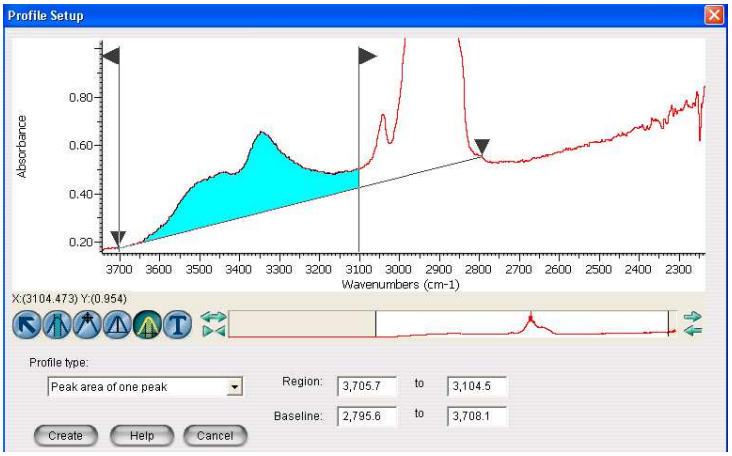

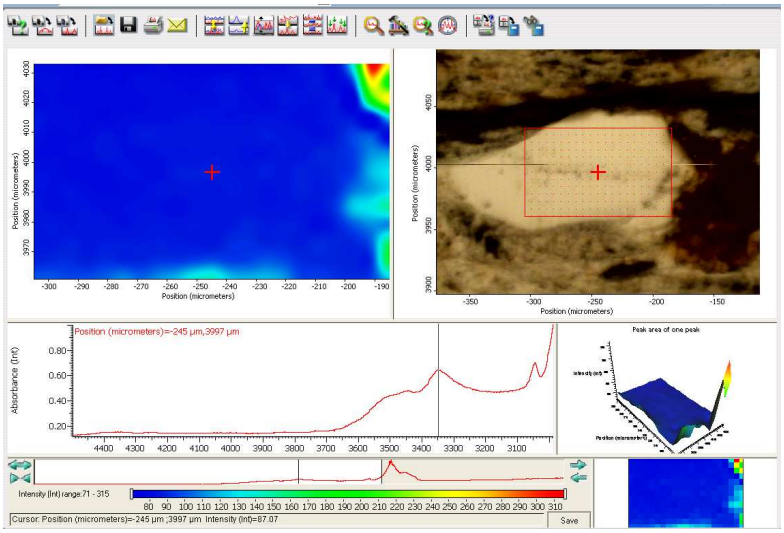

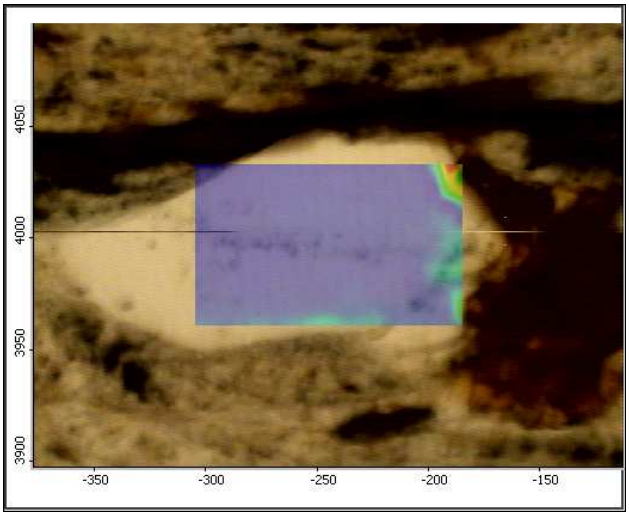

High Strain Gneissic Clast: A08-06-Z3

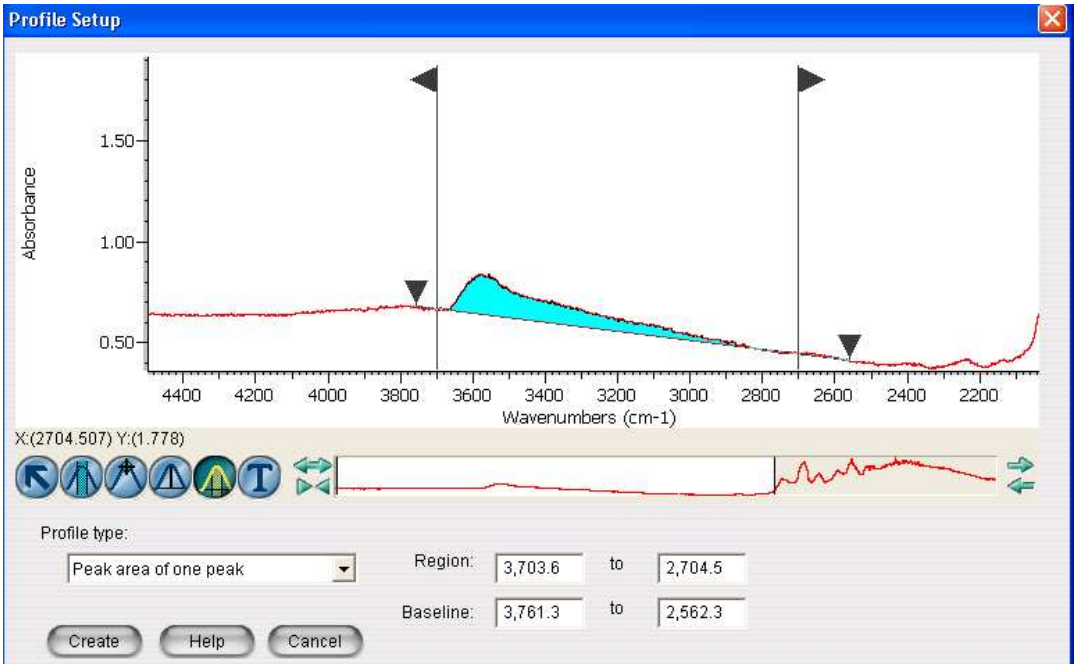

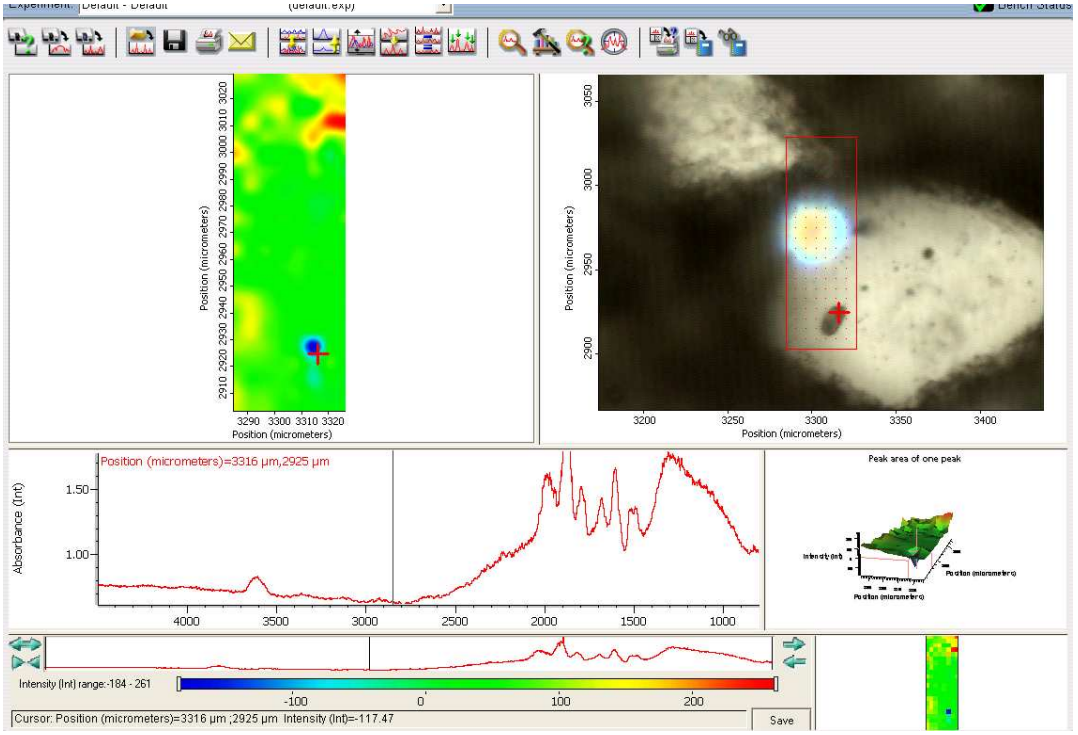

High Strain Gneissic Clast: A08-06-Z3_Map2

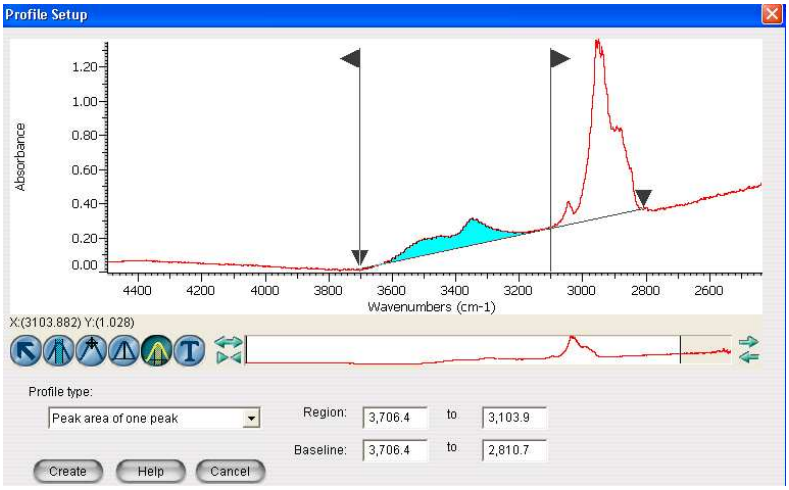

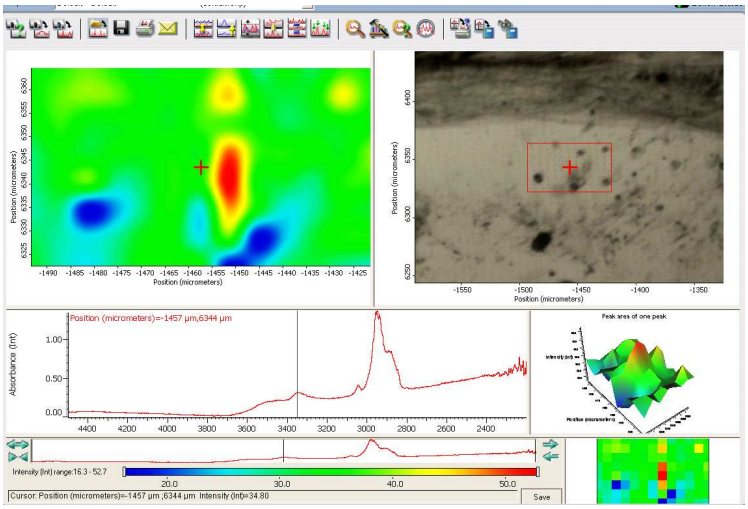

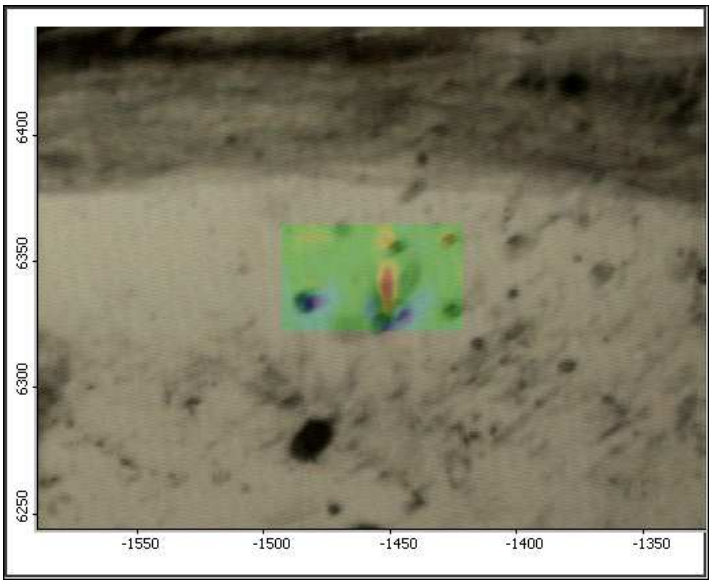

High Strain Gneissic Clast: A08-06-Z4 (Overnight map)

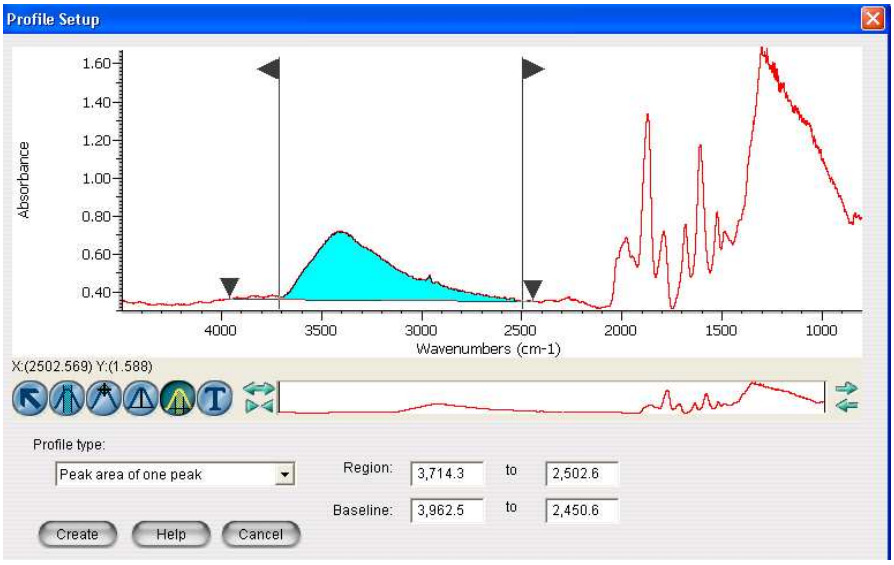

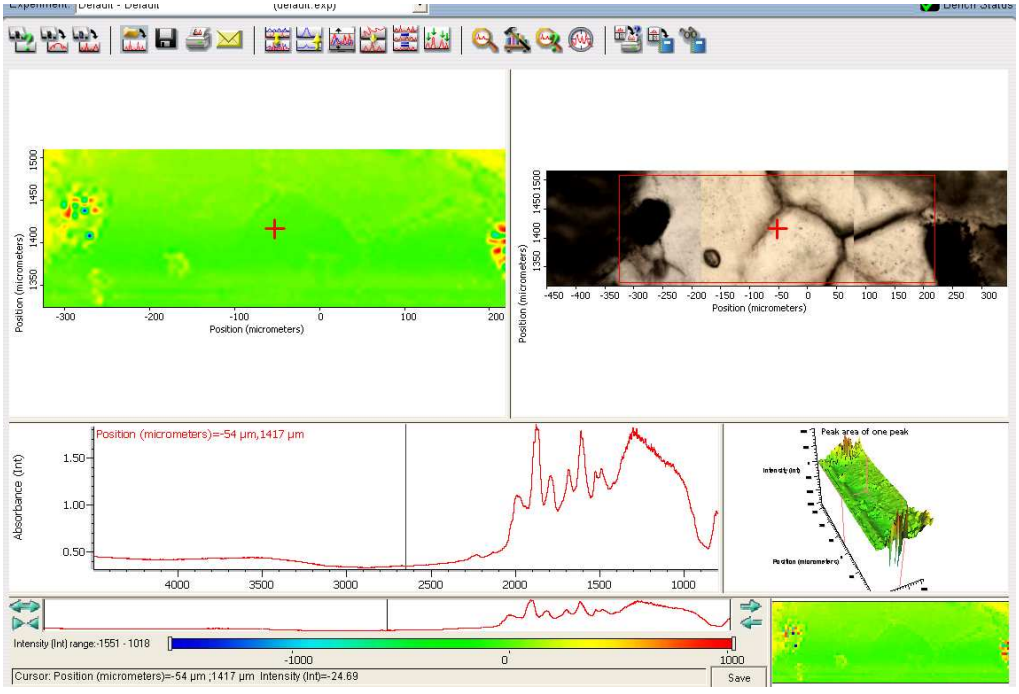

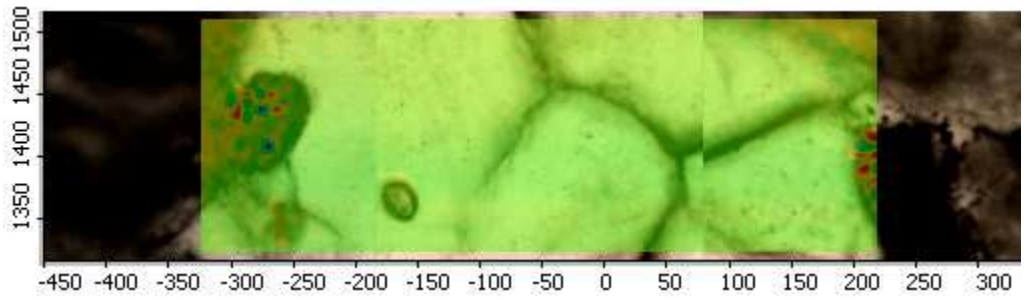

High Strain Gneissic Clast: A08-06-Z4_Map2 Aperture light shows through in the grain map.

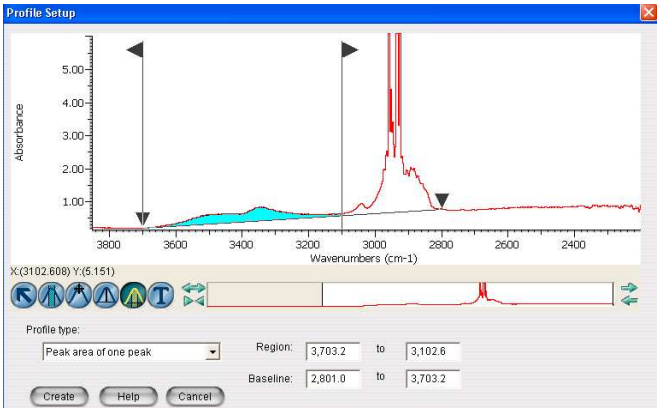

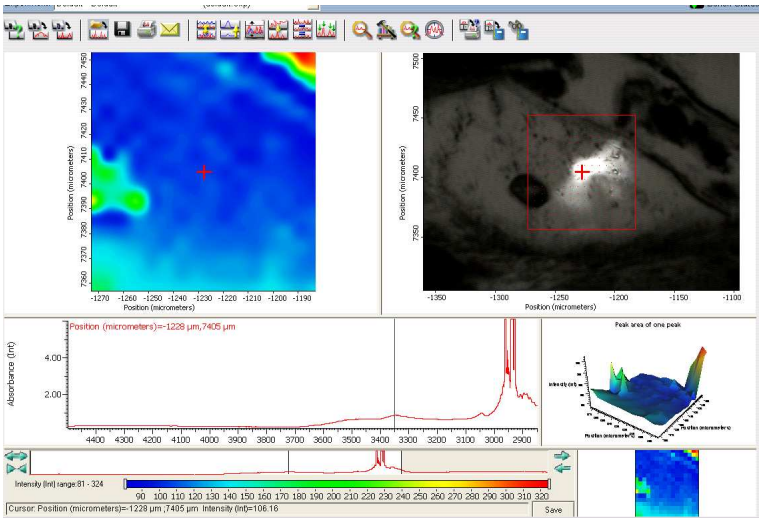

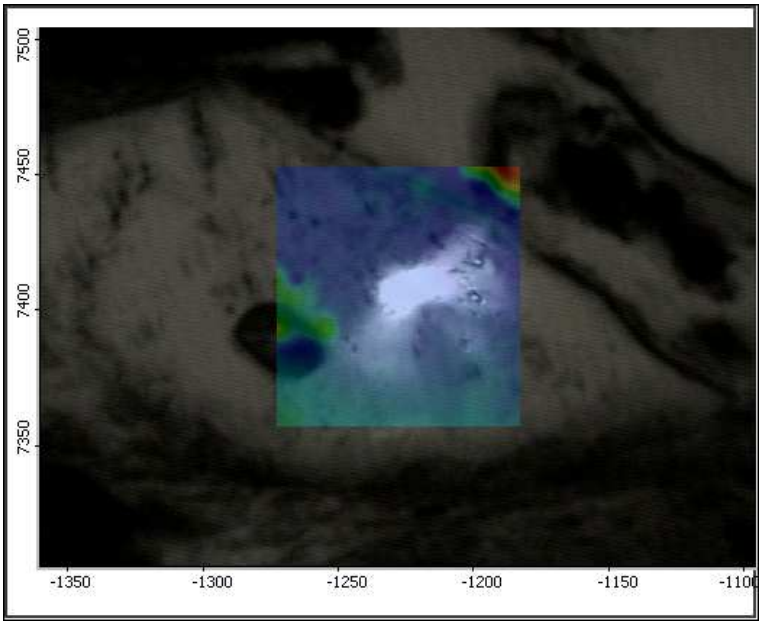

Appendix B: Data Tables for XRF Analyses of Antelope Island

Sample	Na2O (%)	MgO (%)	Al2O3 (%)	SiO2 (%)	P2O5 (%)	K2O (%)	CaO (%)	TiO2 (%)	Fe2O3 (%)	Mn (%)
Quartzite's	ND	0.11	0.81	99.22	ND	0.19	0.09	ND	0.48	ND
STD	ND	0.01	0.09	0.69	ND	0.02	ND	ND	0.22	ND
Granitic	0.63	1.33	12.30	71.09	0.15	4.50	0.38	0.37	6.64	2.17
STD	0.32	0.13	0.40	2.05	0.08	0.26	0.22	0.20	0.29	7.70
Gneissic	0.42	1.35	12.30	71.21	0.16	4.91	0.42	0.50	6.78	3.67
STD	ND	0.21	0.24	3.68	0.03	0.15	0.31	0.09	2.69	5.30

Table B-1. Average Statistics by clast type from Antelope Island

Sample	Na2O (%)	MgO (%)	Al2O3 (%)	SiO2 (%)	P2O5 (%)	K2O (%)	CaO (%)	TiO2 (%)	Fe2O3 (%)	Mn (%)	Sum (%)
A08-06-X2	ND	0.13	0.84	98.72	ND	0.21	ND	ND	0.21	ND	100.25
% error	68.70%	2.39%	1.12%	0.10%	14.40%	0.62%	4.06%	5.08%	2.47%	23.10%	
A08-06-X3	ND	0.11	0.66	98.19	ND	0.15	0.09	ND	1.14	ND	100.43
% error	53.80%	2.89%	1.35%	0.10%	13.60%	0.78%	1.69%	4.67%	0.77%	21.50%	
A08-06-Y2	0.77	1.55	12.4	70.74	0.07	4.51	0.64	0.2	6.78	ND	97.86
% error	1.29%	0.29%	0.24%	0.12%	2.86%	0.12%	0.38%	0.95%	0.30%	3.00%	
A08-06-Y4	0.94	1.4	11.41	73.84	0.05	3.96	0.49	0.21	6.04	ND	98.52
% error	1.13%	0.31%	0.25%	0.12%	3.76%	0.13%	0.45%	0.91%	0.32%	2.97%	
A08-06-Z3	0.59	1.66	12.17	64.78	0.15	4.66	0.91	0.55	11.83	ND	97.61
% error	1.59%	0.28%	0.24%	0.13%	1.35%	0.12%	0.31%	1.07%	0.23%	1.73%	
A08-06-Z4	0.25	1.45	12.56	69.44	0.16	5.5	0.64	0.5	7.29	ND	97.99
% error	3.13%	0.30%	0.24%	0.12%	1.27%	0.11%	0.39%	1.14%	0.29%	3.60%	

Site 06 (High Strain): Major and minor element concentrations

Sample	Y (PPM)	Zr (PPM)	Nb (PPM)	V (PPM)	Zn (PPM)	Ni (PPM)	Cr (PPM)	Co (PPM)	Ce (PPM)	Sr (PPM)	Ba (PPM)
A08-06-X2	ND	ND	ND	ND	ND	ND	ND	155.41	ND	ND	56.67
% error	40.60%	10.30%			16.30%	13.20%	9.85%	3.82%	14.20%	69.80%	18.40%
A08-06-X3	15.63	ND	ND	ND	ND	ND	ND	131.19	ND	ND	ND
% error		12.40%			16.10%	15.30%	11.10%	4.20%	15.80%	48.00%	22.30%
A08-06-Y2	68.58	571.48	67.1	ND	69.26	ND	ND	66.44	259.23	ND	672.54
% error	3.88%	1.01%	9.57%	28.60%	9.03%	8.83%	13.60%	4.96%	3.41%	25.20%	3.38%
A08-06-Y4	56.67	563.78	ND	ND	81.37	ND	ND	ND	221.88	ND	578.13
% error	5.03%	1.03%	43.80%	29.40%	7.91%	8.03%	15.80%	6.43%	3.87%	26.30%	3.80%
A08-06-Z3	60.92	1163.11	69.38	ND	101.1	ND	ND	62.68	190.37	ND	715.03
% error	4.67%	0.58%	9.41%	10.30%	7.19%	9.11%	15.50%	4.29%	3.54%	28.90%	3.15%
A08-06-Z4	54.11	670.75	ND	ND	62.14	ND	ND	ND	116.38	ND	803.57
% error	5.35%	0.88%	12.90%	17.20%	9.77%	8.79%	11.40%	6.53%	3.65%	24.10%	2.94%

Site 06 (High Strain): Trace element abundances

Sample	Na2O (%)	MgO (%)	Al2O3 (%)	SiO2 (%)	P2O5 (%)	K2O (%)	CaO (%)	TiO2 (%)	Fe2O3 (%)	Mn (%)	Sum (%)
A08-05-X1	ND	ND	0.7	100.19	ND	0.15	ND	ND	ND	ND	101.43
% error	24.00%	0.31%	0.24%	0.12%	1.21%	0.12%	0.61%	1.07%	0.38%	2.08%	
A08-05-X2	ND	0.11	0.81	99.37	ND	0.19	ND	ND	0.25	ND	100.89
% error		2.40%	1.15%	0.10%	12.00%	0.67%	4.09%	3.43%	2.17%	5.99%	
A08-05-Y1	0.58	1.31	12.51	67.73	0.2	4.35	0.29	0.56	5.58	ND	93.38
% error	1.56%	0.31%	0.24%	0.13%	1.06%	0.12%	0.66%	1.06%	0.34%	2.88%	
A08-05-Y2	0.22	1.29	12.89	69.72	0.25	4.66	0.59	0.61	7.51	ND	98
% error	3.45%	0.32%	0.23%	0.12%	0.93%	0.12%	0.40%	1.01%	0.29%	2.48%	
A08-05-Z1	ND	1.36	12.1	74.25	0.19	4.79	0.3	0.59	4.08	ND	97.98
% error	16.00%	0.31%	0.24%	0.12%	1.10%	0.12%	0.65%	1.03%	0.39%	1.45%	
A08-05-Z2	ND	1.34	11.96	74.19	0.17	4.82	0.32	0.56	4.32	ND	97.94
% error	24.00%	0.31%	0.24%	0.12%	1.21%	0.12%	0.61%	1.07%	0.38%	2.08%	

Site 05 (Moderate Strain): Major and minor element concentrations

Sample	Y (PPM)	Zr (PPM)	Nb (PPM)	V (PPM)	Zn (PPM)	Ni (PPM)	Cr (PPM)	Co (PPM)	Ce (PPM)	Sr (PPM)	Ba (PPM)
A08-05-X1	ND	ND	ND	ND	ND	ND	ND	280.87	176.64	ND	ND
% error	74.10%	11.50%	764%		20.90%	17.30%	12.50%	2.46%	9.72%	40.40%	22.60%
A08-05-X2	ND	ND	ND	ND	ND	ND	ND	328.89	ND	ND	ND
% error	263%	20.40%			18.60%	12.10%	14.00%	2.17%	10.50%	27.90%	20.90%
A08-05-Y1	46.9	642.98	69.38	ND	83.08	ND	ND	100.42	ND	ND	1177.98
% error	6.32%	0.89%	9.04%	11.60%	7.69%	9.24%	6.06%	4.15%	2.81%	11.20%	2.14%
A08-05-Y2	60.4	1061.84	ND	ND	75.13	ND	ND	106.81	ND	ND	759.93
% error	4.70%	0.61%	11.20%	13.00%	8.54%	9.58%	14.50%	3.90%	3.70%	26.60%	3.00%
A08-05-Z1	55.42	759.38	71.13	ND	83.9	ND	ND	130.01	ND	ND	771.3
% error	5.07%	0.78%	8.81%	17.20%	7.70%	9.47%	11.60%	3.81%	3.88%	24.40%	2.99%
A08-05-Z2	54.12	680.17	72.27	ND	80.46	ND	ND	94.61	ND	ND	772.13
% error	5.22%	0.86%	8.65%	19.70%	7.97%	10.00%	12.50%	4.55%	3.62%	17.30%	3.01%

Site 05 (Moderate Strain): Trace element abundances

Sample	Na2O (%)	MgO (%)	Al2O3 (%)	SiO2 (%)	P2O5 (%)	K2O (%)	CaO (%)	TiO2 (%)	Fe2O3 (%)	Mn (%)	Sum (%)
A08-09-X2	ND	0.09%	0.77%	100.20%	ND	0.15%	ND	ND	ND	ND	101.45
% error	45.50%	3.08%	1.17%	0.10%	12.40%	0.76%	6.12%	4.37%	4.38%		
A08-09-X4	ND	0.12%	1.04%	98.63%	ND	0.27%	ND	ND	0.52%	ND	100.71
% error		2.20%	0.97%	0.10%	12.60%	0.54%	6.93%	4.06%	1.26%	36.50%	
A08-09-Y1	ND	1.13%	11.67%	73.34%	ND	4.46%	0.08%	0.25%	7.20%	ND	98.42
% error	18.70%	0.34%	0.25%	0.12%	3.91%	0.12%	1.95%	1.79%	0.29%	9.27%	
A08-09-Y5	ND	1.31%	12.88%	71.18%	0.15%	5.05%	0.18%	0.36%	6.72%	ND	98.05
% error	24.90%	0.31%	0.23%	0.12%	1.37%	0.11%	0.95%	1.40%	0.30%	10.20%	
A08-09-Z3	ND	1.24%	12.50%	72.45%	0.12%	4.80%	0.16%	0.36%	6.83%	ND	98.68
% error	28.30%	0.32%	0.24%	0.12%	1.69%	0.12%	1.04%	1.39%	0.30%	8.01%	
A08-09-Z4	ND	1.04%	12.49%	72.15%	0.13%	4.86%	0.19%	0.43%	6.35%	ND	97.89
% error	16.30%	0.36%	0.24%	0.12%	1.54%	0.12%	0.90%	1.24%	0.31%	15.30%	

Site 09 (Low Strain): Major and minor element concentrations

Sample	Y (PPM)	Zr (PPM)	Nb (PPM)	V (PPM)	Zn (PPM)	Ni (PPM)	Cr (PPM)	Co (PPM)	Ce (PPM)	Sr (PPM)	Ba (PPM)
A08-09-X2	15.01	ND	ND	ND	ND	ND	ND	224.45	ND	ND	ND
% error		17.00%			16.10%	11.80%	11.60%	2.90%	11.60%	222%	
A08-09-X4	ND	ND	ND	ND	ND	ND	ND	200.7	161.35	ND	ND
% error	83.00%	11.30%			17.40%	11.10%	10.90%	3.15%	9.90%		20.30%
A08-09-Y1	77.37	679.72	ND	ND	ND	ND	ND	69.21	ND	ND	877.16
% error	3.35%	0.87%	20.50%	19.50%	10.10%	9.24%	12.40%	4.83%	3.40%	17.80%	2.73%
A08-09-Y5	42.85	727.92	ND	ND	ND	ND	ND	57.41	221.88	ND	763.57
% error	7.46%	0.82%	48.20%	15.80%	11.30%	9.91%	14.20%	5.25%	3.32%	63.60%	3.04%
A08-09-Z3	47.61	836.73	ND	ND	67.24	ND	ND	107.19	ND	ND	766.36
% error	6.51%	0.74%	19.30%	19.10%	9.10%	8.30%	12.60%	3.93%	3.89%	26.20%	3.05%
A08-09-Z4	44.44	614.88	ND	ND	ND	ND	ND	83.2	ND	71.99	1072.31
% error	7.07%	0.94%	23.70%	30.70%	11.40%	9.21%	12.30%	4.57%	3.25%	9.10%	2.32%

Site 09 (Low Strain): Trace element abundances

Appendix C: Grain Size Histograms for Individual Clasts

C.1 Low Strain

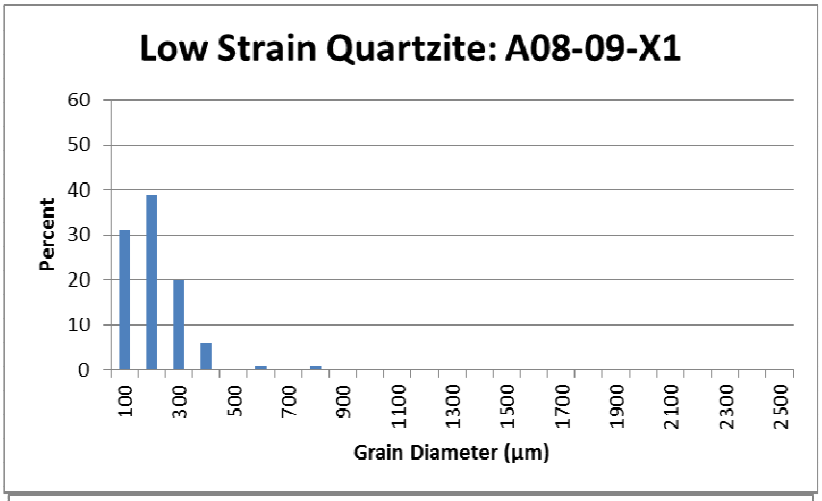

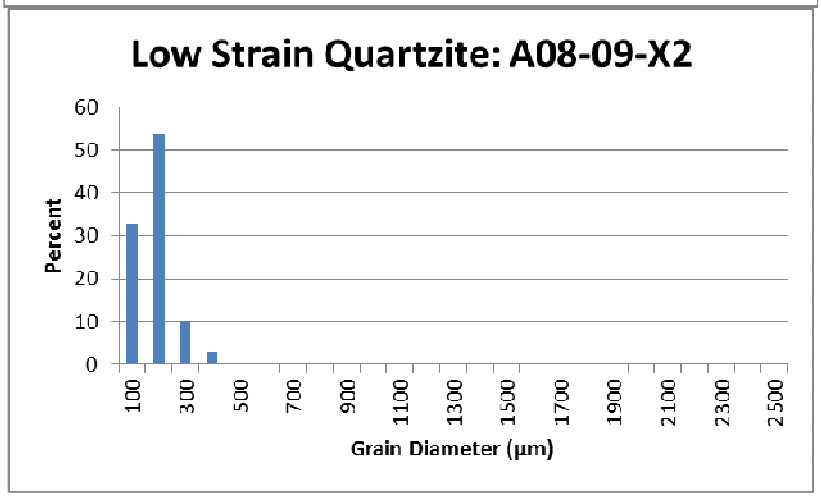

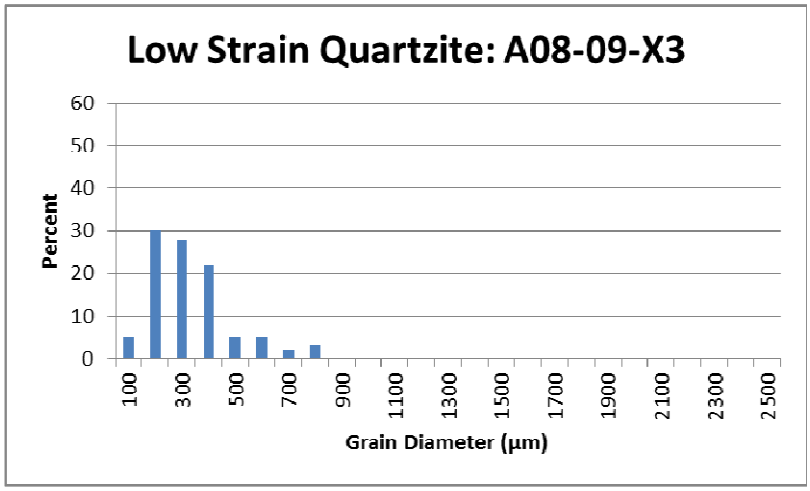

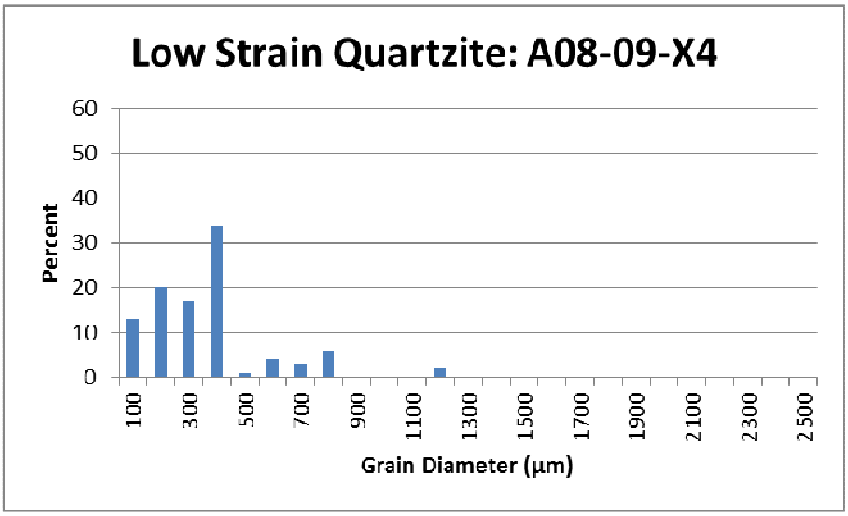
Low Strain Quartzite: A08-09-X4
Percent
60
50
40
30
20
10
0
100
300
500
700
900
1100
1300
1500
1700
1900
2100
2300
2500
Grain Diameter (µm)

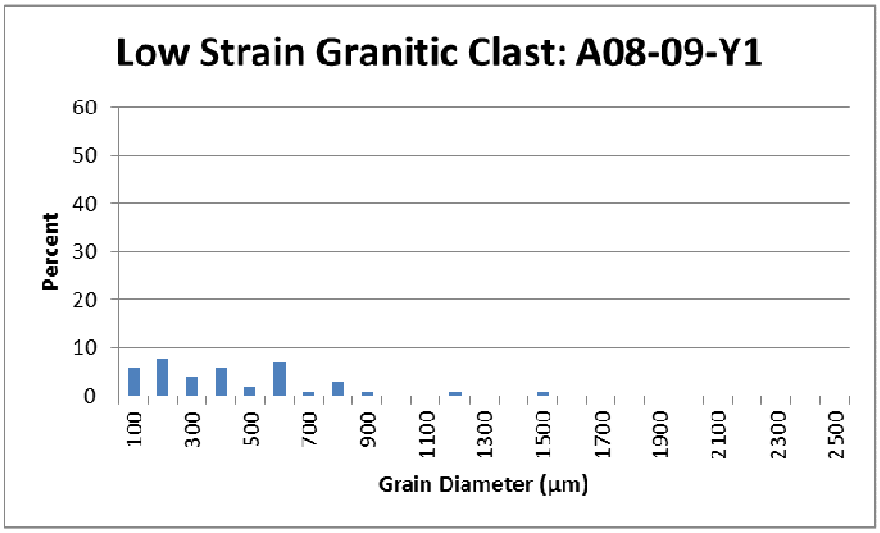
Low Strain Granitic Clast: A08-09-Y1
Percent
60
50
40
30
20
10
0
100
300
500
700
900
1100
1300
1500
1700
1900
2100
2300
2500
Grain Diameter (µm)

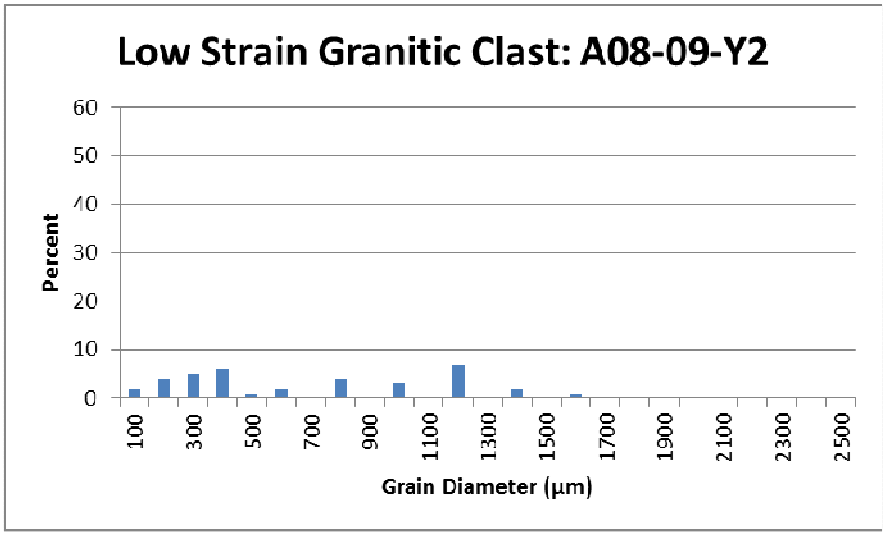
Low Strain Granitic Clast: A08-09-Y2
Percent
60
50
40
30
20
10
0
100
300
500
700
900
1100
1300
1500
1700
1900
2100
2300
2500
Grain Diameter (µm)

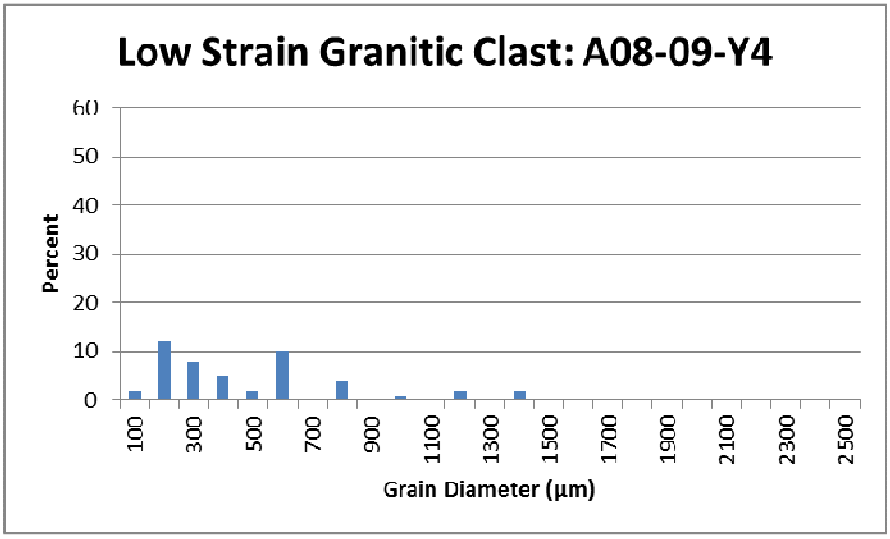
Low Strain Granitic Clast: A08-09-Y4
Percent
60
50
40
30
20
10
0
100
300
500
700
900
1100
1300
1500
1700
1900
2100
2300
2500
Grain Diameter (µm)

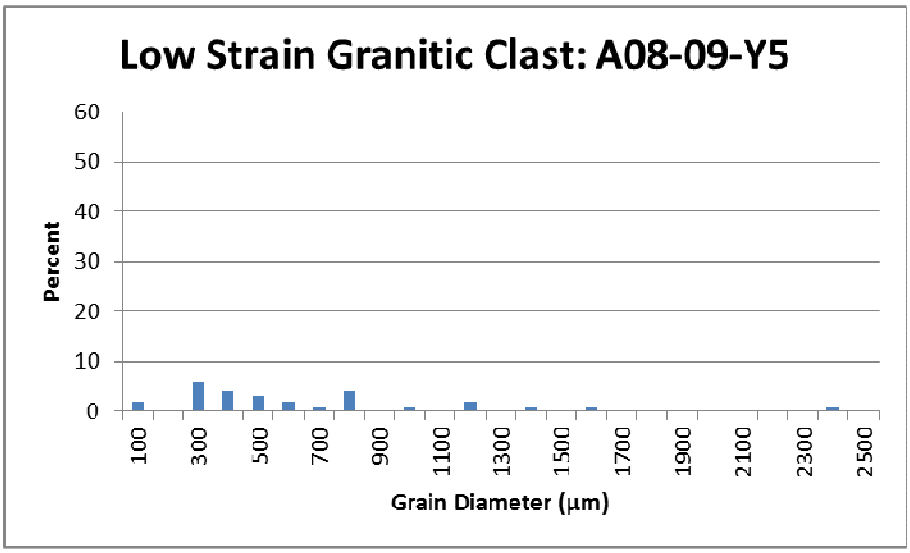
Low Strain Granitic Clast: A08-09-Y5
Percent
60
50
40
30
20
10
0
100
300
500
700
900
1100
1300
1500
1700
1900
2100
2300
2500
Grain Diameter (µm)

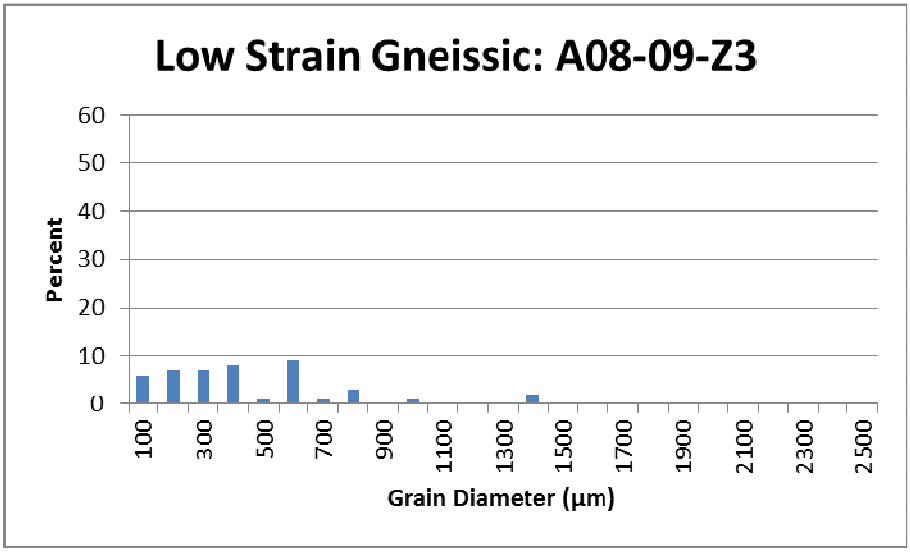
Low Strain Gneissic: A08-09-Z3
Percent
60
50
40
30
20
10
0
100
300
500
700
900
1100
1300
1500
1700
1900
2100
2300
2500
Grain Diameter (µm)

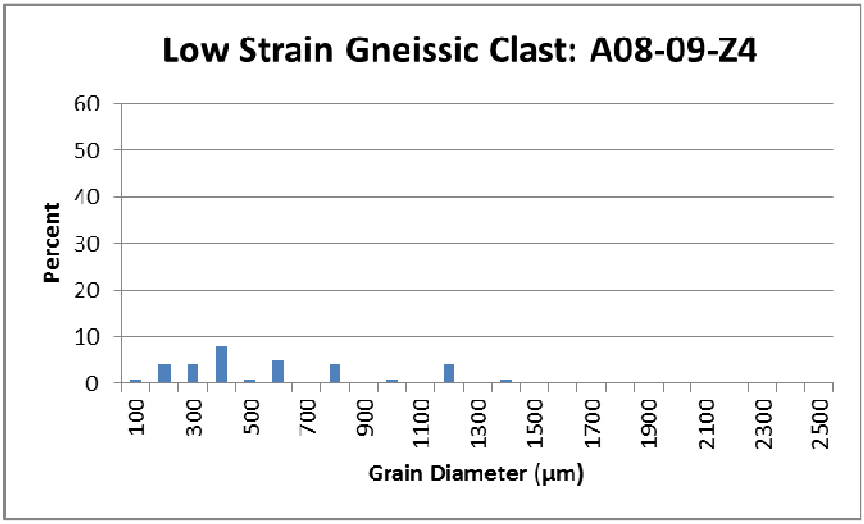
Low Strain Gneissic Clast: A08-09-Z4
Percent
60
50
40
30
20
10
0
100
300
500
700
900
1100
1300
1500
1700
1900
2100
2300
2500
Grain Diameter (µm)

C.2 Moderate Strain

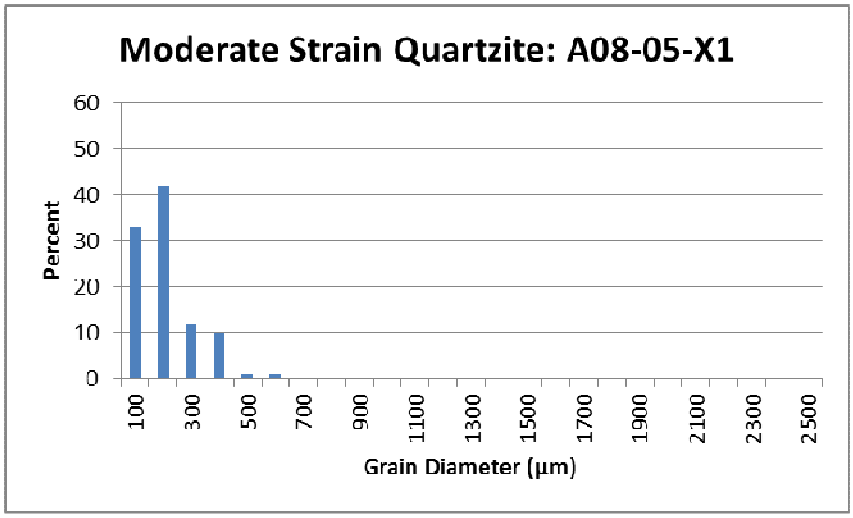

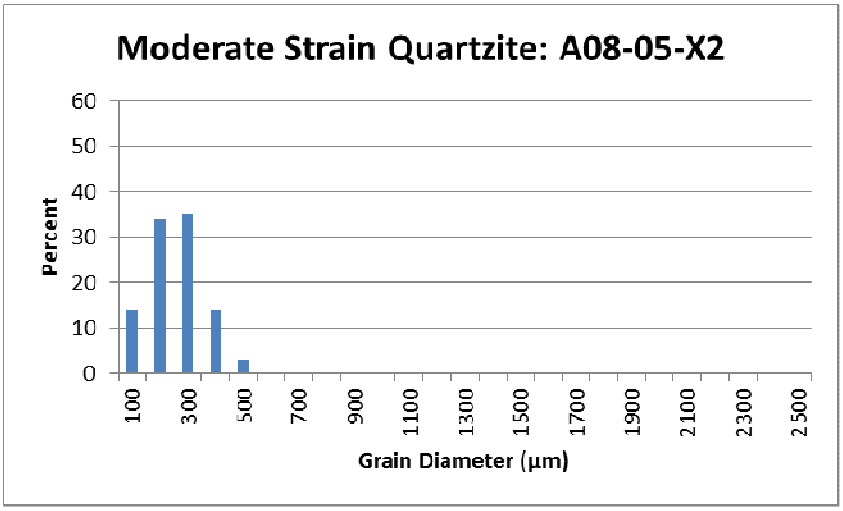

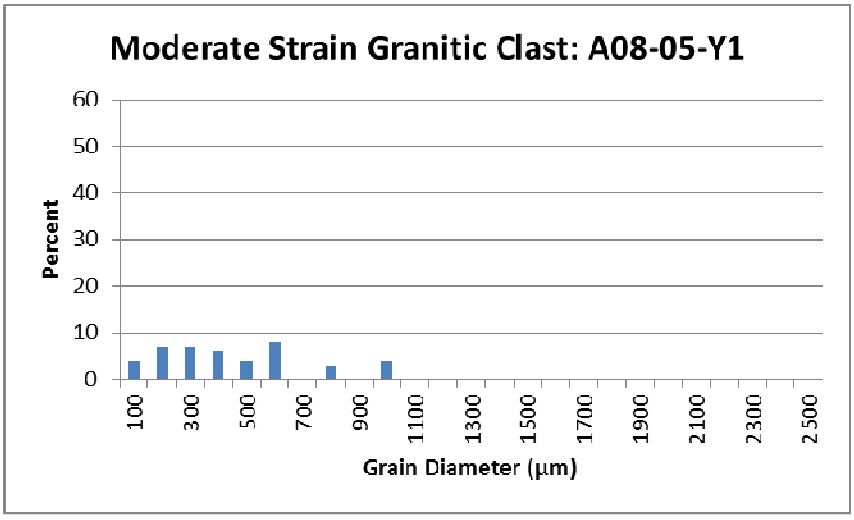

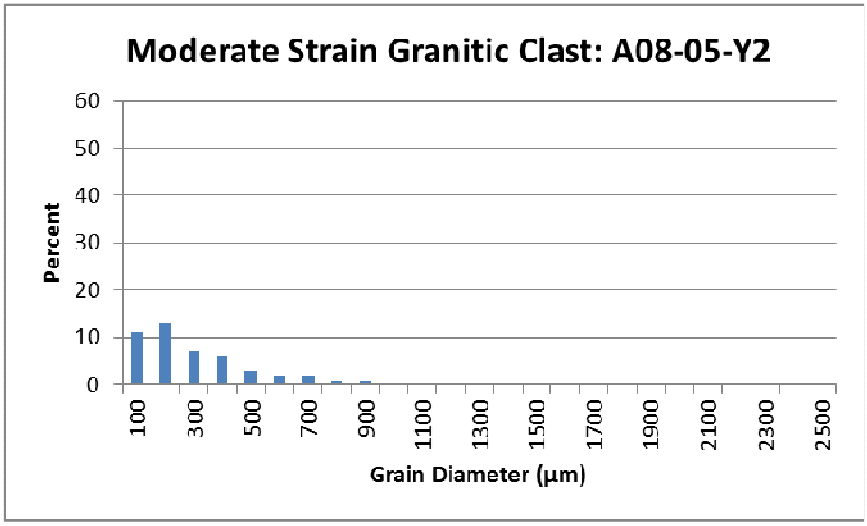
Moderate Strain Granitic Clast: A08-05-Y2
Percent
60
50
40
30
20
10
0
100
300
500
700
900
1100
1300
1500
1700
1900
2100
2300
2500
Grain Diameter (µm)

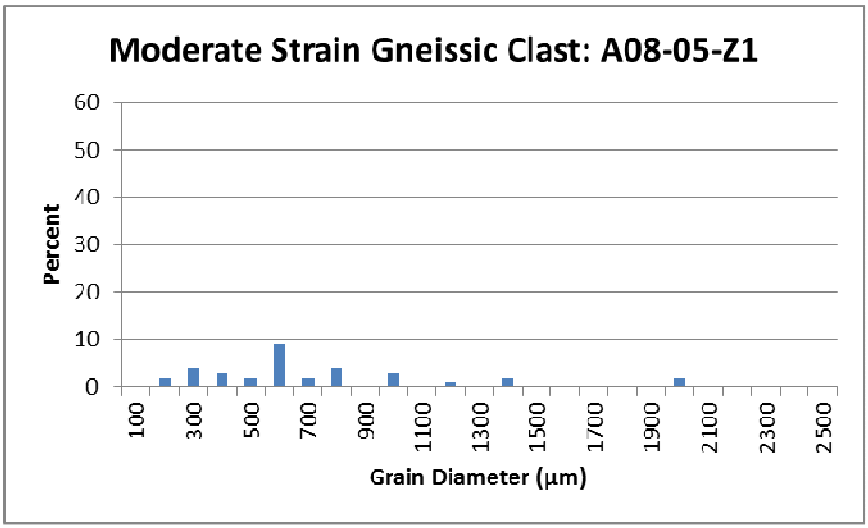
Moderate Strain Gneissic Clast: A08-05-Z1
Percent
60
50
40
30
20
10
0
100
300
500
700
900
1100
1300
1500
1700
1900
2100
2300
2500
Grain Diameter (µm)

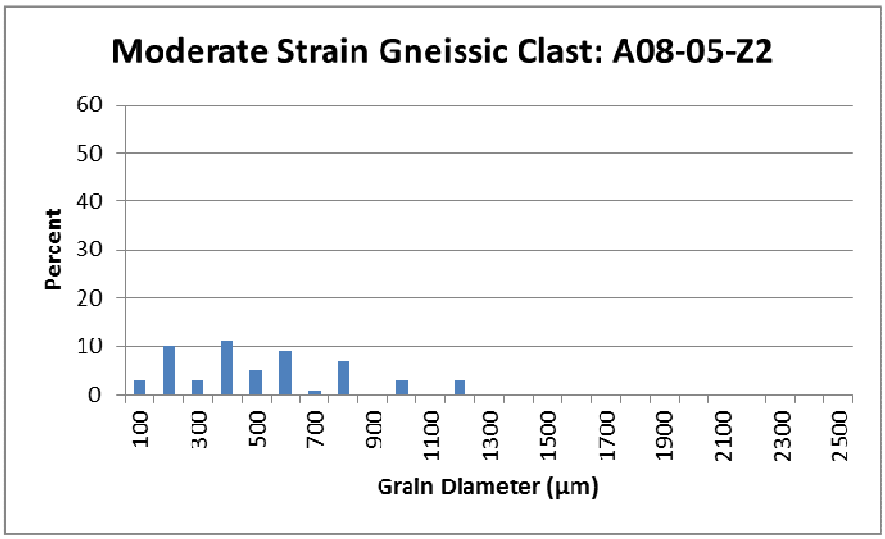
Moderate Strain Gneissic Clast: A08-05-Z2
Percent
60
50
40
30
20
10
0
100
300
500
700
900
1100
1300
1500
1700
1900
2100
2300
2500
Grain Diameter (µm)

C.3 High Strain

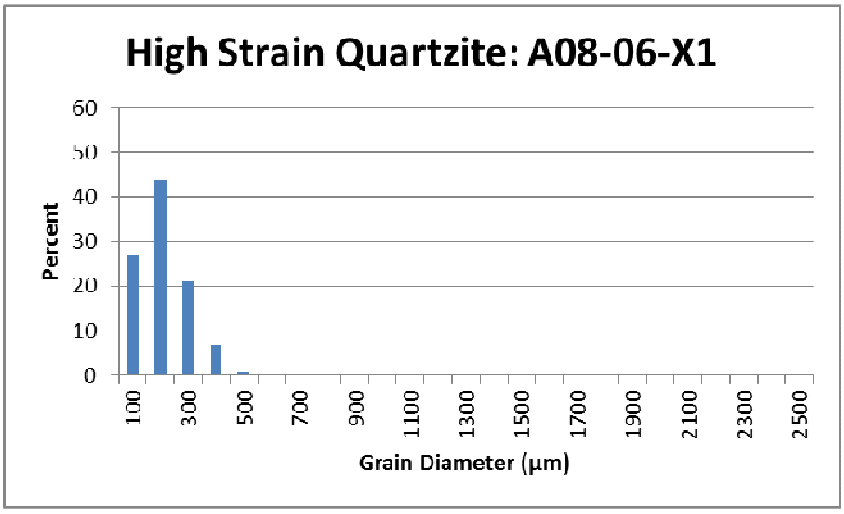

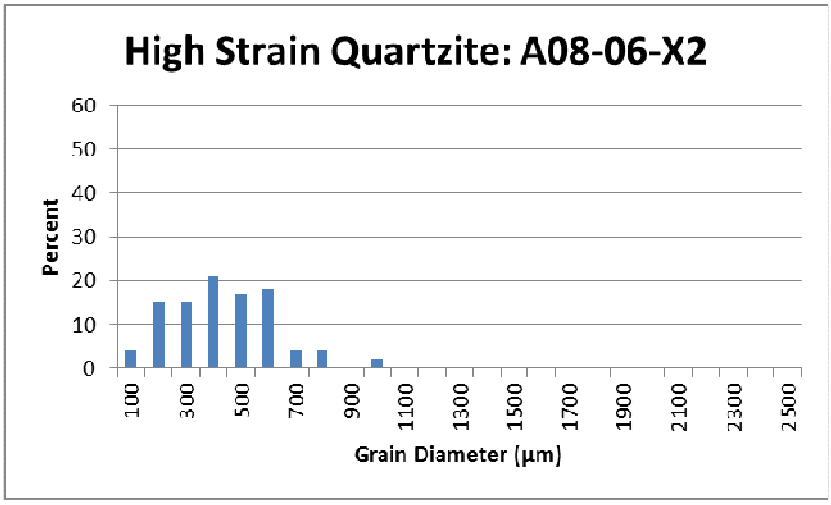

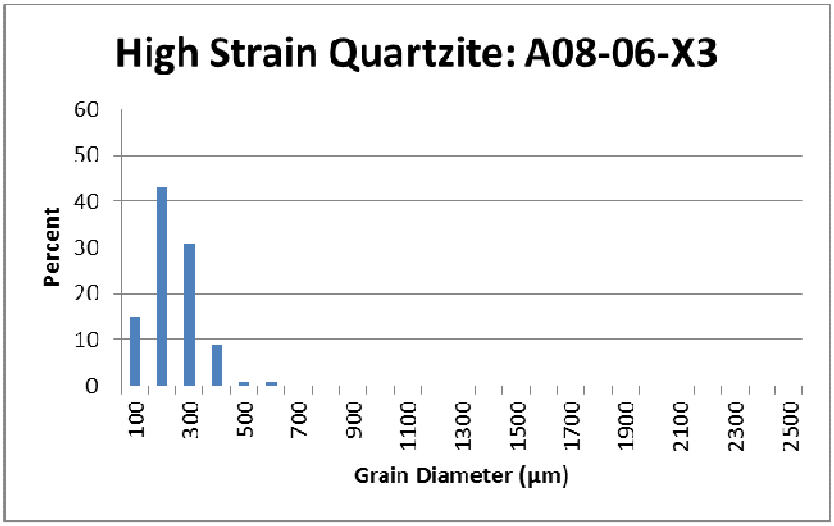

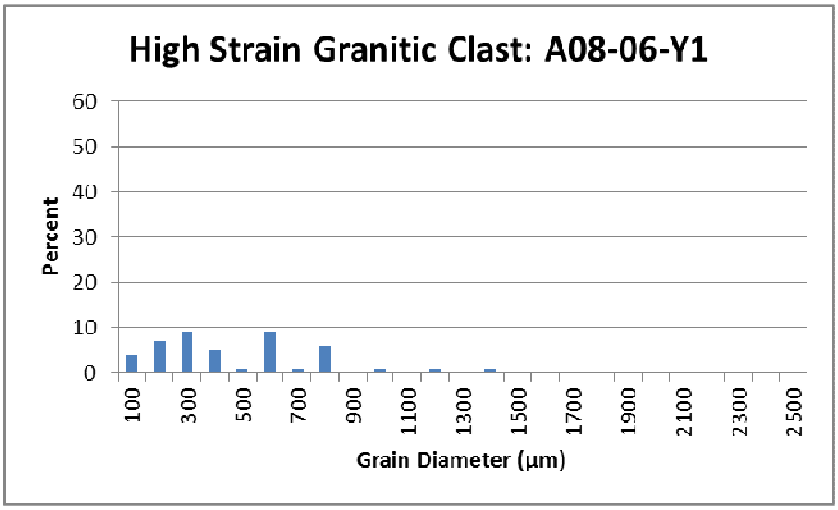
High Strain Granitic Clast: A08-06-Y1
Percent
60
50
40
30
20
10
0
100
300
500
700
900
1100
1300
1500
1700
1900
2100
2300
2500
Grain Diameter (µm)

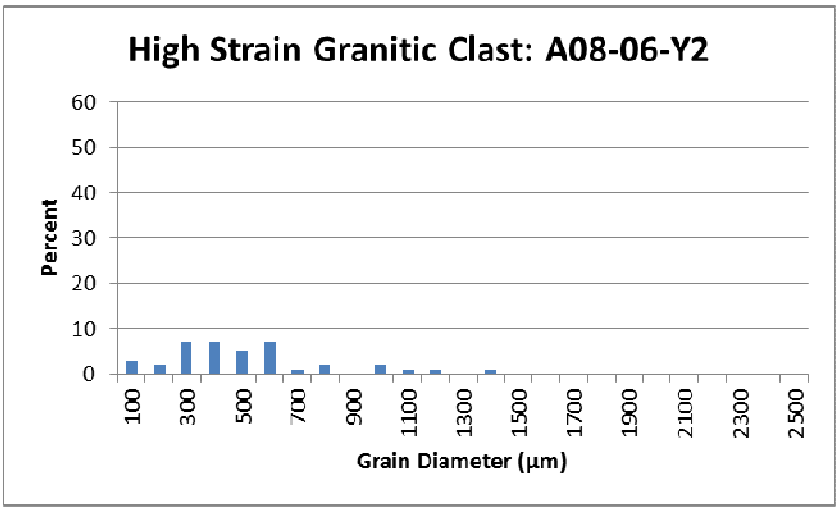
High Strain Granitic Clast: A08-06-Y2
Percent
60
50
40
30
20
10
0
100
300
500
700
900
1100
1300
1500
1700
1900
2100
2300
2500
Grain Diameter (µm)

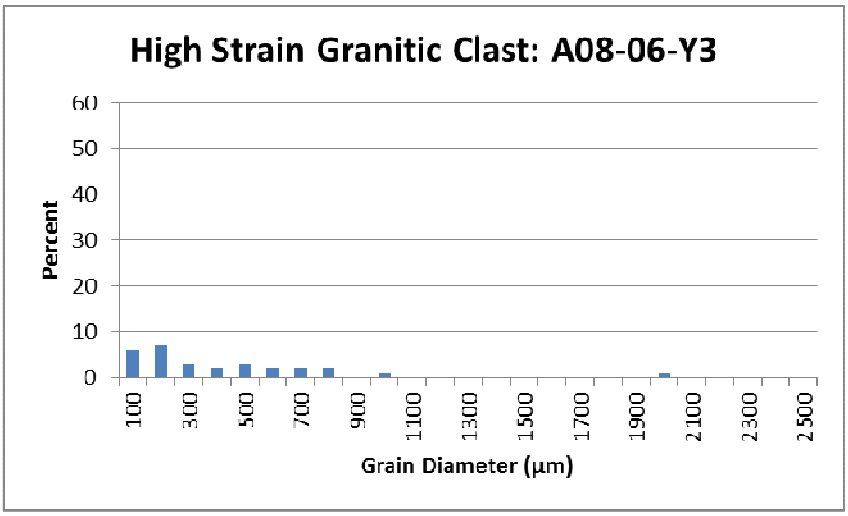
High Strain Granitic Clast: A08-06-Y3
Percent
60
50
40
30
20
10
0
100
300
500
700
900
1100
1300
1500
1700
1900
2100
2300
2500
Grain Diameter (µm)

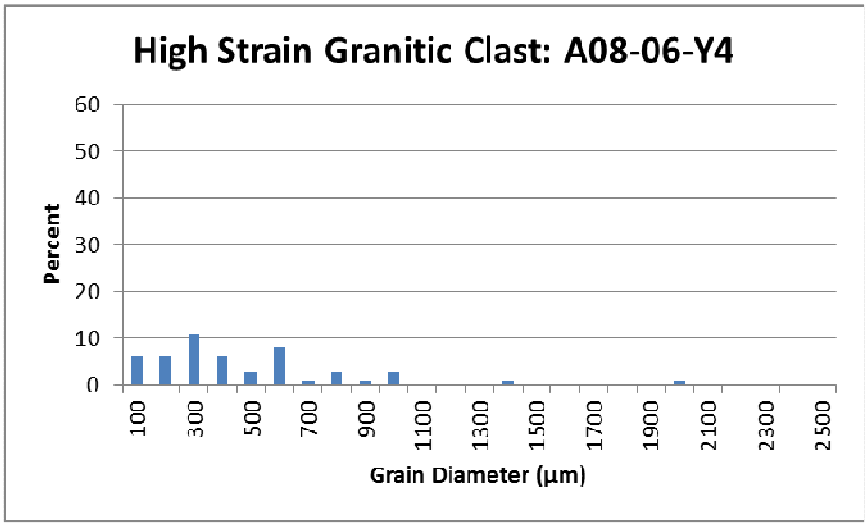
High Strain Granitic Clast: A08-06-Y4
Percent
60
50
40
30
20
10
0
100
300
500
700
900
1100
1300
1500
1700
1900
2100
2300
2500
Grain Diameter (µm)

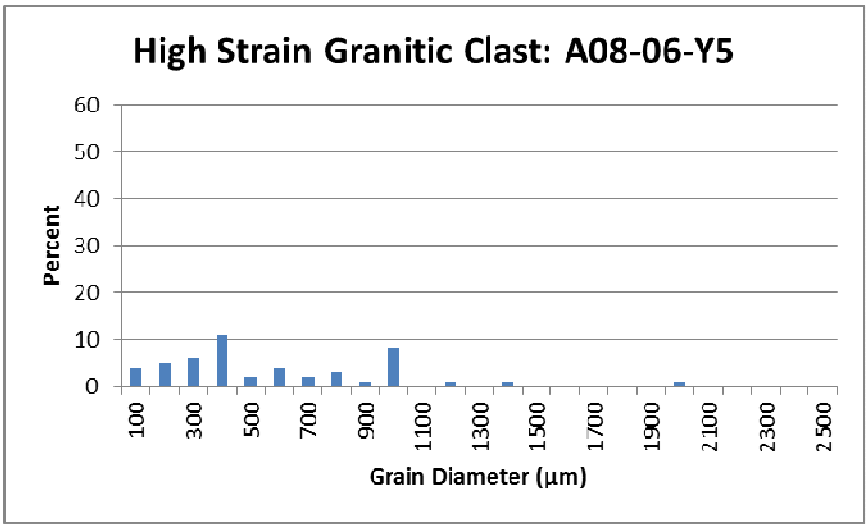
High Strain Granitic Clast: A08-06-Y5
Percent
60
50
40
30
20
10
0
100
300
500
700
900
1100
1300
1500
1700
1900
2100
2300
2500
Grain Diameter (µm)

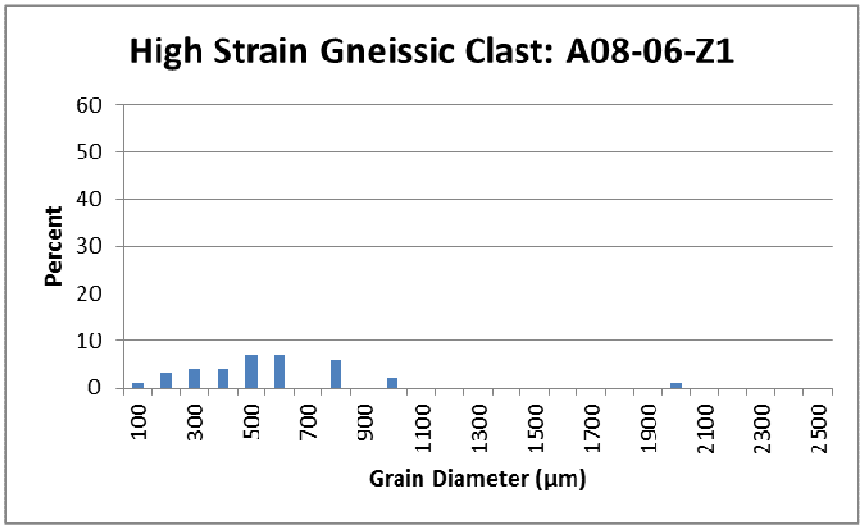
High Strain Gneissic Clast: A08-06-Z1
Percent
60
50
40
30
20
10
0
100
300
500
700
900
1100
1300
1500
1700
1900
2100
2300
2500
Grain Diameter (µm)

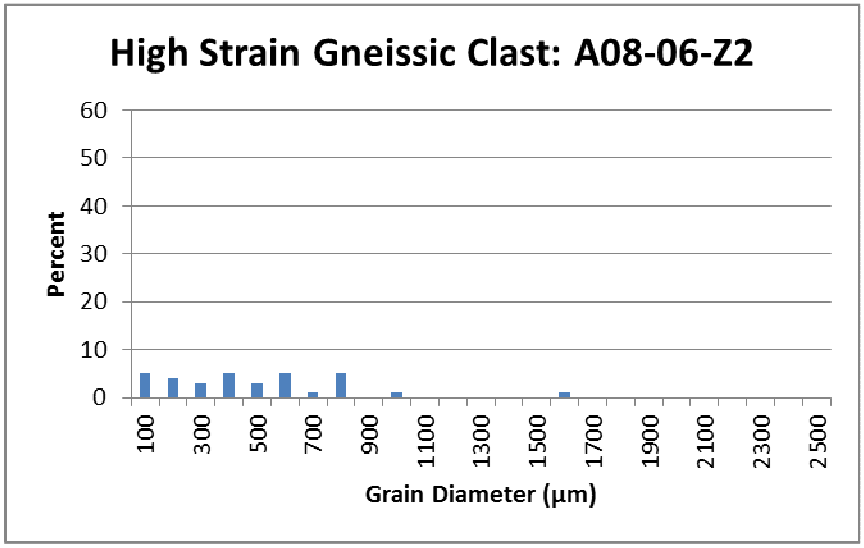
High Strain Gneissic Clast: A08-06-Z2
Percent
60
50
40
30
20
10
0
100
300
500
700
900
1100
1300
1500
1700
1900
2100
2300
2500
Grain Diameter (µm)

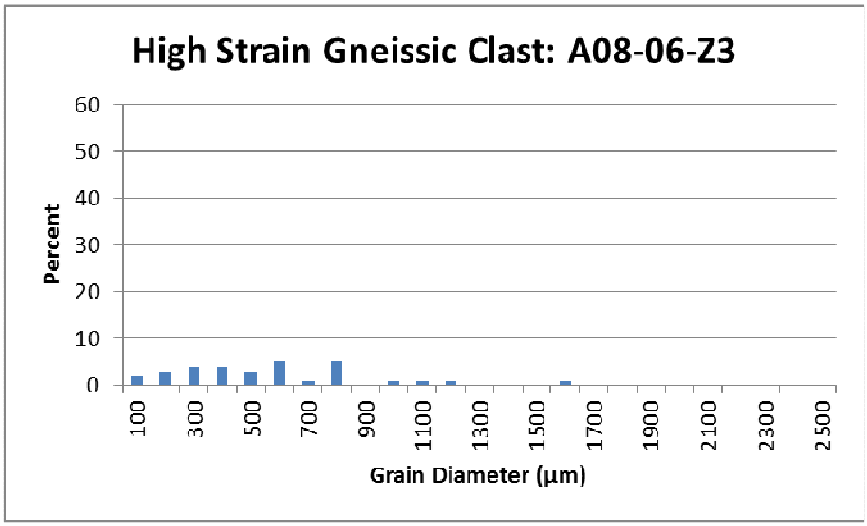
High Strain Gneissic Clast: A08-06-Z3
Percent
60
50
40
30
20
10
0
100
300
500
700
900
1100
1300
1500
1700
1900
2100
2300
2500
Grain Diameter (µm)

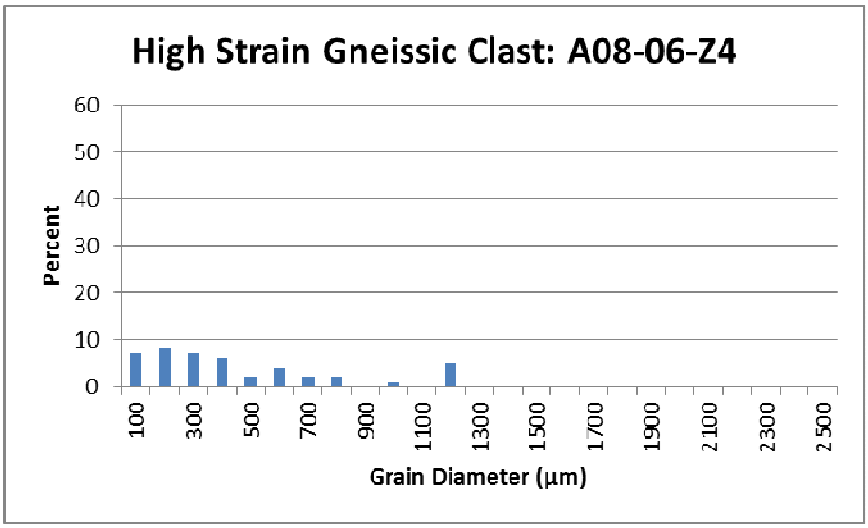
High Strain Gneissic Clast: A08-06-Z4
Percent
60
50
40
30
20
10
0
100
300
500
700
900
1100
1300
1500
1700
1900
2100
2300
2500
Grain Diameter (µm)

Appendix D: Quantitative Microstructural Data in Quartz Grains for Individual clasts at each Sample Site

KEY

Code	Description
Incl's	Fluid Inclusions
Fract	Microfractures
U.E.	Undulose Extinction
Laml	Deformation Lamellae
Subgr	Subgrains
Rexstl	Recrystallization
Bulg.	Bulged Grain Boundary

D.1 Low Strain

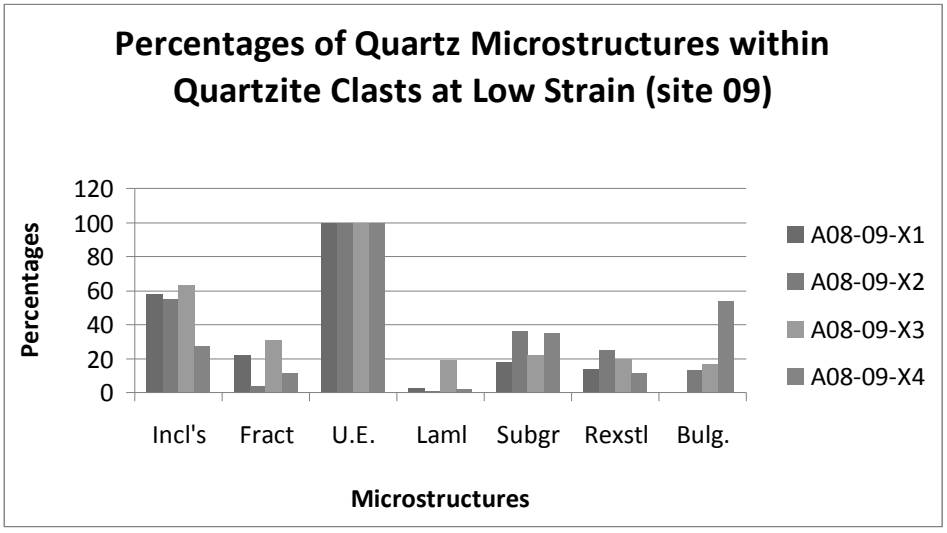

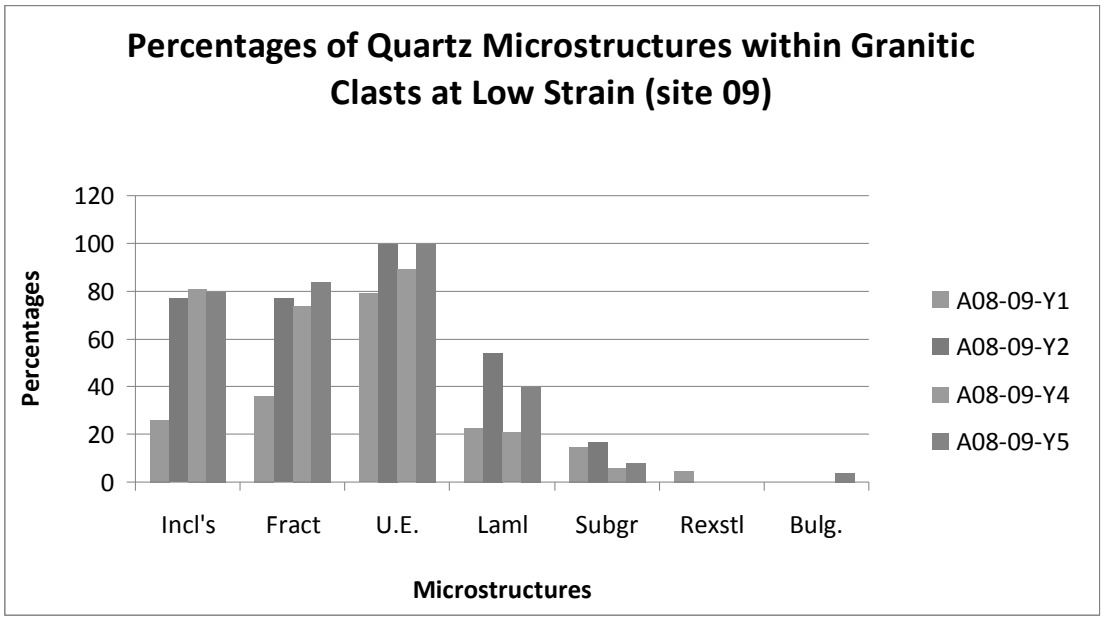
Percentages of Quartz Microstructures within Granitic Clasts at Low Strain (site 09)
120
100
80
60
40
20
0
Percentages
Incl's
Fract
U.E.
Laml
Subgr
Rexstl
Bulg.
Microstructures
A08-09-Y1
A08-09-Y2
A08-09-Y4
A08-09-Y5

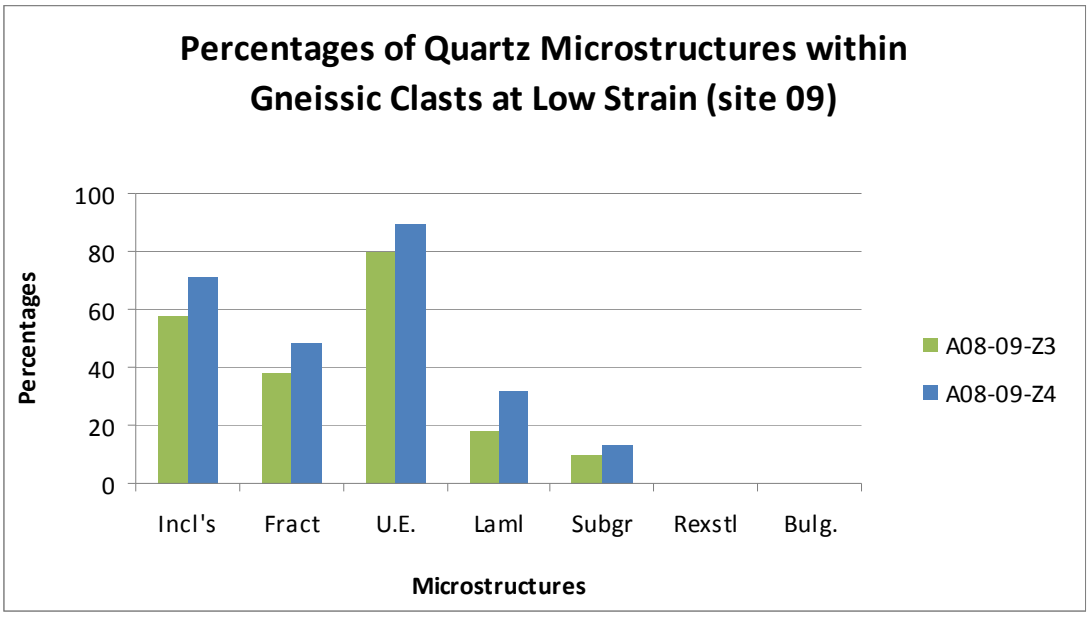
Percentages of Quartz Microstructures within Gneissic Clasts at Low Strain (site 09)
100
80
60
40
20
0
Percentages
Incl's
Fract
U.E.
Laml
Subgr
Rexstl
Bulg.
Microstructures
A08-09-Z3
A08-09-Z4

D.2 Moderate Strain

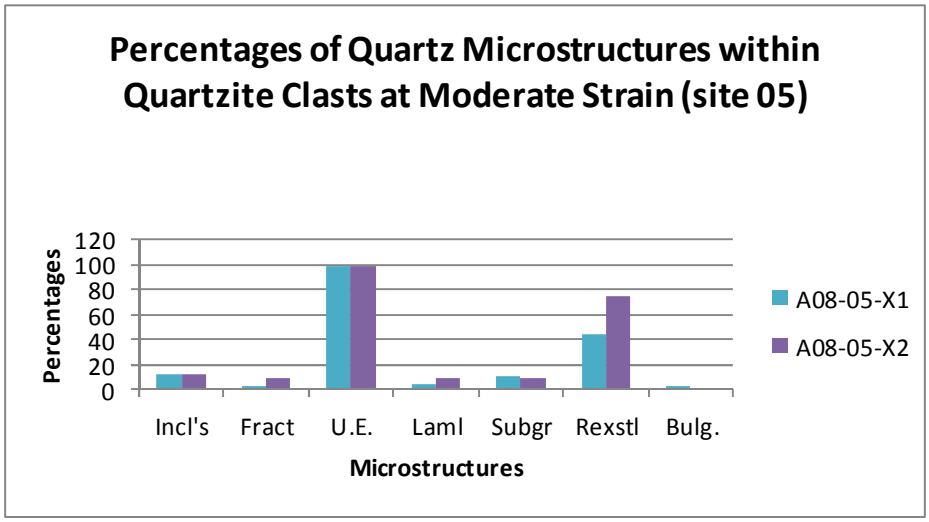

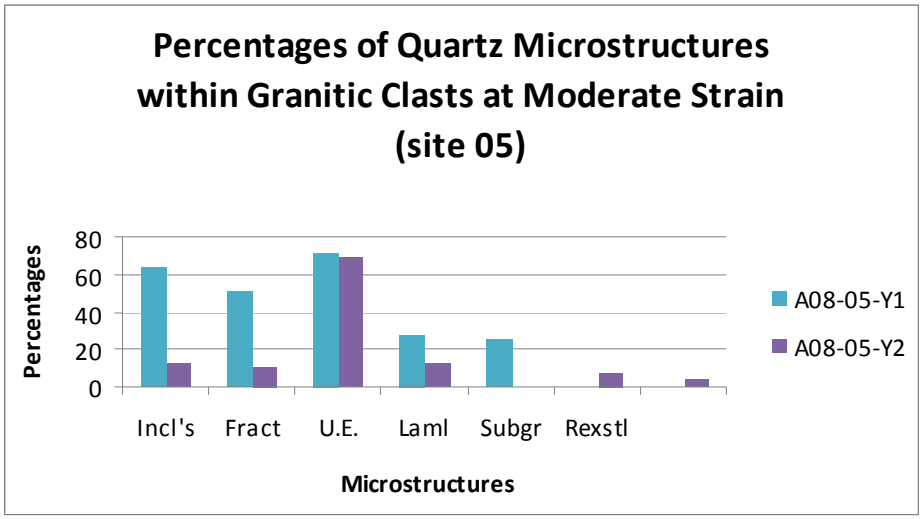

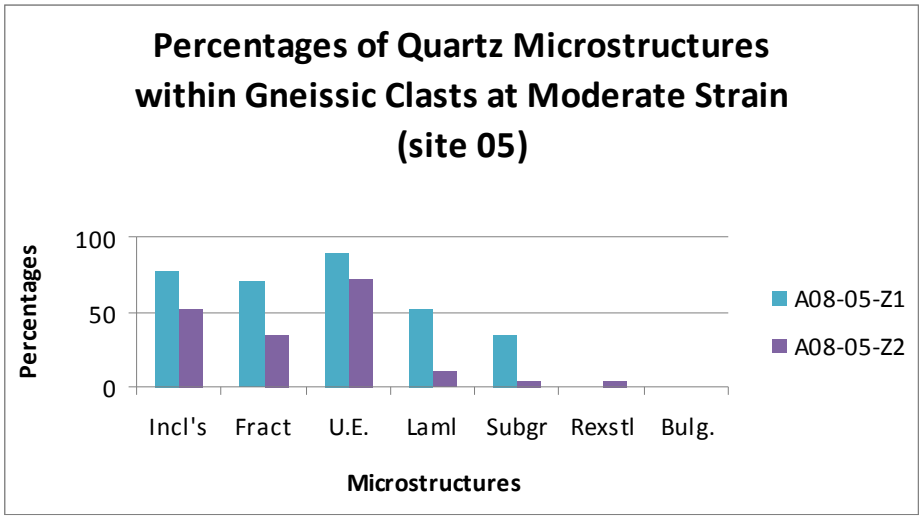

D.3 High Strain

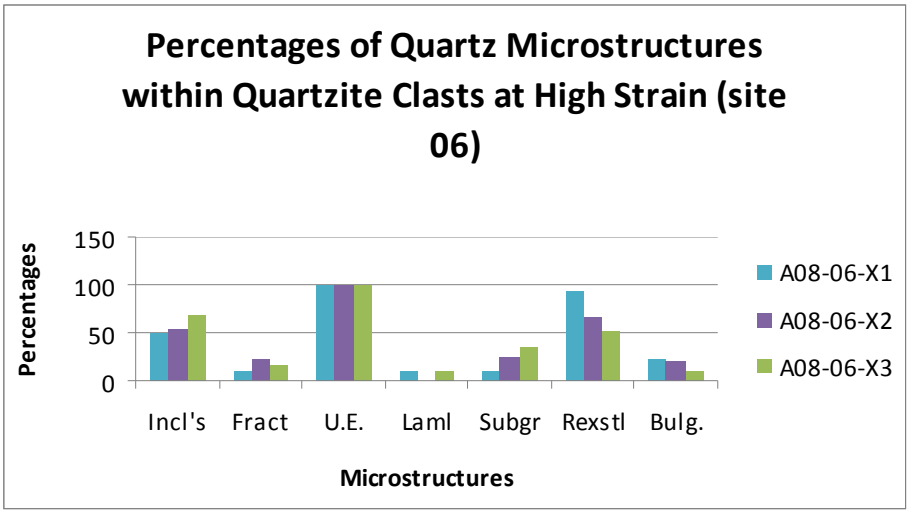

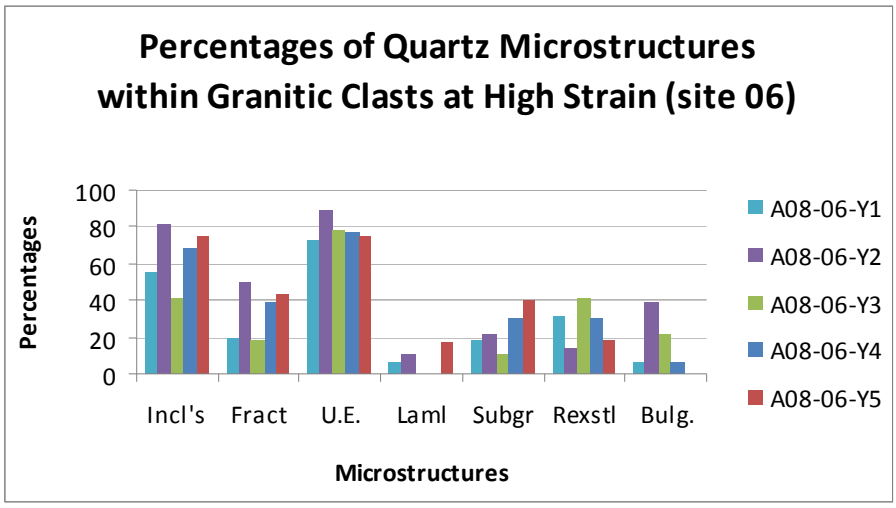

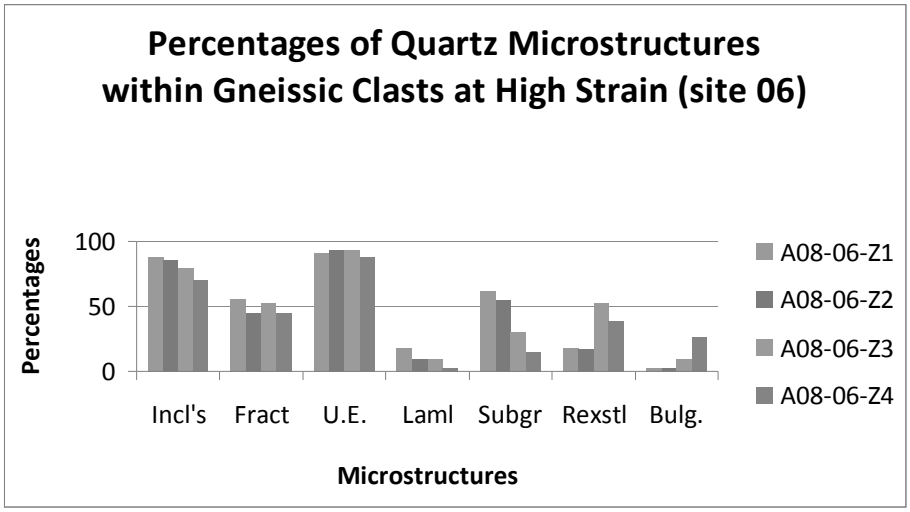

D.4 Average Microstructures for Each Clast Type